INFORMATION TO USERS

This manuscript has been reproduced from the microfilm master. UMI films the text directly from the original or copy submitted. Thus, some thesis and dissertation copies are in typewriter face, while others may be from any type of computer printer.

The quality of this reproduction is dependent upon the quality of the copy submitted. Broken or indistinct print, colored or poor quality illustrations and photographs, print bleedthrough, substandard margins, and improper alignment can adversely affect reproduction.

In the unlikely event that the author did not send UMI a complete manuscript and there are missing pages, these will be noted. Also, if unauthorized copyright material had to be removed, a note will indicate the deletion.

Oversize materials (e.g., maps, drawings, charts) are reproduced by sectioning the original, beginning at the upper left-hand corner and continuing from left to right in equal sections with small overlaps.

Photographs included in the original manuscript have been reproduced xerographically in this copy. Higher quality 6" x 9" black and white photographic prints are available for any photographs or illustrations appearing in this copy for an additional charge. Contact UMI directly to order.

Bell & Howell Information and Learning
300 North Zeeb Road, Ann Arbor, MI 48106-1346 USA
800-521-0600

UMI®

Downloaded from SHAREOK. Persistent Handle URL: https://hdl.handle.net/11244/5968

UNIVERSITY OF OKLAHOMA

GRADUATE COLLEGE

INVESTIGATION OF LIGAND MISDIRECTION USING THE KINETIC ELEMENT EFFECT AND THE KINETIC ENTHALPY EFFECT

A Dissertation

SUBMITTED TO THE GRADUATE FACULTY

in partial fulfillment of the requirements for the

degree of

Doctor of Philosophy

By

Susan Stanislav Alguindigue

Norman, Oklahoma

2000

UMI Number: 9968105

UMI®

UMI Microform9968105
Copyright 2000 by Bell & Howell Information and Learning Company.
All rights reserved. This microform edition is protected against
unauthorized copying under Title 17, United States Code.

Bell & Howell Information and Learning Company
300 North Zeeb Road
P.O. Box 1346
Ann Arbor, MI 48106-1346

INVESTIGATION OF LIGAND MISDIRECTION
USING THE KINETIC ELEMENT EFFECT AND THE KINETIC ENTHALPY EFFECT

A Dissertation APPROVED FOR THE
DEPARTMENT OF CHEMISTRY AND BIOCHEMISTRY

BY

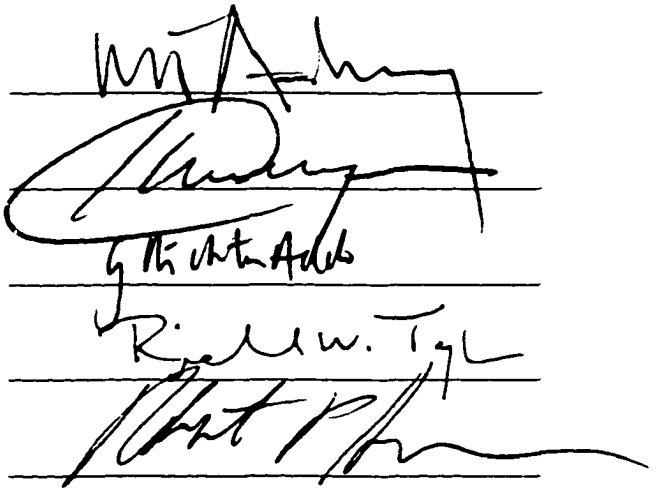

© Copyright by Susan Stanislav Alguindigue 2000
All Rights Reserved.

Acknowledgments

First, I would like to thank my mentor, Dr. Michael T. Ashby for his faith, support and encouragement throughout my graduate work. The time that Dr. Ashby spent teaching me to work in the laboratory, speak about my research and write papers concerning the results has made it possible for me to be successful. I am also grateful to Drs. K. Droegemeier, R. Houser, G. Richter-Addo, and R. Taylor for serving as my advisory committee members. Special thanks to Dr. Masood Khan for X-ray studies and Dr. P.K. Das (Phillips Petroleum Company) for *ab initio* calculations.

I would also like to thank all my coworkers in Dr. Ashby's group: Danny McGuire, V. Sam Asirvathem, John Lilly, Justin Schwane, Dominic Moore, Angela Kowalski and Isaac Manke. I am also thankful for the friendship and support offered from Olga Ivanova and Li Chen.

I am extremely grateful for the funding that I received from the Department of Education G.A.A.N.N. fellowship and the National Science Foundation which made it possible for me to make progress in the laboratory.

Finally, I wish to thank my husband, Hector Alguindigue and his family for helping me write this dissertation by taking care of our son while I was working. I am grateful to my sisters, Sarah Stanislav and Pam Campbell for their constant encouragement. I would like to offer special thanks to my beautiful son, Daniel Alguindigue for his sweet cooperation while I focused my attention away from him. I would like to dedicate this dissertation to my parents, Jerry and Binnie Stanislav for their unfailing love, encouragement and belief in me which made this work possible.

Table of Contents

		Page
List of Tables		ix
List of Figures		xii
Reproduction Permission		xv
List of Abbreviations		xvi
Abstract		xvii
CHAPTER 1	**INTRODUCTION**	
1.1	Bonding in Inorganic and Organometallic Compounds	1
1.2	Misdirected Valency	3
1.3	Periodic Trends in Metal-Ligand Bond Strengths of Transition Metals	5
1.3.1	Transition metal-carbonyl bond strength	6
1.3.2	Transition metal-methyl and metal-hydrogen bond strength	7
1.4	Comparison of the Kinetics of Second-Row and Third-Row Transition Metal Reactions	10
1.4.1	Substitution kinetics	10
1.4.2	Thioether inversion kinetics	13
1.5	Kinetic Element Effect	15
1.6	Summary	23
CHAPTER 2	**KINETICS AND MECHANISM OF THE STEREOCHEMICAL ISOMERIZATION OF AN ARENE-RUTHENIUM COMPLEX OF THE ATROPISOMERIC LIGAND 1,1'-BIPHENYL-2,2'DIAMINE**	
2.1	Introduction	24
2.1.1	Arene-metal half sandwich complexes	24
2.1.2	Isomerization of ethylenediamine metal complexes	26
2.1.3	1,1'-Biphenyl-2,2'-diamine	28
2.2	Synthesis and X-Ray Crystal Structure of $[Ru(bipy)_2(dabp)](PF_6)_2$	29
2.3	Variable Temperature ^1H Nmr Experiments of $[Ru(bipy)_2(dabp)](PF_6)_2$	33
2.4	Synthesis of $(Ar)M(dabp)(Cl)(PF_6)$, M=Ru, Os	35

2.5	X-Ray Crystal Structure of (Ar)Ru(dabp)(Cl)(PF_6)	35
2.6	^{1}H NMR Experiments of (Ar)M(dabp)(Cl)(PF_6), M=Ru, Os	38
2.6.1	Assignment of ^{1}H NMR spectrum	38
2.6.2	Kinetic experiments	43
2.7	Synthesis and ^{1}H NMR Experiments of (Ar)M(dabn)(Cl)(PF_6)	50
2.8	Discussion	50
2.9	Summary	54
CHAPTER 3	**KINETICS OF ARENE-METAL COMPLEXES OF 1,1'-BIISOQUINOLINE, [(Ar)M(Biiq)(X)]$^+$, M=Ru, Os; X=Cl, I**	
3.1	Introduction	55
3.2	Synthesis of [(Ar)M(biiq)(X)]$^+$, M=Ru, Os; X=Cl, I	55
3.3	X-Ray Crystal Structures of [(Ar)M(biiq)(Cl)]$^+$, M=Ru, Os	56
3.4	2D-COSY and 2D-EXSY ^{1}H NMR Experiments	60
3.5	SIT and LSA ^{1}H NMR Kinetic Experiments	60
3.5.1	[(Ar)M(biiq)(Cl)]$^+$, M=Ru, Os;	60
3.5.2	[(Ar)M(biiq)(I)]$^+$, M=Ru, Os;	69
3.6	Discussion	90
3.7	Summary	92
CHAPTER 4	**ROTATIONAL BARRIERS ABOUT THE METAL-SULFUR BONDS OF GROUP IV METAL THIOLATES**	
4.1	Introduction	93
4.2	Synthesis of Bis(cyclopentadienyl)(chloro)(thiolato)zirconium(II) Complexes, (η^5-C_5H_5)$_2$Zr(Cl)(SR)	96
4.3	Rotational Barriers of Bis(cyclopentadienyl)(chloro)(thiolato)zirconium(II) Complexes, (η^5-C_5H_5)$_2$Zr(Cl)(SR)	98
4.4	Synthesis and X-Ray Crystal Structures of Bis(cyclopentadienyl)di(thiolato)zirconium(II)	101

	Complexes, $(\eta^5\text{-}C_5H_5)_2Zr(SR)_2$	
4.5	Computational Study of Bis(cyclopentadienyl)-(chloro)(thiolato)zirconium(II) Complexes, $(\eta^5\text{-}C_5H_5)_2Zr(Cl)(SR)$	105
4.6	Discussion	107
4.7	Summary	118
CHAPTER 5	**EXPERIMENTAL DETAILS**	
5.1	Synthesis of Arene-Metal $[((\eta^6\text{-}C_6H_6)(M)(N\text{-}N)(X)]^+$ and Metal Bipyridine $[M(bipy)_2(N\text{-}N)]^{2+}$ Complexes (M=Ru(II), Os(II); X=Cl,I)	120
5.1.1	Materials and sample preparation	120
5.1.2	N-N = 2,2'-diamino-biphenyl	120
5.1.3	N-N=(S)-1,1'-binapthyl-2,2'-diamine	122
5.1.4	N-N=1,1'-biisoquinoline	123
5.2	X-Ray Crystallography Studies of Arene-Metal $[(\eta^6\text{-}C_6H_6)(M)(N\text{-}N)(X)]^+$ and Metal Bipyridine $[M(bipy)_2(N\text{-}N)]^{2+}$ Complexes (M=Ru(II), Os(II); X=Cl).	125
5.2.1	N-N = 2,2'-diamino-biphenyl	126
5.2.2	N-N=1,1'-biisoquinoline	135
5.3	Synthesis of Zirconcene Thiolate Complexes	143
5.3.1	Materials	143
5.3.2	Bis(η^5-cyclopentadienyl)(chloro)(thiolato)-zirconium(II) complexes,$(\eta^5\text{-}C_5H_5)_2Zr(Cl)(SR)$	143
5.3.3	Bis(cyclopentadienyl)di(thiolato)zirconium(II) Complexes, $(\eta^5\text{-}C_5H_5)_2Zr(SR)_2$	144
5.4	X-Ray Crystallography Studies of Bis(η^5-cyclopentadienyl)di-(thiolato)zirconium(II), $(\eta^5\text{-}C_5H_5)_2Zr(SR)_2$	145
5.5	Computational Studies of Bis(η^5-cyclopentadienyl)-(chloro)(thiolato)zirconium(II) complexes, $(\eta^5\text{-}C_5H_5)_2Zr(Cl)(SR)$	158
5.6	NMR Experiments-Assignment of Resonances	161
5.6.1	Variable temperature	161
5.6.2	Two dimensional experiments: COSY and NOESY	161
5.7	NMR Experiments-Kinetics of Exchange	162
5.7.1	Coalescence temperature	164
5.7.2	Line-shape analysis	164

5.7.3	Spin-inversion transfer	165
5.7.4	2D-exchange spectroscopy	167
CHAPTER 6	**CONCLUSION**	
6.1	Dynamic Effects of Misdirected Metal-Ligand Bonds	169
6.2	Summary of Experimental Work	169
6.3	Results	171
6.3.1	Kinetic element effect	171
6.3.2	Kinetic enthalpy effect	173
6.3.3	Ground-state effect	176
6.4	Future Work	178
6.5	Conclusion	179
	References	181

List of Tables

		Page
Table 1.1	Comparison of Experimental Second-Row and Third-Row Metal-Carbonyl, Metal-Methyl and Metal-Hydrogen Bond Dissociation Energies	8
Table 1.2	Comparison of Theoretical Second-Row and Third-Row Metal-Carbonyl, Metal-Methyl and Metal-Hydrogen Bond Dissociation Energies	9
Table 1.3	Comparison of Second-Row and Third-Row Metal Ligand Exchange and Substitution Kinetics	12
Table 1.4	Comparison of Inversion Barriers of Second-Row and Third-Row Transition Metal-Thioether Complexes	14
Table 2.1	Activation Parameters for the Conformational Interconversion of $[Fe(CN)_4(1,2\text{-diamine})]^+$	27
Table 2.2	Selected Interatomic Distance, Angles and Torsion Angles for $[Ru(bipy)_2(dabp)]PF_6$	31
Table 2.3	Selected Interatomic Distance, Angles and Torsion Angles for $[(Ar)Ru(dabp)(Cl)]PF_6$	36
Table 2.4	Comparison of the Kinetic Data Obtained for the Atropisomerism of $[(Ar)M(dabp)(Cl)]PF_6$, M=Ru, Os	50
Table 3.1	Comparison of Selected Interatomic Distance, Angles and Torsion Angles for $[(Ar)M(biiq)(Cl)]PF_6$, M=Ru, Os	57
Table 3.2	Comparison of the Kinetic Data Obtained for the Atropisomerism of the Ru and Os Derivatives of $[(Ar)M(biiq)(Cl)]PF_6$	78
Table 3.3	Comparison of the Kinetic Data Obtained for the Atropisomerism of the Ru and Os Derivatives of $[(Ar)M(biiq)(I)]PF_6$	87
Table 3.4	Comparison of the Thermodynamic Data Obtained for the Atropisomerization of Ru and Os Derivatives of $[(Ar)M(biiq)(X)]PF_6$	92
Table 4.1	Selected Interatomic Distance, Angles and Torsion Angles for Bent Metallocene Thiolate Complexes	95
Table 4.2	Kinetic Parameters and Zr-SR Rotational Barriers for $Cp_2Zr(Cl)(SR)$	99
Table 4.3	Selected Interatomic Distance, Angles and Torsion Angles for $Cp_2Zr(SR)_2$	102

Table 4.4	Computed Thermodynamic Data for $Cp_2Zr(Cl)(SR)$ at the DFT-B3LYP Level	105
Table 4.5	Selected Computed Interatomic Distances Angles, Torsion Angles and Dihedral Angles for the Ground-State and Transition-State Structures of $Cp_2Zr(Cl)(SR)$	106
Table 4.6	Comparison of Zirconocene and Hafnocene Dithiolate Compounds	118
Table 5.1	Crystal data for Compound $[Ru(bipy)_2(dabp)]PF_6$	127
Table 5.2	Atomic Coordinates and Equivalent Isotropic Displacement Parameters for $[Ru(bipy)_2(dabp)]PF_6$	128
Table 5.3	Anisotropic Displacement Parameters for $[Ru(bipy)_2(dabp)]PF_6$	129
Table 5.4	Hydrogen Coordinates and Equivalent Isotropic Displacement Parameters for $[Ru(bipy)_2(dabp)]PF_6$	130
Table 5.5	Crystal Data for Compound $[(Ar)Ru(dabp)(Cl)]PF_6$	131
Table 5.6	Atomic Coordinates and Equivalent Isotropic Displacement Parameters for $[(Ar)Ru(dabp)(Cl)]PF_6$	132
Table 5.7	Anisotropic Displacement Parameters for $[(Ar)Ru(dabp)(Cl)]PF_6$	133
Table 5.8	Hydrogen Coordinates and Equivalent Isotropic Displacement Parameters for $[(Ar)Ru(dabp)(Cl)]PF_6$	134
Table 5.9	Crystal Data for Compounds $[(Ar)M(biiq)(Cl)]PF_6$, M=Ru, Os	136
Table 5.10	Atomic Coordinates and Equivalent Isotropic Displacement Parameters for $[(Ar)Ru(biiq)(Cl)]PF_6$	137
Table 5.11	Anisotropic Displacement Parameters for $[(Ar)Ru(biiq)(Cl)]PF_6$	138
Table 5.12	Hydrogen Coordinates and Equivalent Isotropic Displacement Parameters for $[(Ar)Ru(biiq)(Cl)]PF_6$	139
Table 5.13	Atomic Coordinates and Equivalent Isotropic Displacement Parameters for $[(Ar)Os(biiq)(Cl)]PF_6$	140
Table 5.14	Anisotropic Displacement Parameters for $[(Ar)Os(biiq)(Cl)]PF_6$	141
Table 5.15	Hydrogen Coordinates and Equivalent Isotropic Displacement Parameters for $[(Ar)Ru(biiq)(Cl)]PF_6$	142
Table 5.16	Crystal data for Compounds $Cp_2Zr(SR)_2$	147

Table 5.17	Atomic Coordinates and Equivalent Isotropic Displacement Parameters for $Cp_2Zr(SCH_3)_2$	148
Table 5.18	Anisotropic Displacement Parameters for $Cp_2Zr(SCH_3)_2$	149
Table 5.19	Hydrogen Coordinates and Equivalent Isotropic Displacement Parameters for $Cp_2Zr(SCH_3)_2$	150
Table 5.20	Atomic Coordinates and Equivalent Isotropic Displacement Parameters for $Cp_2Zr(SCH_2CH_3)_2$	151
Table 5.21	Anisotropic Displacement Parameters for $Cp_2Zr(SCH_2CH_3)_2$	152
Table 5.22	Hydrogen Coordinates and Equivalent Isotropic Displacement Parameters for $Cp_2Zr(SCH_2CH_3)_2$	153
Table 5.23	Atomic Coordinates and Equivalent Isotropic Displacement Parameters for $Cp_2Zr(SCH(CH_3)_2)_2$	154
Table 5.24	Anisotropic Displacement Parameters for $Cp_2Zr(SCH(CH_3)_2)_2$	154
Table 5.25	Hydrogen Coordinates and Equivalent Isotropic Displacement Parameters for $Cp_2Zr(SCH(CH_3)_2)_2$	155
Table 5.26	Atomic Coordinates and Equivalent Isotropic Displacement Parameters for $Cp_2Zr(SC(CH_3)_3)_2$	156
Table 5.27	Anisotropic Displacement Parameters for $Cp_2Zr(SC(CH_3)_3)_2$	156
Table 5.28	Hydrogen Coordinates and Equivalent Isotropic Displacement Parameters for $Cp_2Zr(SC(CH_3)_3)_2$	157
Table 5.29	Details of Computation Methods	160
Table 6.1	Comparison of Thermodynamic Data for Atropisomerization Reactions of Ruthenium and Osmium	173
Table 6.2	Comparison of Reactivity of Group 8 Metal Carbonyl Compounds with PPh_3 at 25°C	175
Table 6.3	Racemization-Rate Constants at 30°C and Activation Parameters for Racemization in 1,1'-Biisoquinolines	178

List of Figures

		Page
Figure 1.1	Types of misdirected bonds	2
Figure 1.2	Mechanism of interconversion of diastereomers of Ru and Os derivatives of $[M(bipy)_2(biiq)]^{2+}$	16
Figure 1.3	Reaction profiles for the atropisomerism of the major and minor isomers of Ru and Os derivatives of $[M(bipy)_2(biiq)]^{2+}$	20
Figure 1.4	Mechanism of inversion of sulfur in isomerization of Ru and Os derivatives of [M(bipy)$_2$(tetrahydrothiophenene)]	21
Figure 1.5	Energy diagram illustrating the Kinetic Isotope Effect	22
Figure 2.1	Molecular structures of $[Ru(bipy)_2(dabp)]^{2+}$	32
Figure 2.2	Variable temperature ^{1}H NMR Spectra of $[Ru(bipy)_2(dabp)]^{2+}$	34
Figure 2.3	Molecular structures of $[(Ar)Ru(dabp)(Cl)]^+$	37
Figure 2.4	2D-COSY and 2D-NOESY Spectra of $[(Ar)Ru(dabp)(Cl)]^+$	39
Figure 2.5	2D-COSY Spectrum of $[(Ar)Os(dabp)(Cl)]^+$	40
Figure 2.6	2D-EXSY Spectrum of $[(Ar)Ru(dabp)(Cl)]^+$	41
Figure 2.7	2D-EXSY Spectrum of $[(Ar)Os(dabp)(Cl)]^+$	42
Figure 2.8	Variable temperature ^{1}H NMR Spectra of $[(Ar)Ru(dabp)(Cl)]^+$	44
Figure 2.9	Linear dependence on temperature of NH chemical shifts for $[(Ar)Ru(dabp)(Cl)]^+$	45
Figure 2.10	Linear dependence on temperature of NH chemical shifts for $[(Ar)Os(dabp)(Cl)]^+$	46
Figure 2.11	SIT fits for $[(Ar)Ru(dabp)(Cl)]^+$ at 20-25 °C	47
Figure 2.12	SIT fits for $[(Ar)Ru(dabp)(Cl)]^+$ at 30-40 °C	48
Figure 2.13	SIT fits for $[(Ar)M(dabp)(Cl)]^+$ at 50 °C for M=Ru and 20 °C for M=Os	49
Figure 2.14	Possible mechanisms and exchange matrices for the isomerization of $[(Ar)M(dabp)(Cl)]^+$; M=Ru, Os.	52

Figure 3.1	Molecular structures of $[(Ar)Ru(biiq)(Cl)]^+$	58
Figure 3.2	Molecular structures of $[(Ar)Os(biiq)(Cl)]^+$	59
Figure 3.3	2D-COSY Spectrum of $[(Ar)Ru(biiq)(Cl)]^+$	61
Figure 3.4	2D-COSY Spectrum of $[(Ar)Os(biiq)(Cl)]^+$	62
Figure 3.5	2D-COSY Spectrum of $[(Ar)Ru(biiq)(I)]^+$	63
Figure 3.6	2D-COSY Spectrum of $[(Ar)Os(biiq)(I)]^+$	64
Figure 3.7	2D-EXSY Spectrum of $[(Ar)Ru(biiq)(Cl)]^+$	65
Figure 3.8	2D-EXSY Spectrum of $[(Ar)Os(biiq)(Cl)]^+$	66
Figure 3.9	2D-EXSY Spectrum of $[(Ar)Ru(biiq)(I)]^+$	67
Figure 3.10	2D-EXSY Spectrum of $[(Ar)Os(biiq)(I)]^+$	68
Figure 3.11	SIT fits of $[(Ar)Ru(biiq)(Cl)]^+$ at 20-25 °C	70
Figure 3.12	SIT fits of $[(Ar)Ru(biiq)(Cl)]^+$ at 34-38 °C	71
Figure 3.13	SIT fits of $[(Ar)Ru(biiq)(Cl)]^+$ at 41-46 °C	72
Figure 3.14	SIT fits of $[(Ar)Ru(biiq)(Cl)]^+$ at 51-55 °C	73
Figure 3.15	SIT fits of $[(Ar)Os(biiq)(Cl)]^+$ at 21-24 °C	74
Figure 3.16	SIT fits of $[(Ar)Os(biiq)(Cl)]^+$ at 29-34 °C	75
Figure 3.17	SIT fits of $[(Ar)Os(biiq)(Cl)]^+$ at 41-46 °C	76
Figure 3.18	SIT fits of $[(Ar)Os(biiq)(Cl)]^+$ at 51-55 °C	77
Figure 3.19	SIT fits of $[(Ar)Ru(biiq)(I)]^+$ at 38-43 °C	79
Figure 3.20	SIT fits of $[(Ar)Ru(biiq)(I)]^+$ at 48-53 °C	80
Figure 3.21	SIT fits of $[(Ar)Ru(biiq)(I)]^+$ at 57-62 °C	81
Figure 3.22	SIT fits of $[(Ar)Os(biiq)(I)]^+$ at 38-43 °C	82
Figure 3.23	SIT fits of $[(Ar)Os(biiq)(I)]^+$ at 48-83 °C	83
Figure 3.24	SIT fits of $[(Ar)Os(biiq)(I)]^+$ at 59 °C	84
Figure 3.25	LSA of $[(Ar)Ru(biiq)(I)]^+$	85
Figure 3.26	LSA fits of $[(Ar)Os(biiq)(I)]^+$	86

Figure 3.27	Eyring plot of kinetic data for $[(Ar)M(biiq)(Cl)]^+$	88
Figure 3.28	Eyring plot of kinetic data for $[(Ar)M(biiq)(I)]^+$	89
Figure 4.1	Endo and Exo conformations for metallocene thiolate complexes	94
Figure 4.2	^1H NMR Spectra of $Cp_2Zr(Cl)(SR)$ at 20° C	97
Figure 4.3	Variable temperature ^1H NMR Spectra of $Cp_2Zr(Cl)(SMe)$	100
Figure 4.4	^1H NMR Spectra of $Cp_2Zr(SR)_2$ at 20° C	103
Figure 4.5	Molecular structures of $Cp_2Zr(SR)_2$	104
Figure 4.6	Comparison of trends in selected metric parameters of computed ground-state and transition-state structures of $Cp_2Zr(Cl)(SMe)$	108
Figure 4.7	Graphical representation of computed thermodynamic data for rotational barriers about the Zr-S bond of $Cp_2Zr(Cl)(SR)$	109
Figure 4.8	Possible axial and equatorial conformations of methyl and ethyl substituted cyclohexane	114
Figure 4.9	Possible ground state and transition state structures for $Cp_2Zr(Cl)(SR)$, R=Me, Et	115

Reproduction Permission

Portions of this dissertation have been reported in the following published or submitted publications.

1. Ashby, M.T.; Alguindigue, S.S.; Khan, M.A.; "Misdirected π-Donor Ligands: $(\eta^5\text{-}C_5H_5)_2Zr(Cl)(SR)$ with Sterically More Demanding R Groups have Lower Rotational Barriers" *Inorg. Chim Acta* **1998**, 270, 227.

2. Alguindigue, S.S.; Khan, M.A.; Ashby, M.T.; "Kinetics and Mechanism of the Stereochemical Isomerization of an Arene-Ruthenium Complex of the Atropisomeric Ligand 1,1'-Biphenyl-2,2'-diamine" *Organometallics* **1999**, 18, 5112.

3. Ashby, M.T.; Alguindigue, S.S.; Khan, M.A.; "Kinetic Element Effect for Atropisomerization of an Organometallic Complex of the Misdirected Ligand 1,1'-Biisoquinoline" *Organometallics* **2000**, 19, 547.

4. Alguindigue, S.S.; Khan, M.A.; Ashby, M.T.; "Syntheses and Molecular Structures of Ruthenium(II) Complexes of the Atropisomeric Ligands 1,1'-Biphenyl-2,2'-diamine and 3,3'-Diamino-2,2'-bipyridine" *Inorg. Chim. Acta* submitted.

5. Das, P.K.; Alguindigue, S.S.; Ashby, M.T.; "A DFT Study of Zr-S Rotational Barriers of $(\eta^5\text{-}C_5H_5)_2Zr(Cl)(SR)$. The Origin of an Inverse Steric Effect." *Can J. Chem.* submitted.

List of Abbreviations

1,1'-biiq	1,1'-biisoquinoline
bipy	2,2'-bipyridine
t-Bu	*tert*-Butyl
CLF	Cellular Ligand Field Analysis
Cp	Cyclopentadiene
Cp*	Pentamethylcyclopentadiene
dabn	1,1'-binapthyl-2,2'-diamine
dabp	1,1'-biphenyl-2,2'-diamine
DFT	Density Functional Theory
Et	Ethyl
KEE	Kinetic Element Effect
KHE	Kinetic Enthalpy Effect
LSA	Line-Shape Analysis
Me	Methyl
i-Pr	*iso*-Propyl
SIT	Spin Inversion Transfer

Abstract

A comparison of the rates of isomerization of the ruthenium and osmium derivatives of $[M(bipy)_2(1,1'\text{-biiq})]^{2+}$, $[(\eta^6\text{-}C_6H_6)M(1,1'\text{-biiq})(Cl)]^+$, $[(\eta^6\text{-}C_6H_6)M(1,1'\text{-biiq})(I)]^+$, and $[(\eta^6\text{-}C_6H_6)M(dabp)(Cl)]^+$ has led to the introduction of the term Kinetic Element Effect (KEE). The misdirected ligands 1,1'-biisoquinoline (1,1'-biiq) and 1,1'-biphenyl-2,2'-diamine (dabp) have bent metal-ligand bonds in the ground-states of these complexes and directed metal-ligand bonds in the transition-states of these isomerization reactions. The KEE is the ratio of the rates of isomerization reactions of second-row and third-row metal-ligand complexes ($KEE=k_{2nd}/k_{3rd}$). A Kinetic Enthalpy Effect (KHE) can be defined as the ratio of enthalpy of activation for the third row and second-row atropisomerization reactions ($KHE= \Delta H^{\ddagger}_{3rd}/\Delta H^{\ddagger}_{2nd}$).

Metal complexes were synthesized with the atropisomeric dabp. X-ray crystal structures were solved for $[Ru(bipy)_2(dabp)]^{2+}$ and $[(\eta^6\text{-}C_6H_6)Ru(dabp)(Cl)]^+$. Only one diastereomer was observed for $[Ru(bipy)_2(dabp)]^{2+}$ in the ^1H NMR spectrum. Exchange was observed and measured for the ruthenium and osmium complexes of $[(\eta^6\text{-}C_6H_6)M(dabp)(Cl)]^+$. An investigation into the mechanism determined that $[(\eta^6\text{-}C_6H_6)M(dabp)(Cl)]^+$ isomerizes on the spin relaxation time scale by atropisomerization of the dabp ligand. The rates of ruthenium and osmium were compared at 20 °C and a small KEE of 0.51 was observed.

$[(\eta^6\text{-}C_6H_6)M(1,1'\text{-biiq})(X)]^+$ (M=Ru,Os; X=Cl,I) were synthesized. X-ray crystal structures were solved for the chloride derivatives. ^1H NMR chemical shifts were assigned by 2D-COSY experiments. Exchange between enantiomers was observed by 2D-EXSY experiments. Rates of atropisomerization of the 1,1'-biiq ligand were measured for all four derivatives by NMR. Rates were found to be faster for the ruthenium derivatives than the osmium derivatives. Thermodynamic data was obtained by Eyring plots from the rate data to show the same inverse relationship between thermodynamic

stability and kinetic lability as in the case of the $[M(bipy)_2(1,1'\text{-biiq})]^{2+}$ (M=Ru, Os) system. The KEE is equal to 0.12 for $[M(bipy)_2(1,1'\text{-biiq})]^{2+}$, and this may be compared with the values of 0.66 for $[(\eta^6\text{-}C_6H_6)M(1,1'\text{-biiq})(Cl)]^+$ and 0.57 for $[(\eta^6\text{-}C_6H_6)M(1,1'\text{-biiq})(I)]^+$ (M=Ru, Os). An inverse KHE is observed in these systems. KHE is equal to 0.93 for $[M(bipy)_2(1,1'\text{-biiq})]^{2+}$, 0.93 for $[(\eta^6\text{-}C_6H_6)M(1,1'\text{-biiq})(Cl)]^+$ and 0.92 for $[(\eta^6\text{-}C_6H_6)M(1,1'\text{-biiq})(I)]^+$ (M=Ru, Os). The osmium complexes have a smaller energy of activation than the ruthenium complexes in each case. More negative entropies of activation are observed for the osmium derivatives than the ruthenium derivatives.

$[M(bipy)_2(1,1'\text{-biiq})]^{2+}$, $[(\eta^6\text{-}C_6H_6)M(1,1'\text{-biiq})(Cl)]^+$, $[(\eta^6\text{-}C_6H_6)M(1,1'\text{-biiq})(I)]^+$ and $[(\eta^6\text{-}C_6H_6)M(dabp)(Cl)]^+$ (M=Ru, Os) are the only examples in the literature of third-row transition metal complexes having faster rates of atropisomerization than their second-row congegers. While the KEE varies among the 1,1'-biiq compounds, the KHE is nearly the same for each system. It can be seen from these results that changing the ancillary ligands does not effect the magnitude of the KHE. KHE may be a better indicator of the misdirected metal-ligand bond.

A series of $Cp_2Zr(Cl)(SR)$ (R=methyl, ethyl, *iso*-propyl, *tert*-butyl) have been synthesized. The ground-state conformation that is adopted by these d^0 metal compounds represent a compromise between stabilizing Mdπ-Spπ interactions and destabilizing R-Cp steric contact. Consequently, the observed conformations for d^0 derivative are not optimal for Mdπ-Spπ bonding. The thiolate ligands in such complexes are therefore misdirected. Rotational barriers ($\Delta G^{\ddagger}$) about the Zr-S bond have been measured by ^1H NMR for the first time. For R=methyl, ethyl, and *iso*-propyl, the barriers are proportional to the steric demand of the ligand and the bond strength of the metal-sulfur bond at 32, 33, and 35 kJ $mole^{-1}$ respectively. A much lower barrier of 26 kJ $mole^{-1}$ was measured for R= *tert*-butyl. X-ray crystal structures were solved for $CpZr(SR)_2$ (R=methyl, ethyl, *iso*-propyl, *tert*-butyl). Nothing unusual was observed in these structures that would explain the lower

rotational barrier for the *tert*-butyl derivative. DFT calculations carried out on $Cp_2Zr(Cl)(SR)$ (R=Methyl, ethyl, *iso*-propyl, *tert*-butyl) suggested that enthalpy was the dominant contributor to magnitude of the rotational barrier. A significantly lower enthalpic term was calculated for the *tert*-butyl derivative. Metric parameters for the ground-state and transition-state structures were computed. Differences in the ground-state structure for the *tert*-butyl derivative suggest that the origin of the lower $\Delta H^{\ddagger}$ is due to a weaker M-S bond in the ground-state structure.

CHAPTER 1

INTRODUCTION

1.1 Bonding in Inorganic and Organometallic Compounds

Transition metal ligand bonds have been of interest since the discovery of the first organometallic and inorganic coordination compounds. The platinum olefin salt $K[(C_2H_4)PtCl_3]$,[1] the first organotransition metal compound, was discovered by Zeise in 1827. The first π-bonded chromium arene complexes were discovered in 1919 by Hein.[2] Alfred Werner won the Nobel Prize in Chemistry in 1913 for his work with cobalt amine coordination compounds.[3] It has taken many years for the molecular and electronic structures of these complexes to be understood. Much work has been done in an attempt to explain and describe the bonding in such organometallic and inorganic coordination compounds. The main theories postulated include valence bond,[4] crystal field [5] and molecular orbital theory.[6] Some metal-ligand bonds exist in high-symmetry environments; however, other metal-ligand bonds are not symmetrical. The ligand group may be constrained in some way so that the best possible overlap may not be concentrated along straight lines from the metal center. For example, bending of a metal-ligand bond with a local symmetry of C_{2v} would result in lowering the local metal-ligand bond symmetry to C_s. Gerloch refered to this phenomenon as "misdirected valency".[7]

A misdirected bond is one which is oriented away from optimal overlap. One may envisage three types of misdirection involving σ and π bonds. These are illustrated in Figure 1.1. One type of misdirection involves σ bonds. The ligand orbital is tilted away from the metal orbital, but the orbitals remain in the same plane. There are two types of misdirection involving π bonding. The first type has the ligand orbital tilted away from the metal orbital, but again the two orbitals remain the same

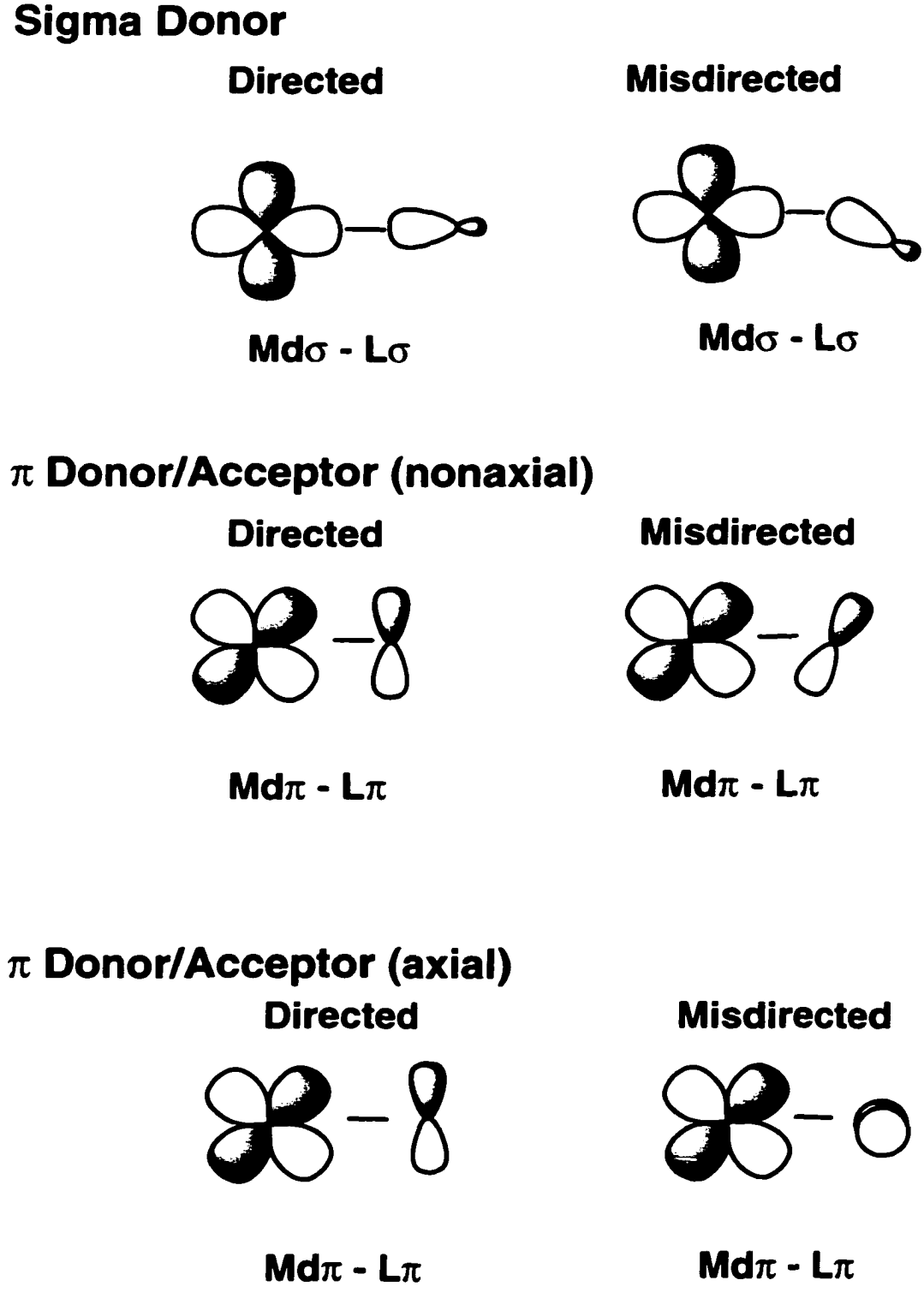

Figure 1.1. Types of misdirected bonds found in metal-ligand complexes.

plane. The second type involves the ligand orbital rotating out of the plane of the metal until it is orthogonal to the metal orbital.

1.2 Misdirected Valency

Liehr published a theoretical study in 1964 concerning the role of geometry in inducing optical activity in six-coordinate dihedral metal compounds.[8] The copper(II) tris-ethylenediamine cation and the tris-oxalatocopper(II) anions were the focus of the study. It was demonstrated for both σ and π bonding that the bent metal-ligand bonds must be included in the parameters of the molecular orbital calculations in order to account theoretically for the optical properties of these complexes. The sign and magnitude of rotational and spectral strengths depend on the angle of metal-ligand orbital mismatch.[8] It was suggested that including the exact orbital geometries between the metal-ligand bonds would result in more accurate results.

Gerloch et al. have modeled the static characteristics of metal complexes containing bent metal-ligand bonds using ligand field analysis.[7,9-17] Ligand field analysis may be used to quantitatively reproduce the magnitude and orientations of paramagnetic susceptibilities, electron-spin resonance g values, d-d transition energies, absorption intensities, and the rotatory strengths recorded in circular dichroism experiments.[7] This may be accomplished for any single-center transition metal complex of any coordination number or geometry.[7] In most cases, the complexes used for Gerloch's study had already been modeled without taking into account misdirected valency in the metal-ligand bonds. This had resulted in calculations which failed to reproduce the physical data. Misdirected valency in a metal-ligand bond lowers the local *pseudo*-symmetry of the metal-ligand bond. For example, a metal-ligand bond having C_{2v} symmetry is lowered to C_s symmetry, which requires a local ligand-field matrix element that mixes the d_σ and d_π orbitals.[9] This results in off-diagonal terms in the ligand field matrix that require an extra parameter to be included in

the ligand field calculatons.[17] Gerloch referred to this method of ligand field analysis as cellular field analysis (CLF).

One example of Gerloch's work is the ligand field analysis of a series of four- and five-coordinated copper(II) complexes with various substituted acetylacetonates.[10] The copper-oxygen bond lengths, chelate bite angles, and chelate ring geometries varied insignificantly among the series of compounds. However, the tilt angle between the acetylacetone planes and the CuO_4 coordination planes changed markedly. This increasing tilt angle was found to be associated with increasing spectral splitting at ~15,000 and ~19,000 cm^{-1}. An essentially two-peak spectrum for a near-planar complex resolves into a four-peak spectrum for the most bent molecule. Misalignment of the ligand orbitals and metal-oxygen vectors is caused by the geometrical constraints imposed by the chelate. A conventionally parameterized model is not able to account for the spectral splitting of the bent molecules. All transition energies in the series were quantitatively reproduced by recognition of the Cu-O bent bonding.

Gerloch also studied nickel(II) thiocyanate complexes.[11] Conventional ligand field analysis defined isothiocyanate as a π-donor ligand in *trans*-$Ni(NH_3)_4(NCS)_2$ and a π-acceptor ligand in $Ni(ethylenediamine)_2(NCS)_2$. The complexes have very different Ni-N-CS angles: 180° and 140° for *trans*-$Ni(NH_3)_4(NCS)_2$ and $Ni(ethylenediamine)_2$-$(NCS)_2$, respectively. The d-d transition energies are reproduced and the role of π-donor is restored to the thiocyanate ligand by taking into account misdirected valency in the Ni-N bonds of the ethylenediamine complex.

Other examples of compounds which Gerloch analyzed by CLF include five-coordinate Schiff-base complexes of nickel(II) in which the transition energies and intensity distributions in the d-d spectra were reproduced.[13] Crystal susceptibilities, d-d optical transition energies and g values were accurately reproduced for $[M(OAsPh_2Me)_4NO_3]^+NO_3^-$ (M=Co(II), Ni(II)).[12] The g tensors of two low-spin square-planar cobalt(II) complexes were reproduced.[9] The energies, electric-dipole

absorbances, and rotatory strengths of d-d transitions in a series of the trigonal-bipyramidal chromophores M(S-tan)X (M=Co(II), Ni(II); X=NCS^-, Cl^-, Br^-, I^-; S-tan = $Me_2NCH_2CH(Me)N(CH_2CH_2NMe_2)_2$) were reproduced by taking into account the misdirected valency between the amines and the central metal in the δδδ conformation of the S-tan ligand.[14] $[Ni(en)_3]^{2+}$ (en = ethylenediamine) provided an ideal system in which to model using CLF as there is only one donor type with σ bonding between the nitrogens and the metal requiring only one energy parameter and one intensity parameter.[17] The transition energies and intensity distributions in both the linearly and circularly polarized spectrum were easily reproduced using CLF.

Gerloch used modern ligand-field analysis to evidence bent bonding. Inclusion of misdirected valency in the parameterization of ligand field analysis permitted reproduction of physical data which had not been previously understood. A review article explains the theory of cellular ligand field analysis as applied to systems with bent metal-ligand bonds.[7]

1.3 Periodic Trends in Metal-Ligand Bond Strengths of Transition Metals

Metal-ligand bond strengths are not the same for analogous second-row and third-row transition metal-ligand bonds. In 1990, Simões and Beauchamp published a review article which lists the transition metal-hydrogen and metal-carbon bond strengths for compounds in groups 3-10.[18] There are relatively little data that compare identical second-row and third-row metal derivatives of complexes under the same conditions. For the data that exist, error analysis is not always included in these studies. Experiments to determine bond dissociation energies are carried out in both the gas phase and in solution.[19] Different sources of error are associated with the different methods. Nonetheless, a general trend is seen in which third-row transition metals form stronger bonds than their second-row congeners. A 2% - 54% increase in

bond dissociation energies is observed when comparing second-row and third-row transition metal complexes (Table 1.1 and Table 1.2). This is due to better metal-ligand overlap as the 5d orbitals are larger than the 4d orbitals and the 6s orbitals in the third row are contracted with respect to the 5s orbitals in the second row, resulting in an overall increase in bonding interaction.[20]

1.3.1 Transition metal-carbonyl bond strength

Metal carbonyl compounds such as $M(CO)_6$ (M=Mo,W), $M(CO)_5$ (M=Ru, Os), and $M(CO)_4$ (M=Pd,Pt) are classic examples of stronger third row metal-carbon bonds. The bond energy, D(M-CO), and the first bond dissociation energy, ΔH°, are a measure of the M-CO bond interaction. The first bond dissociation energy corresponds to the process:

$$M(CO)_n \rightarrow M(CO)_{n-1} + CO(g)$$

This differs from the mean bond dissociation energy which corresponds to:

$$M(CO)_n(g) \rightarrow M(g) + nCO(g)$$

Included in the mean bond dissociation energy is the energy required to promote the metal atom from its high spin electronic ground-state to its low spin valence configuration. This term is different for different metals. Therefore, the mean bond dissociation energy cannot be used for a comparison of a triad of metals. However, the first bond dissociation energy, ΔH°, only includes the breaking of the M-C bond. Therefore, ΔH° is directly related to the M-C bond strength and can be used to make comparisons.

A pulsed laser pyrolysis technique was used to study the gas-phase thermal decomposition of Group 6 hexacarbonyls.[21] The first bond dissociation energy was obtained from these experiments. Solution kinetic methods were used to estimate ΔH° for $Ru(CO)_5$ and $Os(CO)_5$. ΔH° for these compounds is shown in Table 1.1. Ziegler used Density Functional Theory (DFT) to calculate the first metal-carbonyl dissociation

energy for $M(CO)_6$ (M= Mo,W), $M(CO)_5$ (M=Ru,Os), $M(CO)_4$ (M= Pd,Pt),[22,23] $(\eta^5\text{-}C_5H_5)M(CO)_2$ and $(\eta^5\text{-}C_5H_5)M(PH_3)(CO)$ (M=Rh(III) and Ir(III)).[24] These values are shown in Table 1.2. In every case ΔH^o is larger for the third-row than the second-row metal. It may be concluded that in general third-row metal-carbonyl bonds are stronger than the second-row metal-carbonyl bonds.

1.3.2 Transition metal-methyl and metal-hydrogen bond strength

Solution calorimetry has been used to determine the metal-methyl and metal-hydrogen bond strengths for cyclopentadienyl complexes of Group 3[25,26] and Group 6 metals.[27,28] (Table 1.1). DFT calculations were used to calculate the metal-hydrogen and metal-methyl bond strengths for cyclopentadienyl complexes of Group 7 metals[29] and carbonyl compounds of Group 7 and Group 9 metals.[30] Bond strengths were also calculated for the early transition metal systems, Cl_3ML (M=Zr, and Hf; L=OH, OCH_3, SH, NH_2, PH_2, CH_3, SiH_3, CN and H)[31] (Table 1.2). A general trend is found in which third row metal-hydrogen and metal-methyl bonds are stronger than second row metal-hydrogen and metal-methyl bonds.

Table 1.1. Comparison of Experimental Second-Row and Third-Row Metal-Carbonyl, Metal-Methyl and Metal-Hydrogen Bond Dissociation Energies

Compound	Bond Dissociation Energy ΔH°, kJ/mole	Reference
$Mo(CO)_6$	169(8)	21
$W(CO)_6$	192(8)	21
$Ru(CO)_5$	115	23
$Os(CO)_5$	128	23
$(\eta^5\text{-}C_5Me_5)_2Zr(H)_2$	339(2)	25
$(\eta^5\text{-}C_5Me_5)_2Hf(H)_2$	346(7)	25
$(\eta^5\text{-}C_5Me_5)_2Zr(CH_3)_2$	284(2)	25
$(\eta^5\text{-}C_5Me_5)_2Hf(CH_3)_2$	306(7)	25
$Cp^{tt}{}_2Zr(CH_3)_2$	180(4)	26
$Cp^{tt}{}_2Hf(CH_3)_2$	199(4)	26
$(\eta^5\text{-}C_5H_5)_2Mo(H)_2$	257(8)	32
$(\eta^5\text{-}C_5H_5)_2W(H)_2$	311(4)	32
$(\eta^5\text{-}C_5H_5)_2Mo(CH_3)_2$	166(8)	27
$(\eta^5\text{-}C_5H_5)_2W(CH_3)_2$	221(3)	27
$(\eta^5\text{-}C_5Me_5)_2(CO)_3MoH$	255(1)	28
$(\eta^5\text{-}C_5Me_5)_2(CO)_3WH$	272(1)	28

Cp^{tt}= η^5-1,3-di-*tert*-butylcylopentadienyl

Table 1.2. Comparison of Theoretical Second-Row and Third-Row Metal-Carbonyl, Metal-Methyl and Metal-Hydrogen Bond Dissociation Energies

Compound	Bond Dissociation Energy $\Delta H°$, kJ/mole	Reference
$Mo(CO)_6$	166	23
$W(CO)_6$	183	23
$Ru(CO)_5$	138	23
$Os(CO)_5$	145	23
$(\eta^5\text{-}C_5H_5)Rh(CO)_2$	191	24
$(\eta^5\text{-}C_5H_5)Ir(CO)_2$	239	24
$(\eta^5\text{-}C_5H_5)Rh(PH_3)(CO)$	183	24
$(\eta^5\text{-}C_5H_5)Ir(PH_3)(CO)$	283	24
$Pd(CO)_4$	51	23
$Pt(CO)_4$	66	23
$(\eta^5\text{-}C_5H_5)_2Tc(H)_2$	247	29
$(\eta^5\text{-}C_5H_5)_2Re(H)_2$	250	29
$(\eta^5\text{-}C_5H_5)_2Tc(CH_3)_2$	152	29
$(\eta^5\text{-}C_5H_5)_2Re(CH_3)_2$	156	29
$Tc(CO)_5H$	252	30
$Re(CO)_5H$	282	30
$Tc(CO)_5CH_3$	178	30
$Re(CO)_5CH_3$	200	30
$Rh(CO)_4H$	255	30
$Ir(CO)_4H$	286	30
$Rh(CO)_4CH_3$	190	30
$Ir(CO)_4CH_3$	212	30
Cl_3ZrH	297.2	31
Cl_3HfH	313.5	31
Cl_3ZrCH_3	309.5	31
Cl_3HfCH_3	326.6	31
$Tc(CO)_5H$	252	30
$Re(CO)_5H$	282	30
$Tc(CO)_5(CH_3)$	178	30
$Re(CO)_5(CH_3)$	200	30

Table 1.2. Continued

Compound	Bond Dissociation Energy ΔH°, kJ/mole	Reference
$Rh(CO)_4H$	255	30
$Ir(CO)_4H$	286	30
$Rh(CO)_4(CH_3)$	190	30
$Ir(CO)_4(CH_3)$	212	30

1.4 Comparison of the Kinetics of Second-Row and Third-Row Transition Metal Reactions

Because there are often free-energy relationships that relate thermodynamic and kinetic parameters,[33] a comparison of kinetic rates involving the breaking or perturbing or a metal-ligand bond may be used as an indication of bond strength. Most examples in the literature observe a third-row metal complex exhibiting slower kinetics than the analogous second-row metal complex (Table 1.3 and Table 1.4).

1.4.1 Substitution kinetics

Substitution kinetics offers insight into the bond strengths of metal-ligand bonds. For example, the rate of solvent exchange (solvolysis) can be taken as a measure of the "lability" or inertness of the solvated metal ion.[34] However, relatively little data exists comparing second-row and third-row complexes under the same conditions. In 1985, Lawrence showed that rate constant ratios for solvolysis of $[M(NH_3)_5(OSO_2CF_3)](CF_3SO_3)_2$ (M=Co, Rh, Ir) varied little with solvent and were approximately 90:40:1.[35] In 1994, Taube published a paper comparing the rates of substution in $[Ru(NH_3)_5H_2O]^{3+}$ and $[Os(NH_3)_5H_2O]^{3+}$.[36] One of the results of this

study was to observe that substitution of the aqua ligand is slower for the osmium derivative than the ruthenium derivative.[36] In 1995, Merbach et al. showed for the mixed ligand complex of $[Cp^*M(bipy)(H_2O)]^{2+}$ that substitution of the aqua ligand was 6.3 times faster for Rh(III) than Ir(III).[37] It was determined that M-O(water) bond breaking was the rate determining step (i.e., the mechanism is dissociative). In 1996, Merbach studied the hexaaquairidium(III) complex and determined by variable temperature ^{17}O NMR spectroscopy the water exchange rate to be 1.1×10^{-10} s^{-1}, corresponding to the slowest aqua ligand exchange at a mononuclear metal center.[38] Table 1.3 compares degenerate ligand exchange and substitution kinetics under similar conditions for series of second-row and third-row derivatives of transition metal complexes.

Substitution kinetics can be an indication of the strength of a metal-ligand bond. It is a general trend that second-row metal complexes exhibit faster kinetic rates than third-row metal complexes. It can be presumed from these results that third row metal-ligand bonds are stronger than second-row metal-ligand bonds.

Table 1.3. Comparison of Second-Row and Third-Row Metal Ligand Exchange and Substitution Kinetics

Compound	Exchanging Ligand	Temp °C	Rate	Ref
$(\eta^5\text{-}C_5Me_5)_2Zr(CH_2Ph)_2$	$((CH_3)_3C)_2NO\cdot$	35	4.9×10^{-2} M^{-1} s^{-1}	39
$(\eta^5\text{-}C5Me5)_2Hf(CH_2Ph)_2$	$((CH_3)_3C)_2NO\cdot$	35	4.6×10^{-5} M^{-1} s^{-1}	39
$[Ru(NH_3)_5(H_2O)]^{3+}$	$[Fe(CN)_6]^{4-}$	20	1.1×10^{-4} s^{-1}	36
$[Os(NH_3)_5(H_2O)]^{3+}$	$[Fe(CN)_6]^{4-}$	20	1.0×10^{-5} s^{-1}	36
$[Rh(NH_3)_5(OSO_2CF_3)](CF_3SO_3)_2$	H_2O	25	189×10^{4} s^{-1}	35
$[Ir(NH_3)_5(OSO_2CF_3)](CF_3SO_3)_2$	H_2O	25	2.61×10^{-4} s^{-1}	35
$[(\eta^5\text{-}C_5Me_5)Rh(bipy)(H_2O)]^{2+}$	Br^-	40	580 s^{-1}	37
$[(\eta^5\text{-}C_5Me_5)Ir(bipy)(H_2O)]^{2+}$	Br^-	40	100 s^{-1}	37
$[(\eta^5\text{-}C_5Me_5)Rh(H_2O)_3]^{3+}$	H_2O	40	1.6×10^{5} s^{-1}	37
$[(\eta^5\text{-}C_5Me_5)Ir(H_2O)_3]^{3+}$	H_2O	40	2.53×10^{4} s^{-1}	37
$[Rh(NH_3)_5(H_2O)]^{3+}$	H_2O	40	8.6×10^{-6} s^{-1}	40
$[Ir(NH_3)_5(H_2O)]^{3+}$	H_2O	40	6.1×10^{-8} s^{-1}	40
$[Rh(H_2O)_6]^{3+}$	H_2O	40	2.2×10^{-9} s^{-1}	41
$[Ir(H_2O)_6]^{3+}$	H_2O	40	1.1×10^{-10} s^{-1}	38
$[Pd(S_2CNEt_2)_2]$	CN^-	25	206 s^{-1}	42
$[Pt(S_2CNEt_2)_2]$	CN^-	25	4.7×10^{-2} s^{-1}	42
$[Pd(S_2CNEt_2)_2(CN)_2]^-$	CN^-	25	2.1×10^{-1} s^{-1}	42
$[Pt(S_2CNEt_2)_2(CN)_2]^-$	CN^-	25	2.65×10^{-2} s^{-1}	42
$[Pd(H_2O)_4]^{2+}$	H_2O	40	10.2 M^{-1} s^{-1}	43
$[Pt(H_2O)_4]^{2+}$	H_2O	40	7.1×10^{-6} M^{-1} s^{-1}	44
$[Pd(CN)_4]^{2-}$	EtOH	40	124 M^{-1} s^{-1}	45
$[Pt(CN)_4]^{2-}$	EtOH	40	25 M^{-1} s^{-1}	45
$[Pd(Me_2S)_4]^{2+}$	CD_3NO_2	40	2140 M^{-1} s^{-1}	46
$[Pt(Me_2S)_4]^{2+}$	CD_3NO_2	40	1.54 M^{-1} s^{-1}	47
$[Pd(1,4\text{-dithiane})_2]^{2+}$	CD_3NO_2	40	9780 M^{-1} s^{-1}	47
$[Pt(1,4\text{-dithiane})_2]^{2+}$	CD_3NO_2	40	28.8 M^{-1} s^{-1}	47

1.4.2. Thioether inversion kinetics

Inversion of the pyramidal configuration at coordinated chalcogen atoms has been observed for various metal complexes.[48] The rates of inversion at thioethers have been previously investigated for a wide range of metal complexes.[48] A significant barrier exists for inversion at the sulfur atom of the thioether ligand. This is due to the nature of the bonding between the metal and the sulfur atom of the thioether ligand. The lone pair of the thioether ligand may be viewed as essentially unhybridized atomic orbitals.[49] as hybridization of the valence orbitals of divalent chalcogenides is not as important beyond the second period.[50,51] The principal σ-donor of a thioether ligand is an out-of plane sulfur 3p lone pair. The other lone pair is a sulfur 3s orbital which is an ineffectual donor as compared with the p-type lone pair. Inversion involves a trigonal planar transition-state in which there is a substantially weakened M-S bond.[48] Inversion at the sulfur atom may be viewed as directed M-S orbitals in the ground-state and misdirected M-S orbitals in the transition-state. The barriers for inversion with simple thioether ligands range from 28 kJ/mole[49] to 81 kJ/mole.[52] Studies have been carried out with group 6[53,54] and group 10[52,55-58] metals which compare the rates of inversion of second-row and third-row thioether complexes. Second-row thioether metal complexes exhibit faster inversion than third-row thioether complexes as evidenced by lower inversion barriers for second-row complexes as compared to third-row complexes (Table 1.4).

Table 1.4. Comparison of Inversion Barriers of Second-Row and Third-Row Transition Metal-Thioether Complexes

Compound	$\Delta G^{\ddagger}$ kJ mole^{-1}	Reference
$[Mo(CO)_4(C_6H_5CH_2SCH_2CH_2SCH_2C_6H_5)]$	44.7	53
$[W(CO)_4(C_6H_5CH_2SCH_2CH_2SCH_2C_6H_5)]$	51.5	53
$[Mo(CO)_5(SC_2H_4SCH_2)]$	41.2	54
$[W(CO)_5(SC_2H_4SCH_2)]$	44.1	54
cis-$[PdCl_2(MeSCH_2CH_2SMe)]$	70.2	52
cis-$[PtCl_2(MeSCH_2CH_2SMe)]$	81.4	52
cis-$[PdI_2(MeSCH_2CH_2SMe)]$	60.9	52
cis-$[PtI_2(MeSCH_2CH_2SMe)]$	75.3	52
cis-$[PdCl_2(MeSCH{:}CHSMe)]$	58.3	52
cis-$[PtCl_2(MeSCH{:}CHSMe)]$	68.6	52
cis-$[PdI_2(MeSCH{:}CHSMe)]$	48.7	52
cis-$[PtI_2(MeSCH{:}CHSMe)]$	62.9	52
cis-$[PdCl_2(o\text{-}MeS(C_6H_3Me)SMe)]$	59.5	52
cis-$[PtCl_2(o\text{-}MeS(C_6H_3Me)SMe)]$	71.3	52
cis-$[PdI_2(o\text{-}MeS(C_6H_3Me)SMe)]$	50.3	52
cis-$[PtI_2(o\text{-}MeS(C_6H_3Me)SMe)]$	63.9	52
trans-$[PdCl_2(S(CH_2SiMe_3)_2)_2]$	54.6	55
trans-$[PtCl_2(S(CH_2SiMe_3)_2)_2]$	61.3	55
trans-$[PdCl_2(S(Me)CH_2SiMe_3)_2]$	54.5	56
trans-$[PtCl_2(S(Me)CH_2SiMe_3)_2]$	61.3	56
trans-$[PdCl_2(S(Ph)CH_2SiMe_3)_2]$	53.2	56
trans-$[PtCl_2(S(Ph)CH_2SiMe_3)_2]$	59.3	56
trans-$[PdCl_2(SCH_2CMe_2CH_2)_2]$	60.9	57
trans-$[PtCl_2(SCH_2CMe_2CH_2)_2]$	69.6	57
trans-$[PdCl_2(SC_2H_4SCH_2)_2]$	56.6	58
trans-$[PtCl_2(SC_2H_4SCH_2)_2]$	63.9	58
trans-$[PdCl_2(SC_2H_4SCMe_2)_2]$	49.4	58
trans-$[PtCl_2(SC_2H_4SCMe_2)_2]$	56.0	58

1.5 Kinetic Element Effect

It has been explained in the previous sections that a metal-ligand bond can be bent or straight and that third-row transition metal-ligand bonds are stronger than second-row transition metal-ligand bonds. It is assumed that a directed bond is stronger than a misdirected bond. Dynamic properties of bond strengths can be investigated by observing isomerization reactions in solution. When a metal complex with a bond which is misdirected in the ground-state rotates around that bond through a transition-state involving a redirected bond, it would be expected that the metal-ligand bond would be stronger in the transition-state than the ground-state. This idea was tested by designing a system in which diastereomers interconvert by a mechanism of atropisomerization. Atropisomerization refers to isomerization of conformational isomers about a hindered σ bond. In 1994, a mechanistic study of $[Ru(bipy)_2(biiq)]^{2+}$ (bipy=2,2'-bipyridine; biiq=1,1'-biisoquinoline) was published by this group which showed two diastereomers interconverting through a mechanism of atropisomerization.[59] The isomerization took place through rotation about the C_1-$C_{1'}$ bond of 1,1'-biiq (Figure 1.2). The kinetics of atropisomerization were followed using spin-labeling ^1H NMR techniques. The bipyridine ligands are flat and have directed σ bonds between the bipyridine nitrogens and ruthenium. However, 1,1'-biiq is nonplanar because of an unfavorable steric interaction between the $H_8/H_{8'}$ hydrogen atoms (Figure 1.2). Twisting of 1,1'-biiq produces misdirected nitrogen donor orbitals with respect to the dσ acceptor orbitals at the metal center. Accordingly, the 1,1'-biiq donor orbitals are misdirected and the Ru-N(biiq) bonds are bent. $[Ru(bipy)_2(biiq)]^{2+}$ exists as a pair of two diastereomers as it has two chiral centers. It is chiral at the metal (Δ/Λ– tris(chelate) configurational isomers) and chiral at the 1,1'-biiq ligand (δ/λ– conformational isomers). The two diastereomers are observed to interconvert in solution by spin-labeling NMR methods. A mechanistic study rules out configurational

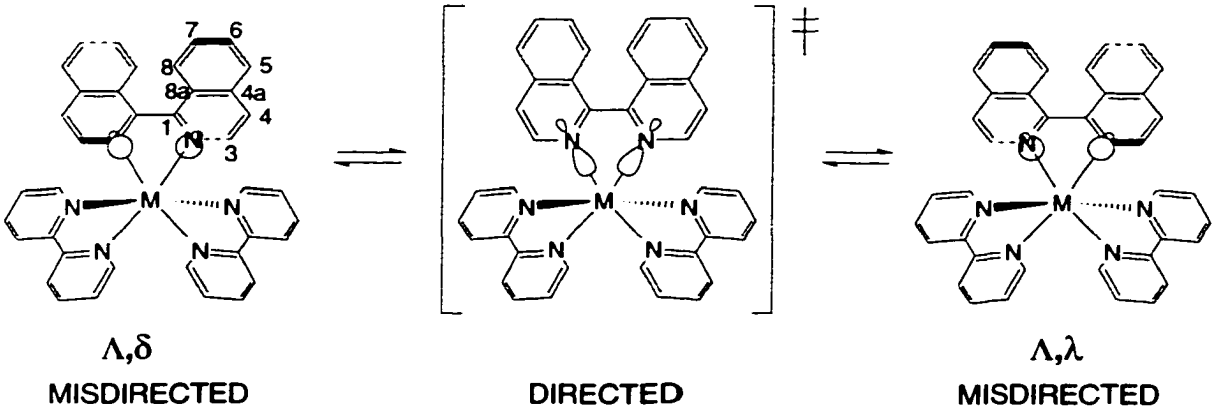

Figure 1.2. Mechanism of interconversion of diastereomers of $[M(bipy)_2(biiq)]^{2+}$ (M = Ru(II), Os(II)) illustrating the misdirected metal-nitrogen bonds in the ground-state and the directed metal-nitrogen bonds in the transition-state.

isomerism (inversion at the metal) and instead evidences conformational isomerism (inversion at the 1,1'-biiq ligand). As the two diastereomers of $[Ru(bipy)_2(biiq)]^{2+}$ interconvert via rotation about the C_1-C_1 bond, a planar transition-state occurs in which the biiq nitrogen-ruthenium bonds are redirected (Figure 1.2). The metal-nitrogen bonds are presumed to be stronger in the transition-state than the ground-state, which should result in an inverse relationship between thermodynamic and kinetic stability i.e., the stronger the M-ligand bonds the faster atropisomerization. In 1995, a study was published from this group comparing the kinetics of this atropisomerization reaction of the ruthenium compound with the analogous osmium compound.[60] This comparison is relevant because the two metals are nearly the same size due to the lanthanide contraction.[20] This results in essentially identical metric parameters for the two metal derivatives, which was evidenced by X-ray crystallography. Thus, the effect of strengthening the metal ligand bonds in the transition-state should be more pronounced for the third-row complex than the second-row metal complex as the third-row metal-ligand bonds are stronger than the second-row metal-ligand bonds, but the geometric parameters are the same. The kinetic study showed that the osmium complex exhibited faster kinetics by an order of magnitude than the ruthenium compound. When the free energy diagrams of the isomerization betwen the major and minor diastereomers of the two derivatives were compared, the ruthenium compound had a larger activation barrier while the osmium compound was more stable thermodynamically (Figure 1.3).[60] This was the first example of a stronger bond being more reactive in an equilibrium reaction.

A series of compounds that undergo inversion at their thioether S-donor atom were synthesized by our group. Like the atropisomerization of 1,1'-biiq, the mechanism of inversion of thioether ligands does not involve cleavage of a metal-ligand bond; therefore, it should not be necessary to correct for solvation effects. In the case of the thioether complexes, the metal-sulfur bonds are directed in the ground-state and

misdirected in the transition-state (Figure 1.4). A direct comparison was made between the ruthenium and osmium derivative of Δ/Λ-chloro(tetrahydro-thiophene)bis(2,2'-bipyridine)metal(II). The rate for ruthenium was 17(1) s^{-1} and the rate for osmium was 1.9(4) s^{-1}.[61] This is an example of a regular relationship between thermodynamic stability and kinetic rate of isomerization.

Comparison of the rates of isomerization of the ruthenium and osmium derivatives of $[M(bipy)_2(biiq)]^{2+}$ has led to the introduction of the term Kinetic Element Effect (KEE).[61] The KEE is the ratio of the rates of isomerization reactions of second-row and third-row metal-ligand complexes ($KEE=k_{2nd}/k_{3rd}$). In defining this concept, the KEE can be related to the kinetic isotope effect. Isotopic substitution often influences the rates of a reaction.[62] The major factor that determines the magnitude of the kinetic isotope effect is the difference in the zero-point energies of the bonds formed by the isotopic atoms. If you consider a C-H bond versus a C-D bond, the difference in the zero point energy is due to the difference in mass between hydrogen and deuterium. Rate constants will depend on the isotopic masses. The heavier isotope has the larger activation barrier resulting in a slower rate (Figure 1.5). The largest effect will be seen when the bond in question is completely broken. This is a primary kinetic isotope effect. A smaller effect is seen when the bonds are only perturbed but not broken. This is a secondary kinetic isotope effect. The ratio of the rates of reactions involving the isotopic atoms can give information concerning the transition-state of the reaction. In general, primary kinetic isotope effects are always regular, but secondary kinetic isotope effects can be regular or inverse. A regular effect is seen when the ratio is greater than one which is indicative of a weakening of the bonds in the transition-state. An inverse effect is observed when the ratio is less than one showing a strengthening of the bonds in the transition-state. The KEE is related to the kinetic isotope effect because of the lanthanide contraction. Similar to hydrogen and deuterium, second-row and third-row transition metals are the same size with different

masses.[20] The different bond dissociation energies of the second-row and third-row transition metals give rise to an opportunity to explore bond strength without changing the steric effects in a system. Therefore, comparison of rates of second-row and third-row transition metal isomerization reactions that do not involve the breaking of bonds can give information concerning the transition-states of these reactions. In the context of misdirected ligands, rates of isomerization reactions in which the ligand atropisomerizes can be used to compare bond strength of second-row and third-row transition metal complexes. A KEE of greater than one is indicative of a weakening of the bonds in the transition-state, while a KEE of less than one evidences a strengthening of bonds in the transition-state. The KEE gives information on how a misdirected metal-ligand bond effects the dynamic properties of a metal complex.

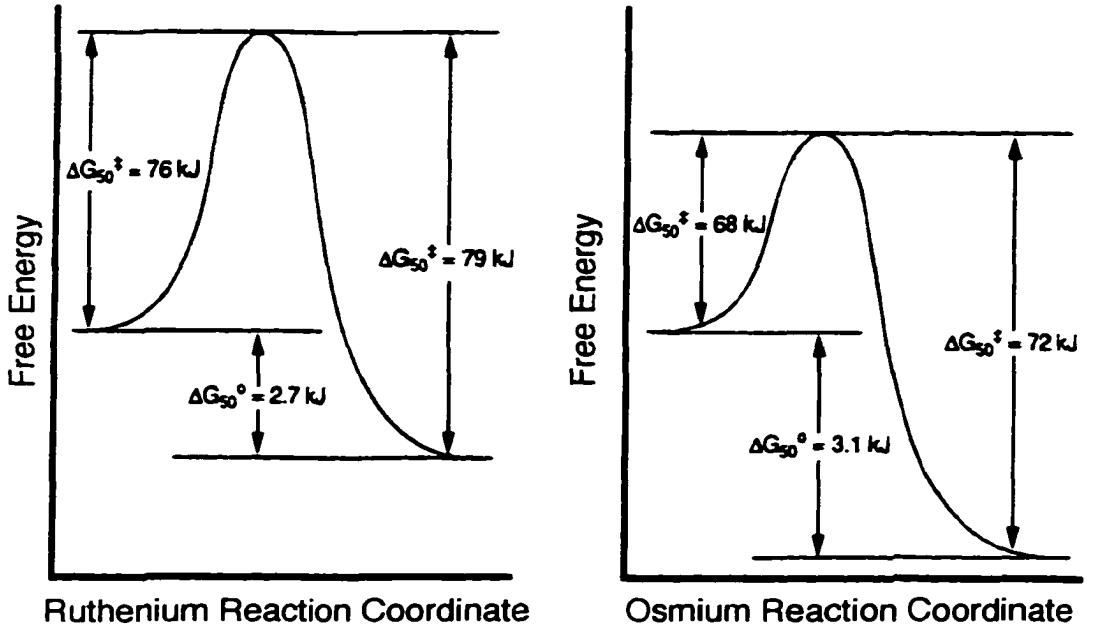

Figure 1.3. Reaction profiles for the atropisomerization of the major and minor isomers of $[M(bipy)_2(biiq)]^{2+}$, M=Ru, Os.

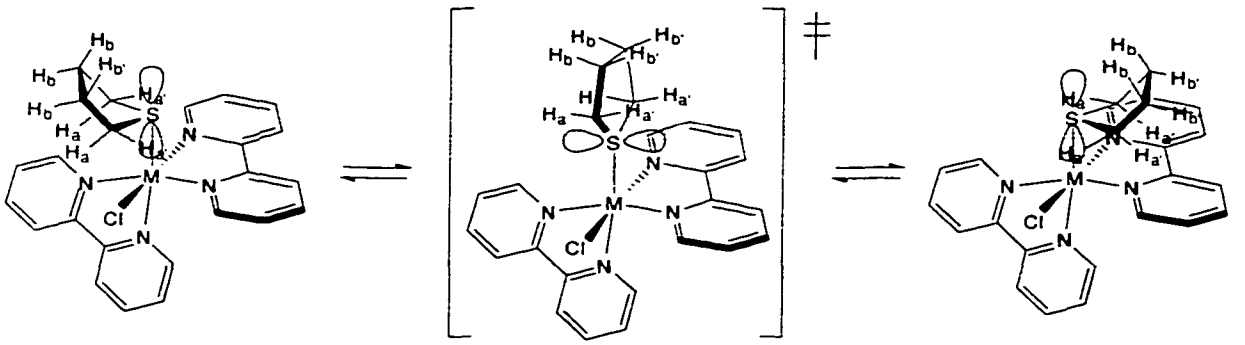

Figure 1.4. Mechanism of inversion of sulfur in isomerization of $[M(bipy)_2(tetrahydrothiophene)(Cl)]$ (M=Ru(II), Os(II)), illustrating the directed metal-sulfur bond in the ground-state and misdirected metal-sulfur bond in the transition-state.

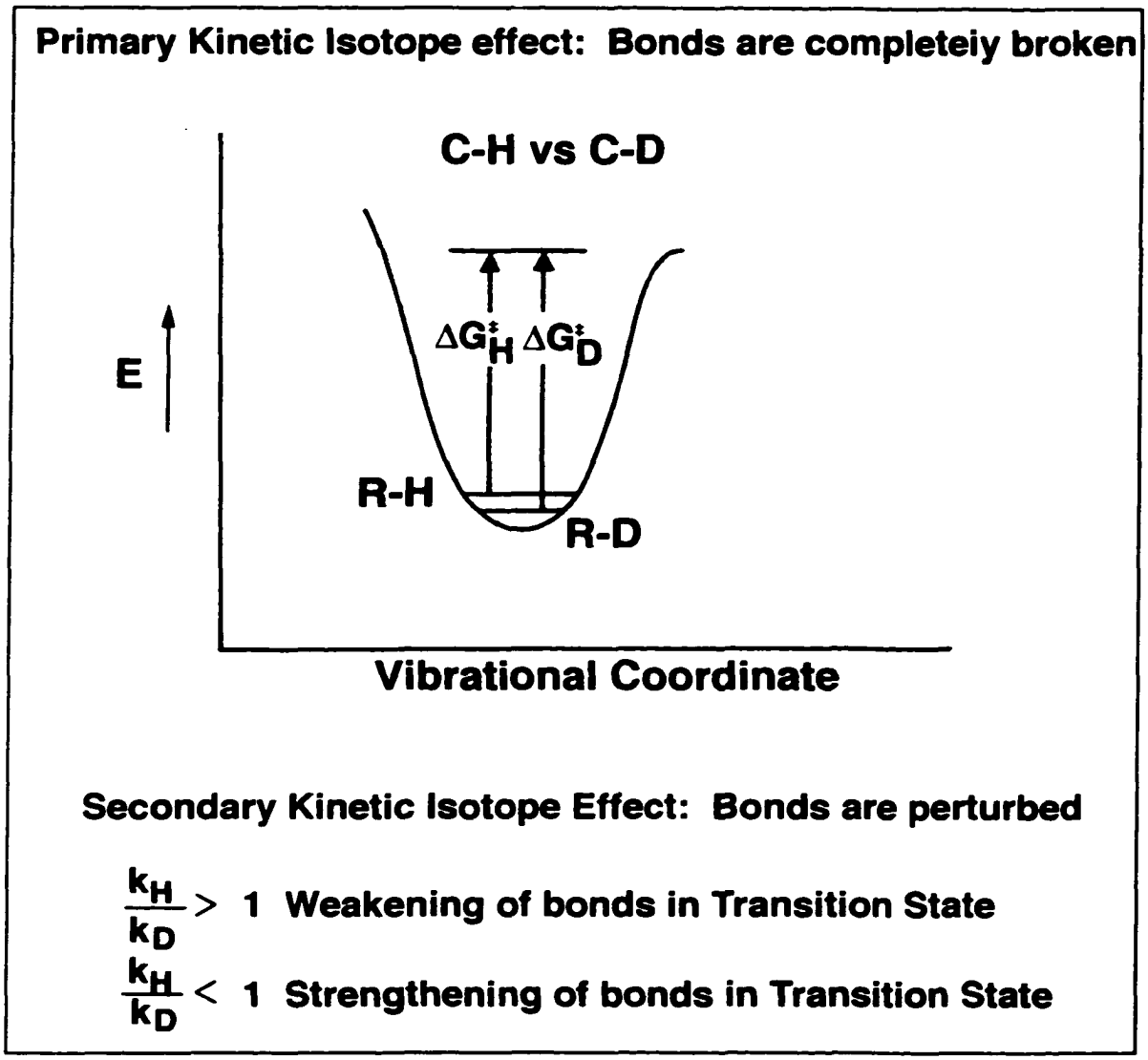

Figure 1.5. Energy diagram illustrating the Kinetic Isotope Effect.

1.6 Summary

There is a general trend in the literature that third-row transition metal-ligand bonds are stronger than second-row transition metal-ligand bonds. Due to the lanthanide contraction, second-row and third-row transition metals are approximately the same size.[20] These properties afford an opportunity to investigate bond strength of transition-states in which metal-ligand bonds are not broken, but pertubed. A comparison of the rates of reactions of a second-row derivative with its third-row congener is called the Kinetic Element Effect (KEE). Prior to the studies reported herein, $[M(bipy)_2(biiq)]^{2+}$ (M=Ru(II), Os(II)) was the only published example of an inverse KEE, where the third row metal complex shows significantly faster kinetics than the second row complex. The discovery of this inverse KEE raises some significant questions. Is the inverse KEE a special property of the 1,1'-biiq ligand or is this a general trend for ligands which have bent metal ligand bonds in the ground-state? Is the inverse KEE a special property of Ru(II) and Os(II) or will other transition metals also exhibit an inverse KEE in the complex $[M(bipy)_2(biiq)]^{n+}$? Will Ru(II) and Os(II) complexes of 1,1'-biiq exhibit an inverse KEE if the ancillary ligands are changed? The purpose of this research has been to more thoroughly investigate the concept of KEE by studying the dynamic properties of metal-ligand bonds that are misdirected. The ability of organometallic and inorganic coordination compounds to exhibit fluxional behavior will be taken advantage of in order to compare the bond energies of complexes with bent bonds in either the ground-state or transition-state of isomerization reactions.

CHAPTER 2

KINETICS AND MECHANISM OF THE STEREOCHEMICAL ISOMERIZATION OF AN ARENE-RUTHENIUM COMPLEX OF THE ATROPISOMERIC LIGAND 1,1'-BIPHENYL-2,2-DIAMINE

2.1 Introduction

The next two chapters will describe the effect of changing the ligands on the KEE of ruthenium and osmium. In this chapter an effort will be made to answer the question of whether the inverse KEE is a unique result of the 1,1'-biiq ligand. Chapter 3 will address the role of ancillary ligands. Half-sandwich arene metal compounds with bidentate nitrogen donor ligands will be used in both of these studies. Half-sandwich arene metal compounds can have piano-stool type geometry with C_1 symmetry. Twisting of a bidentate ligand renders piano-stool type complexes chiral thereby allowing for the possibility of observing the isomerization of conformational isomers by proton NMR spectroscopy.

2.1.1. Arene-metal half sandwich complexes

Organometallic compounds have been studied extensively due to their use in organic synthesis as stoichiometric and catalytic reagents. This includes half-sandwich chiral ruthenium complexes, which have the structure $[(\eta^6\text{-}C_6H_6)Ru(L\text{-}L)(X)]^+$ (L-L = bidentate ligand; X = halogen). A review article appeared in 1987 that concerns half-sandwich chiral ruthenium complexes.[63] Arene ruthenium complexes first appeared in the literature in 1967 with the preparation of the insoluble $[(\eta^6\text{-}C_6H_6)RuCl_2]_2$.[64] More ruthenium compounds have been reported than osmium compounds.

The dimers $[(\eta^6\text{-}C_6H_6)MCl_2]_2$ (M = Ru, Os) have been prepared in good yield and they serve as starting materials for compounds of the type $[(\eta^6\text{-}C_6H_6)M(L)_2(Cl)]^+$.[65,66] The reactivity of arene ruthenium and osmium

compounds was reviewed in 1989.[67] Nitrogen donor ligands such as ethylene diamine, hydrazine, and pyridine readily react with the arene chloride dimer to give monomeric species.[68] Tertiary phosphine ligands also cleave the halogen bridge to give $[(\eta^6\text{-}C_6H_6)M(L)_2(Cl)]^+$ type complexes.[69] $[(\eta^6\text{-}C_6H_6)M(N\text{-}N)(Cl)]^+$ (N-N= 1,10-phenanthroline, 2,2'-bipy) complexes react with tertiary phosphines in methanol to give the dicationic $[(\eta^6\text{-}C_6H_6)M(N\text{-}N)(PR_3)]^{2+}$. Binuclear complexes of the type $(\mu\text{-}L\text{-}L)[(C_6H_6)RuCl_2]_2$ have been synthesized by refluxing benzene solutions of $[(\eta^6\text{-}C_6H_6)MCl_2]_2$ with the bidentate ligands $Ph_2AsCH_2CH_2AsPh_2$ and $Ph_2P(CH_2)_nPPh_2$ (n = 2,3,4) in a 1:1 metal to ligand ratio. Cationic monnuclear complexes of the same ligands were synthesized by refluxing in ethanol instead of benzene in a 1:2 metal to ligand ratio.[70]

Considerable work has been done in studying the mechanism of isomerization of arene ruthenium complexes. The rates of isomerization of chiral arene metal diastereomers have been measured.[71] Optical activity of arene ruthenium complexes has been investigated by Brunner and coworkers.[71-75] Brunner resolved the first ruthenium compound that was chiral at a metal center: $(\eta^6\text{-}C_6H_6)Ru(Me)(Cl)$-$[Ph_2PNHCH(Me)Ph]$.[76] The diastereomers were separated by chromatography. Both isomers were stable at room temperature and no epimerization was observed even upon heating at 60°C for 18 hours. In 1994, Brunner synthesized $[(\eta^6\text{-}C_6H_6)Ru(PPh_3)$(1-phenylethylsalicylaldimine)$](PF_6)$.[75] During the synthesis diastereomers were formed which differed from each other in the configuration at the ruthenium center. Crystal structures were obtained for both diastereomers. Epimerization of the diastereomers took place at temperatures greater than 5°C. Brunner concluded that the epimerization occurred by a rate determining dissociation of the PPh_3 ligand. In a later study of $(\eta^6\text{-}C_6H_6)$Ru(2-methyl-pyridine)(1-phenylethylsalicylaldimine)(PF_6). ^1H NMR signals for two atropisomers in a ratio of 54:46 were seen when the sample was cooled to -80° C. From coalescence temperature the free energy of activation for the rotational process

was determined to be $\Delta G^{\ddagger} = 44.5(5)$ kJ mole^{-1}. Brunner stated that a conformational analysis based on NMR spectroscopic results showed two main factors which governed the orientation of the 1-phenylethyl group in the structure: face-on orientation of the phenyl substituent with respect to the π-bonded aromatic benzene ligand and steric demand of the unidentate ligands with respect to the 1-phenylethyl group.[72]

In a later paper, Brunner demonstrated that during the synthesis of triphenylphosphane complexes abstraction of chloride by $AgPF_6$ in the presence of PPh_3 proceeded without retention of the metal configuration.[73] It was concluded that the substitution reactions proceed through the formation of a configurationally labile solvent intermediates containing coordinated acetone. The barrier to inversion of the ruthenium configuration in methanol solution of the solvated complexes was shown to be $\Delta G^{\ddagger}_{273} = 57.6(8)$ kJ mole^{-1}.[71] In the same study, Brunner showed that for the complex $[(\eta^6\text{-}C_6H_6)Ru(L\text{-}L)Cl]$ where L-L is equal to the anion of (S)-N-(1-phenylethyl)pyrrole-carbaldimine, the N,N donor set of the ligand conferred an increased configurational stability on the ruthenium atom center.

2.1.2 Isomerization of ethylenediamine metal complexes

Planar and octahedral complexes of ethylenediamine-type ligands have been synthesized with a variety of metals.[77-82] Coordination of the diamines with a metal ion can form five- and six-membered rings which have stereochemical characteristics that are similar to cyclopentane and cyclohexane.[80] Five-membered diamine chelate rings exist in the rapidly interconverting λ and δ twisted conformations.[81] The populations of the two conformers have been investigated for diamine complexes of Co(III), Cr(0), Mo(0), Ru(II), Rh(III), Pd(II), Pt(II), Pt(IV), and Ni(II) by NMR spectroscopy.[77,80,81] The methylene protons are inequivalent in the puckered conformations and are made equivalent as the conformations interconvert. The interconversion can potentially be observed by variable temperature NMR. The rates

of interconversion were measured for $[Fe(CN)_4(1,2\text{-diamine})]^-$. It was possible to measure the rates for this system as the chemical shifts of the diamine protons were resolved because the complex is paramagnetic, and $\delta \rightleftharpoons \lambda$ interconversion was observed between 183 and 323 K. The experiments were repeated for three derivatives of ethylenediamine type complexes. It was observed that increasing the bulkiness of the carbon substituent slows the interconversion and increases the enthalpy of activation ($\Delta H^{\ddagger}$). It is proposed that this increase is due to the increase in steric repulsion resulting in a higher barrier to interconversion. The rates and activation energies are shown in Table 2.1.

Table 2.1. Activation Paramters for the $\delta \rightleftharpoons \lambda$ Conformational Interconversion of $[Fe(CN)_4(1,2\text{-diamine})]^-$ in CD_3OD /DCl at 25° C[81]

Diamine	k s^{-1}	$\Delta H^{\ddagger}$ kJ mol^{-1}	$\Delta S^{\ddagger}$ J K^{-1} mol^{-1}	$\Delta G^{\ddagger}_{298}$ kJ mol^{-1}
ethanediamine	3×10^8	25(4)	0(27)	25(4)
(2R,3S)-butanediamine	2×10^7	30(4)	-3(19)	31(2)
(1R,2S)-*cis*-cyclohexanediamine	8×10^4	43(2)	-8(8)	45.0(5)

Six-membered diamine chelate rings coordinate in three basic types: chair, boat, and a skew (twisted) boat.[80] The skew boat is chiral and exists in δ and λ conformations. 2,4-Pentanediamine(dmtn) is an optically active ligand which has been coordinated to cobalt(II) to form a six-membered ring. The meso ligand (R,S-dmtn) exists in the chair conformation and the racemic ligand (R,R,:S,S-dmtn) is in the skew conformation.[79,80] These diastereomers are separable and stable. Circular dichroism experiments were performed on a series of *trans*-$[Co(R,R\text{-dmtn})_2X_2]^+$ ($X=N_3^-$, NCS^-, NO_2^-, NH_3) complexes. Circular dichroism is much more intense for these six-membered rings than analagous five-membered ring complexes. The intensity of the

bands causes a relative insensitivity to solvent which is also in contrast to five-membered diamine-metal chelate rings.

2.1.3. 1,1'-Biphenyl-2,2'-diamine

The ligand chosen to replace 1,1'-biiq was 1,1'-biphenyl-2,2'-diamine (dabp). Upon binding the diamine ligand to a metal, a rigid seven-membered ring is formed which is highly twisted. The resulting chiral metal complex gives rise to four inequivalent N-H protons in the ^{1}H NMR spectrum. These protons are a stereochemical handle to follow the kinetics and elucidate the mechanism of isomerization. Observed stereospecificity of the potentially atropisomeric ligand dabp when coordinated to platinum[83,84] and cobalt[78,85] (vide infra) suggested experiments to determine if atropisomerization could be measured and compared for $[M(bipy)_2(dabp)]^{2+}$ or $[(\eta^6\text{-}C_6H_6)M(dabp)(Cl)]^+$ (M=Ru, Os). The question of whether the twisting of the ligand causes the metal-nitrogen bonds to be bent will be addressed by the KEE approach.

1,1'-Biphenyl-2,2'-diamine (dabp) has been synthesized by the reduction of the commercially available 1,1'-biphenyl-2,2'-dinitro ligand with sodium borohydride and palladium on carbon in methanol to give the ligand in 94% yield.[86] A crystal structure of dabp was solved by X-ray diffraction in 1977.[87] Each phenyl ring is planar. The rings are twisted by an angle of 58.2° with respect to each other.[87] The authors concluded that the factor determining the configuration of dabp was an intra-molecular N-N hydrogen bond.

2,2'-Dinitrogen substituted biphenyls and conformationally restricted biphenyls have been used to synthesize dissymmetric metal-Schiff base ligand complexes.[88] The biphenyl moieties control geometry in the backbone of the Schiff base ligand.[89] 2,2'-Biaryl bridging units have been used in the study of binuclear Ni(II), Pd(II), and

Pt(II) complexes.[90] 2,2'-Dinitrogen substituted biphenyls have also been used in the design of spiroconjugated charge-transfer dyes.[91]

In 1973, two papers appeared in the literature that discussed the conformation of the dabp ligand when bound to a metal center.[78,85] It was found that the complex $[Co(en)_2(dabp)]^{3+}$ gives only one pair of diastereomers, $\Delta(\lambda)$ and $\Lambda(\delta)$ or $\Delta(\delta)$ and $\Lambda(\lambda)$. It was suggested that the absolute configuration of the complex determines the conformation of the dabp ligand. The authors concluded the preferred conformation on the basis of steric hindrance should be $\Delta(\lambda)$ and $\Lambda(\delta)$. The same preferred conformation was proposed for the complexes $[Co(trien)(dabp)]^{3+}$, and $[Co(bpy)_2(dabp)]^{3+}$.[78] Similar results were found by Douglas and coworkers.[85] Their study concluded that the dabp ligand coordinates stereoselectively with bis(en) and trien complexes of Co(III). The conformation of the coordinated ligand can be determined by using R-6,6'-dimethyl-2,2'-diaminobiphenyl (a ligand that is not likely to undergo atropisomerization) in its place and comparing the CD spectra of the two complexes.[85] Platinum (II) complexes of 2,2'-diaminobiphenyl, $[Pt(R\text{-pn})(dabp)]Cl_2$ and $[Pt(R,R\text{-chxn})(dabp)]Cl_2$, where R-pn is R-1,2-diaminopropane, and R,R-chxn is R,R-trans-1,2-diaminocyclohexane have also been prepared.[83] The dabp ligand shows stereospecificity upon coordination, being in the λ conformation in both complexes. The authors conclude that the stereospecificity observed is due to nonbonded interaction between the hydrogens bonded to nitrogens.

2.2 Synthesis and X-Ray Crystal Structure of $[Ru(bipy)_2(dabp)](PF_6)_2$

$[Ru(bipy)_2(dabp)](PF_6)_2$ was synthesized by adding excess ligand to $Ru(bipy)_2Cl_2$ in a water/ethanol mixure and heating overnight. Thin plates of X-ray quality crystals were obtained by vapor diffusion of ether into a saturated acetone solution at room temperature. Selected interatomic distances, angles, and torsion angles are given in Table 2.2. A diagram showing the thermal ellipsoids (at the 50%) level of

the molecule and labeling scheme is given in Figure 2.1. Crystallographic details are discussed in Section 5.2.1 with crystal data, atomic coordinates, anisotropic displacement parameters and hydrogen coordinates.

The X-ray structure shows C_2 symmetry in which one half of the molecule is equivalent with the other half. Many bis(bipyridine) ruthenium(II) compounds can be found in the literature. They are six coordinate octahedral molecules. This compound is unremarkable in that it has octahedral geometry. The seven-membered chelate ring is δ when the configuration at the metal is Δ. Both diastereomers are present in the centrosymmetric crystals. The observed Ru-N interatomic distances of 2.154(5)Å are comparable to those that have been reported previously for related compounds such as $[Ru(bipy)_2(PhCH_2NH_2)_2](PF_6)_2$ (2.17Å).[92] The bipyridine ligands are nearly flat with a torsion angle of 2.33°. The biphenyl rings are twisted with a torsion angle of 69.9(6)°. This compares to the torsion angle of the free ligand of 59.79°.[87] Together, these metric data suggest the seven-membered chelate ring that is formed when the dabp ligand is coordinated is not highly strained and the Ru-N bonds are quite normal.

Table 2.2. Selected Interatomic Distances (Å), Angles (deg), and Torsion Angles (deg) for $[Ru(bipy)_2(dabp)]^{2+}$

Ru-N	2.172(8)
Ru-N(1)	2.054(5)
Ru-N(2)	2.073(4)
Ru-N(3)	2.154(5)
N(1)-Ru-N(1A)#1	96.6(3)
N(1)-Ru-N(2)	78.7(2)
N(1A)#1-Ru-N(2)	95.6(2)
N(2)-Ru-N(2A)#1	171.4(3)
N(1)-Ru-N(3)	87.1(2)
N(1A)#1-Ru-N(3)	173.9(2)
N(2)-Ru-N(3)	89.9(2)
N(2A)#1-Ru-N(3)	96.2(2)
N(3)-Ru-N(3A)#1	89.7(3)
C(16)-C(15)-C(15A)#1-C(16A)#1	69.9(6)

Symmetry transformations used to generate equivalent atoms:
#1 -x,y,-z+1/2

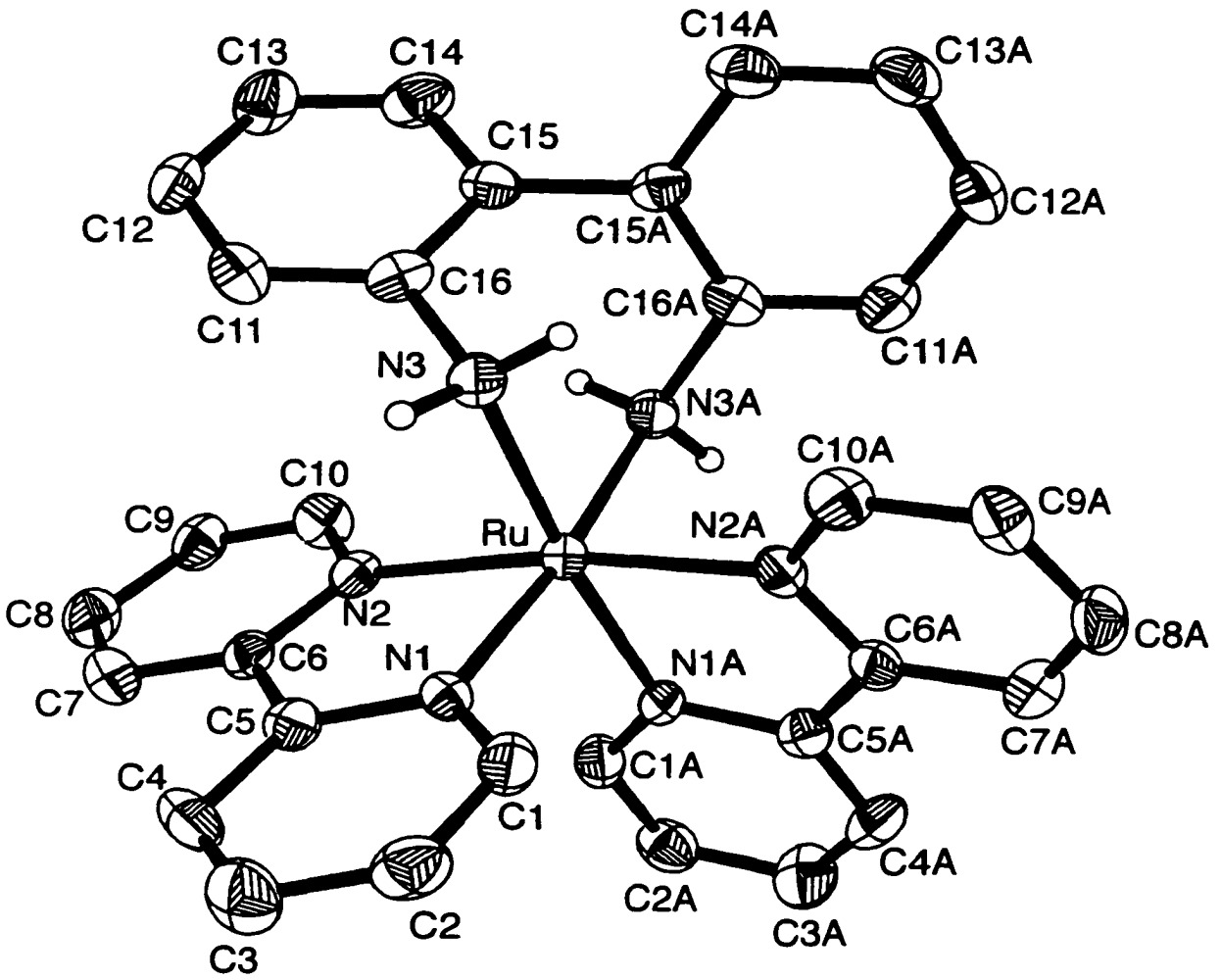

Figure 2.1. Molecular structure of $[Ru(bipy)_2(dabp)]^{2+}$ showing the atom labeling scheme and the thermal vibration ellipsoids (50% probability). All of the hydrogen atoms have been omitted for the sake of clarity except those on N3 and N3A.

2.3. Variable Temperature ^{1}H NMR of $[Ru(bipy)_2(dabp)]^{2+}$

The C_2 symmetry of $[Ru(bipy)_2(dabp)]^{2+}$ is preserved in solution as only 14 resonances are observed for the 28 protons. Only one diastereomer is seen in solution. Low temperature ^{1}H NMR experiments were carried out in acetone-d_6, methylene chloride-d_2 and the deuterated freon $CDCl_2F$. The acetone-d_6 and $CDCl_2F$ spectra show two doublets for the amine nitrogens at room temperature. There is no change in the spectra as the temperature is lowered to the limit for each solvent. The spectrum in methylene chloride-d_2 shows only one broad singlet for the amine nitrogens at room temperature. This peak resolves into two broad doublets as the temperature is lowered. This is illustrated in Figure 2.2. Chemical shifts of peaks can move as a result of fluxional behavior in solution or as a result of temperature changes unrelated to dynamic behavior. Lowering the temperature to -150°C in $CDCl_2F$ failed to reveal any further resolution of the bipyridine or biphenyl resonances. 2D-EXSY spectroscopy and spin-labeling ^{1}H NMR techniques failed to demonstrate any exchange between these protons. It is likely that in this case the movement of the amine peaks is a function of temperature.

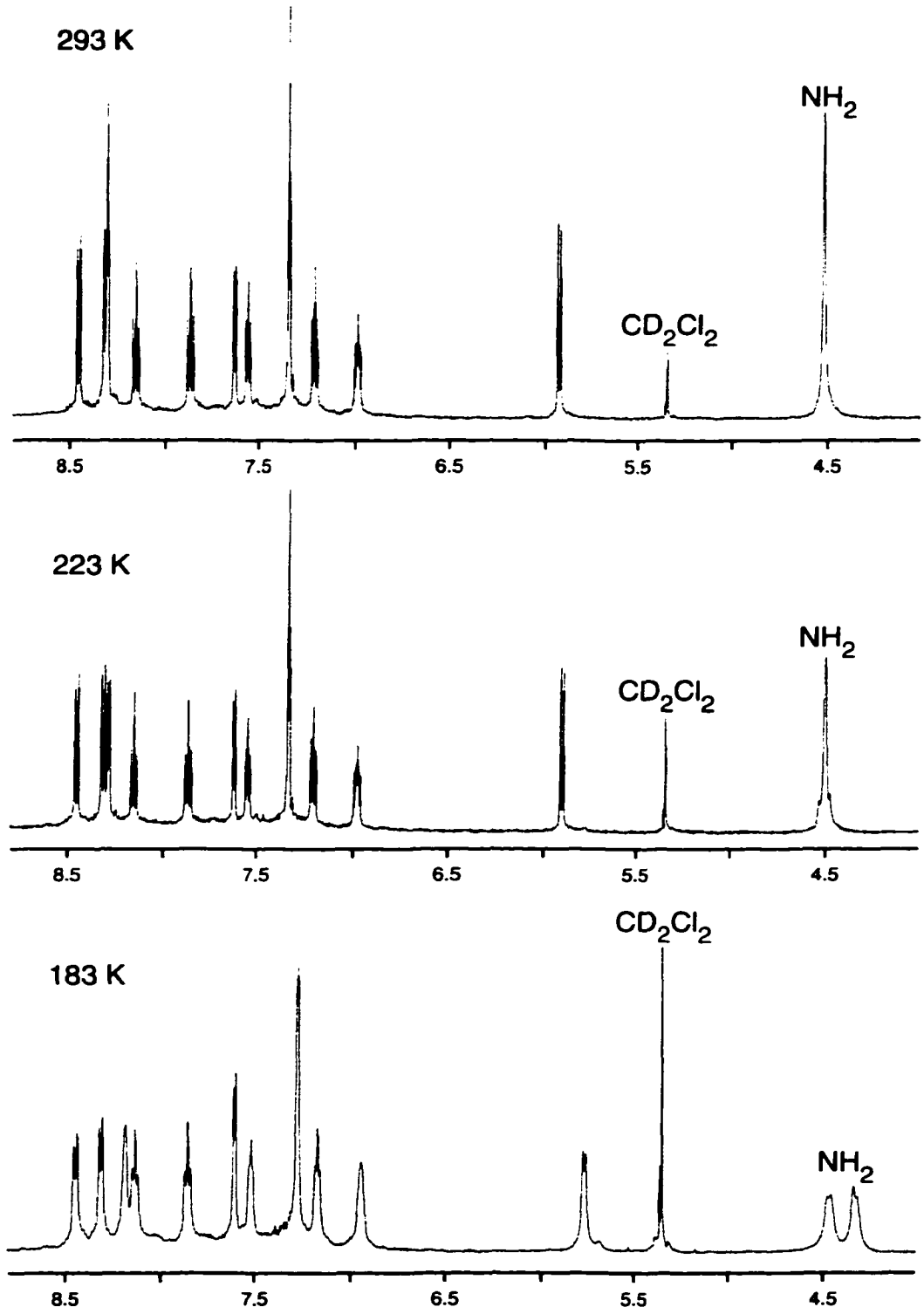

Figure 2.2. Variable temperature ^1H NMR spectra of $[Ru(bipy)_2(dabp)]^{2+}$ in CD_2Cl_2 illustrating the movement of the NH_2 peaks.

2.4 Synthesis of $[(\eta^6\text{-}C_6H_6)M(dabp)(Cl)](PF_6)$ for M = Ru, Os

$[(\eta^6\text{-}C_6H_6)Ru(dabp)(Cl)](PF_6)$ was synthesized by adding excess dabp to the $[(\eta^6\text{-}C_6H_6)RuCl_2]$ dimer in methanol and heating for 30-40 minutes. Orange crystals were isolated from the reaction mixture after adding NH_4PF_6 and removing some of the methanol by vacuum transfer. The osmium derivative was synthesized by heating excess ligand with the acetonitrile adduct, $(\eta^6\text{-}C_6H_6)Os(CH_3CN)Cl_2$ overnight in methanol. The osmium derivative was much less stable than the ruthenium derivative and it was not possible to isolate X-ray quality crystals.

2.5 X-Ray Crystal Structure of $[(\eta^6\text{-}C_6H_6)Ru(dabp)(Cl)](PF_6)$

Diffraction quality crystals were grown from the reaction mixture. Selected interatomic distances, angles, torsion angles and other metric parameters are given in Table 2.3. A diagram showing the thermal ellipsoids (at the 40% level) of the molecule and labeling scheme is given in Figure 2.3. Crystallographic details are discussed in Section 5.2.1 with crystal data, atomic coordinates, anisotropic displacement parameters and hydrogen coordinates.

The rigid nature of the seven-membered chelate ring formed by the diamine ligand renders $[(\eta^6\text{-}C_6H_6)Ru(dabp)(Cl)](PF_6)$ chiral. The compound has C_1 symmetry and piano stool geometry. This is clearly seen in the molecular structure (Figure 2.3). In fact, $[(\eta^6\text{-}C_6H_6)Ru(dabp)(Cl)](PF_6)$ spontaneously resolves and crystallizes in a chiral space group ($P2_12_12_1$). In acetone solution, the four hydrogen atoms that are bound to the two nitrogen atoms of $[(\eta^6\text{-}C_6H_6)Ru(dabp)(Cl)](PF_6)$ are chemically inequivalent in the ^1H NMR spectrum at 20 °C. There are closer contacts from the protons on C_3 of each ring to one proton on each nitrogen. This is shown by the dashed lines in Figure 2.3. These close contacts between protons were employed to absolutely assign the chemical shifts of the protons in ^1H NMR.

Table 2.3. Selected Interatomic Distances (Å), Angles (deg), and Torsion Angles (deg) for $[(\eta^6\text{-}C_6H_6)Ru(dabp)(Cl)]^+$

Ru(1) - N	2.172(8)
Ru(1) - N'	2.175(6)
Ru(1) - Cl(1)	2.414(2)
Ru(1) - Ar_{cent}	1.661(8)
H(A).....H(3)	2.3(1)
H(B).....H(3)	3.1(1)
H(C).....H(3')	3.4(1)
H(D).....H(3')	2.3(1)
N - Ru(1) - N'	84.1(3)
N - Ru(1) - Cl(1)	84.2(2)
N' - Ru(1) - Cl(1)	86.1(2)
Ar_{cent} - Ru(1) - Cl(1)	128.6(3)
Ar_{cent} - Ru(1) - N	128.2(4)
Ar_{cent} - Ru(1) - N'	129.7(4)
C(2)-C(1)-C(1')-C(2')	60(1)

[a] Ar is defined to be the least-squares plane that contains an arene ligand. Ar_{cent} is the centroid of the arene ligand.

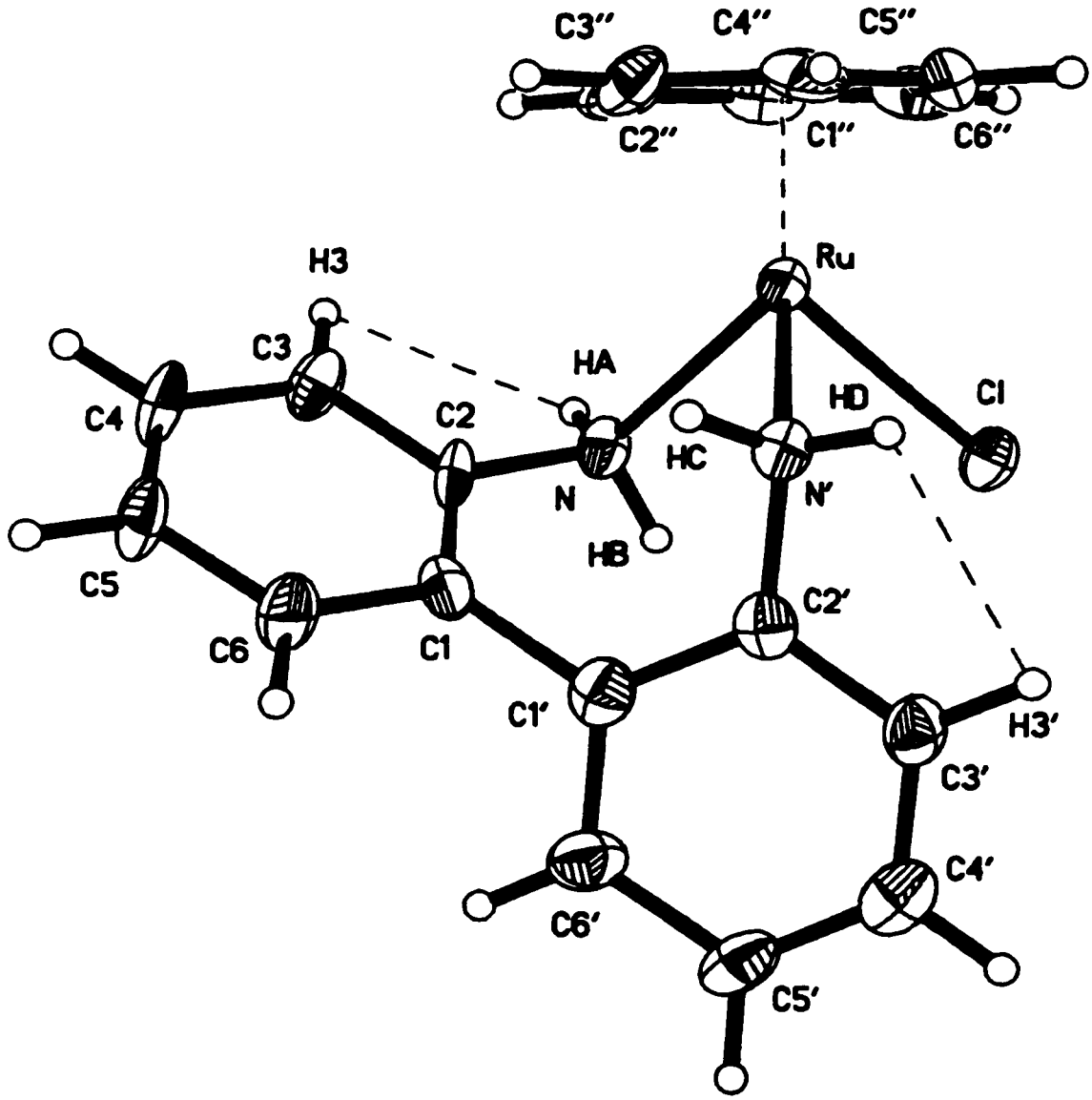

Figure 2.3. Molecular structure of $[(\eta^6\text{-}C_6H_6)Ru(dabp)(Cl)]^+$ showing the atom labeling scheme and the thermal vibration ellipsoids (50% probability). All of the hydrogen atoms have been omitted for the sake of clarity except for HA, HB, HC, and HD. The dashed lines represent close contacts between protons in the NMR spectrum.

2.6 ^{1}H NMR Experiments of $[(\eta^6\text{-}C_6H_6)Ru(dabp)(Cl)]^+$ for M=Ru, Os

2.6.1 Assignment of ^{1}H NMR Spectrum

Since it was important for the mechanistic study (vide infra) to make an absolute assignment of the peaks in the ^{1}H NMR, 2D-NOESY and COSY spectra were measured at 185 K (Figure 2.4 for M=Ru). The spectra were collected at low temperature because the peaks were better resolved and dynamic behavior was suppressed at this temperature. The COSY experiment gives geminal coupling information (Figure 2.4, top). There are four amine proton resonances in the spectrum. Three are grouped downfield (A,C,D) and one is upfield (B). The COSY demonstrates which protons are on each nitrogen. The NOESY experiment gives information about through-space coupling. The NOESY is illustrated in the bottom of Figure 2.4 and shows contact between proton A to proton 3 and between proton D to proton 3'. Proton 3 and 3' are on the biphenyl rings. These NOE contacts demonstrate which proton of each nitrogen is closest to the ring. These are assigned to the close contacts that are seen from the crystal structure (Figure 2.3). This information combined with the crystal structure gives an absolute assignment of the ^{1}H NMR spectrum at low temperature. Figure 2.5 shows the same genimal coupling for the osmium derivative. Details of the COSY and NOESY experiments are given in Section 5.6.2.

Dynamic behavior for $[(\eta^6\text{-}C_6H_6)Ru(dabp)(Cl)]^+$ was observed at 20° C by 2D-EXSY NMR. This experiment is illustrated in Figure 2.6 for M=Ru and Figure 2.7 for M=Os. The cross peaks show the pairwise magnetic exchange of the amine protons as well as the exchange of the protons on each half of the biphenyl ring. These pairwise exchanges can provide information as to the mechanism of the isomerization. It is important to determine what mechanism is causing the isomerization in order to make a valid comparison between the ruthenium and osmium derivatives. Alternate mechanisms to atropisomerization must be ruled out (vide infra) if a valid comparison is to be made.

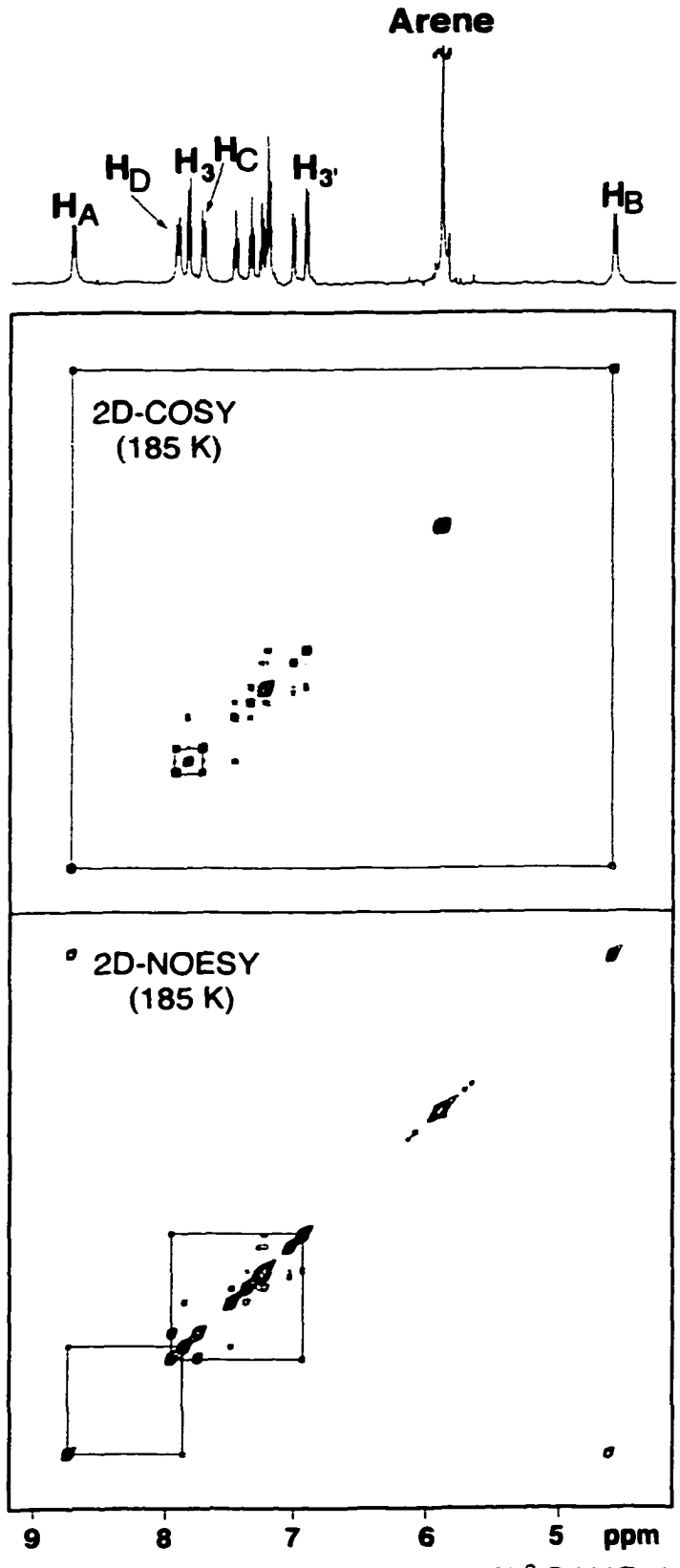

Figure 2.4. 2D-COSY and 2D-NOESY Spectrum of $[(\eta^6\text{-}C_6H_6)Ru(dabp)(Cl)]^+$ at 500 MHz in acetone-d_6.

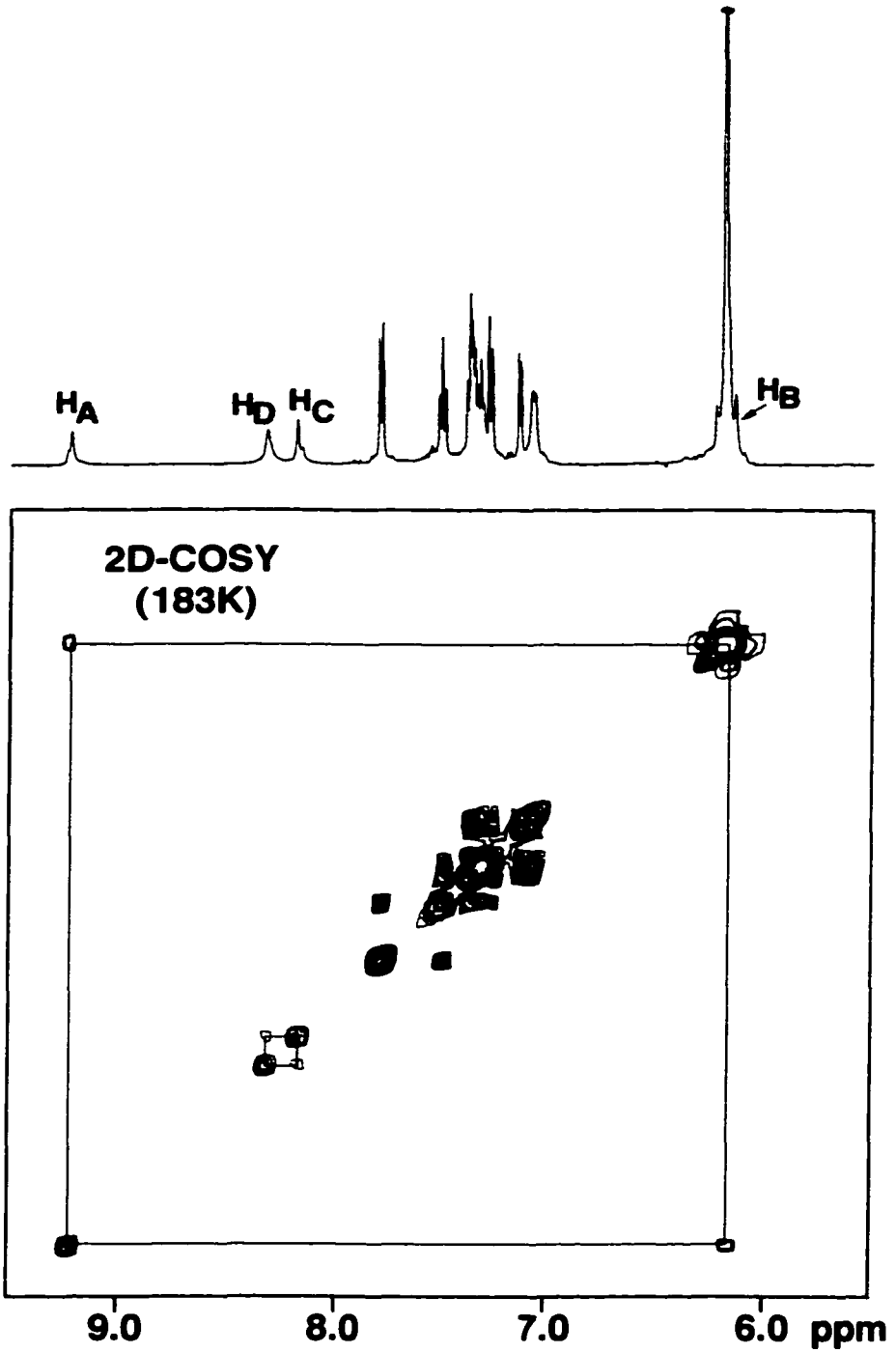

Figure 2.5. 2D-COSY Spectrum of $[(\eta^6\text{-}C_6H_6)Os(dabp)(Cl)]^+$ at 500 MHz in acetone-d_6.

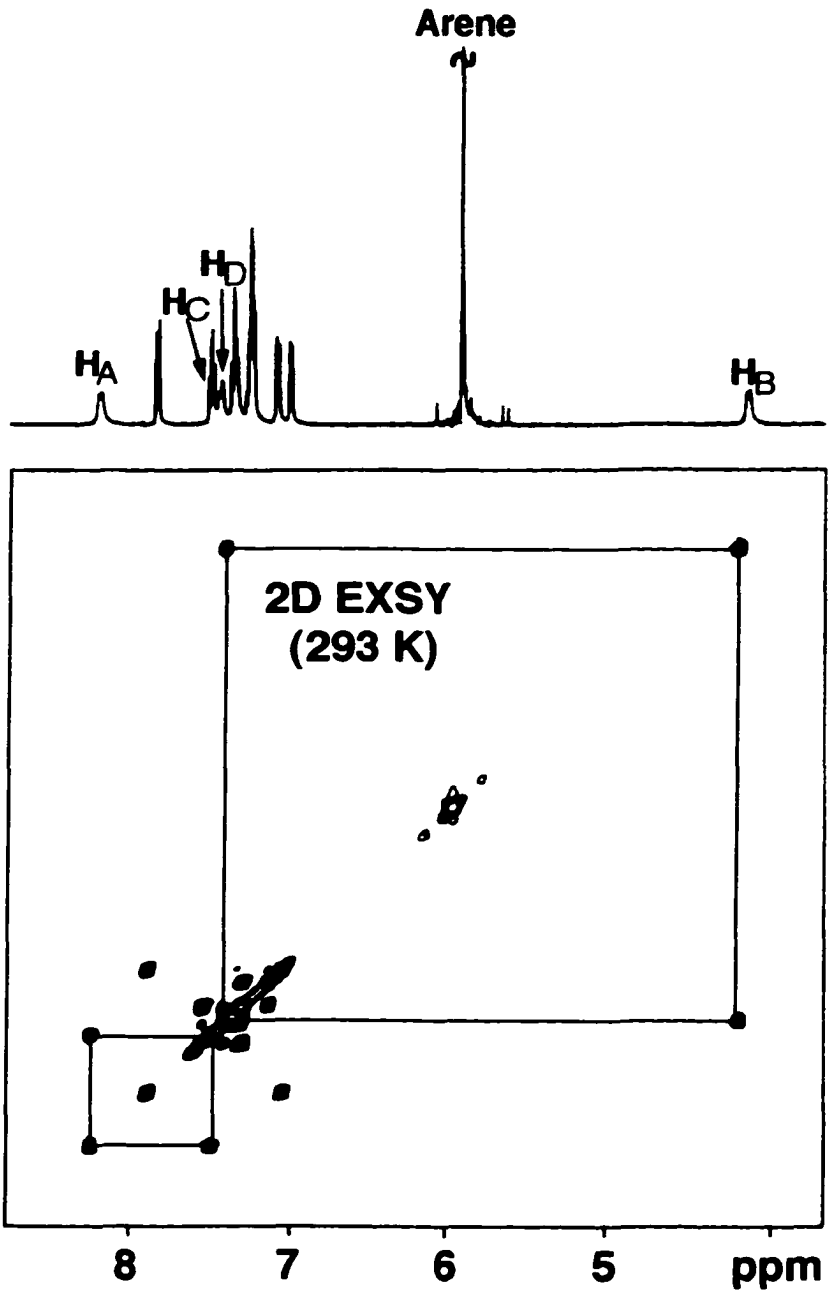

Figure 2.6. 2D-EXSY Spectrum of $[(\eta^6\text{-}C_6H_6)Ru(dabp)(Cl)]^+$ illustrating the pairwise exchange of the amine protons.

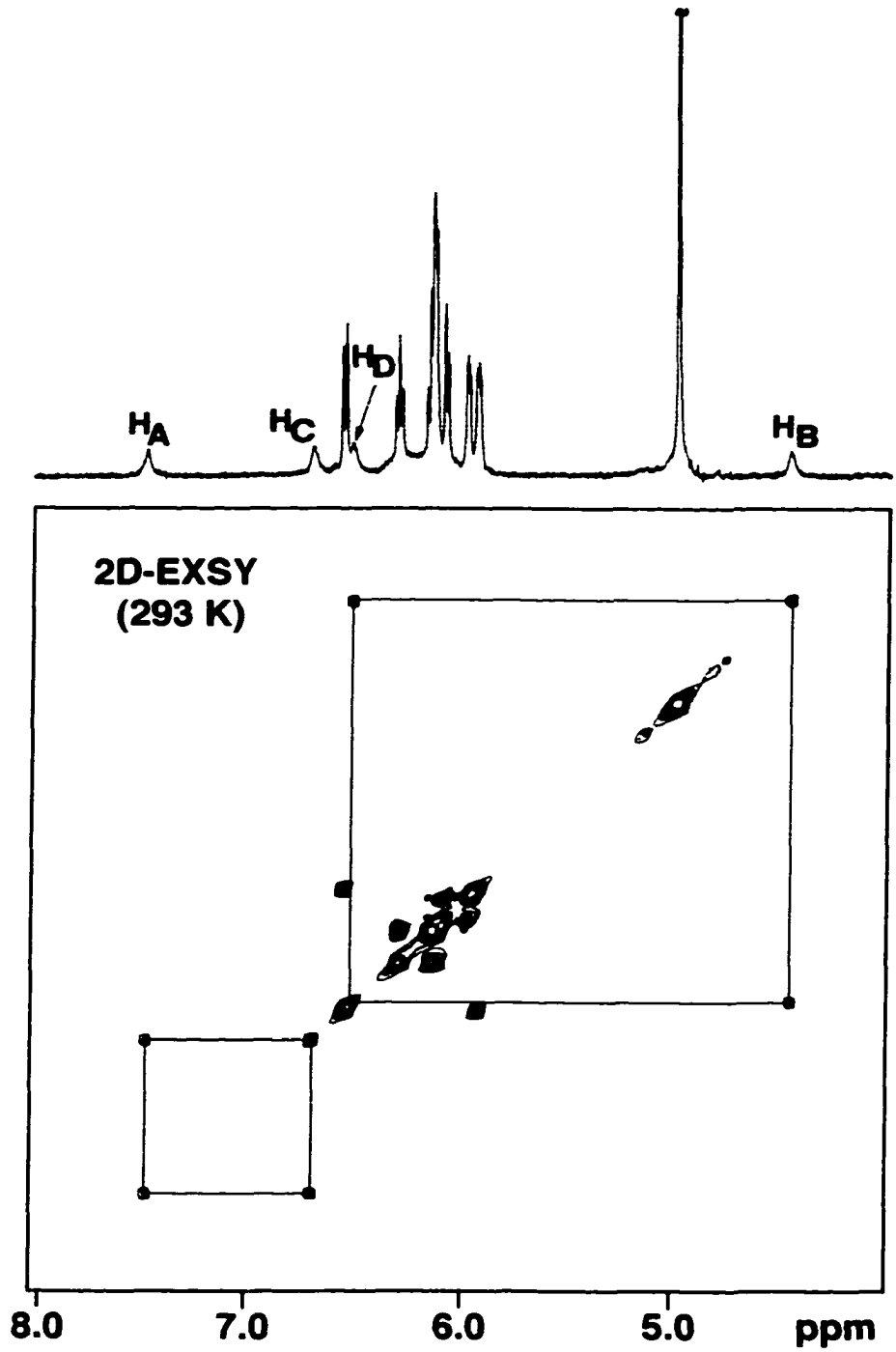

Figure 2.7. 2D-EXSY Spectrum of $[(\eta^6\text{-}C_6H_6)Os(dabp)(Cl)]^+$ illustrating the pairwise exchange of the amine protons.

The ^1H NMR spectra changes when the temperature is raised. This is illustrated in Figure 2.8 for the ruthenium derivative. The chemical shift of the amine peaks change as a function of temperature. The assignment of the spectrum was made at low temperature, while the exchange was observed at room temperature. Several spectra were recorded at various temperatures to follow the movement of the amine chemical shifts. Proton C is downfield from proton D at room temperature, but proton D is downfield from proton C at low temperature. It is clear from plotting the temperature versus chemical shifts of peaks C and D that they are indeed exchanging relative chemical shifts. This plot is shown in Figure 2.9 (M=Ru) and Figure 2.10 (M=Os).

2.6.2 Kinetic Experiments

The spin-labeling ^1H NMR experiment spin inversion transfer (SIT) was used to measure the kinetics for this system. SIT is explained in detail in the experimental section (Section 5.7.3). The kinetic data are summarized in Table 2.4. The fits that were used to obtain the rate constants are shown in Figure 2.11 (M=Ru, 20-25°C), Figure 2.12 (M=Ru, 30-40°C), Figure 2.13 (M=Ru, 50°C; M=Os, 20°C). It was possible to measure the rate of atropisomerization of the ruthenium derivative at several temperatures. However the osmium derivative was much less stable and it decomposed at higher temperatures. It was only possible to measure the rate of isomerization of the osmium derivative at 20 °C. The rate of osmium is almost twice as fast as ruthenium at this temperature. A small KEE of 0.51 (KEE = $k_{2nd\ row}/k_{3rd\ row}$) was observed for this system.

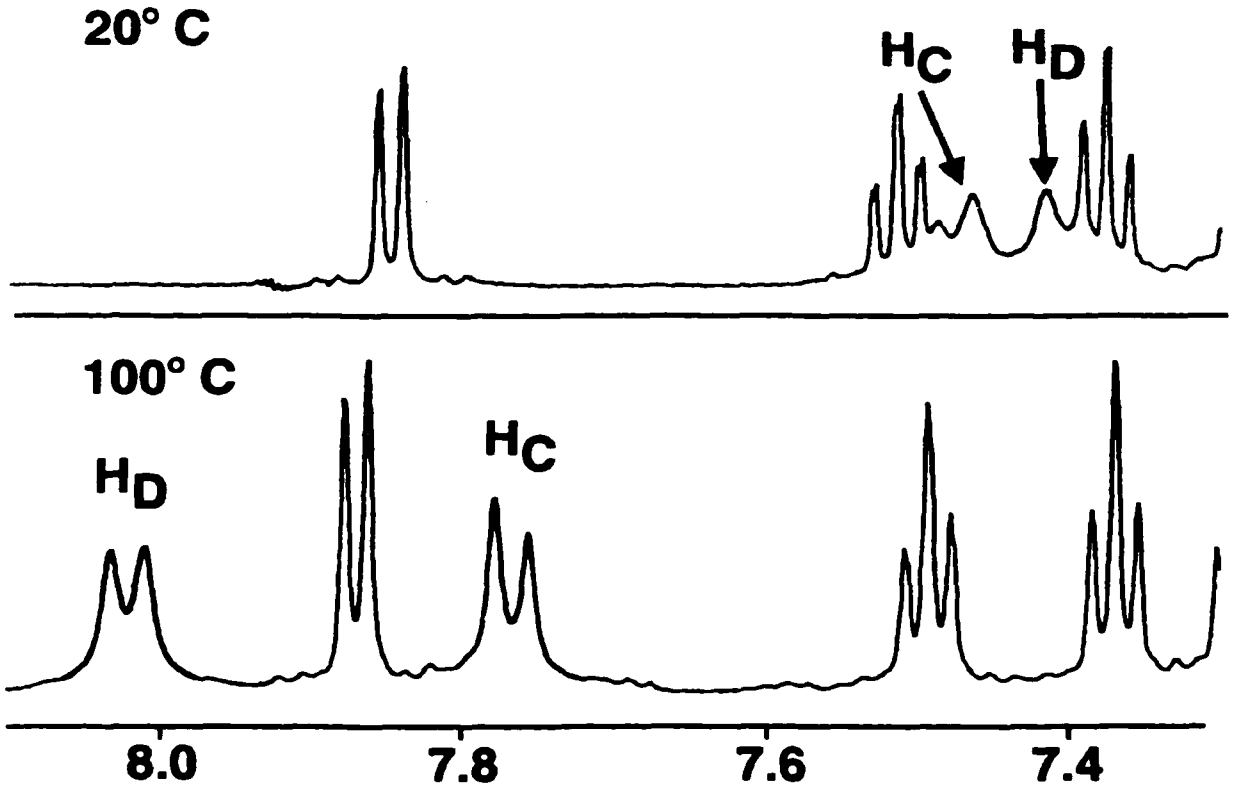

Figure 2.8. Variable temperature ^1H NMR of $[(\eta^6\text{-}C_6H_6)Ru(dabp)(Cl)]^+$ illustrating the movement of HC and HD as a function of temperature.

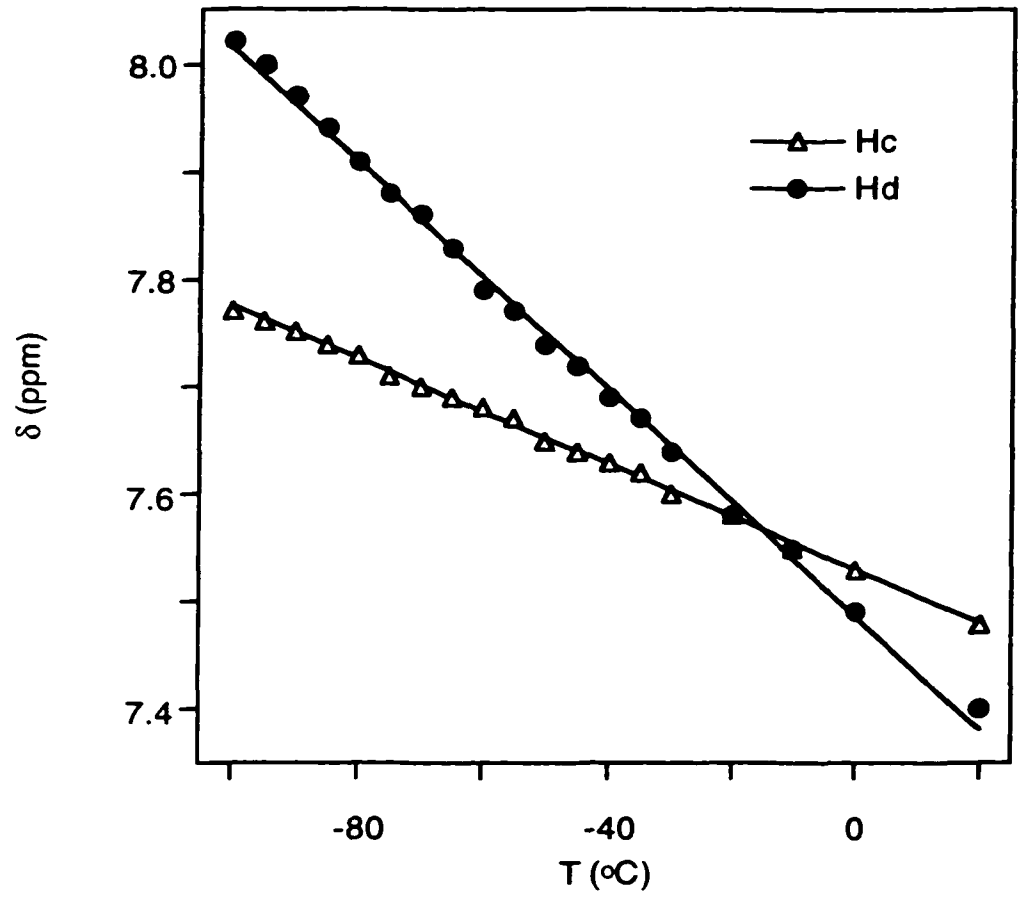

Figure 2.9. The linear dependence on temperature observed for the NH chemical shifts for $[(\eta^6\text{-}C_6H_6)Ru(dabp)(Cl)]^+$ that allow their unambiguous assignment at 20 °C.

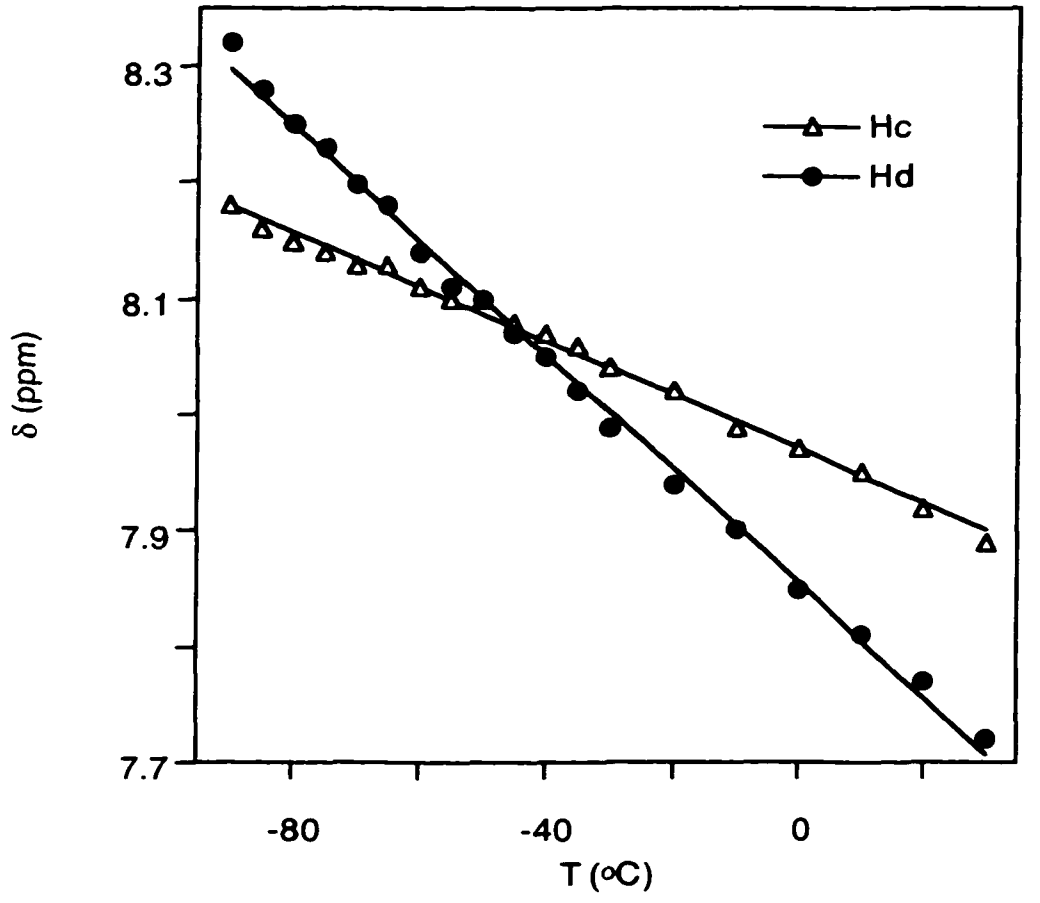

Figure 2.10. The linear dependence on temperature observed for the NH chemical shifts for $[(\eta^6\text{-}C_6H_6)Os(dabp)(Cl)]^+$ that allow their unambiguous assignment at 20 °C.

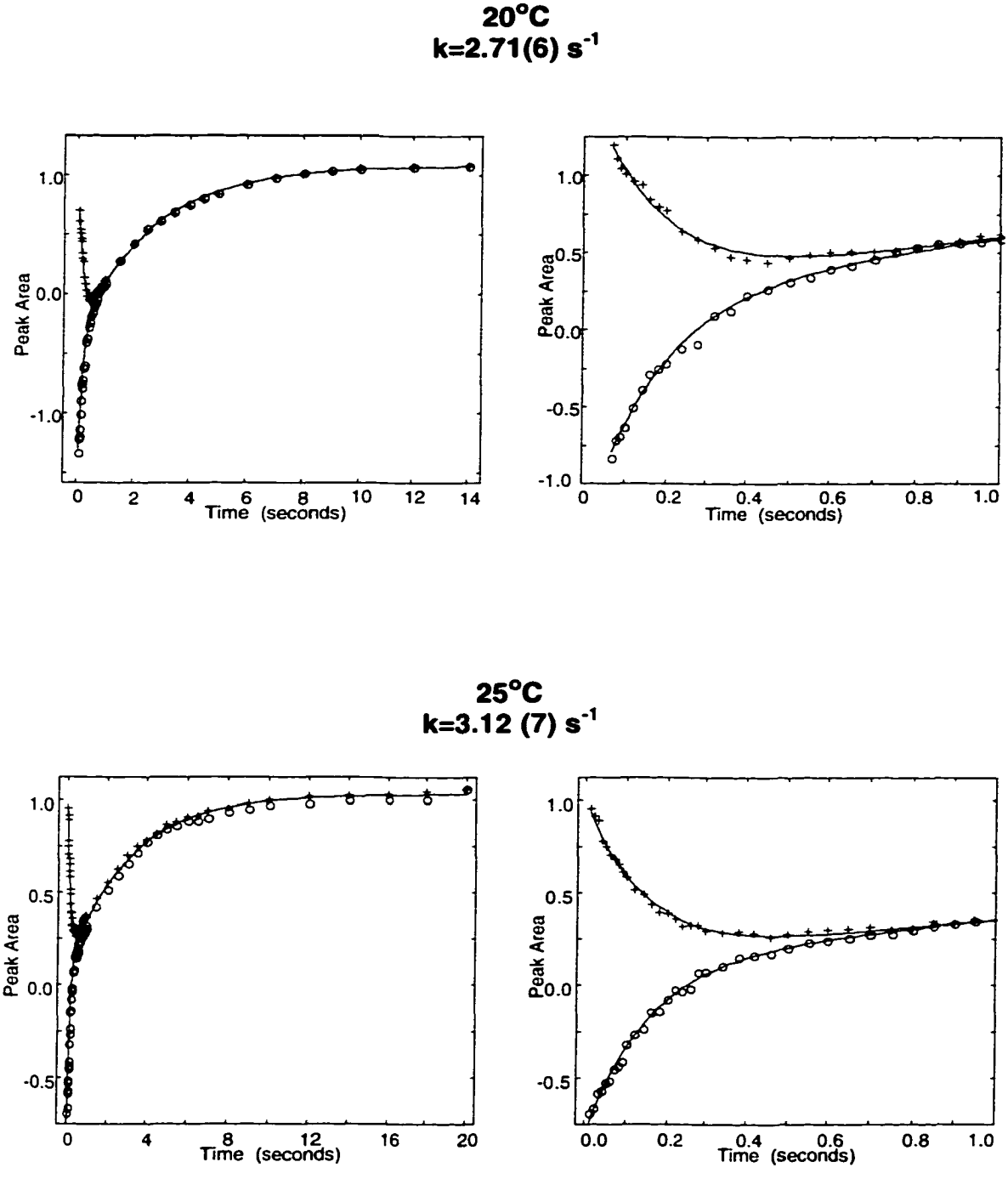

Figure 2.11. SIT fits for $[(\eta^6\text{-}C_6H_6)Ru(dabp)(Cl)]^+$.

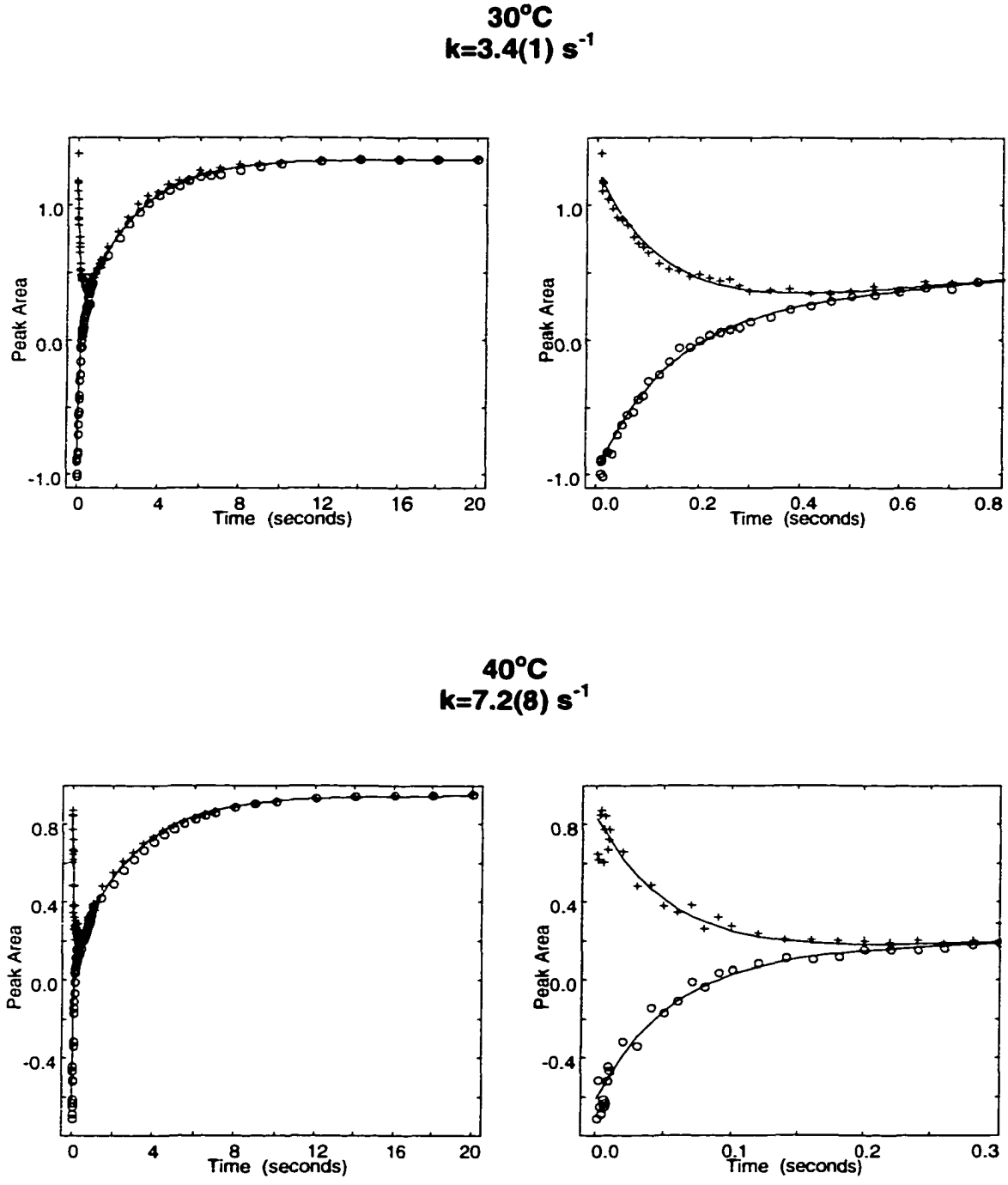

Figure 2.12. SIT fits for $[(\eta^6\text{-}C_6H_6)Ru(dabp)(Cl)]^+$.

M=Ru
50°C
k=9.4(9) s^{-1}

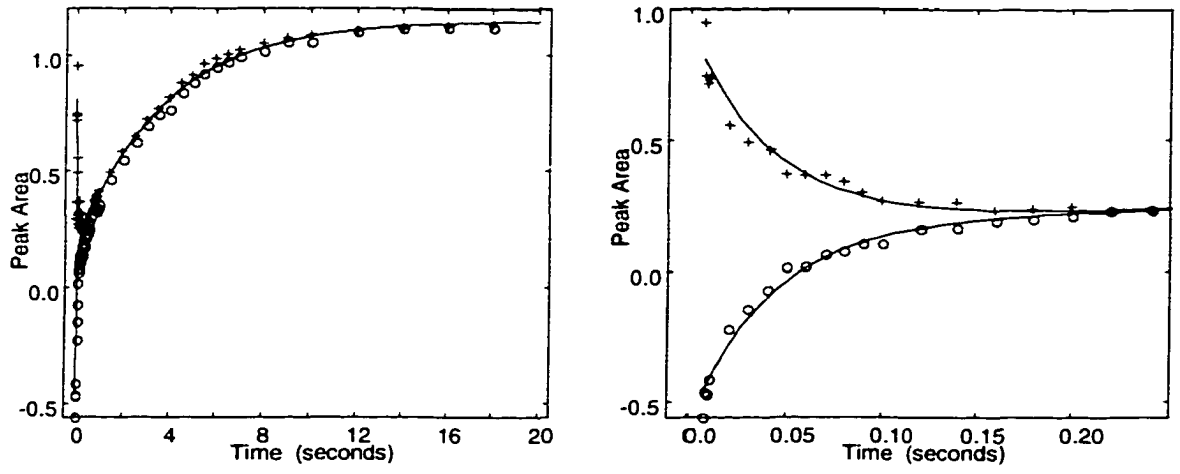

M=Os
20°C
k=5.3(6) s^{-1}

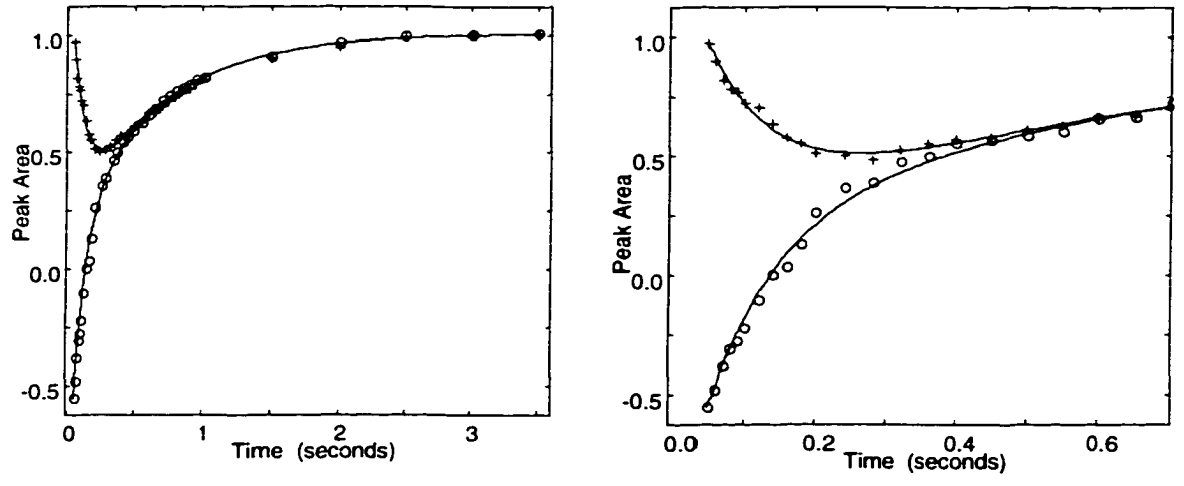

Figure 2.13. SIT fits for $[(\eta^6\text{-}C_6H_6)M(dabp)(Cl)]^+$.

Table 2.4. Comparison of the Kinetic Data Obtained for the Atropisomerization of the Ru and Os Derivatives of $[(\eta^6\text{-}C_6H_6)Ru(dabp)(Cl)]^{+a}$

	M = Ru k_1 (s^{-1})	M = Os k_1 (s^{-1})
20	2.71(6)	5.3(6)
25	3.12(7)	
30	3.4(1)	
40	7.2(8)	
50	9.4(9)	

[a] For **(M=Ru)**, $\Delta G_{283K}^{\ddagger}$ = 66.8 kJ mol^{-1}, $\Delta H^{\ddagger}$ = 33.0 kJ mol^{-1}, and $\Delta S^{\ddagger}$ = -125 J K^{-1} mol^{-1}. [a] For **(M=Os)**, $\Delta G_{283K}^{\ddagger}$ = 65.3 kJ mol^{-1}.

2.7 Synthesis and ^{1}H NMR Experiments of $[(\eta^6\text{-}C_6H_6)Ru(dabn)(Cl)]^+$

$[(\eta^6\text{-}C_6H_6)Ru(dabn)(Cl)](PF_6)$ was synthesized in the same manner as the dabp derivative. The (S)-1,1'-binaphthyl-2,2'-diamine (dabn) ligand is not likely to undergo atropisomerization due to steric hinderances. Isomerization of this metal complex would be more likely to occur via inversion at the metal center or a mechanism in which the halide comes on and off the complex. Two-dimensional exchange spectroscopy and spin-labeling techniques failed to reveal a magnetic exchange of NH resonances. This differs from the analogous dabp complex which shows the pair-wise exchange of the NH resonances.

2.8 Discussion

The ^{1}H NMR Spectrum of $[Ru(bipy)_2(dabp)]^{2+}$ showed one amine resonance which split into two peaks at low temperature in methylene chloride-d_2. Spin-labeling NMR techniques failed to demonstrate exchange between these peaks. The observed movement of amine chemical shift is simply a function of temperature. The C_2 symmetry of $[Ru(bipy)_2(dabp)]^{2+}$ results in two pairs of symmetry-related amine

protons. $[(\eta^6\text{-}C_6H_6)M(dabp)(Cl)]^+$ has C_1 molecular symmetry, resulting in four inequivalent amine protons. The protons of $[(\eta^6\text{-}C_6H_6)M(dabp)(Cl)]^+$ also move as a function of temperature. However, spin-labeling NMR techniques reveal chemical exchange between these protons. The four inequivalent amine protons simplify the problem because they provide a handle which may be used to investigate the mechanism of chemical exchange which is taking place in solution. The COSY, NOESY and variable temperature ^1H NMR spectra allow for an absolute assignment of the protons in the NMR spectrum. The 2D-EXSY spectra reveal a pair-wise exchange of the amine nitrogens (Figure 2.6 (M=Ru) and Figure 2.7 (M=Os)). There are three possible mechanisms which may account for the observed pairwise exchange: inversion at the metal center, inversion at the ligand, or simultaneous inversion at the metal center and ligand. These three mechanisms are illustrated in Figure 2.14. An exchange matrix is shown at the bottom of each mechanism to account for the exchange of the amine protons. Each mechanism has a different exchange matrix. The only mechanism which is in agreement with the experimental evidence is inversion at the ligand. This mechanism accounts for proton A exchanging with proton C and proton B exchanging with proton D. In support of this mechanismm, the analogous compound was made with (S)-1,1'-binaphthyl-2,2'-diamine(dabn). This ligand is not likely to undergo atropisomerization due to steric hinderances. The exchange spectrum of $[(\eta^6\text{-}C_6H_6)Ru(dabn)(Cl)]^+$ did not show pair-wise exchange of the amine protons. The mechanism of atropisomerization of the dabp ligand is futher evidenced by the fact that a single crystal of $[(\eta^6\text{-}C_6H_6)Ru(dabp)(Cl)]^+$ which crystallizes in the chiral space group $P2_12_12_1$ does not exhibit a circular dichroism spectrum when dissolved in acetone. Atropisomerism of the dabp ligand has two possible transition-states. A *syn* transition state is possible in which the torsion angle between the biphenyl rings is reduced to approximately 0°. An *anti* transition-state is also possible in which one of the metal-nitrogen bond breaks during rotation about the biphenyl rings forming a solvent

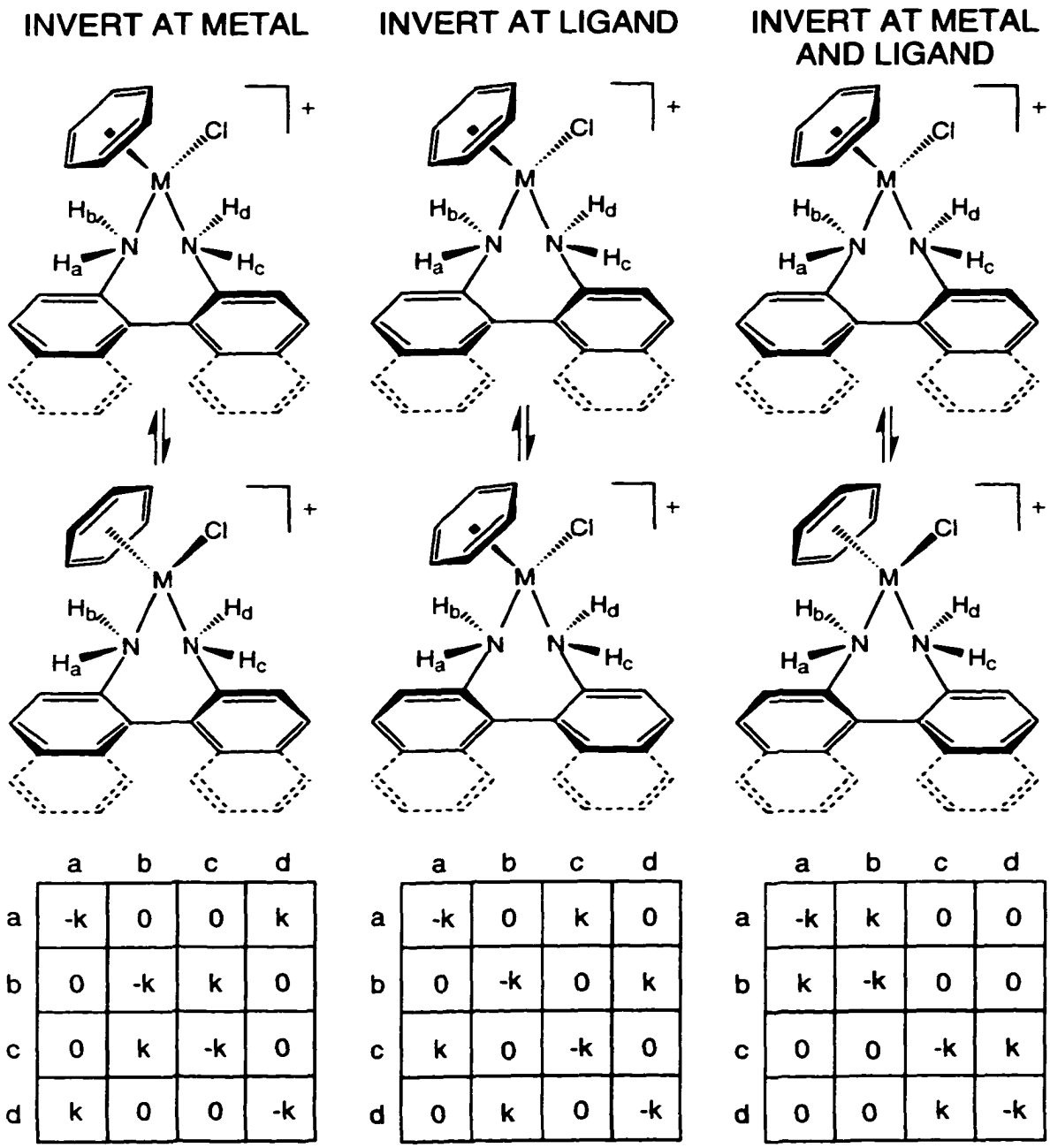

	a	b	c	d
a	-k	0	0	k
b	0	-k	k	0
c	0	k	-k	0
d	k	0	0	-k

	a	b	c	d
a	-k	0	k	0
b	0	-k	0	k
c	k	0	-k	0
d	0	k	0	-k

	a	b	c	d
a	-k	k	0	0
b	k	-k	0	0
c	0	0	-k	k
d	0	0	k	-k

Figure 2.14. Possible mechanisms and corresponding exchange matrices for the isomerization of $[(\eta^6\text{-}C_6H_6)M(dabp)(Cl)]^+$, M=Ru, Os.

coordinated intermediate. Since pyramidal nitrogens readily invert, an *anti* transition-state should result in chemical exchange of the geminal amine protons. This is not observed experimentally. The solvated intermediate would likely undergo inversion at the metal center.[73] This is also not observed. It was concluded from this evidence that $[(\eta^6\text{-}C_6H_6)Ru(dabp)(Cl)]^+$ isomerizes by a mechanism of atropisomerization of the dabp ligand through a *syn* transition-state involving no breakage of the metal-ligand bonds.

Determining the mechanism of isomerization is essential in order to make a valid comparison of the rates of atropisomerization between the second-row and third-row complexes. It is necessary for both derivatives to isomerize through the same mechanism. It was found that the osmium compound exhibited the same pairwise exchange of amine protons as the ruthenium derivative. The isomerization of $[(\eta^6\text{-}C_6H_6)M(dabp)(Cl)]^+$ (M=Ru and Os) proceeds through a mechanism of atropisomerization of the dabp ligand in which there is no breakage of the metal-nitrogen bonds. Therefore, this system is ideal for a KEE comparison. It was unfortunate that a comparison between the osmium and ruthenium derivatives of $[(\eta^6\text{-}C_6H_6)M(dabp)(Cl)]^+$ could only be made at one temperature. This does not allow for the separation of the enthalpic and entropic activation parameters. At 20 °C, ruthenium is faster than osmium by a factor of about 2. Thus, the KEE is 0.51. This relatively small KEE suggests that the metal-nitrogen bonds are not substantially perturbed in the isomerization. The aliphatic nature of the RNH_2 donor of the dabp ligand can possibly compensate for the ring strain during atropisomerization by rehybridization at the nitrogen. This would redirect the σ-donor orbital of the nitrogen. Nonetheless, the elucidation of this mechanism is important in the study of similiar compounds such as $[(\eta^6\text{-}C_6H_6)M(biiq)(X)]^+$. $[(\eta^6\text{-}C_6H_6)M(biiq)(X)]^+$ is a system in which the rates can be measured at a larger temperature range, but has no

stereochemical handle to determine the mechanism of isomerization. The 1,1'-biiq system will be discussed in the following chapter.

2.9 Summary

Metal complexes were synthesized with the atropisomeric ligand 1,1'-biphenyl-2,2-diamine. Only one diastereomer was observed for $[Ru(bipy)_2(dabp)]^{2+}$ in the ^1H NMR spectrum. Exchange was observed and measured for the ruthenium and osmium complexes of $[(\eta^6\text{-}C_6H_6)M(dabp)(Cl)]^+$. It has been determined that $[(\eta^6\text{-}C_6H_6)M(dabp)(Cl)]^+$ isomerizes on the spin relaxation time scale by atropisomerization of the dabp ligand. The rates of ruthenium and osmium were compared at 20 °C and a small KEE of 0.51 was observed. This small KEE suggests the M-N bond strengths are not substantially perturbed during the stereoisomerization. However, the existence of this small inverse KEE also suggests that this effect can be seen for other ligands than 1,1'-biiq.

CHAPER 3

KINETICS OF ARENE-METAL COMPLEXES OF 1,1'-BIISOQUINOLINE, $[(\eta^6\text{-}C_6H_6)M(Biiq)(X)]^+$ M=Ru(II),Os(II); X=Cl, I

3.1 Introduction

Half-sandwich metal 1,1'-biiq, $[(\eta^6\text{-}C_6H_6)M(1,1'\text{-biiq})(X)]^+$, complexes offer another opportunity to measure and compare the rates of atropisomerization of ruthenium and osmium complexes. 1,1'-Biiq is a heterocyclic diimine ligand which is highly twisted when bound to a metal center. This results in bent metal-nitrogen bonds. The $[(\eta^6\text{-}C_6H_6)M(1,1'\text{-biiq})(X)]^+$ complexes afford the opportunity to change the ancillory ligands while keeping the metals and 1,1'-biiq ligand the same as in the $[Ru(bipy)_2(1,1'\text{-biiq})]^{2+}$ and $[Os(bipy)_2(1,1'\text{-biiq})]^{2+}$ study.[60] $[M(bipy)_2(1,1'\text{-biiq})]^{2+}$ has C_2 symmetry resulting in stereochemically equivalent biiq halves. Atropisomerization was measured by measuring the rate of diastereomerization. The $[(\eta^6\text{-}C_6H_6)(M)(1,1'\text{-biiq})(X)]^+$ complexes have C_1 symmetry which renders the two halves of the biiq ligand symmetry inequivalent. The exchange of the biiq rings may be observed using ^1H NMR spin-labeling methods, allowing for the measurement of the kinetics of atropisomerization of the compounds. Thus, the rate of isomerization between equally populated enantiomers is determined.

3.2 Synthesis of $[(\eta^6\text{-}C_6H_6)M(1,1'\text{-biiq})(X)]^+$ (M=Ru(II),Os(II); X=Cl,I)

The title compounds were made from the dichloride dimer $[(\eta^6\text{-}C_6H_6)M(Cl)_2]_2$,[65,93] which were in turn synthesized using literature methods. $[(\eta^6\text{-}C_6H_6)Ru(1,1'\text{-biiq})(Cl)]^+$ was made by direct addition of the 1,1'-biiq ligand to the dichloride dimer. $[(\eta^6\text{-}C_6H_6)Os(1,1'\text{-biiq})(Cl)]^+$ was synthesized by adding the

1,1'-biiq ligand to the acetonitrile adduct $[(\eta^6\text{-}C_6H_6)Os(CH_3CN)(Cl)_2]$.[66] $[(\eta^6\text{-}C_6H_6)Ru(1,1'\text{-biiq})(I)]^+$ and $[(\eta^6\text{-}C_6H_6)Os(1,1'\text{-biiq})(I)]^+$ and were made by adding the 1,1'-biiq ligand to the $[(\eta^6\text{-}C_6H_6)M(I)_2]_2$ dimer. The $[(\eta^6\text{-}C_6H_6)M(I)_2]_2$ dimers were made by halide metathesis reactions of $[(\eta^6\text{-}C_6H_6)M(Cl)_2]_2$ with NaI.[65] These syntheses are explained in detail in section 5.1.4.

3.3 X-Ray Crystal Structures of $[(\eta^6\text{-}C_6H_6)(M(1,1'\text{-biiq})(Cl)]^+$ (M=Ru(II), Os(II))

Diffraction quality crystals were grown by vapor diffusion of ether in acetone solutions of $[(\eta^6\text{-}C_6H_6)M(1,1'\text{-biiq})(Cl)]^+$ (Ru(II),Os(II)). Selected interatomic distances, angles, and torsion angles are given in Table 3.1. A diagram showing the thermal ellipsoids at the 50% level of the molecule and the labeling scheme are shown in Figure 3.1 (M=Ru) and Figure 3.2 (M=Os). Crystallographic details are discussed in Section 5.2.2 with crystal data, atomic coordinates, anisotropic displacement parameters and hydrogen coordinates.

$[(\eta^6\text{-}C_6H_6)M(1,1'\text{-biiq})(Cl)]^+$ have C_1 symmetry because the twisting of the 1,1'-biiq ligand renders the compounds chiral. This can be clearly seen in the molecular structure diagrams (Figure 3.1 and Figure 3.2). The structures are very similiar to each other and other similiar compounds in the literature.[94 -100] The M-N bond lengths in these structures are all about 2.08 Å. The N-M-N bond angles are both about 76°. They both have piano stool geometry. The only significant difference in the structures is a more acute N-C(1)-C(1')-N' torsion angle for Os (25.5°) than Ru (27.0°). These torsion angles are comparable to the range of 20.1-26.4° that has beeen found for five other $(\eta^2\text{-}1,1'\text{-biiq})$-metal complexes.[59,60,101,102] It is interesting to note that for the cystal structures of $[M(bipy)_2(1,1'\text{-biiq})]^{2+}$, a more acute N-C(1)-C(1')-N' torsion angle is also observed for the Os derivative (20.1°) than the Ru derivative (24.1°). This may indicate that the stronger Os-N bonds are able to overcome

the interatomic repusion of $H_8/H_{8'}$ to a larger extent. Due to the C_1 symmetry the two halves of the biiq rings are in inequivalent environments. This environment is maintained in solution as different chemical shifts can be seen for protons on each half of the biiq rings.

Table 3.1. Comparison of Selected Interatomic Distances (Å), Angles (deg),and Torsion Angles (deg) for $[(\eta^6\text{-}C_6H_6)M(1,1'\text{-biiq})(Cl)](PF_6)$

	M=Ru	M=Os
M – N	2.087(2)	2.086(3)
M – N'	2.085(2)	2.086(3)
M - Cl	2.388(1)	2.392(1)
M - Arcent (1)	1.679(4)	1.675(3)
M - Arcent (2)	1.682(4)	
N - M – N'	76.38(5)	75.9(1)
N - M - Cl	82.0(1)	81.40(9)
N' - M - Cl	87.4(1)	86.59(9)
N - M - Arcent (1)	132.9(2)	132.7(1)
N - M - Arcent (2)	132.6(2)	
N' - M – Arcent (1)	132.0(2)	131.3(1)
N' - M – Arcent (2)	128.7(2)	
Cl - M – Arcent (1)	127.5(1)	129.5(1)
Cl - M - Arcent (2)	130.8(1)	
N-C(1)-C(1')-N'	27.0(2)	25.5(4)

[a] Ar is defined to be the least-squares plane that contains an arene ligand. Arcent (1) is the centroid of the arene ligand C1"-C" for M=Ru and M=Os. Arcent (2) is the centroid of the arene ligand C1'"-C6'" for M=Ru.

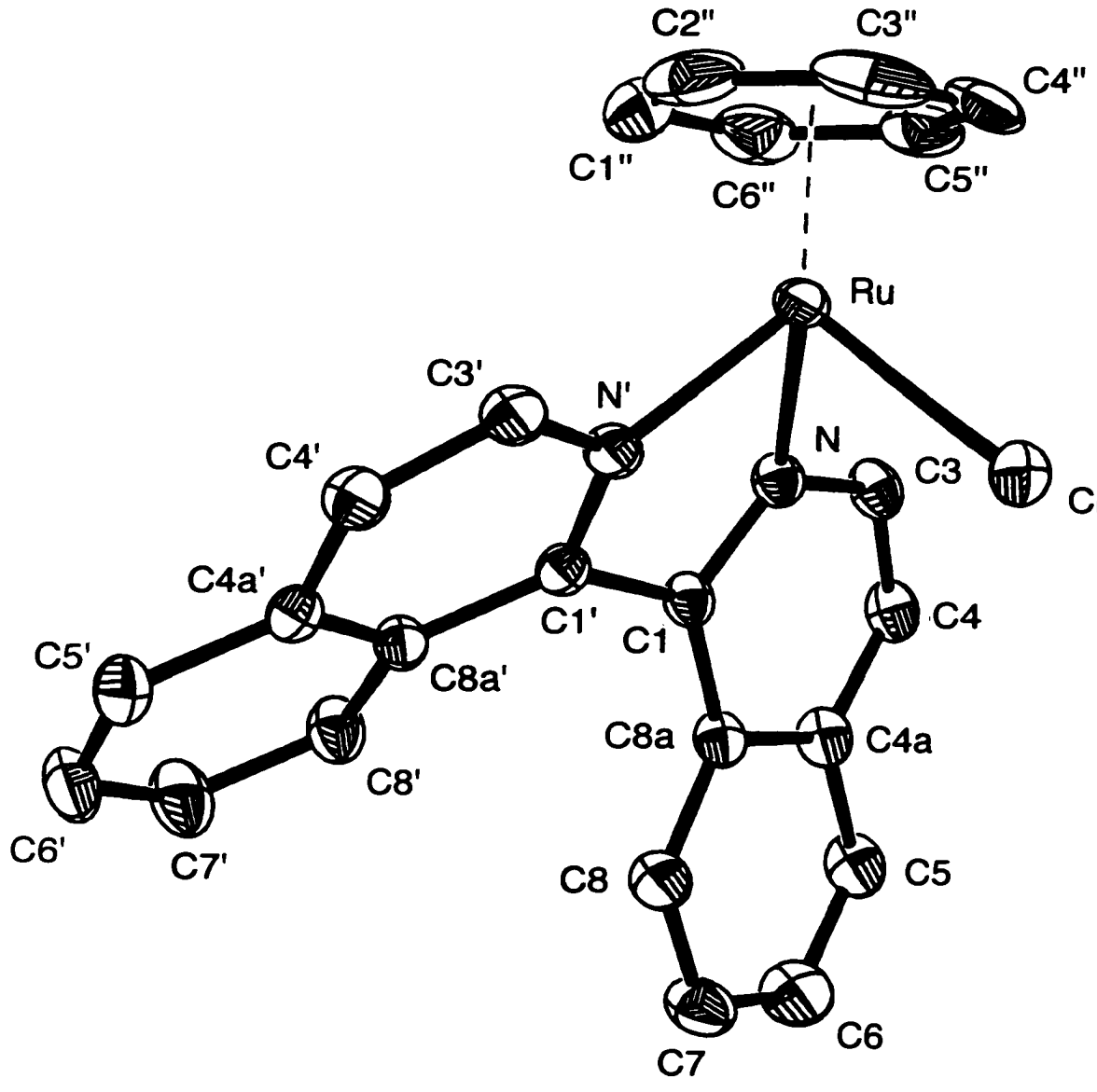

Figure 3.1. Molecular structure of $[(\eta^6\text{-}C_6H_6)Ru(biiq)(Cl)]^+$ showing the atom labeling scheme and the thermal vibration ellipsoids (50% probability). Hydrogen atoms have been omitted for the sake of clarity.

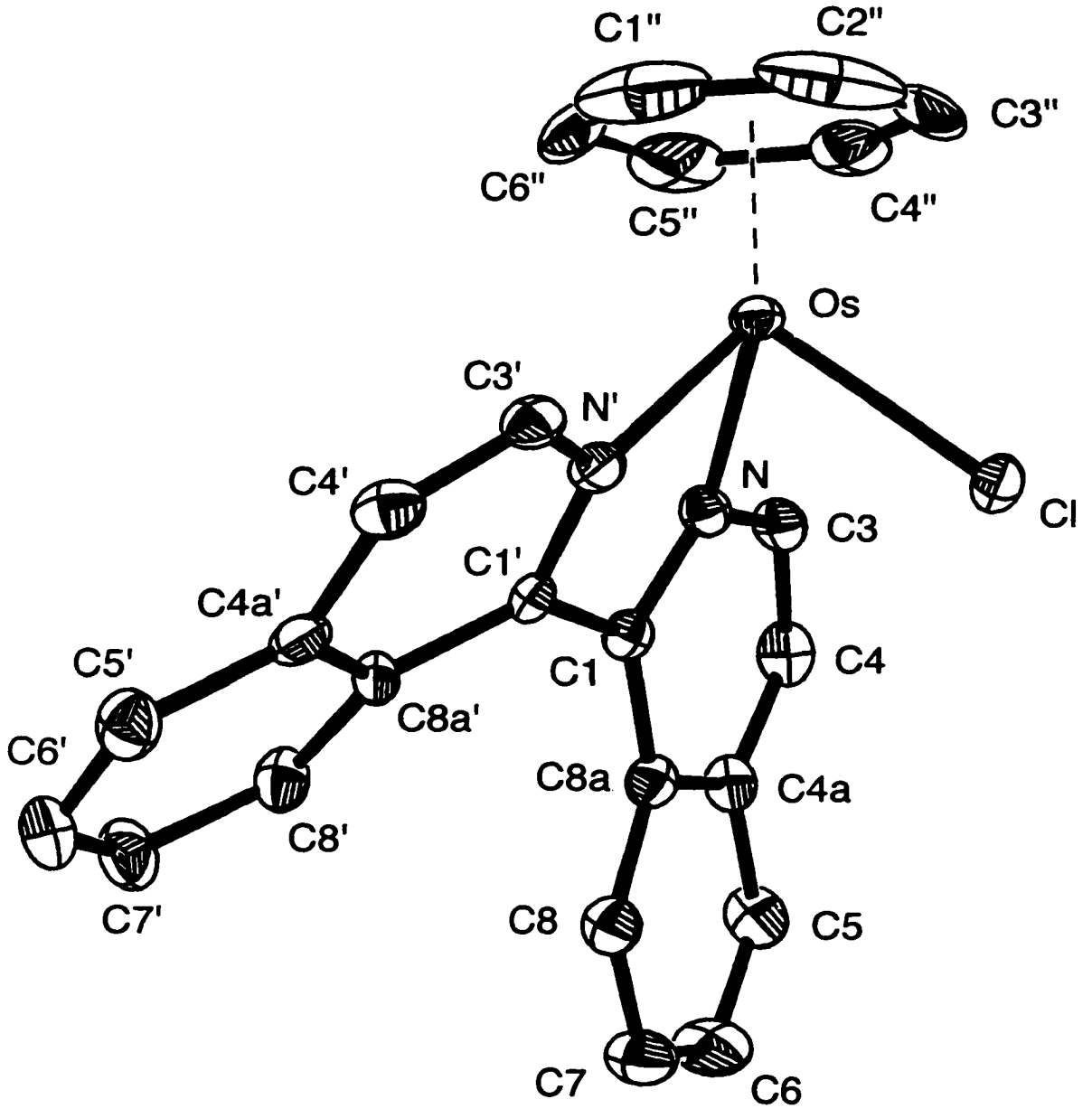

Figure 3.2 Molecular structure of $[(\eta^6\text{-}C_6H_6)Os(biiq)(Cl)]^+$ showing the atom labeling scheme and the thermal vibration ellipsoids (50% probability). Hydrogen atoms have been omitted for the sake of clarity.

3.4 2D-COSY and 2D-EXSY ^{1}H NMR Experiments

Assignment of the ^{1}H NMR chemical shifts was aided by 2D-COSY experiments and comparison to other metal 1,1'-biiq compounds. The details of the COSY experiment are given in Section 5.6.2. The COSY experiments were carried out in acetone-d_6 and are shown with their peak assignments in Figure 3.3 (M=Ru, X=Cl), Figure 3.4 (M=Os, X=Cl), Figure 3.5 (M=Ru, X=I), and Figure 3.6 (M=Os, X=I).

Magnetic exchange of the protons on the 1,1'-biiq rings was demonstrated by 2D-EXSY experiments. Details of the 2D-EXSY experiment are presented in Section 5.7.4. Cross peaks show the exchange of protons as the compound isomerizes in solution. These experiments were carried out in acetone-d_6 and are shown with their peak assignments in Figure 3.7 (M=Ru, X=Cl), Figure 3.8 (M=Os, X=Cl), Figure 3.9 (M=Ru, X=I), and Figure 3.10 (M=Os, X=I). It is clear from these figures that each half of the biiq ring exchanges with the other as the compound isomerizes in solution.

3.5 Spin-Inversion Transfer (SIT) and Line-Shape Analysis (LSA) ^{1}H NMR Kinetic Experiments

3.5.1 $[(\eta^6\text{-}C_6H_6)M(1,1'\text{-biiq})(Cl)]^+$ (M=Ru,Os)

The rate of atropisomerism was measured from 21-55 °C for both the ruthenium and osmium derivatives by SIT experiments. SIT is explained in detail in Section 5.7.3. The rate constants that were obtained from these experiments are shown in Table 3.2. It was not possible to measure the rate constants at temperatures outside of this range as the compound began to decompose at higher temperatures and the rate was too slow at lower temperatures. The fits for the SIT rate experiments are shown in Figure 3.11 (M=Ru, 24-29 °C), Figure 3.12 (M=Ru, 34-38 °C), Figure 3.13 (M=Ru, 41-46 °C), and Figure 3.14 (M=Ru, 51-55 °C), Figure 3.15 (M=Os, 21-24 °C), Figure 3.16 (M=Os, 29-34 °C), Figure 3.17 (M=Os, 41-46 °C), and Figure 3.18 (M=Os, 51-55 °C).

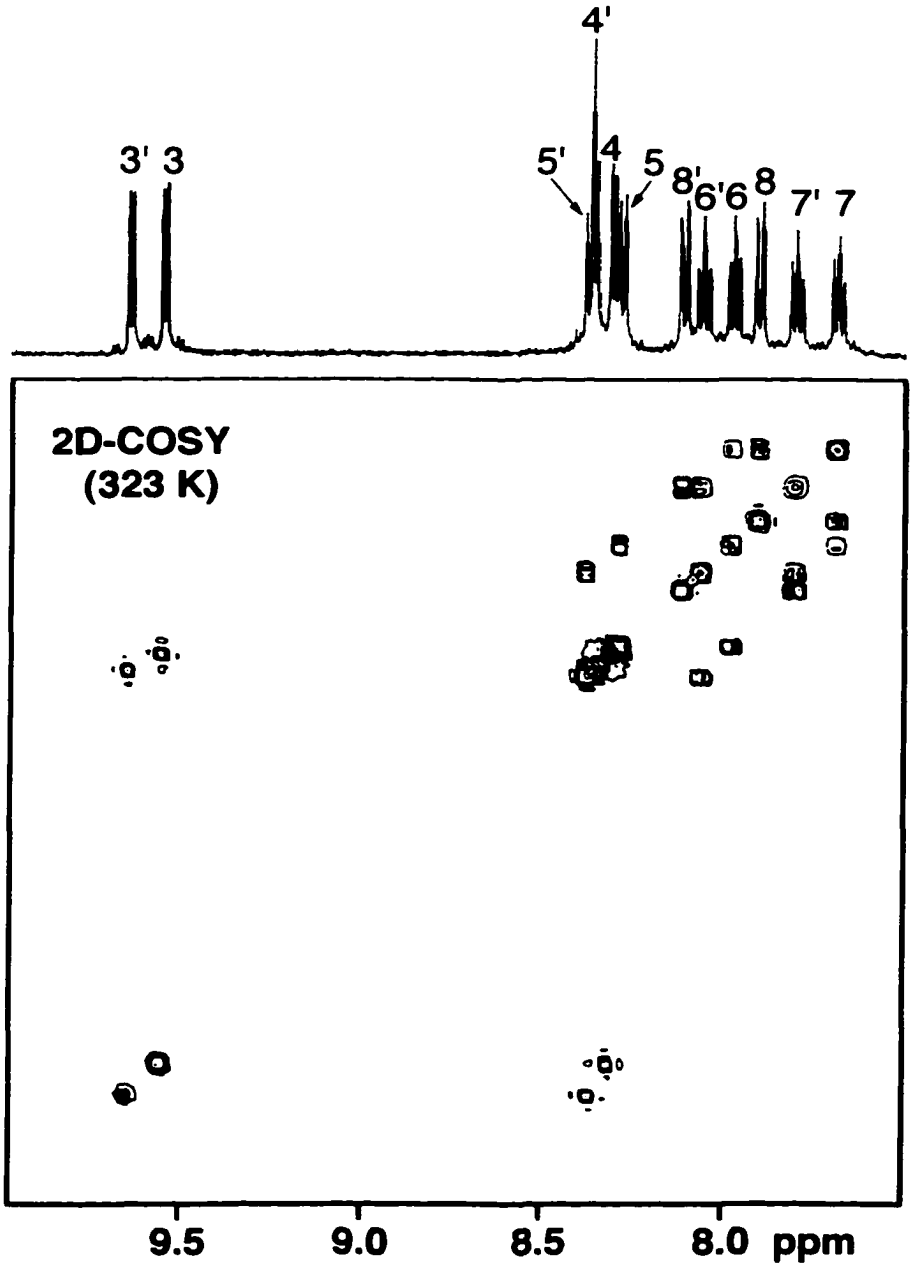

Figure 3.3. 2D-COSY Spectrum of $[(\eta^6\text{-}C_6H_6)Ru(biiq)(Cl)]^+$ at 50°C and 500 MHz in acetone-d_6 with peak assignments.

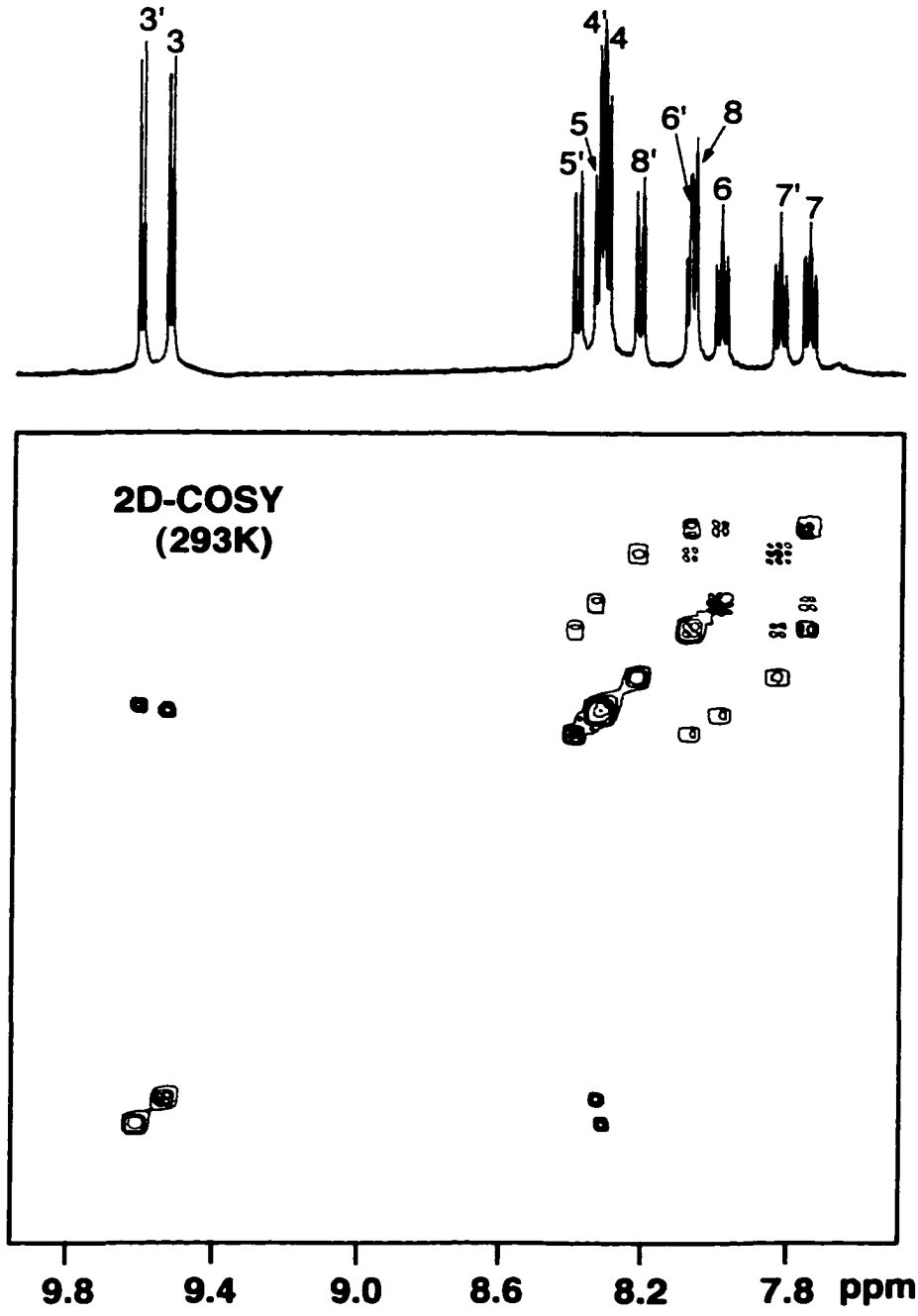

Figure 3.4. 2D-COSY Spectrum of $[(\eta^6\text{-}C_6H_6)Os(biiq)(Cl)]^+$ at 20°C and 500 MHz in acetone-d_6 with peak assignments.

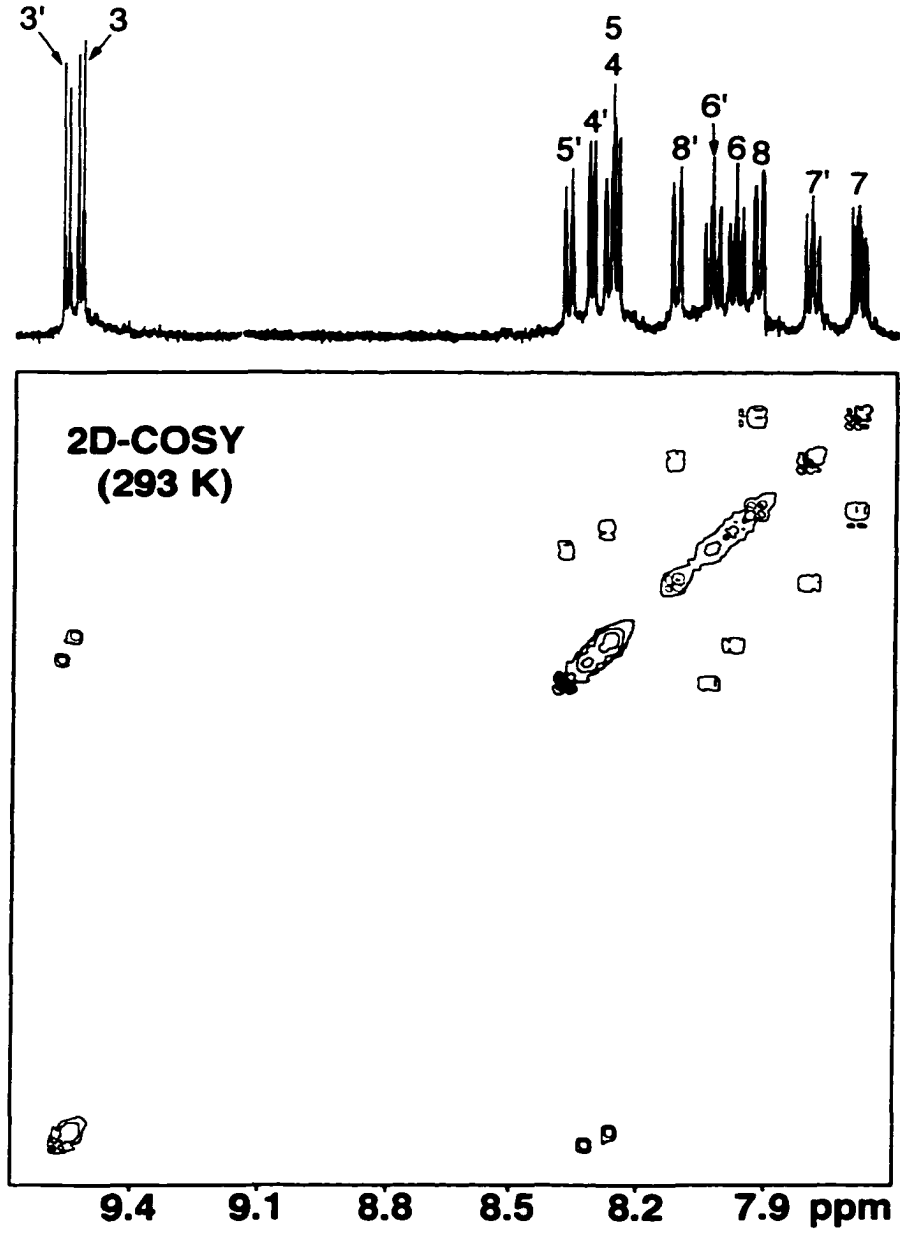

Figure 3.5. 2D-COSY Spectrum of $[(\eta^6\text{-}C_6H_6)Ru(biiq)(I)]^+$ at 20°C and 500 MHz in acetone-d_6 with peak assignments.

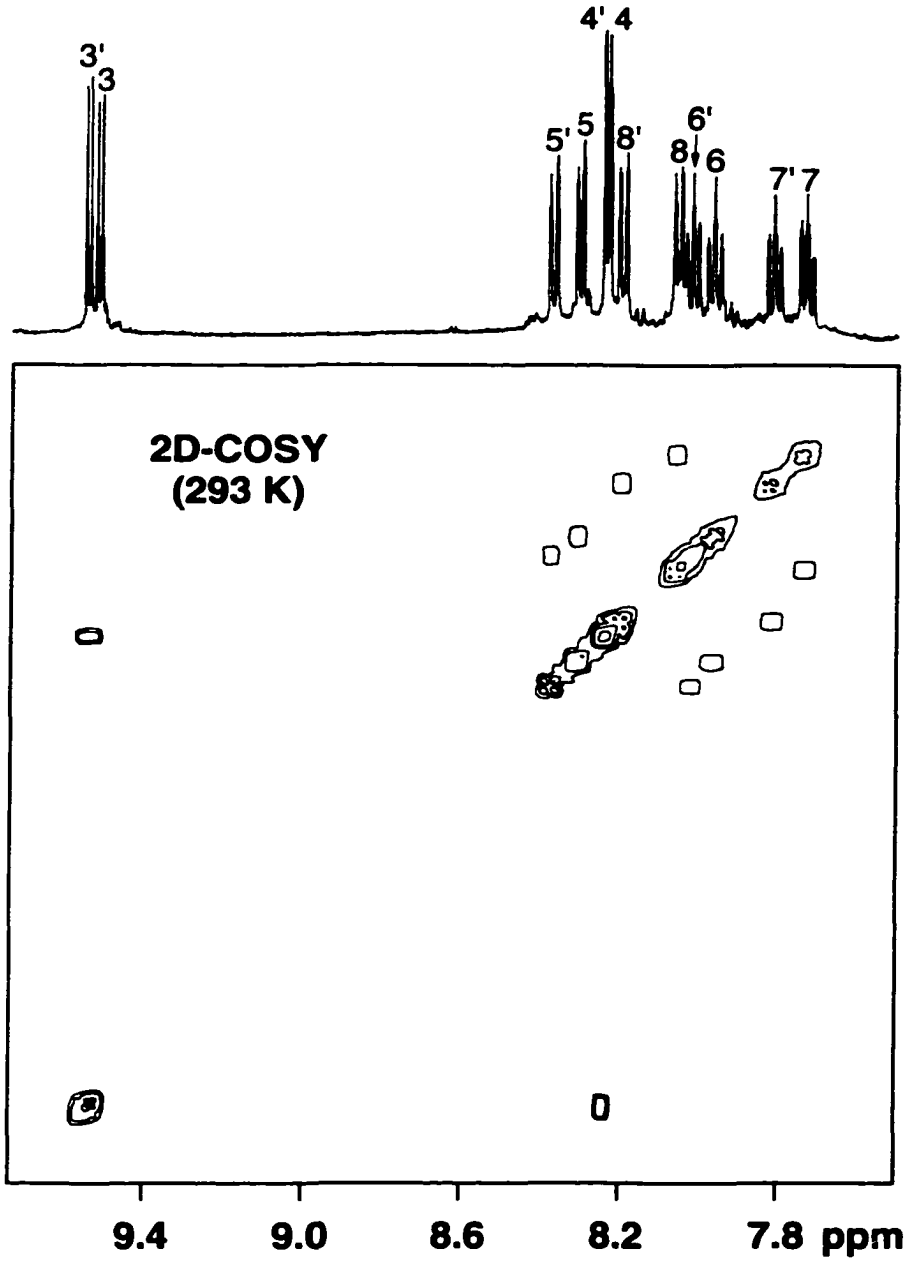

Figure 3.6. 2D-COSY Spectrum of $[(\eta^6\text{-}C_6H_6)Os(biiq)(I)]^+$ at 20°C and 500 MHz in acetone-d_6 with peak assignments.

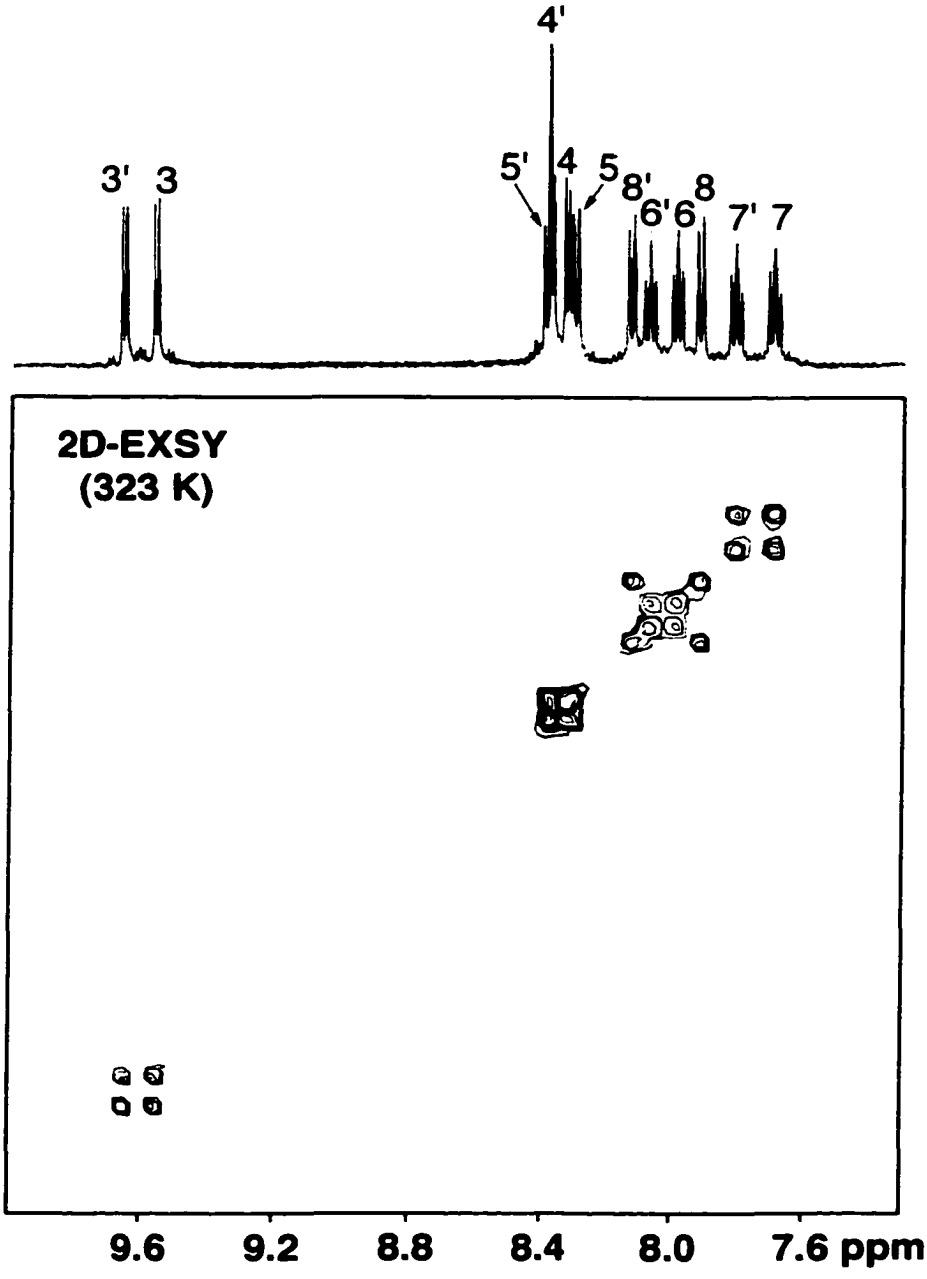

Figure 3.7. 2D-EXSY Spectrum of $[(\eta^6\text{-}C_6H_6)Ru(biiq)(Cl)]^+$ at 50°C and 500 MHz in acetone-d_6 with peak assignments.

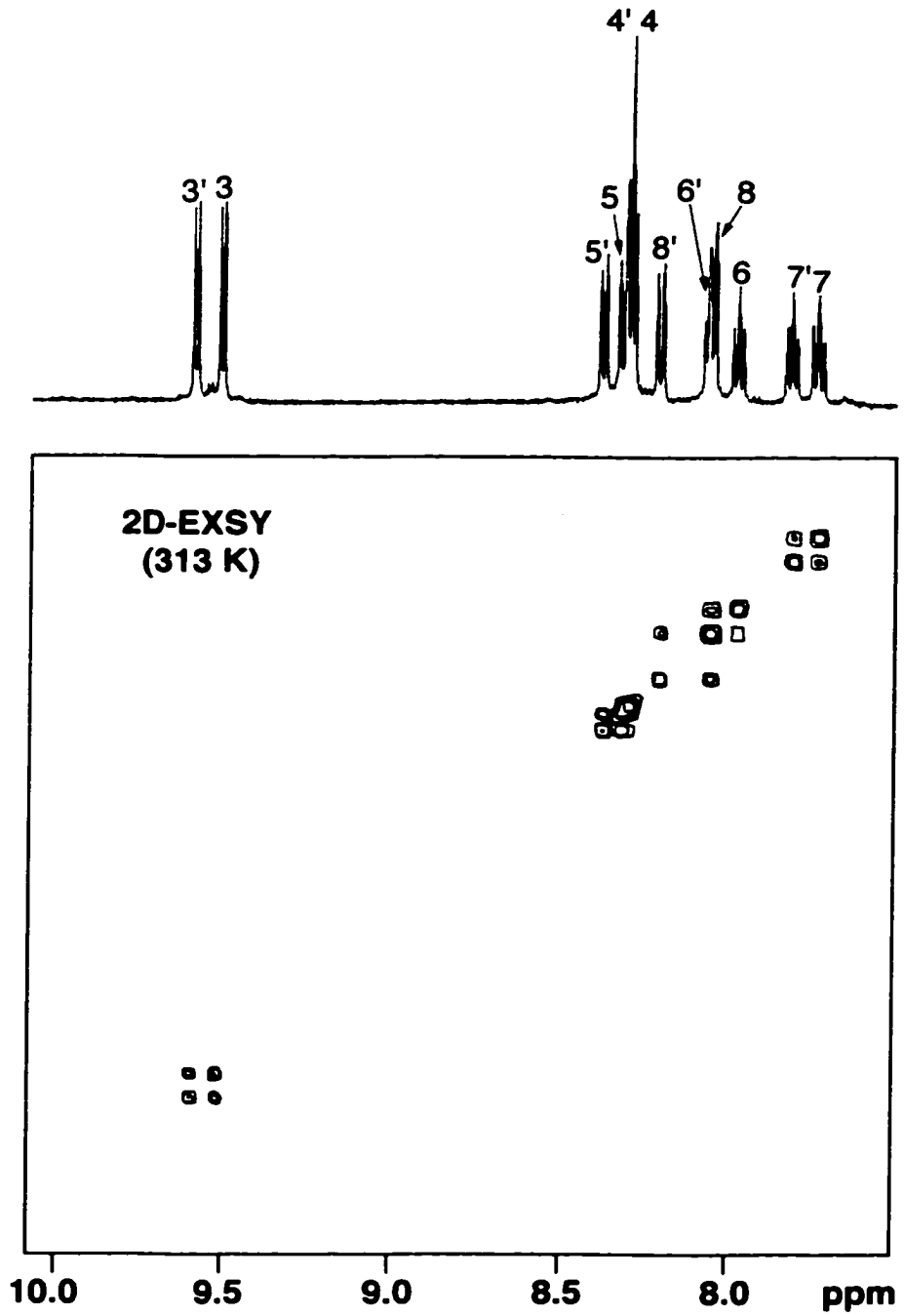

Figure 3.8. 2D-EXSY Spectrum of $[(\eta^6\text{-}C_6H_6)Os(biiq)(Cl)]^+$ at 40°C and 500 MHz in acetone-d_6 with peak assignments.

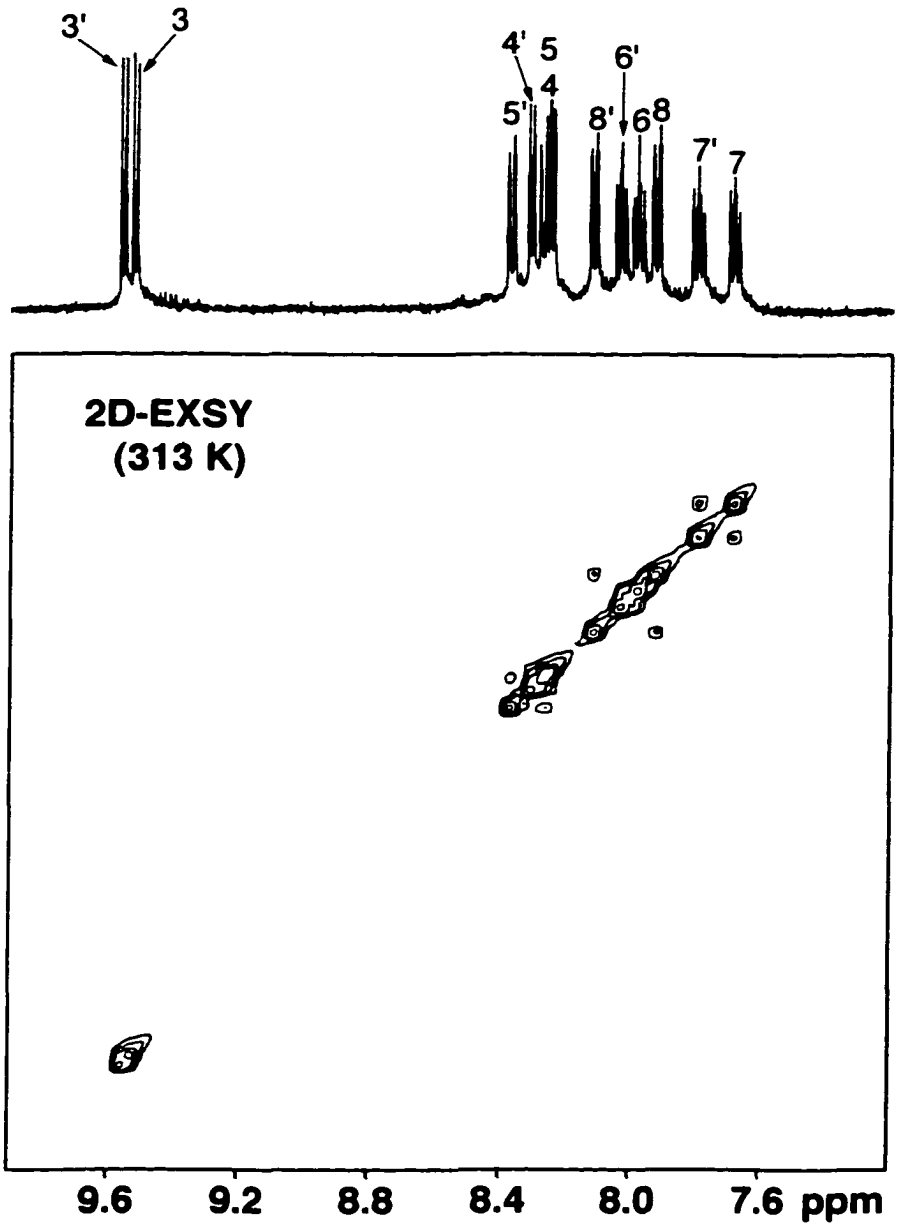

Figure 3.9. 2D-EXSY Spectrum of $[(\eta^6\text{-}C_6H_6)Ru(biiq)(I)]^+$ at 40°C and 500 MHz in acetone-d_6 with peak assignments.

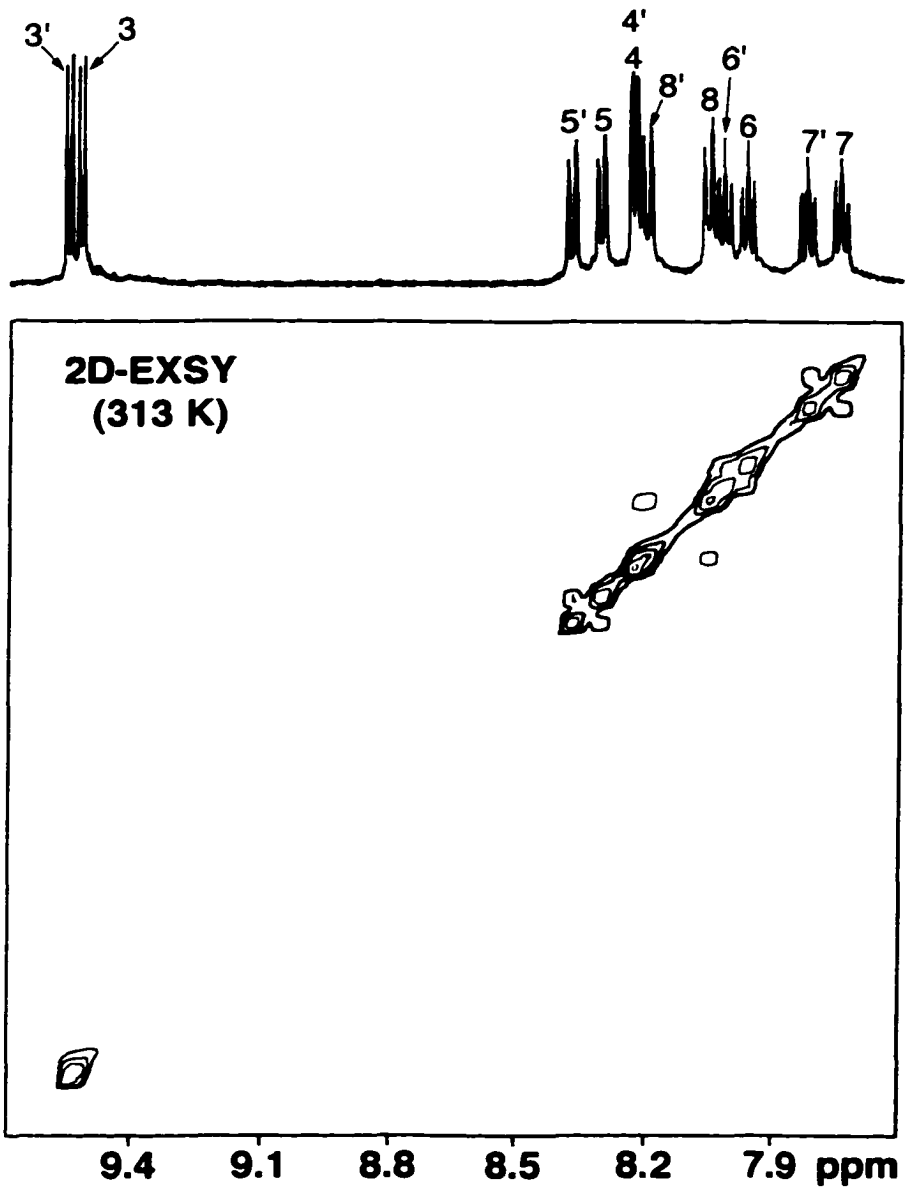

Figure 3.10. 2D-EXSY Spectrum of $[(\eta^6\text{-}C_6H_6)Os(biiq)(I)]^+$ at 40°C and 500 MHz in acetone-d_6 with peak assignments.

3.5.2 $[(\eta^6\text{-}C_6H_6)M(1,1'\text{-biiq})(I)]^+$ (M=Ru,Os)

The rate of atropisomerism was measured from 38-62 °C for both the ruthenium and osmium derivatives by SIT. The fits for the SIT rate experiments are shown in Figure 3.19 (M=Ru, 38-43 °C), Figure 3.20 (M=Ru, 48-53 °C), Figure 3.21 (M=Ru, 57-62 °C), Figure 3.22 (M=Os, 38-43 °C), Figure 3.23 (M=Os, 48-53 °C), and Figure 3.24 (M=Os, 59 °C). It was possible to extend the temperature range of rate measurements to 90 °C (M=Ru) and 75 °C (M=Os) by Line Shape Analysis (LSA). LSA is explained in detail in Section 5.7.2. Coalescence was observed for the H_3/H_3. protons at 93 °C (M=Ru) and 79° (M=Os). Coalescence is explained in Section 5.7.1. The fits for the LSA rate experiments are illustrated in Figure 3.25 (M=Ru, 67-90 °C) and Figure 3.26 (M=Os, 61-75 °C). The rate constants that were obtained from these experiments are shown in Table 3.3. Rate data that were collected at the same temperature using the SIT and LSA methods are in good agreement. An Eyring plot that includes both the SIT and LSA data is shown in Figure 3.27.

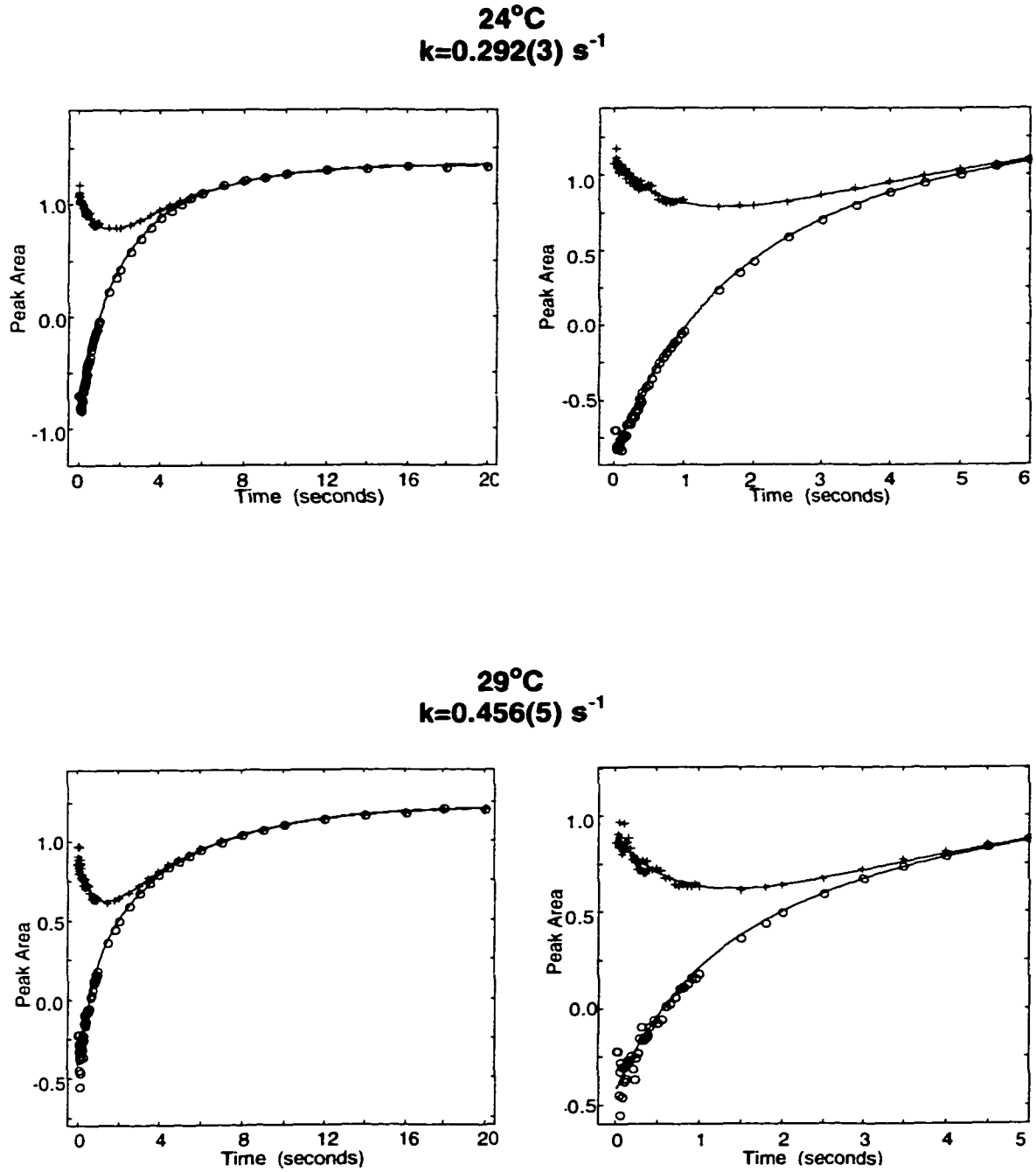

Figure 3.11. SIT fits for $[(\eta^6\text{-}C_6H_6)Ru(biiq)(Cl)]^+$.

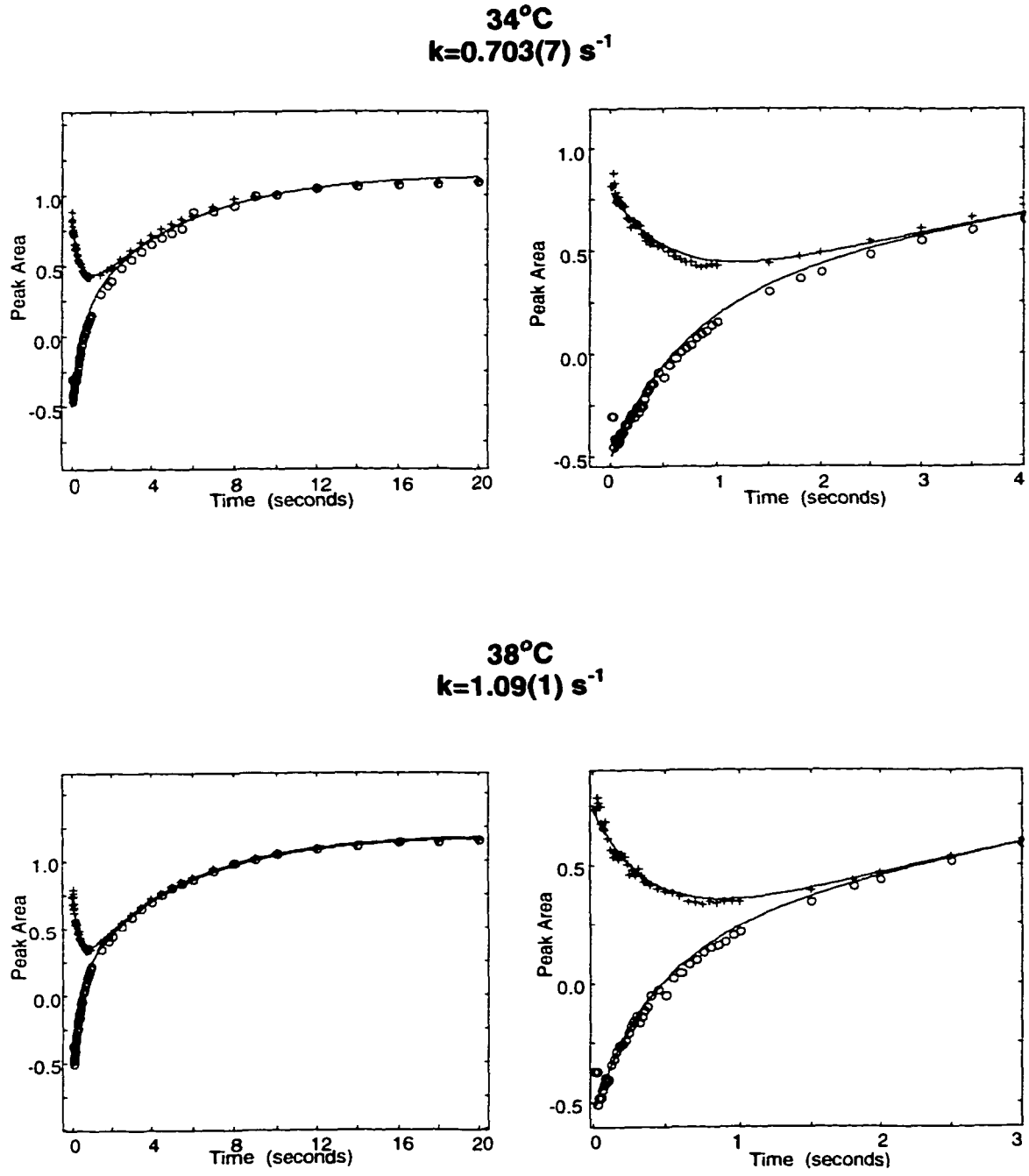

Figure 3.12. SIT fits for $[(\eta^6\text{-}C_6H_6)Ru(biiq)(Cl)]^+$.

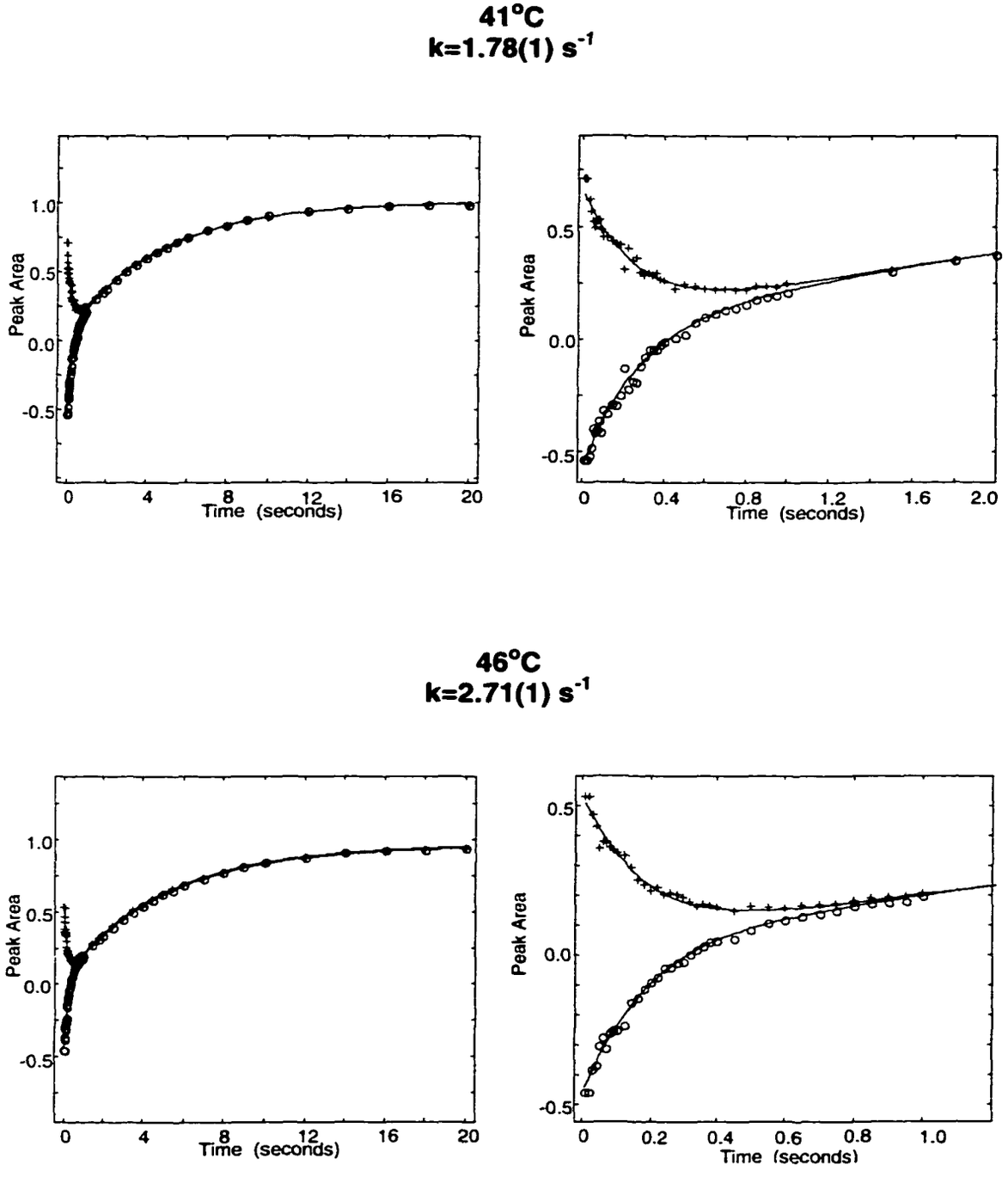

Figure 3.13. SIT fits for $[(\eta^6\text{-}C_6H_6)Ru(biiq)(Cl)]^+$.

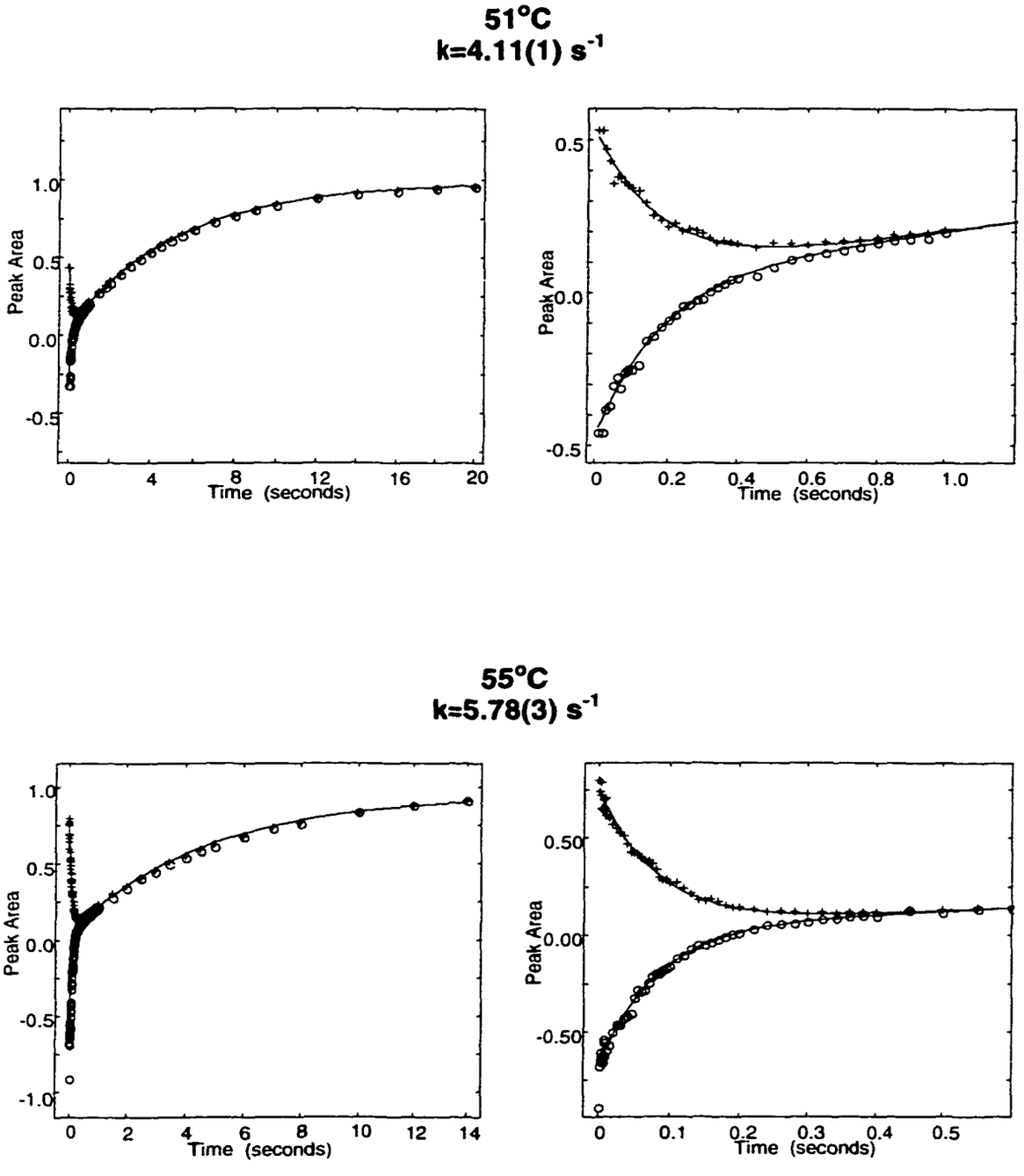

Figure 3.14. SIT fits for $[(\eta^6\text{-}C_6H_6)Ru(biiq)(Cl)]^+$.

21°C
k=0.36(1) s^{-1}

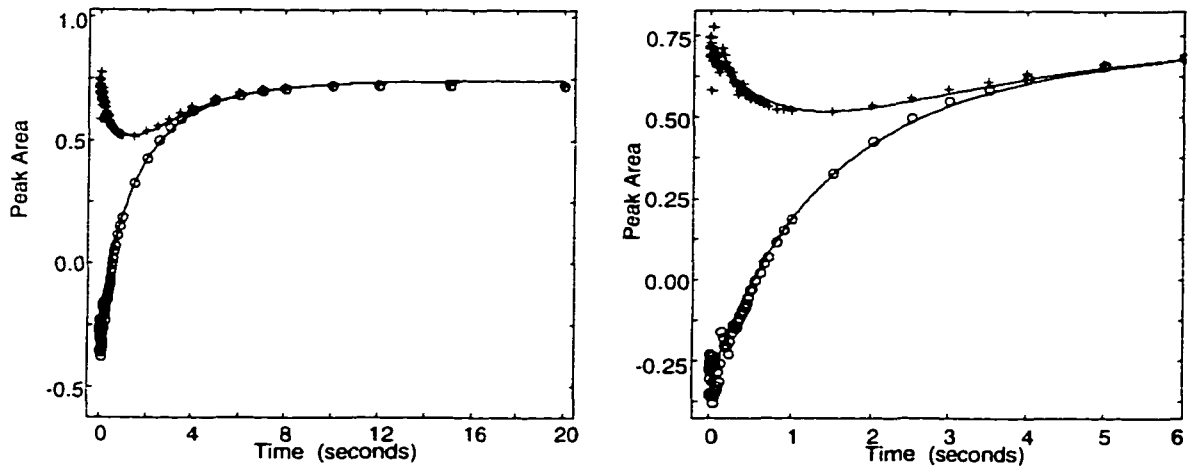

24°C
k=0.439(3) s^{-1}

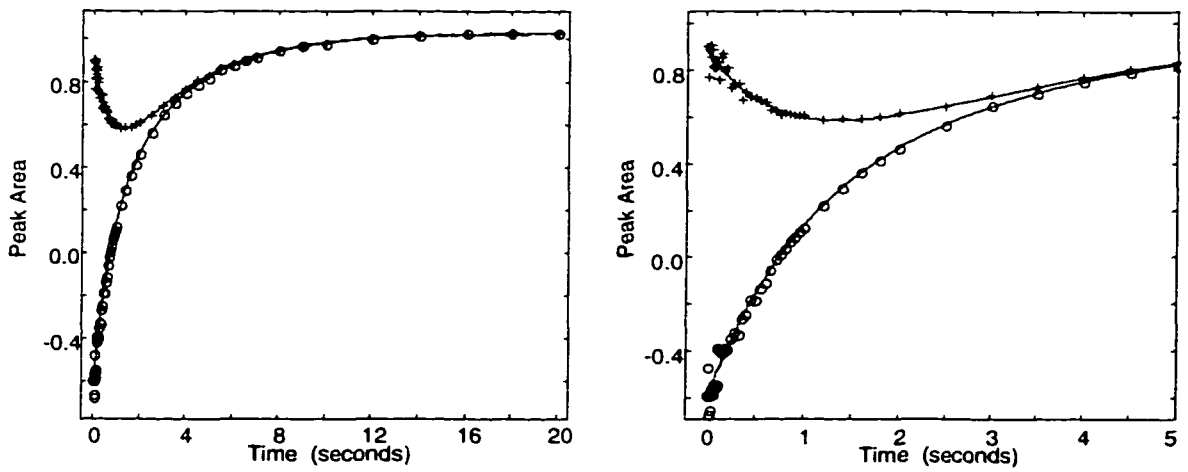

Figure 3.15. SIT fits for $[(\eta^6\text{-}C_6H_6)Os(biiq)(Cl)]^+$.

29°C
k=0.820(7) s^{-1}

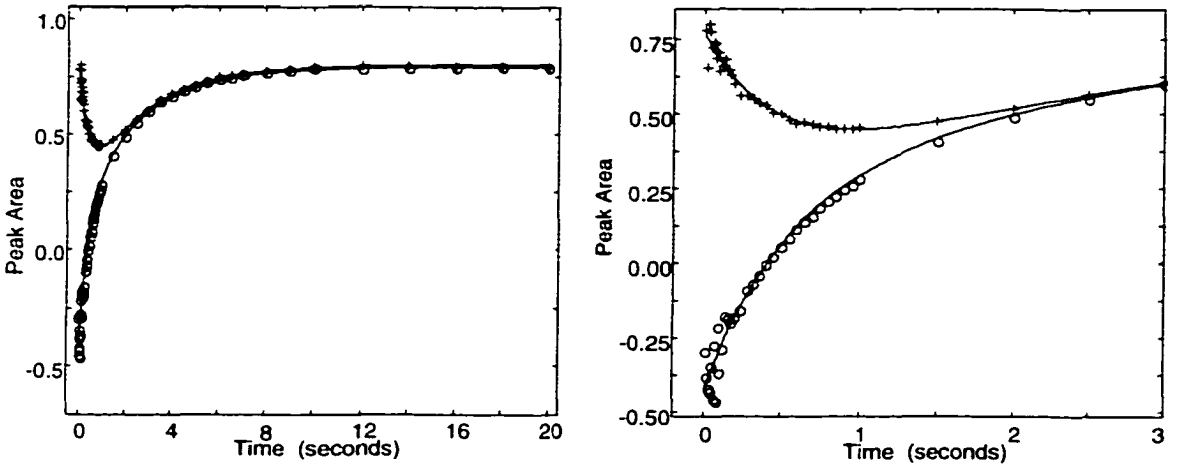

34°C
k=1.07(1) s^{-1}

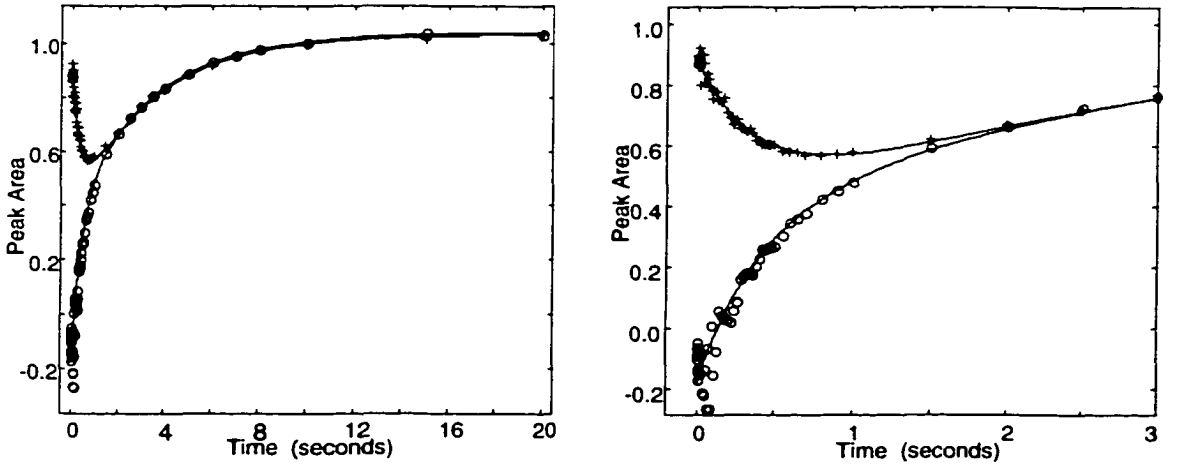

Figure 3.16. SIT fits for $[(\eta^6\text{-}C_6H_6)Os(biiq)(Cl)]^+$.

41°C
k=2.24(3) s^{-1}

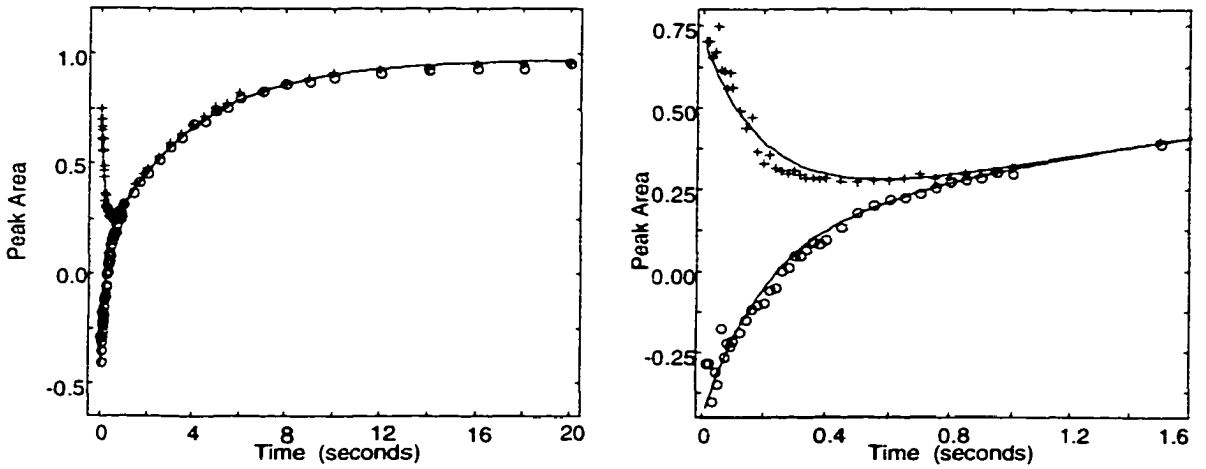

46°C
k=3.48(2) s^{-1}

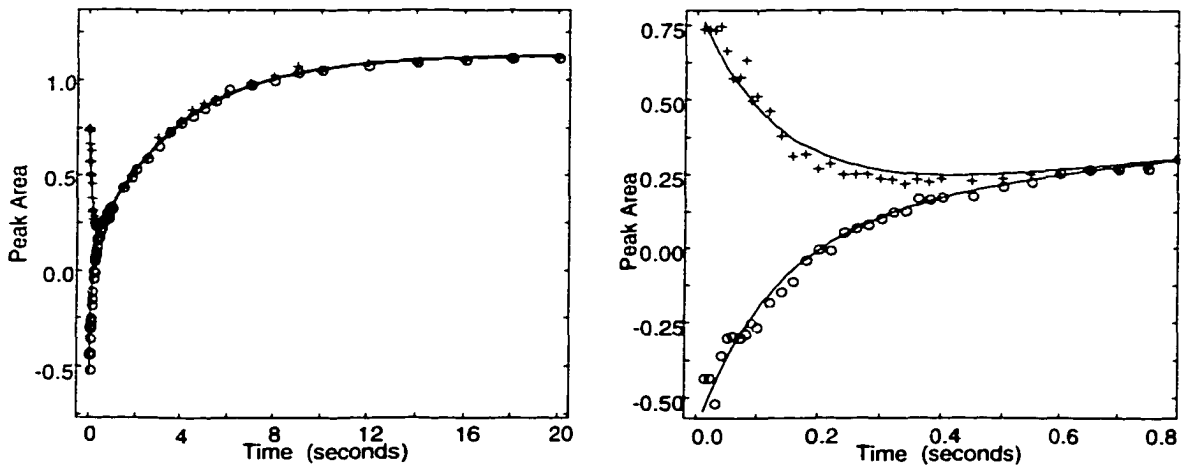

Figure 3.17. SIT fits for $[(\eta^6\text{-}C_6H_6)Os(biiq)(Cl)]^+$.

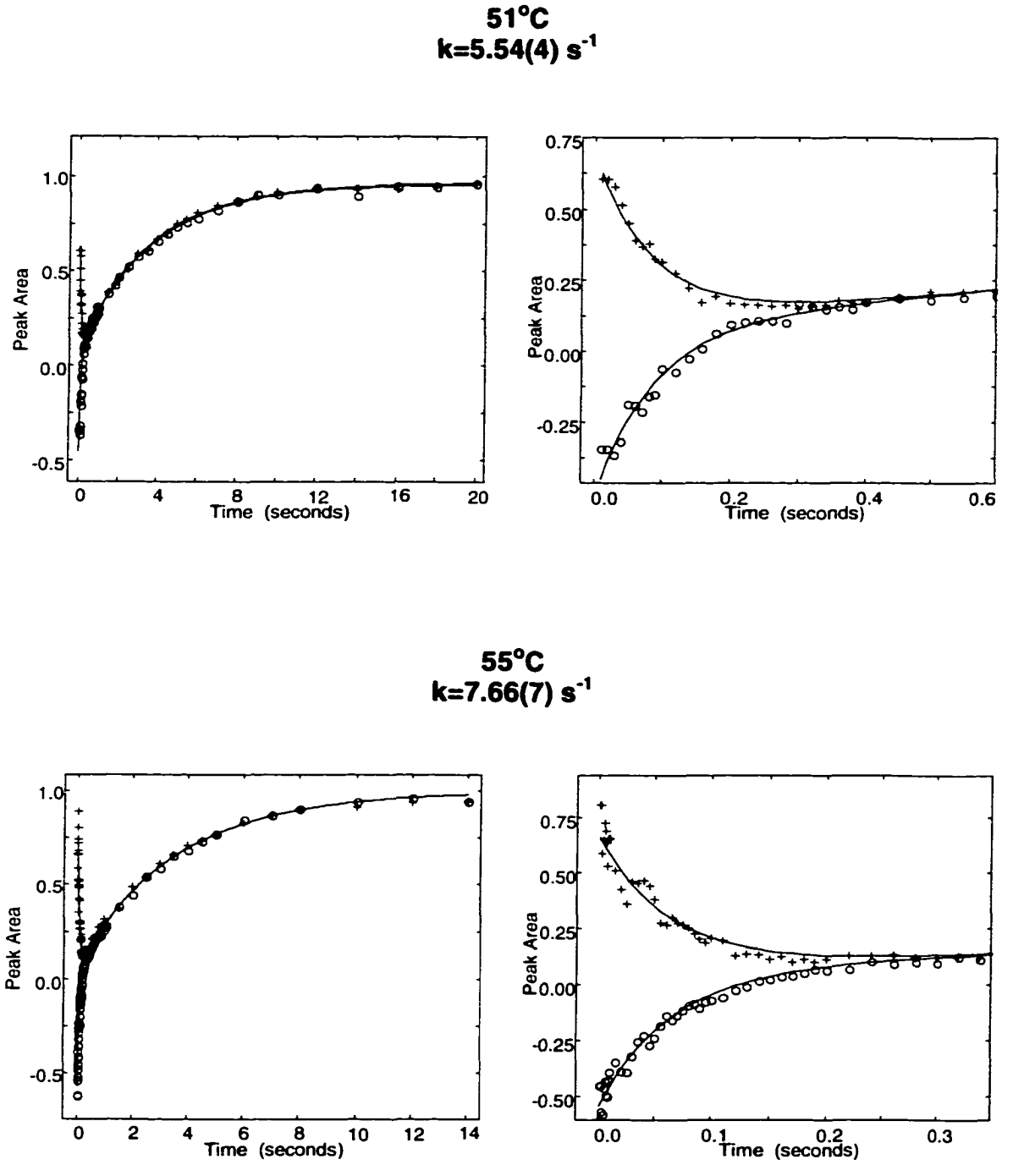

Figure 3.18. SIT fits for $[(\eta^6\text{-}C_6H_6)Os(biiq)(Cl)]^+$.

Table 3.2. Comparison of the Kinetic Data Obtained for the Atropisomerization of the Ru and Os Derivatives of $[(\eta^6\text{-}C_6H_6)M(1,1'\text{-biiq})(Cl)]^+$

Temp °C	M = Ru k_1 (s^{-1})	M = Os k_1 (s^{-1})
21	-	0.36(1)
24	0.292(3)	0.439(3)
29	0.456(5)	0.820(7)
34	0.703(7)	1.07(1)
38	1.09(1)	-
41	1.78(1)	2.24(3)
46	2.71(1)	3.48(2)
51	4.11(1)	5.54(4)
55	5.78(3)	7.66(7)

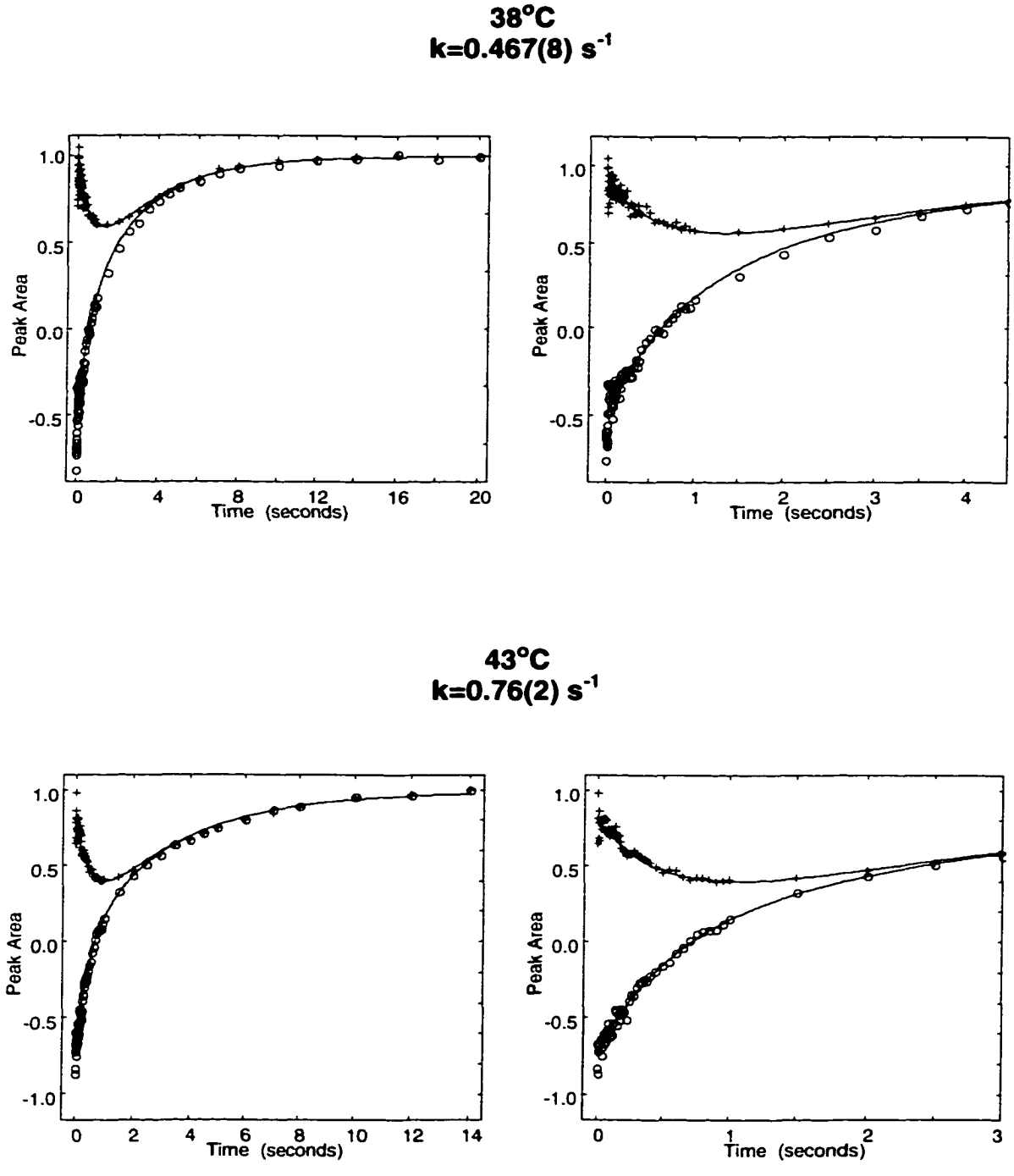

Figure 3.19. SIT fits for $[\eta^6\text{-}C_6H_6)Ru(biiq)(I)]^+$.

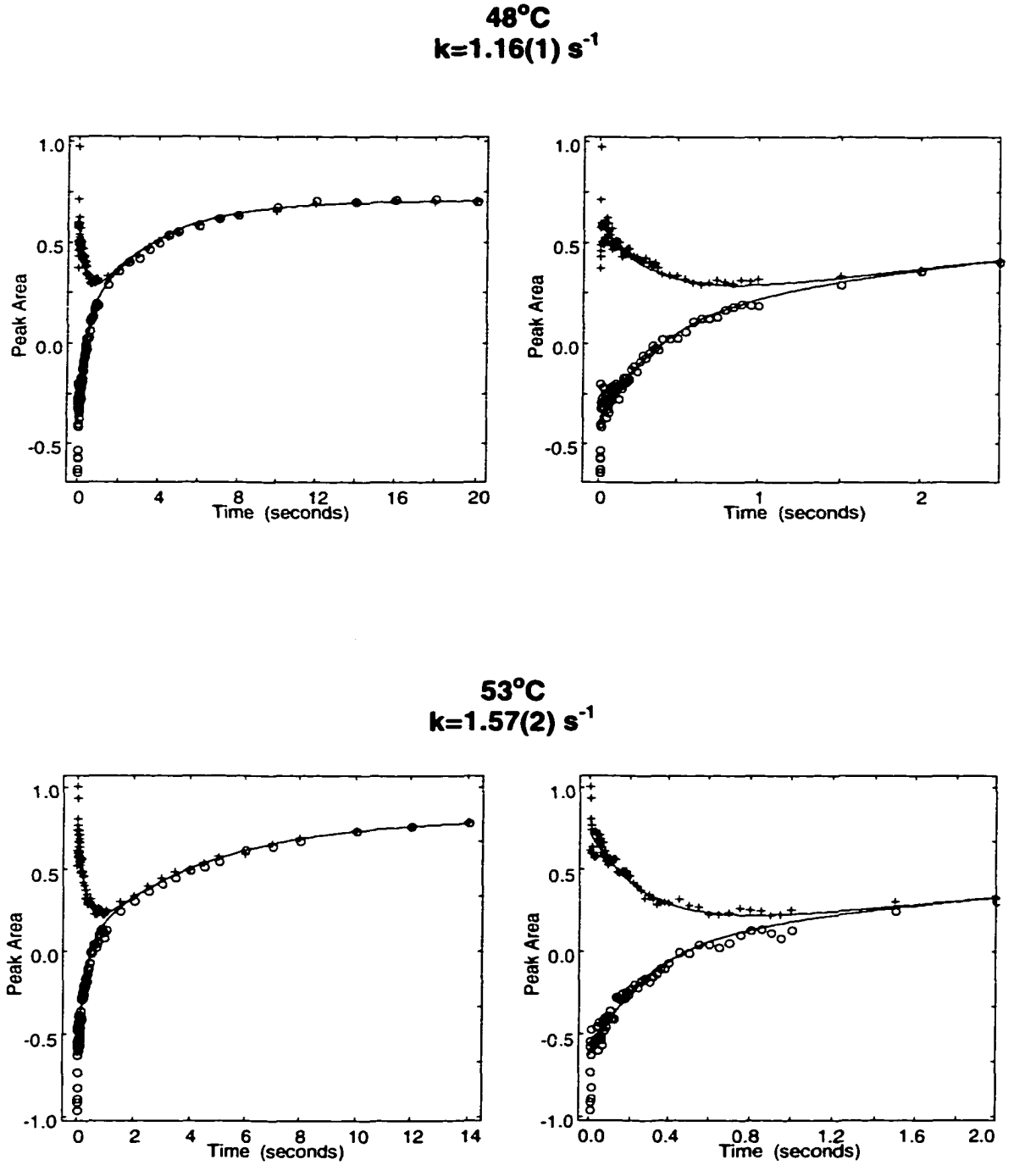

Figure 3.20. SIT fits for $[(\eta^6\text{-}C_6H_6)Ru(biiq)(I)]^+$.

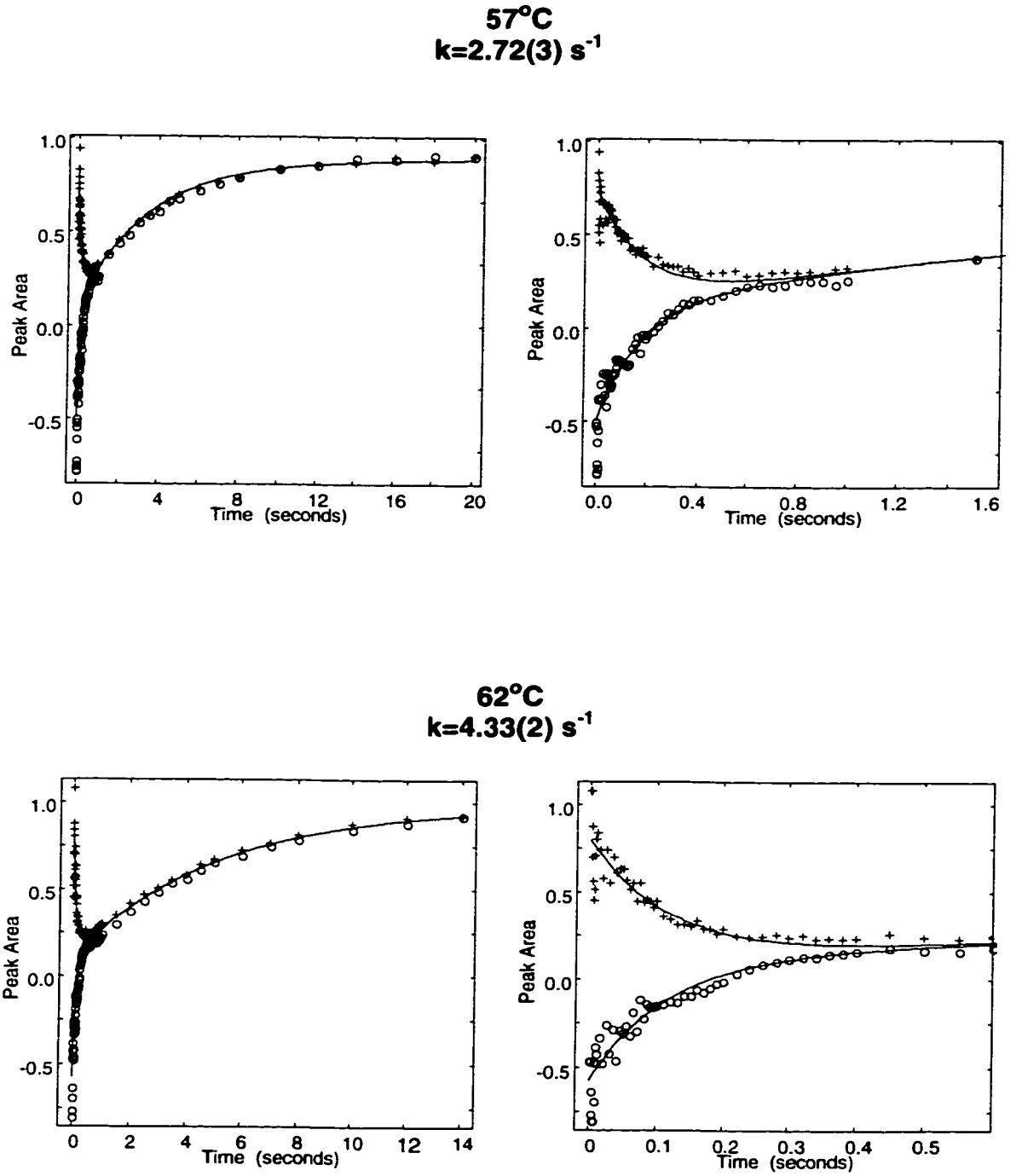

Figure 3.21. SIT fits for $[(\eta^6\text{-}C_6H_6)Ru(biiq)(I)]^+$.

38°C
k=.82(1) s^{-1}

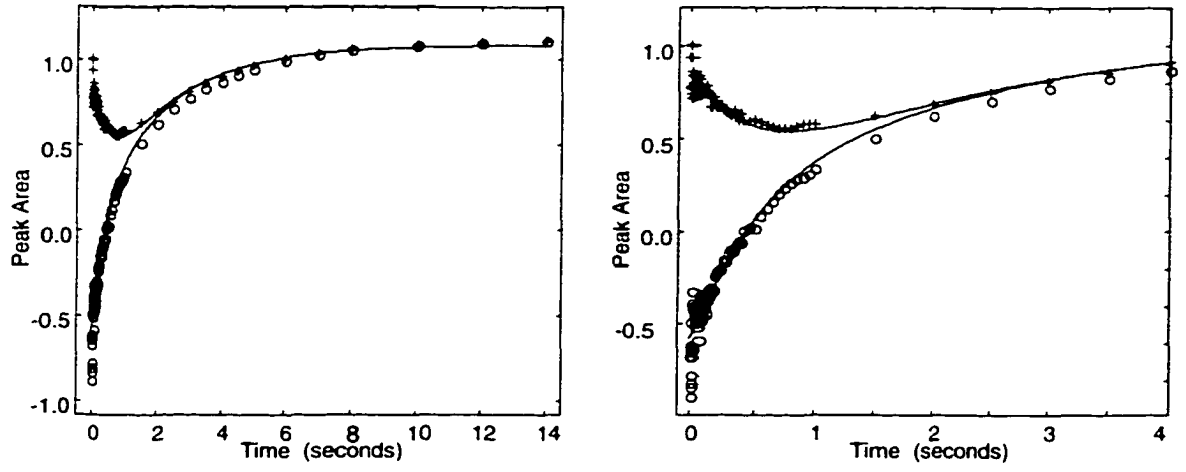

43°C
k=1.36(1) s^{-1}

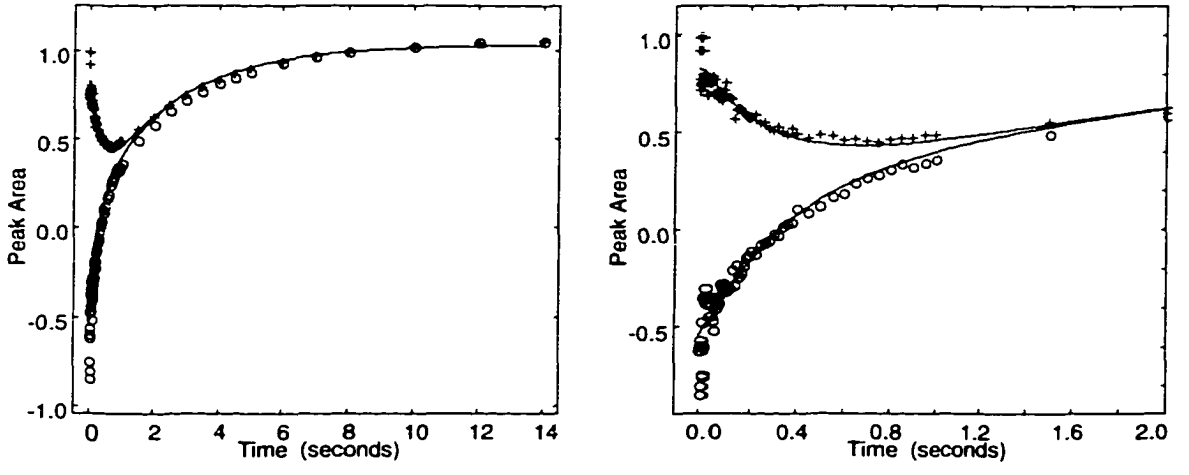

Figure 3.22. SIT fits for $[(\eta^6\text{-}C_6H_6)Os(biiq)(I)]^+$.

48°C
k=1.71(1) s^{-1}

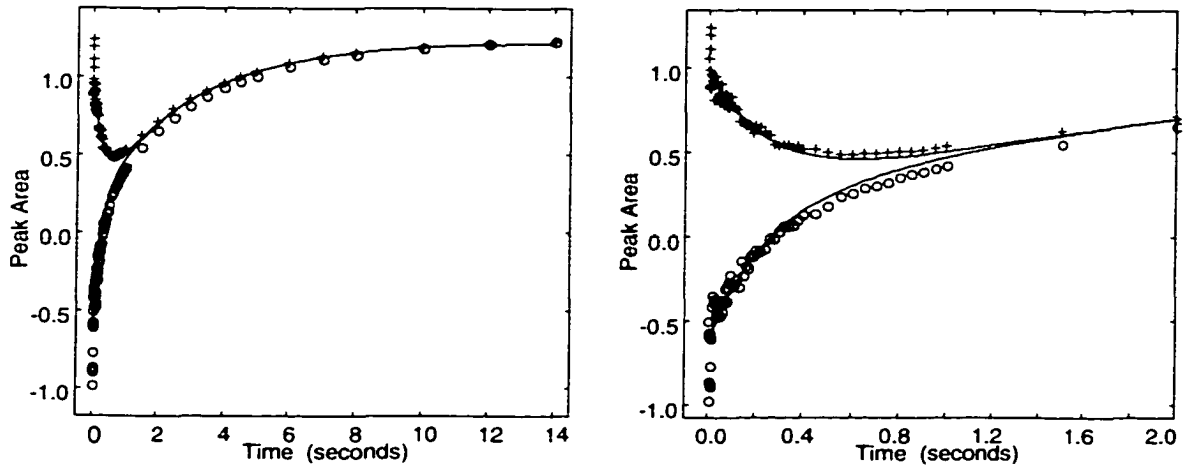

53°C
k=3.24(3) s^{-1}

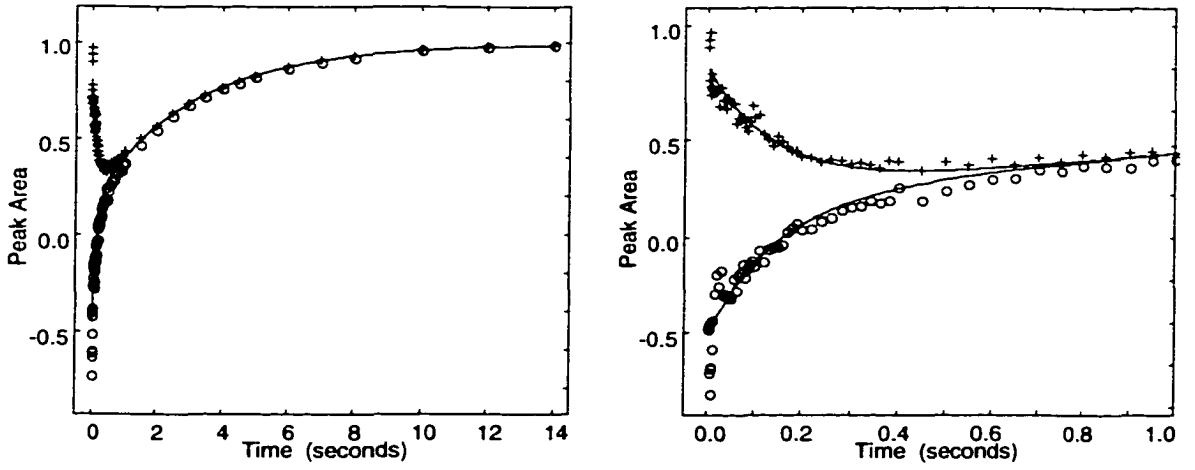

Figure 3.23. SIT fits for $[(\eta^6\text{-}C_6H_6)Os(biiq)(I)]^+$.

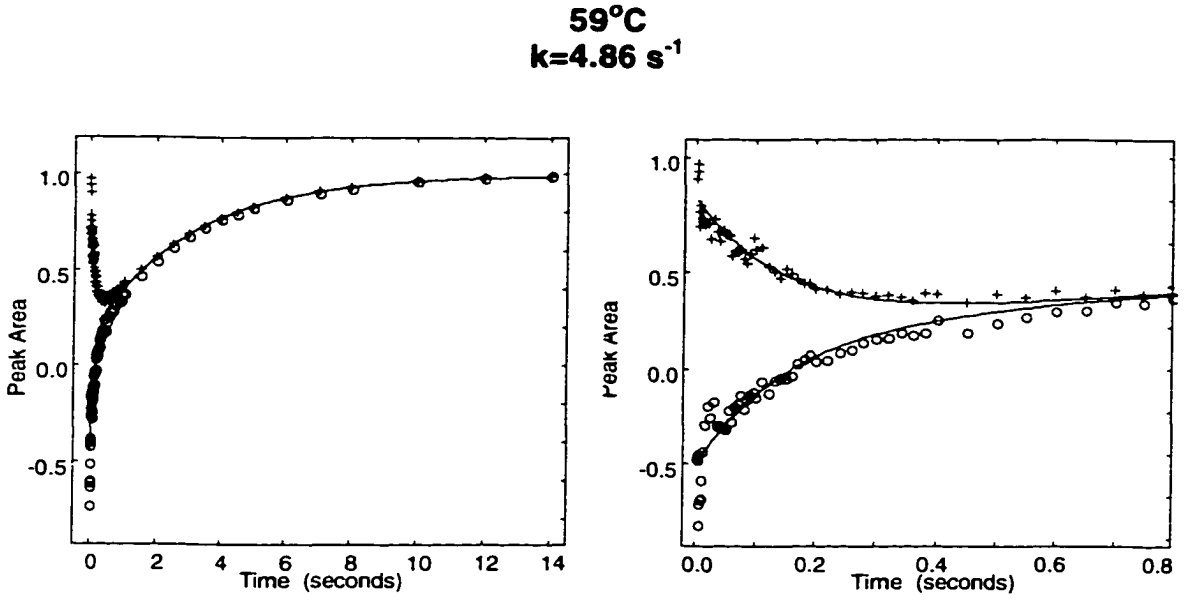

Figure 3.24. SIT fits for $[(\eta^6\text{-}C_6H_6)Os(biiq)(I)]^+$.

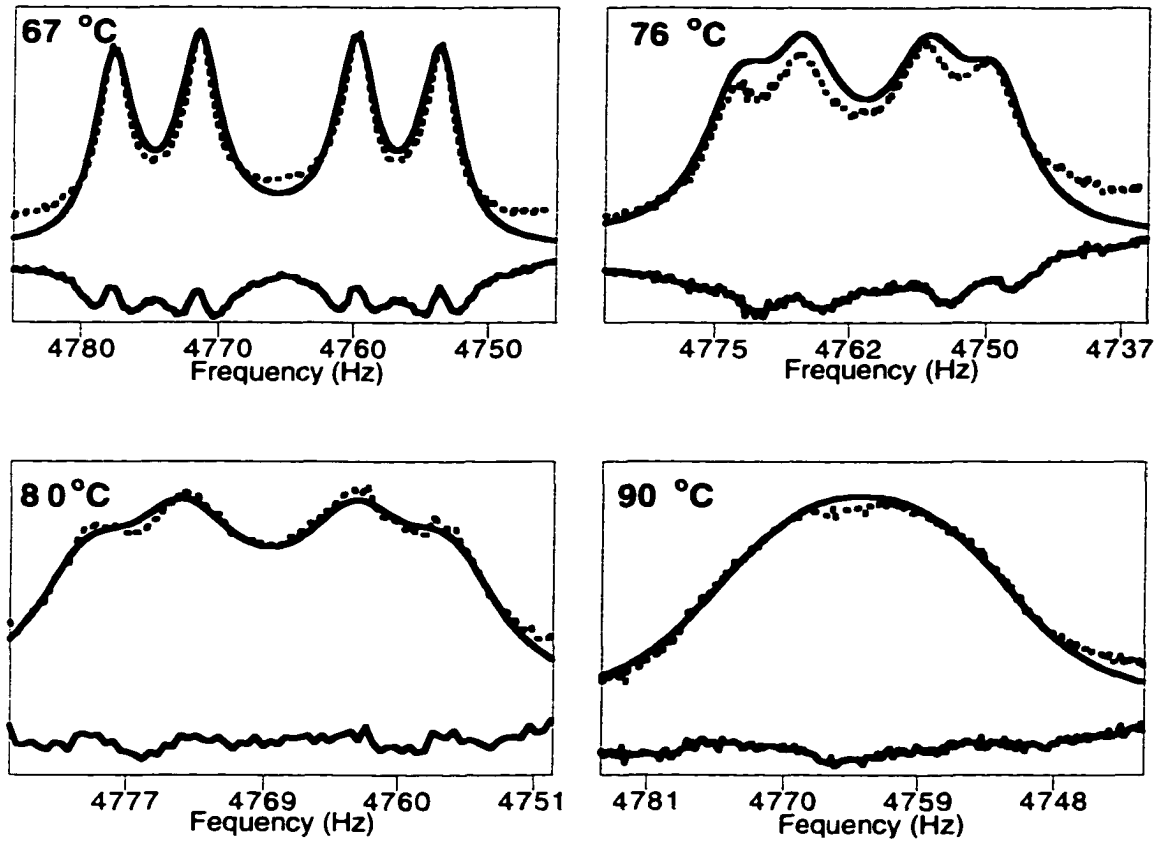

Figure 3.25. Line-Shape Analysis fit of for $[(\eta^6\text{-}C_6H_6)Ru(biiq)(I)]^+$. (— represents calculated spectrum, ··· represents experimental spectrum, difference spectrum is shown at the bottom of each graph).

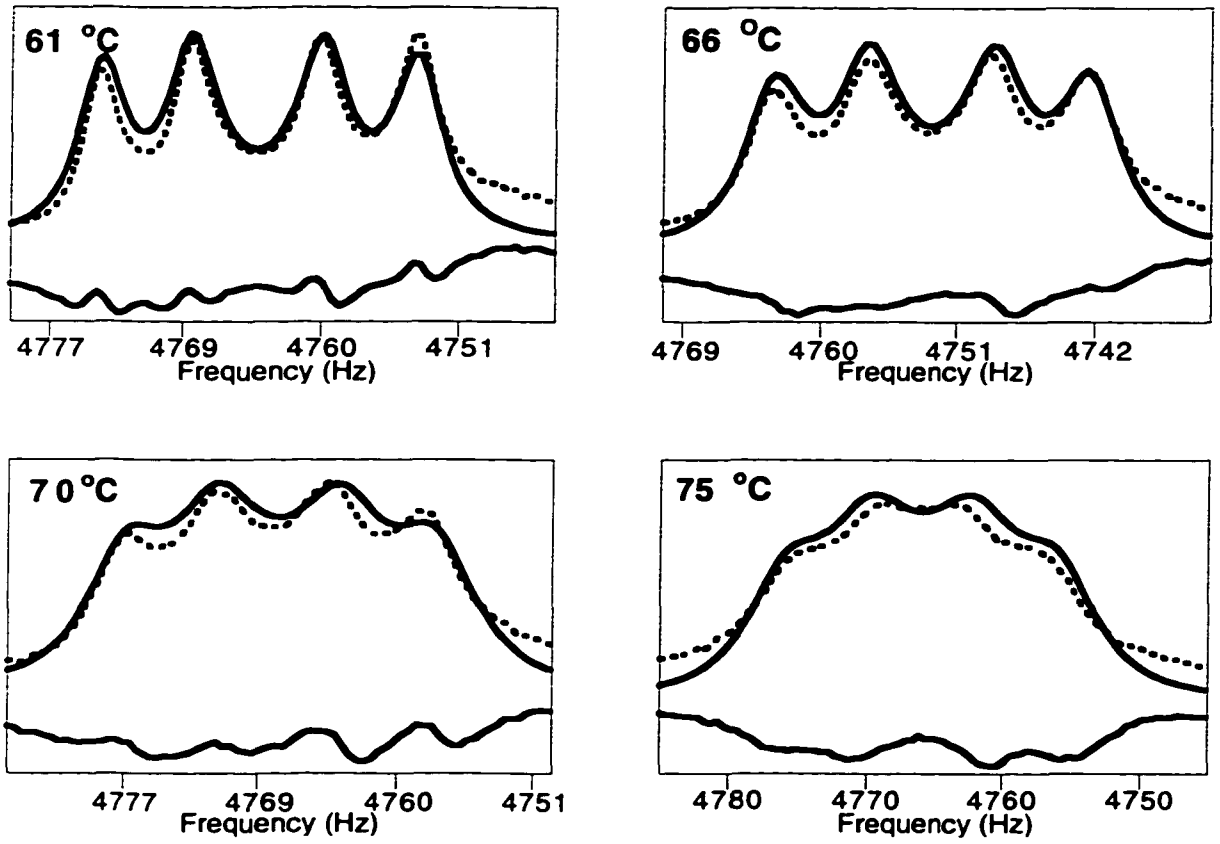

Figure 3.26. Line-Shape Analysis fit of for $[(\eta^6\text{-}C_6H_6)Os(biiq)(I)]^+$. (— represents calculated spectrum, ··· represents experimental spectrum, difference spectrum is shown at the bottom of each graph).

Table 3.3. Comparison of the Kinetic Data Obtained for the Atropisomerization of the Ru and Os Derivatives of $[(\eta^6\text{-}C_6H_6)M(1,1'\text{-biiq})(I)]^+$

Temp °C	M = Ru k_1 (s^{-1})	M = Os k_1 (s^{-1})
38	0.467(8) [a]	0.82(1) [a]
43	0.76(2) [a]	1.36(1) [a]
48	1.16(1) [a]	1.71(1) [a]
53	1.57(2) [a]	3.24(3) [a]
57	2.72(3) [a]	-
59	-	4.86(6) [a]
61	-	5.8(1) [b]
62	4.33(2) [a]	-
66	-	8.2(6) [b]
67	6.3(1) [b]	-
70	-	11.5(8) [b]
75	-	17(1) [b]
76	11.2(7) [b]	-
80	15.6(6) [b]	-
90	32.3(6) [b]	-

[a] Spin Inversion Transfer [b] Line-Shape Analysis

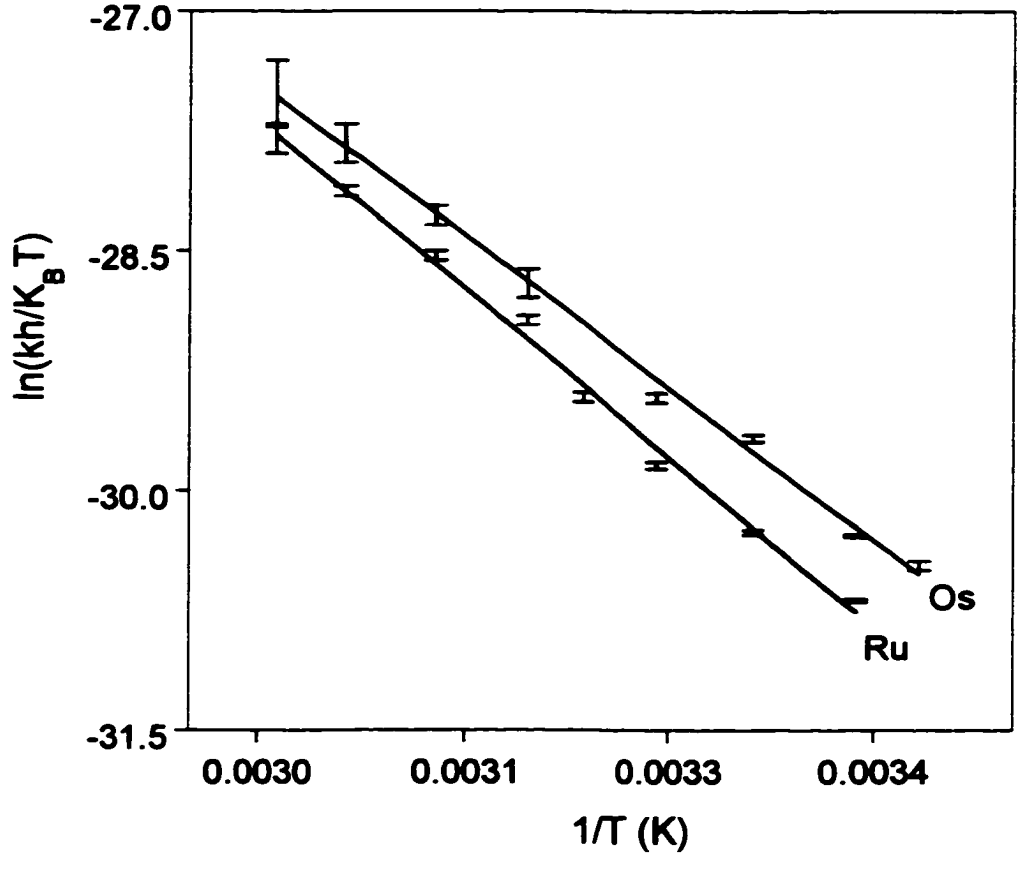

Figure 3.27. Eyring plot of kinetic data for $[(\eta^6\text{-}C_6H_6)M(biiq)(Cl)]^+$ M=Ru, Os. Error bars represent three times the error in the rate measurement.

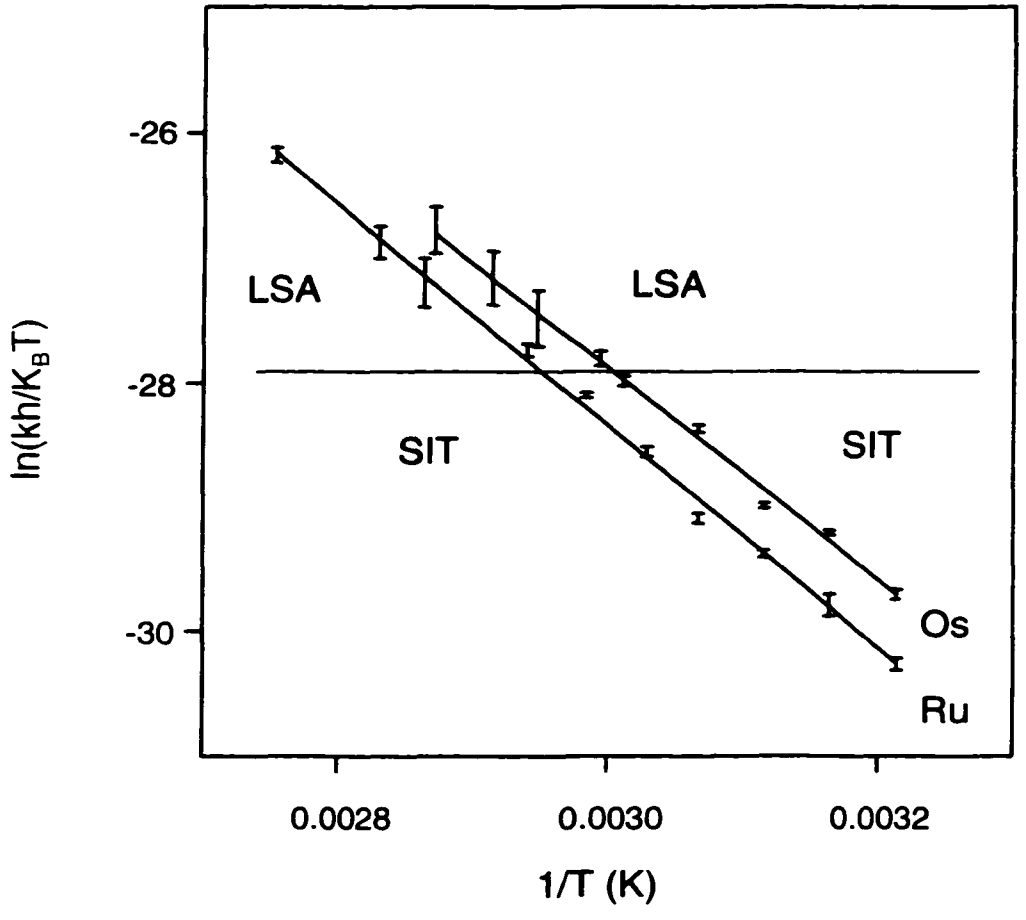

Figure 3.28. Eyring plot of kinetic data for $[(\eta^6\text{-}C_6H_6)M(biiq)(I)]^+$ M=Ru, Os. Error bars represent three times the error in the rate measurement.

3.6 Discussion

The rates of atropisomerization of the osmium derivatives are faster than the rates of the ruthenium derivatives for $[(\eta^6\text{-}C_6H_6)M(1,1'\text{-biiq})(X)]^+$ (X=Cl,I). X-ray crystal structures show nearly identical structures for the chloride derivatives. The 2D-EXSY experiments have shown that each half of the 1,1'-biiq ring is exchanging with the other half. It was shown in Chapter 2 that the mechanism of isomerization of $[(\eta^6\text{-}C_6H_6)Ru(dabp)(Cl)]^+$ proceeds through atropisomerization of the ligand. It was possible to rule out the alternate mechanisms of inversion of the metal center or simultaneous inversion of the metal center and inversion at the ligand. It has been shown that $[Ru(bipy)_2(1,1'\text{-biiq})]^{2+}$ isomerizes through a mechansim of atropisomerism of the 1,1'-biiq ligand.[59,60] It is concluded that $[(\eta^6\text{-}C_6H_6)M(1,1'\text{-biiq})(X)]^+$ (M=Ru,Os; X=Cl,I) complexes also isomerize by a mechanism of atropisomerization of the 1,1'-biiq ligand through a *syn* transition-state. This means that the 1,1'-biiq ligand is approximately planar in the transition state of the isomerization reaction. As the 1,1'-biiq ligand becomes planar the metal-nitrogen bonds are straightened and become stronger. Table 3.4 compares the activation data which was obtained from Eyring plots of the rate data (Figure 3.27). The results for the Cl and I derivatives are very similiar. The rates for the I derivatives were collected over a larger temperature range which should result in more accurate activation data. The data support the above argument in that the energies of activation are larger for the ruthenium derivatives than the osmium derivatives. The differences in $\Delta G^{\ddagger}$ are only about 1 kJ/mole, but the differences in the enthalpy of activation are about 6 kJ/mole larger for ruthenium than for osmium. It is important to compare $\Delta H^{\ddagger}$ instead of $\Delta G^{\ddagger}$. $\Delta H^{\ddagger}$ is directly related to bond strength. $\Delta G^{\ddagger}$ can be separated into enthalpic and entropic contributions, thus $\Delta G^{\ddagger}$ is not directly related to bond strength as it contains entropic contributions. A comparison between values of $\Delta H^{\ddagger}$ for second-row and third-row metal complexes can be made. A "Kinetic Enthalpy Effect" (KHE) can be defined as the ratio of enthalpy of

activation for the third row and second-row atropisomerization reactions (KHE= $\Delta H^{\ddagger}_{3rd}/\Delta H^{\ddagger}_{2nd}$). A regular effect would be seen when KHE is greater than one. This would be relative to a higher activation barrier for a reaction for the third-row complex with its presumably stronger bonds. An inverse KHE is observed in these systems. KHE is equal to 0.93 for $[M(bipy)_2(1,1'\text{-biiq})]^{2+}$,[60] 0.93 for $[(\eta^6\text{-}C_6H_6)M(1,1'\text{-biiq})(Cl)]^+$ and 0.92 for $[(\eta^6\text{-}C_6H_6)M(1,1'\text{-biiq})(I)]^+$ (M=Ru, Os). The osmium complexes have a smaller energy of activation than the ruthenium complexes in each case. The KEE is equal to 0.12 for $[M(bipy)_2(1,1'\text{-biiq})]^{2+}$,[60] and this may be compared with the values of 0.66 for $[(\eta^6\text{-}C_6H_6)M(1,1'\text{-biiq})(Cl)]^+$ and 0.57 for $[(\eta^6\text{-}C_6H_6)M(1,1'\text{-biiq})(I)]^+$ (M=Ru, Os). More negative entropies of activation are observed for the osmium derivatives than the ruthenium derivatives. The origin of these entropic differences are unclear, but the same trend was seen in the previous study of $[M(bipy)_2(1,1'\text{-biiq})]^2$.[60]

As in the case of $[M(bipy)_2(1,1'\text{-biiq})]^{2+}$, the thermodynamically more stable $[(\eta^6\text{-}C_6H_6)Os(1,1'\text{-biiq})(X)]^+$ exhibits faster atropisomerization kinetics. The KEE was much more dramatic for the $[M(bipy)_2(1,1'\text{-biiq})]^{2+}$ system in which atropisomerism of the osmium derivative was an order of magnitude faster than the ruthenium derivative. However, the KHE are comparable. KHE may be a better indicator of bond strength. Changing the ancillary ligands changed the magnitude of the KEE, but the existance of an inverse KEE and trends in the activation data remained the same.

Table 3.4. Comparison of the Activation Data Obtained for Atropisomeriza-tion of Ru and Os Derivates of $[(\eta^6\text{-}C_6H_6)M(1,1'\text{-biiq})(X)]^+$

	M=Ru X=Cl	M=Os X=Cl	M=Ru X=I	M=Os X=I
$\Delta H^{\ddagger}$ (kJ/mole)	77.3(2)	71.2(2)	76.5(3)	70.2(5)
$\Delta S^{\ddagger}$ (J/K mole)	4.8(7)	-11.6(7)	-5 (1)	-21 (1)
$\Delta G^{\ddagger}_{(50)}$(kJ/mole)	75.8	75.0	78.4	77.1

3.7 Summary

$[(\eta^6\text{-}C_6H_6)M(1,1'\text{-biiq})(X)]^+$ (M=Ru,Os; X=Cl,I) were synthesized. X-ray crystal structures were solved for the chloride derivatives. ^1H NMR chemical shifts were assigned by 2D-COSY experiments. Exchange between enantiomers was observed by 2D-EXSY experiments. Rates of atropisomerization of the 1,1'-biiq ligand were measured for all four derivatives by NMR. Rates were found to be faster for the ruthenium derivatives than the osmium derivatives. Activation data was obtained by Eyring plots from the rate data to show the same inverse relationship between thermodynamic stability and kinetic lability as in the case of the $[M(bipy)_2(1,1'\text{-biiq})]^{2+}$ (M=Ru, Os) system. This is attributed to a strengthening of the metal-nitrogen bonds of 1,1'-biiq in the transition state relative to the ground state.

CHAPTER 4

ROTATIONAL BARRIERS ABOUT THE METAL-SULFUR BONDS OF GROUP IV METAL THIOLATES

4.1 Introduction

Metallocene dithiolate complexes were first synthesized in 1967 by two groups. Kopf and Schmidt synthesized compounds of titanium[103] while Green and Lindsell synthesized compounds of molybdenum and tungsten.[104] Later studies continued with vanadium[105] and niobium.[106] The d-electron count of the metal in these compounds can be d^0, d^1, or d^2, which are respectively 16, 17 and 18 electron complexes. Several studies have been carried out to investigate the bond energetics of metallocene dithiolate compounds. These investigations include theoretical,[107-113] crystallographic, [105,106,114-121] thermochemical,[108,122,123] structural[106,114] and bimetallic studies.[106,118,124-129] These experiments give information on molecular orbital energies, changes in bond lengths and bond angles due to steric and electronic vibrations, trends in bond dissociation energies, and the effect of binding a second metal on structural and electronic properties.

Studies concerning the spatial orientation of the bonding interactions of bent metallocene thiolate compounds have appeared in the literature. Extended Hückel,[110] Fenske-Hall[111] and ab initio[109] calculations predict that when a ligand is a single sided, two-electron donor such as a thiolate, the d^0 system will choose the *endo* conformation, while the d^2 system will choose the *exo* conformation (Figure 4.1).[109-111] The *endo* conformation is one in which the thiolate 3p-type lone pair is co-planar with the metal d-orbital. The *exo* conformation is one in which the ligand p-orbital is rotated out of the plane of the metal d-orbital until the two orbitals are orthogonal to each other. The *exo* conformation is chosen by the d^2 sytems in order to avoid a 4-electron destabilizing interaction.[50]

A list of crystal structures that have been solved for metallocene thiolate compounds is given in Table 4.1. The *endo* conformation is strictly defined as having a S-M-S-R torsion angle of less than 90° while the *exo* conformation torsion angle is greater than 90°. It is seen from the table that all d^0 compounds have the *endo* conformation, the d^2 compounds have the *exo* conformation and the d^1 derivatives have both conformations. This agrees with the predictions from the theoretical studies.[109-111] In solution, the thiolate group rotates around the metal-sulfur bond. For the d^0 electron-deficient early transition metals, the thiolate group rotates from the *endo* conformation, which is the ground-state, through the *exo* conformation, which is the transition-state. In the *endo* conformation, steric conflict between the R group and one of the Cp ligands is maximized. Thus, the ground-state conformation that is adopted by the d^0 metal derivatives represent a compromise between stabilizing Mdπ-Spπ interactions and destabilizing R-Cp steric contact. Consequently, the observed conformations for d^0 derivative are not optimal for Mdπ-Spπ bonding. The thiolate ligands in such complexes are therefore misdirected.

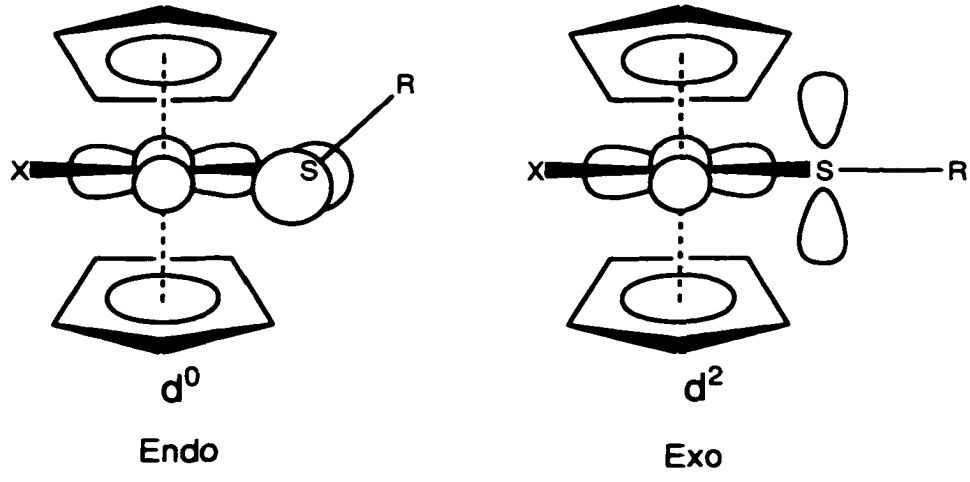

Figure 4.1. *Endo* and *exo* conformations proposed for metallocene thiolate complexes.

Table 4.1. Selected Interatomic Distances (Å), Angles (deg), and Torsion Angles (deg) for Bent Metallocene Thiolate Complexes.

Compound	d-electrons	M-S	S-M-S	S-M-S-R	Ref
$Cp_2Ti(SCH_3)_2$	0	2.403(1)	93.7(1)	56.9(6)	117
$Cp_2Ti(SCH_2CH_3)_2$	0	2.398(3)	93.791(1)	58	116
$Cp_2Ti(S(CH_3)_3)_2$	0	2.417(4)	99.88(3)	59	130
$Cp_2Ti(SC_6H_5)_2$	0	2.395(8)	99.319(3)	65	105
$Cp_2Ti(S(CH_2)_3PPh_2)_2$	0	2.384(6)	93.3(2)	53	118
$Cp_2Ti(SC_6H_5)(SSSC_6H_5)$	0	2.381(5)	98.27(1)	66	131
$Cp_2Zr(SC_6H_4Cl\text{-}p)_2$	0	2.526(1)	98.9(3)	64	132
$[Cp_2Zr(SC_6H_5)_2]O$	0	2.542(2)	98.7(1)	68	133
$[Cp_2Zr(S\text{-}t\text{-}C_4H_9)(THF)]^+$	0	2.462(1)	94.98(7)	72	134
$[Cp_2Zr(S\text{-}t\text{-}C_4H_9)_2$	0	2.510(1)	102.40(3)	57.9(1)	130
$[Cp_2Nb(S\text{-}p\text{-}C_6H_4\text{-}Cl)_2]^+$	0	2.406(3)	102.3(1)	59	114
$[Cp_2Nb(SC_6H_5)_2]^+$	0	2.418(1)	101.4(1)	65	106
$Cp_2V(SC_6H_5)_2$	1	2.472(3)	94.101	59	105
$Cp_2V(SCH_3)_2$	1	2.442(1)	88.7(1)	53	119
$Cp_2Nb(S\text{-}p\text{-}C_6H_4\text{-}Cl)_2$	1	2.508(3)	98.7(1)	50	114
$Cp_2Nb(S\text{-}p\text{-}C_6H_4OCH_3)_2$	1	2.513(1)	79.1(1)	163	114
$Cp_2Nb(S\text{-}p\text{-}C_6H_4CH_3)_2$	1	2.522(3)	77.1(1)	146	114
$Cp_2Nb(SC_6H_5)_2$	1	2.516(7)	75.4(9)	163	106
$Cp_2Ta(SC(O)C_6H_5)_2$	1	2.516(3)	79.4(8)	179	120
$Cp_2Mo(S(CH_3)_3)_2$	2	2.491(1)	71.1(1)	173	121
$Cp_2Mo(SC_6H_5)(CH(CN)CH_3)$	2	2.500(1)	77.39(8)	156	135
$[Cp_2Mo(SC_6H_5)(NH_3)]^+$	2	2.465(5)	76.4(4)	179	116
$[Cp_2Mo(SC_6H_5)(p\text{-}(CH_3)_2NC_6H_4CN)]^+$	2	2.473(1)	79.8(1)	171.4(1)	136

$Cp=(\eta^5\text{-}C_5H_5)$

4.2 Synthesis of Bis(η^5-cyclopentadienyl)(chloro)(thiolato)-zirconium(II) complexes, $(\eta^5\text{-}C_5H_5)_2Zr(Cl)(SR)$

A series of zirconocene monothiolate complexes have been synthesized for the first time. They were made by mixing sodium hydride and methyl, ethyl, or *iso*-propyl thiol in THF. After evolution of hydrogen and formation of sodium thiolate, zirconocene dichloride was added. The *tert*-butyl derivative was made by reacting $[(\eta^5\text{-}C_5H_5)_2Zr(Cl)(H)]_n$ directly with *tert*-butyl thiol in THF. These compounds are air and moisture sensitive. After making relatively pure monothiolate compounds, it was discovered that in polar solvents the monothiolate compound rapidly disproportionates into a statistical mixture of the dichloride, chlorothiolate and dithiolate species. The deuterated freon $CDCl_2F$ that was used in the NMR experiments promoted disproportionation. However, after assigning all of the peaks, the mixture of compounds did not interfere with the NMR experiments; therefore, no further attempt was made to synthesize pure compounds. Accordingly, a statistical mixture of these three compounds were used in the NMR measurements that are described herein. Assignment of the ^1H NMR peaks were made by integration and the observation of splitting of resonances (cyclopentadienyl groups and diastereotopic methylene and methyl groups) at low temperature. In general, the order of the resonances was dichloro, chlorothiolato, and dithiolato, where the dichloro derivative was furthest down field. Figure 4.2 illustrates the ambient temperature ^1H NMR spectra of all four derivatives in $CDCl_2F$. Fast exchange conditions are seen at room temperature, the cyclopentadienyl groups (and the other stereotopic groups) are rendered magnetically equivalent and the spectrum becomes consistent with overall C_s symmetry as is indicated by the observation of one cyclopentadienyl resonance for each derivative (Figure 4.2).

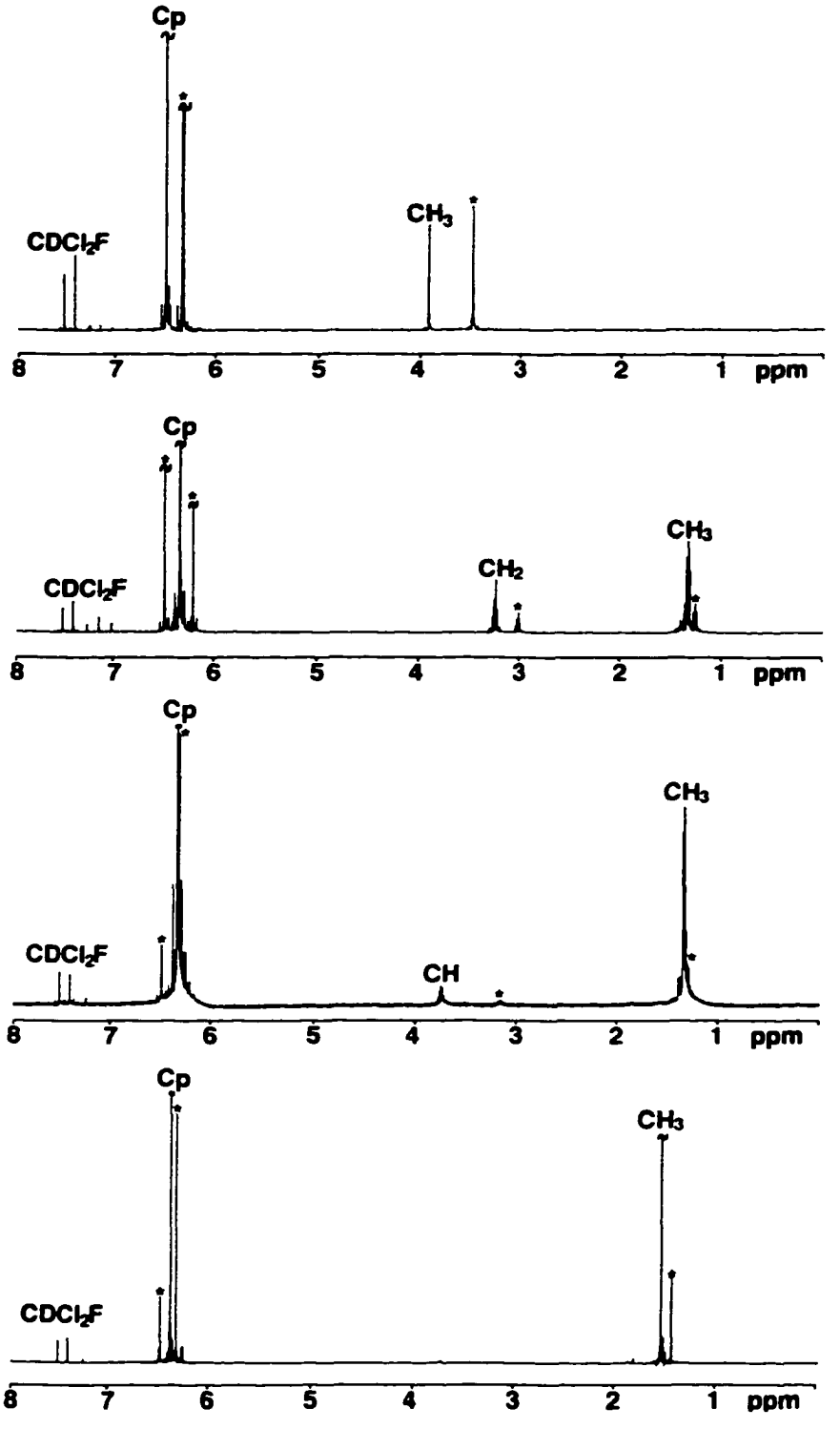

Figure 4.2. 500 ^{1}H NMR Spectra of $Cp_2Zr(Cl)(SR)$ in $CDCl_2F$ at 20° C. From top to bottom, R= Me, Et, *i*-Pr, and *t*-Bu. The dichloride and dithiolate impurities are indicated by an asterisk (*).

4.3 Rotational Barriers of Bis(η^5-cyclopentadienyl)(chloro)-(thiolato)zirconium(II) complexes, (η^5-$C_5H_5)_2Zr(Cl)(SR)$

The barriers of rotation about the zirconium-sulfur bond were measured by variable temperature NMR.[137] At low temperature, slow exchange conditions are observed. The cyclopentadienyl groups become inequivalent in the ^1H NMR spectra. This is consistent with the C_1 symmetry of the compounds. The ethyl and *iso*-propyl derivatives also reveal inequivalent methyl and methylene groups at lower temperatures. Therefore, the rate and energy of rotation can be calculated by measuring the coalescence temperature and the difference in the chemical shift of the decoalesced peaks at the lower temperature limit. The coalescence temperature rate calculations are explained in detail in Section 5.7.1.

Resonances for the cyclopentadienyl groups were used to measure the rotational barriers for the methyl, *iso*-propyl, and *tert*-butyl derivatives. This was not possible for the ethyl derivative as the cyclopentadienyl groups did not coalescence in the temperature range of the solvent, so the diastereotopic methylene group was used instead. For the *iso*-propyl derivative, barriers measured using the cyclopentadienyl ligands and the diastereotopic methyl groups are in agreement with one another. Because of the relatively small magnitude of the rotational barriers and the small differences in chemical shifts between the stereotopic resonances, very low temperatures were required to carry out these experiments. The only solvent that proved suitable was $CDCl_2F$, which freezes at -120 °C, but can be supercooled to -150 °C for short periods of time. Samples were transferred to 5 mm NMR tubes that had been glass-blown onto vacuum-line adapters fitted with high-vacuum Teflon stopcocks. The samples were placed under vacuum, $CDCl_2F$ was vacuum transferred, the solutions were frozen with liquid nitrogen, then the tubes were flame sealed while the solutions were still frozen. Figure 4.3 shows the variable temperature spectra of the methyl derivative which illustrates one cyclopentadienyl resonance at 20 °C and two cyclopentadienyl resonances at low

temperature. The kinetic data are summarized in Table 4.2. The table lists the resonance that was followed in the NMR, the coalescence temperature, the difference in chemical shift at the lower termperature limit, the rate constant and the energy of rotation in kJ/mole. These temperatures are very low and it was not possible to separate the enthalpy and entropy contributions to the energy of rotation. It was not possible to use line-shape analysis experiments to separate the enthalpic and entropic contributions because the mixture of compounds in solution interfered with the line shapes of the resonances. The data shows an unexpected trend. The energy increases for methyl, ethyl and *iso*-propyl, but drops significantly for the *tert*-butyl derivative.

Table 4.2. Kinetic Parameters and Zr-SR Rotational Barriers for $Cp_2Zr(Cl)(SR)$

R	Resonance	Tc (°C)	$\delta\Delta$ (Hz)	k (s^{-1})	$\Delta G^{\ddagger}$ (kJ/mol)
Methyl	Cp	-125	6	13.6	32
Ethyl	CH_2	-104	119	264	33
iso-Propyl	Cp	-109	6	20.0	35
	CH_3	-95	71	158	35
tert-Butyl	Cp	-140	60	133	26

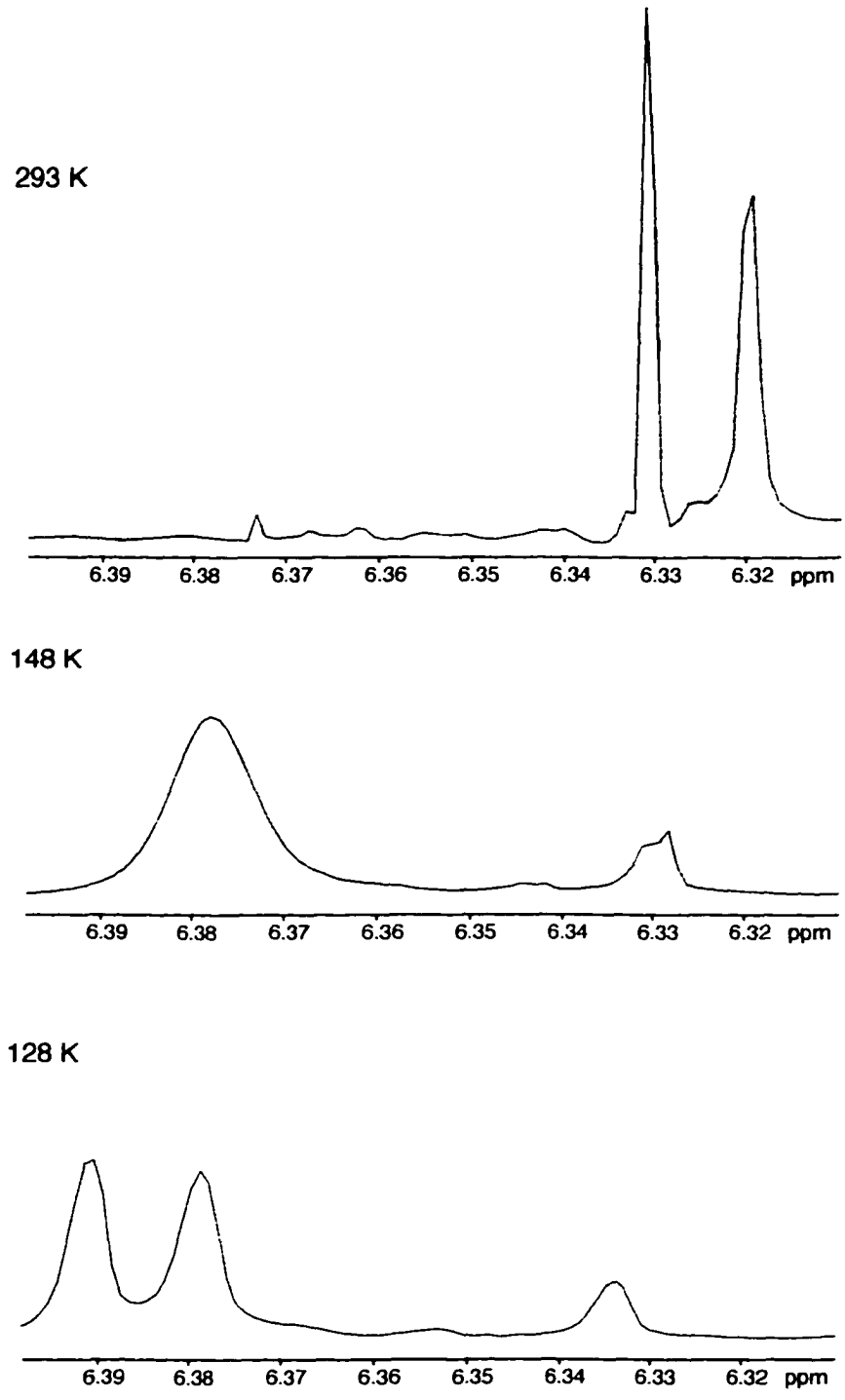

Figure 4.3. Variable temperature ^1H NMR of $Cp_2Zr(SMe)(Cl)$, illustrating room temperature, coalescence temperature and the lower temperature limit of the cyclopentadiene resonance.

4.4 Synthesis and X-Ray Crystal Structures of (Bis)(η^5-cyclopentadienyl)di(thiolato)zirconium(II) Complexes, $(\eta^5\text{-}C_5H_5)_2Zr(SR)_2$

It was desirable to determine the X-ray crystal structures of the zirconcene monothiolate compounds in order gain information to rationalize the trend in rotational barriers. However, crystallization of the monothiolate zirconium compounds was not possible due to the problem of disproportionation. Therefore, we synthesized the same series of dithiolate zirconium compounds. The thiolates were synthesized by mixing two equivalents of sodium hydride with two equivalents of methyl, ethyl, *iso*-propyl or *tert*-butyl thiol in THF. After the evolution of hydrogen, zirconocene dichloride was added to give the metallocene product. These compounds are air and moisture sensitive. They were recrystallized by vapor diffusion of pentane into THF in a nitrogen filled glove box at room temperature and were characterized by ^1H NMR and elemental analysis. Figure 4.4 illustrates the ^1H NMR spectra in CD_2Cl_2 at ambient temerature for all four derivatives. The methyl, *iso*-propyl and *tert*-butyl derivatives have pseudo C_2 symmetry. The ethyl derivative has overall C_1 symmetry because the ethyl groups are in different conformations. They all exhibit *endo* conformations. Their metric parameters vary systematically with the change in size of the R group. A previously solved structure of $Cp_2Zr(SC(CH_3)_3)_2$ appears in the literature (Table 4.1).[130] The structure crystallized into the C2/c space group in contrast to our structure which is in the space group $P4_32_12$. The metric parameters are very comparable with the exception of a more acute S-M-S angle (102.40(3)°) and S-Zr-S-C torsion angle (57.9(1)°). The Zr-S bond lengths of related zirconium compounds $[Cp_2Zr(S\text{-}t\text{-}C_4H_9)(THF)]^+$ (2.462(1) Å)[134] and $[Cp_2Zr(SC_6H_5)_2]O$ (2.542(2) Å)[133] are comparable to the Zr-S bond lengths of $Cp_2Zr(SCH_3)_2$ (2.5044(8) Å), $Cp_2Zr(SCH_2CH_3)_2$ (2.486(1) Å), $Cp_2Zr(SCH(CH_3)_2)_2$ (2.5017(7) Å), and $Cp_2Zr(SC(CH_3)_3)_2$ (2.5294(7) Å). The S-Zr-S bond angle of 106.1(1)° for $Cp_2Zr(SC(CH_3)_3)_2$ is the largest angle for the metallocene thiolate

structures (Table 4.1). This is not surprising due to repulsion from the large *tert*-butyl groups. In contrast, $Cp_2Mo(SC(CH_3)_3)_2$ which exhibits the *exo* conformation has the most acute S-M-S bond angle (71.1(1)°).[121] Selected bond lengths, bond angles and torsion angles are shown in Table 4.3. The thermal ellipsoid drawing of the molecular structures as determined by single-crystal X-ray diffraction are showin in Figure 4.5. Crystallographic details are discussed in Section 5.4 with crystal data, atomic coordinates, anisotropic displacement parameters and hydrogen coordinates.

Table 4.3. Selected Interatomic Distances (Å), Angles (deg), and Torsion Angles (deg) for $Cp_2Zr(SR)_2$

	R = CH_3	R = CH_2CH_3	R = $CH(CH_3)$	R = $C(CH_3)_3$
Zr-S	2.5044(8)	2.4863(12)	2.5017(7)	2.5294(7)
Zr-S'	2.5067(7)	2.5105(7)	2.5017(7)	2.5294(7)
Zr-Cp_{cent}	2.203(3)	2.210(2)	2.211(1)	2.220(1)
Zr-Cp_{cent}'	2.207(3)	2.211(2)	2.211(1)	2.220(1)
Zr-S-C	108.7(1)	108.65(7)	113.35(8)	123.65(8)
Zr-S'-C'	107.8(1)	109.26(8)	113.35(8)	123.65(8)
S'-Zr-S-C	61.1(1)	54.96(8)	66.07(9)	60.2(1)
S-Zr-S'-C'	55.7(1)	61.60(9)	66.07(9)	60.2(1)
Cp_{cent}-Zr-Cp_{cent}'	129.8(1)	130.4(1)	129.4(3)	127.7(3)
S-Zr-S'	97.1(1)	99.0(1)	100.2(1)	106.1(1)
Cp_{cent}-Zr-S	101.1(1)	111.2(1)	101.3(1)	98.4(1)
Cp_{cent}-Zr-S'	111.6(1)	100.2(1)	109.7(1)	112.5(1)
Cp'_{cent}-Zr-S	111.9(1)	101.1(1)	101.3(1)	98.4(1)
Cp'_{cent}-Zr-S'	101.0(1)	111.1(1)	109.7(1)	112.5(1)
Dihedral Angles				
Cp-Cp	127.7(1)	127.9(1)	129.4(1)	125.8(1)
Cp -(S/M/S')	27.0(1)	27.0(1)	25.8(1)	28.4(1)
Cp'-(S/M/S')	27.2(1)	26.8(1)	25.8(1)	28.4(1)
(Cp_{cent}/Zr/Cp_{cent}') - (S/M/S')	82.4(1)	82.7(1)	84.2(1)	81.5(1)

[a] Cp is defined to be the least-squares plane that contains a cyclopentadienyl ligand. Cp_{cent} is the centroid of a cyclopentadienyl ligand.

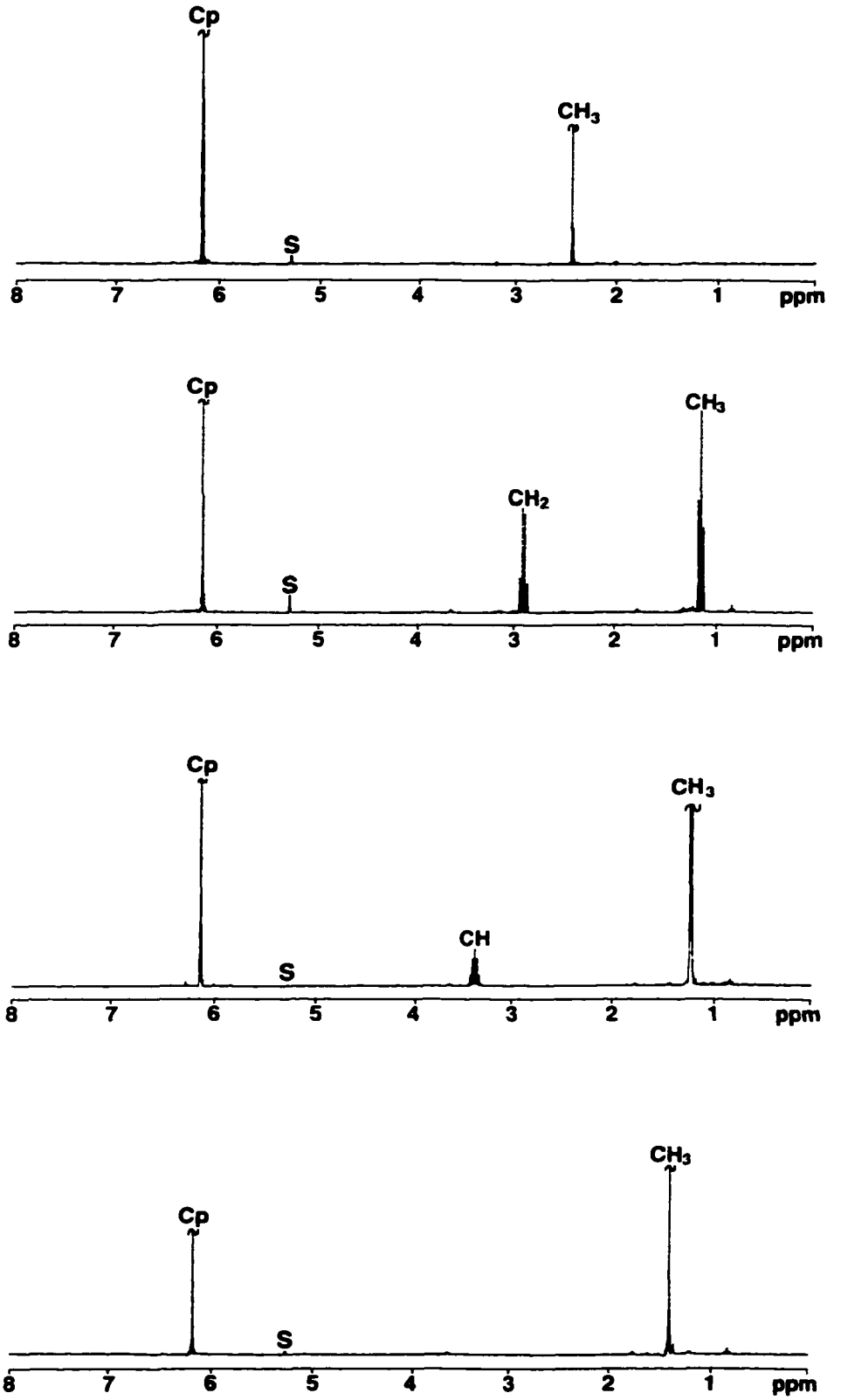

Figure 4.4. 300 MHz ^{1}H NMR spectra of $Cp_2Zr(SR)_2$ in methylene chloride-d_2 at ambient temperature. From top to bottom R=Me, Et, *i*-Pr, and *t*-Bu.

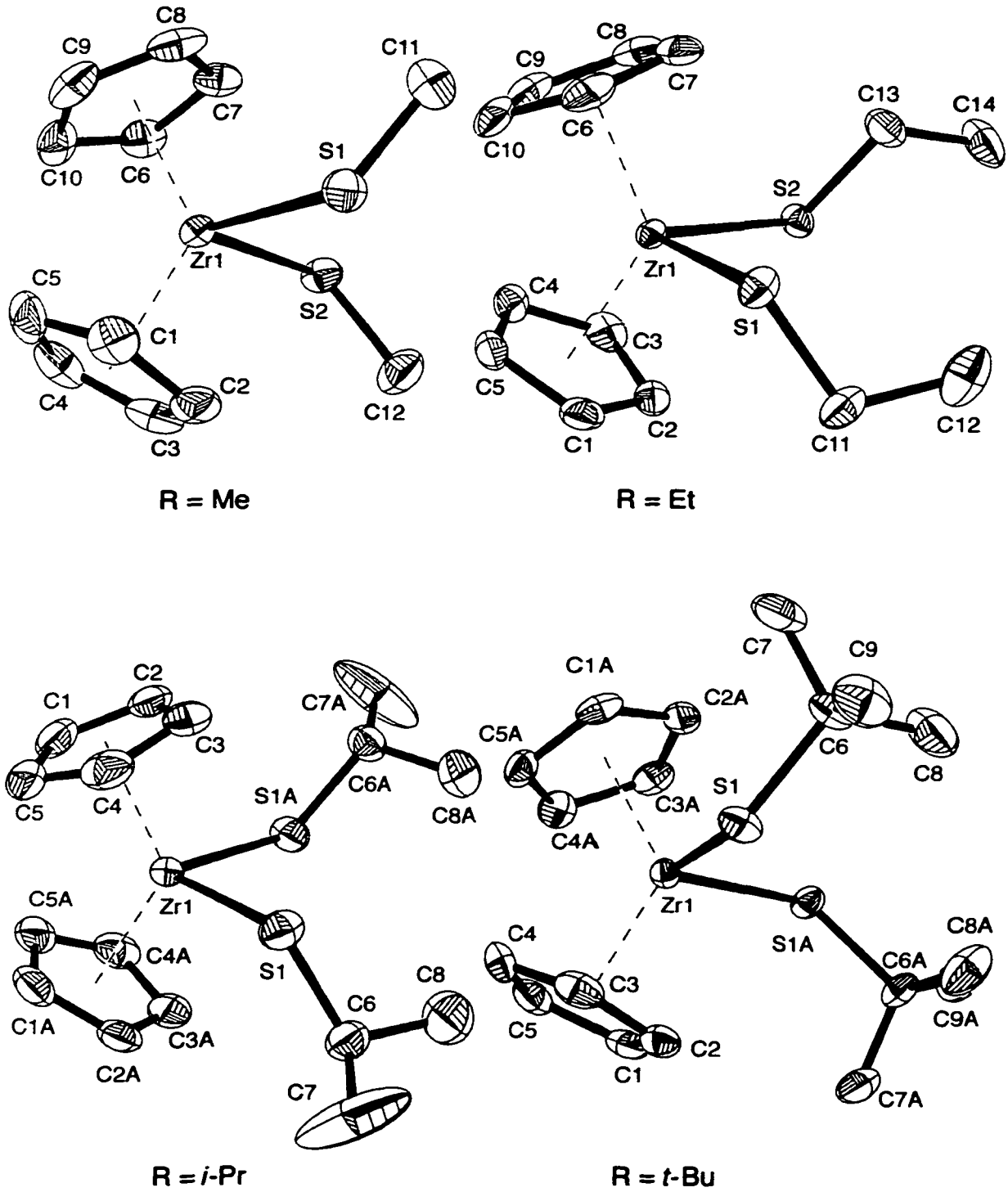

Figure 4.5. Molecular structure of $Cp_2Zr(SR)_2$ showing the atom labeling scheme and the thermal vibration ellipsoids (50% probability). Hydrogen atoms were omitted for the sake of clarity.

4.5. Computational Study of Bis(η^5-cyclopentadienyl)(chloro)-(thiolato)zirconium(II) Complexes, $(\eta^5\text{-}C_5H_5)_2Zr(Cl)(SR)$

Ab initio electronic structure computations were performed for $(\eta^5\text{-}C_5H_5)_2Zr(Cl)(SR)$ (R=methyl, ethyl, *iso*-propyl, *tert*-butyl) using density functional theory (DFT) as implemented in GAUSSIAN 94 and 98.[138,139] The B3LYP method[140] based on Becke's 3-parameter hybrid exchange functionals[141] and Lee-Yang-Parr correlation functionals[142,143] was used. The correlation functionals provide a good way to calculate correlation energies from electron densities.[142] Optimized ground-state and transition-state geometries, free energies ($\Delta G^{\ddagger}$), enthalpies ($\Delta H^{\ddagger}$), entropies ($\Delta S^{\ddagger}$), and zero-point energies were calculated from the results. The details of these calculations are explained in Section 5.5. The activation data are listed in Table 4.4. Selected computed metric parameters for the ground-state and transition-state structures are listed in Table 4.5. There is good agreement between the calculated and experimental roational barriers for the four derivatives.

Table 4.4. Computed Activation Data for $(\eta^5\text{-}C_5H_5)_2Zr(Cl)(SR)$ at the DFT-B3LYP Level

R	Temperature K	$\Delta H^{\ddagger}$ kJ/mol	$\Delta S^{\ddagger}$ (e.u.)	$\Delta G^{\ddagger}$(calc.) kJ/mol	$\Delta G^{\ddagger}$(exp.) kJ/mol
Methyl	298	30.08	-1.59	30.54	-
Methyl	148	30.96	2.43	30.58	32.
Ethyl	298	28.91	-0.99	30.41	-
Ethyl	169	29.74	-0..63	29.83	33
iso-Propyl	298	27.44	-9.99	30.41	-
iso-Propyl	178	28.15	-6.94	29.37	35
tert-Butyl	298	17.40	-9.58	20.25	-
tert-Butyl	133	18.49	-4.43	18.66	26

Table 4.5. Selected Computed Interatomic Distances (Å), Angles (deg), Torsion Angles (deg), and Dihedral Angles (deg) for the Ground-State and Transition-State Structures of $[(\eta^5\text{-}C_5H_5)_2Zr(Cl)(SR)$; R=Me, Et, *i*Pr, *t*Bu.

	Ground-State				Transition-State			
	Me	Et	*i*Pr	*t*Bu	Me	Et	*i*Pr	*t*Bu
				Distances				
Zr-S	2.5401	2.5355	2.5330	2.5413	2.5972	2.5873	2.5778	2.4940
Zr-Cl	2.5020	2.5040	2.5080	2.5080	2.4840	2.4850	2.4880	2.4940
Zr-Cp	2.2533	2.2549	2.2555	2.2602	2.2660	2.2679	2.2702	2.2396
Zr-Cp'	2.2613	2.2624	2.2627	2.2679	2.2657	2.2670	2.2689	2.2677
				Angles				
Zr-S-C	109.08	109.44	112.32	120.66	104.89	109.44	108.11	116.00
Cl-Zr-S	99.40	99.33	100.58	101.07	99.57	99.34	99.42	103.13
Cp-Zr-Cp'	130.22	130.11	129.94	128.72	128.80	128.68	128.28	127.79
Cp-Zr-S	100.15	100.39	100.40	99.57	104.83	105.15	105.79	105.32
Cp'-Zr-S	109.87	110.00	110.11	112.57	106.44	106.60	106.51	106.17
Cp-Zr-Cl	108.18	108.06	107.49	106.85	107.46	107.37	107.43	106.95
Cp'-Zr-Cl	104.99	104.93	104.75	104.87	106.04	105.98	105.81	105.05
				Torsion Angles				
Cl-Zr-S-C	-62.70	-62.44	-65.14	-60.04	1.99	2.25	3.13	3.47
Cp-Zr-S-C	-173.24	-172.89	-175.33	-169.46	-109.08	-108.73	-108.12	-108.51
Cp'-Zr-S-C	47.10	47.30	44.99	51.34	111.98	112.13	112.83	113.67
				Dihedral Angles				
Cp/Zr/Cp-Cl/Zr/S	85.40	85.47	85.63	84.86	88.94	89.01	89.19	89.06
C_5-C_5'	51.65	51.73	52.01	53.11	53.48	53.51	53.99	54.28

It can be seen from comparing the trends in the metric parameters of the computed ground-state and transition-state structures that there is a difference in the ground-state structure of the *tert*-butyl derivative as compared to the methyl, ethyl and *iso*-propyl derivatives (Figure 4.6). This difference in ground-state structure is reflected in the lower Zr-S rotational barrier which is observed experimentally and theoretically. Figure 4.7 illustrates the trends in calculated activation data for the four zirconocene derivatives. It is observed from this data that the rotational barriers ($\Delta G^{\ddagger}$) are dominated by the contribution from the enthalpy term ($\Delta H^{\ddagger}$), while contribution from the entropy term ($\Delta S^{\ddagger}$) is relatively insignificant

4.6 Discussion

The rotational barriers that have been measured for the series of compounds, $Cp_2Zr(Cl)(SR)$, (R=methyl, ethyl, *iso*-propyl, *tert*-butyl) show an unexpected trend in which the rotational barriers increase for methyl, ethyl, *iso*-propyl and then decrease significantly for the *tert*-butyl derivative (Table 4.2). There are potentially two factors that contribute to the magnitude of these rotational barriers: enthalpic and entropic effects.

Enthalpic effects relate to the making and breaking of the Mdπ-Spπ bond as it rotates from the *endo* conformation (ground-state) through the *exo* conformation (transition-state). The change in enthalpy is a measure of the relative strength of bonding in the ground-state versus the transition-state.[51] In 1988, Dias studied $Cp_2Mo(SR)_2$ compounds by solution calorimetry where R was equal to a series of different alkyl groups.[108] The mean bond dissociation energy (BDE) and bond enthalpy (BE) were measured. The conclusion of this study was that increasing the bulkiness of the R group decreases the BDE and BE, while increasing the length of the alkyl chain increases the BDE and BE. The metal-sulfur bond becomes stronger as the alkyl chain gets longer. This is reflected in the increasing rotational barrier for the

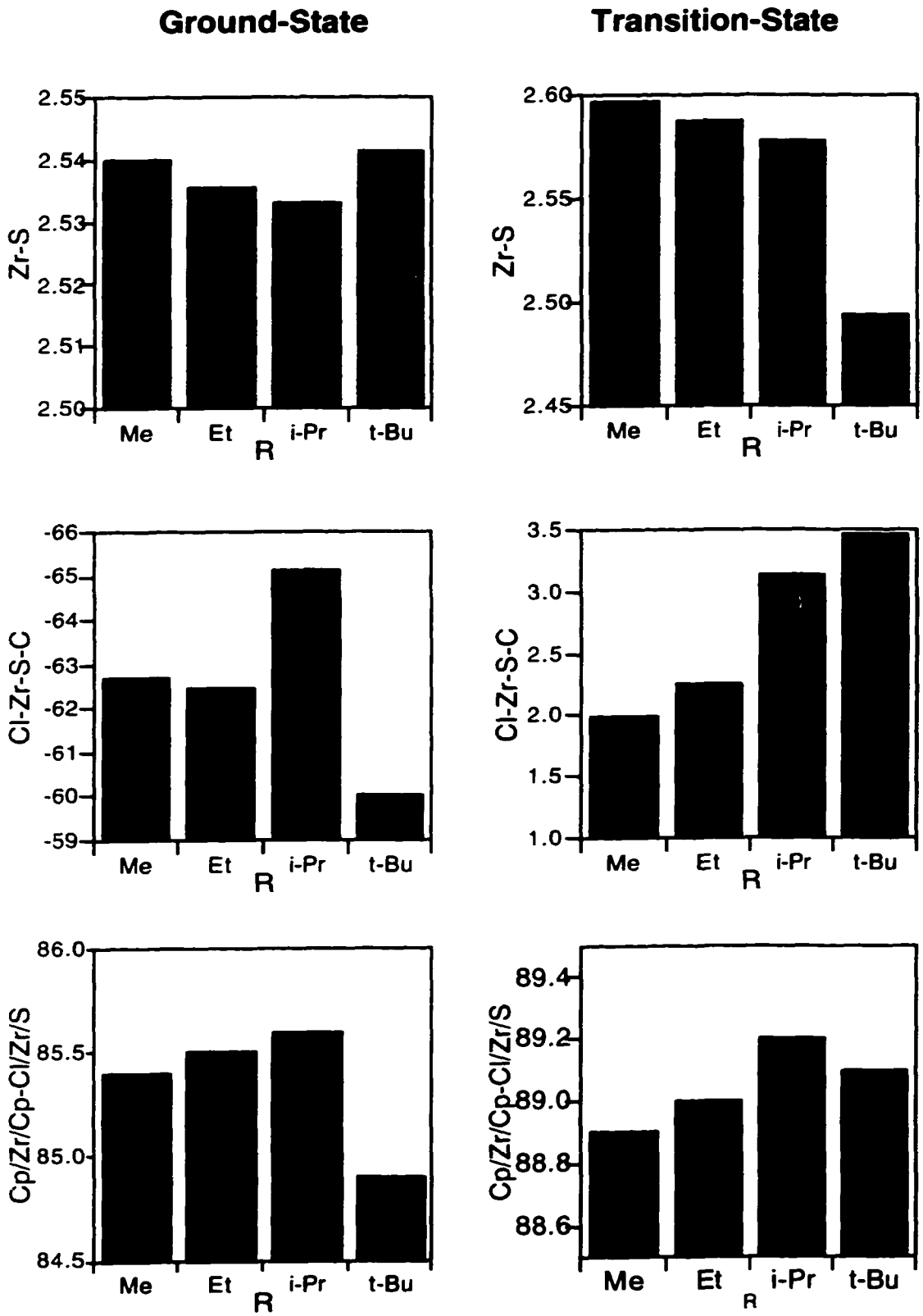

Figure 4.6. Comparison of trends in selected metric parameters of computed ground-state and transition-state structures of $Cp_2Zr(SR)(Cl)$.

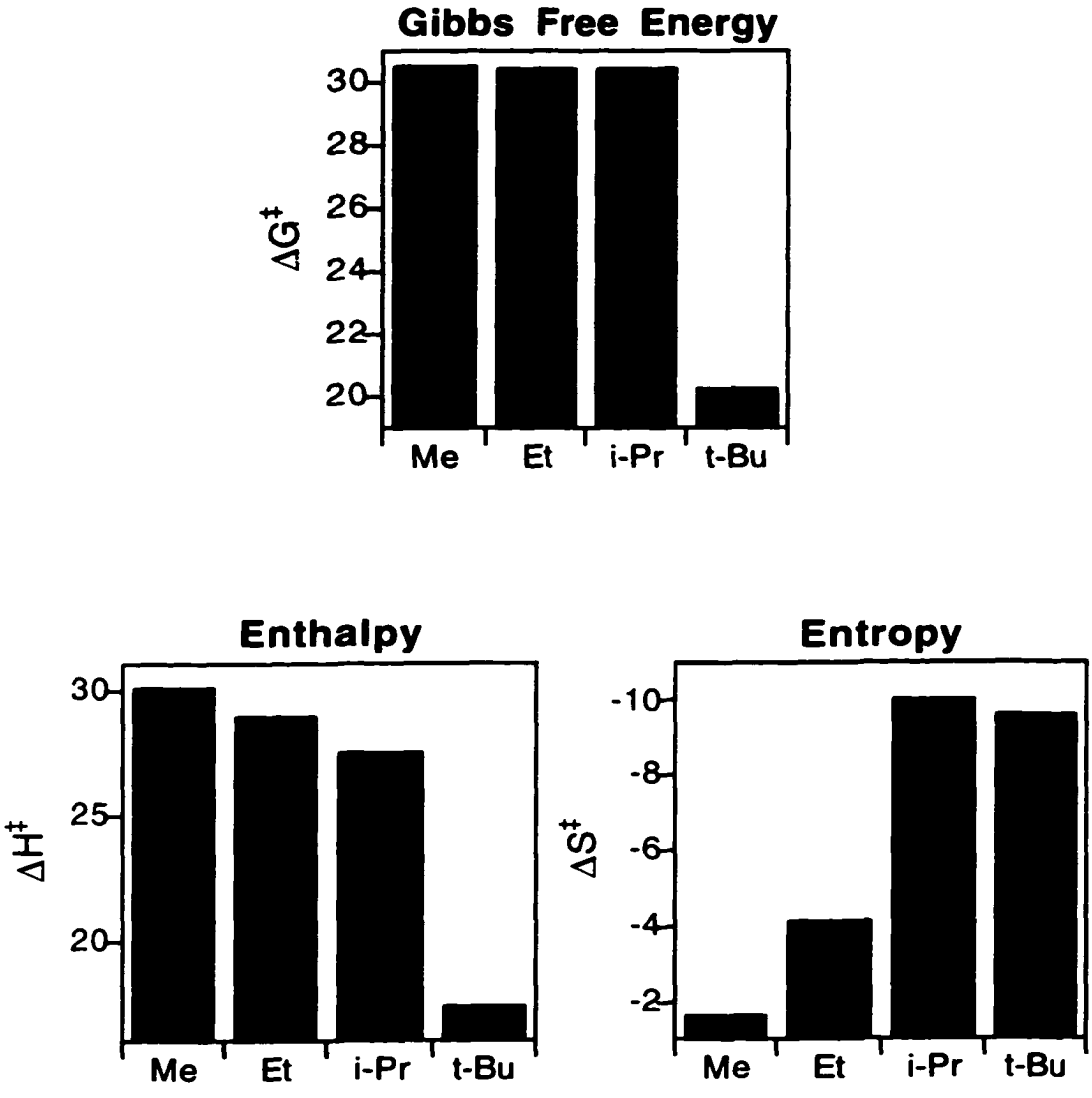

Figure 4.7. Graphical representation of computed activation data for rotational barriers about the Zr-S bond of $Cp_2Zr(SR)(Cl)$.

methyl, ethyl and *iso*-propyl derivatives. The metal-sulfur bond is weaker for the bulkier R groups. This is also reflected by a drop in rotational energy for the *tert*-butyl derivative.

Entropic effects relate to the steric interaction of the R groups bound to the sulfur atom with the halide and Cp groups that are bound to the zirconium metal center. Entropy is described as freedom of motion. A positive entropy term means that the transition-state has more freedom than the ground-state. The increase in the kinetic barrier ($\Delta G^{\ddagger}$) with the steric demand of the R-group for $Cp_2Zr(Cl)(SR)$, (R=methyl, ethyl, *iso*-propyl) is similar to the thermodynamic trend that is observed for the axial/equatorial equilibrium mixture of alkyl-substituted cyclohexanes $C_6H_{11}R$ (R = methyl, ethyl, *iso*-propyl), for which $\Delta G°$ increases with the steric demand of the R-group.[144] In other words, K = [equatorial]/[axial] increases with the steric demand of the R-group, apparently reflecting a preference for placing the large R-group in an equatorial position at all temperatures. However, the trends in $\Delta H°$ and $\Delta S°$ oppose one another. Consequently, $\Delta G°$ is dominated by the $\Delta H°$ term at temperatures below ca. 40 K and the preference for an equatorial orientation follows the order methyl > ethyl > *iso*-propyl. However, the $T\Delta S°$ term dominates at higher temperatures and the preference for equatorial orientation becomes methyl < ethyl < *iso*-propyl. The trend in $\Delta H°$ can be attributed to *gauche*-butane interactions. *Gauche*-butane interactions are the repulsive interactions of the R substitutent with the hydrogens of the cylcohexane ring and are assumed to be the dominate non-bonding interactions. The trend in $\Delta S°$ may be attributed roughly to the relative numbers of energetically accessible rotomers. Since similar factors may be important for $Cp_2Zr(Cl)(SR)$, it is necessary to describe the enthalpic and entropic factors for alkylcyclohexanes in sufficient detail to permit a transfer of the concepts to the present problem of the effect of changing R-groups on the Zr-S rotational barriers of $Cp_2Zr(Cl)(SR)$. The argument that has been made to rationalize the trend in axial/equatorial equilibria will be repeated

for the case of $C_6H_{11}R$ (R =methyl, ethyl) only, but the argument may be extended to include R = *iso*-propyl. We will consider the enthalpic factors first. Assuming that the *gauche*-butane (g.b.) interactions dominate the relative energetics of the conformers and that such interactions are additive, the number of such interactions to determine the relative enthalpic stability of any given two conformers must be added. Thus for for $C_6H_{11}CH_3$ there are two g.b. interactions for the axial conformer and zero for the equatorial. This is shown in Figure 4.8 with the g.b. interactions in bold. Consequently, the equatorial conformation is more stable than the axial conformation by two g.b. interactions. For $C_6H_{11}CH_2CH_3$, we must consider rotomers about the C_6H_{11}-(CH_2CH_3) bond. For the axial conformer of C_6H_{11}-(CH_2CH_3), only the two (equivalent) conformers that do not orient a methyl group toward the axial hydrogen atoms are significantly populated. These are also shown in Figure 4.8. The two populated axial conformations for the ethyl derivative both have three g.b. interactions. In contrast to the restricted rotomers of the axial conformer, all three rotomers of the equatorial conformer of C_6H_{11}-(CH_2CH_3) are presumably populated, albeit unequally since the rotomers are energetically different. Two of the equatorial rotomers have one g.b. interaction each (shown in bold), but the third rotomer has two g.b. interactions (one of two symmetry-related interactions is shown in bold). While the relative populations of the ethyl equatorial conformations cannot be predicted *a priori*, it is safe to say the overall enthalpy average (which is going to simply be the population-weighted average of the three rotomers) is going to be less than two. Thus, the equatorial conformation is more stable than the axial conformation by something *less* than two g.b. interactions. Accordingly, $\Delta H°$(R = methyl) > $\Delta H°$(R = ethyl). This argument may be extended to include the derivative where R = *iso*-propyl.

The observed increase in $-\Delta S°$ from R = methyl to R = ethyl ($\Delta S°$(R = methyl) > $\Delta S°$(R = ethyl)) may be roughly attributed to an increase in the number of energetically-accessible rotomers of the equatorial conformers relative to the number of

energetically-accessible rotomers of the axial conformers. The methyl derivative has three equivalent rotomers of the equatorial conformation and three equivalent rotomers of the axial conformation, while the ethyl derivative has three equivalent rotomers of the equatorial conformation and two rotomers of the axial conformation (Figure 4.8). Thus the equatorial/axial ratio increases from R=methyl to R=ethyl resulting in an increase of $\Delta S°$.

In order to extend the cyclohexane argument to the $Cp_2Zr(Cl)(SR)$ series, it is necessary to consider the possible ground-state and transition-state conformations. It is possible to draw three structures for the ground-state and three structures for the transition-state for the methyl derivative, while only two ground-state structures are possible for the ethyl derivative in which the methyl-Cp repulsions are minimized. This is illustrated in Figure 4.9. The methyl, ethyl, and *iso*-propyl derivatives have three, two and one ground-state structures which minimize the Cp-methyl repulsions. There are three possible transition-state structures which minimize this repulsion for each derivative. Therefore, the entropy term decreases from methyl, ethyl to the *iso*-propyl derivative. The trend in increasing $\Delta G^{\ddagger}$ can be attributed to a opposing $\Delta S^{\ddagger}$ and $\Delta H^{\ddagger}$ contribution. However, there is no way to minimize the Cp-R repulsion for the *tert*-butyl derivative in the ground-state. The low rotational barrier for this derivative could therefore be attributed to destabilization of the ground-state.

In 1989, Abel measured the inversion barrier for a series of thioether compounds.[145] He used the methyl, ethyl, *iso*-propyl and *tert*-butyl derivatives of molybdenum tetracarbonyl. In this case the inversion barriers were high enough that it was possible to separate the enthalpic and entropic contributions to the inversion barriers by carrying out variable temperature measurements. Enthalpy was the dominant factor in this system. The trend in $\Delta G^{\ddagger}$ was found to be methyl > ethyl > *iso*-propyl >*tert*-butyl. This was attributed to a relief of steric strain upon changing the geometry at sulfur from pyramidal to trigonal planar. It is interesting to note that the

trend in $\Delta H^{\ddagger}$ is methyl > ethyl >*iso*-propyl >*tert*-butyl , but the trend in $\Delta S^{\ddagger}$ is methyl < ethyl < *iso*-propyl < *tert*-butyl, which is the trend that would be expected based on the cyclohexane argument. The same trends are seen for the entropic and enthalpic contributions of *cis*-[$Mo(CO)_4(RSCH_3CH_2CH_2SR)$] as are being proposed for the present $Cp_2Zr(Cl)(SR)$ system.

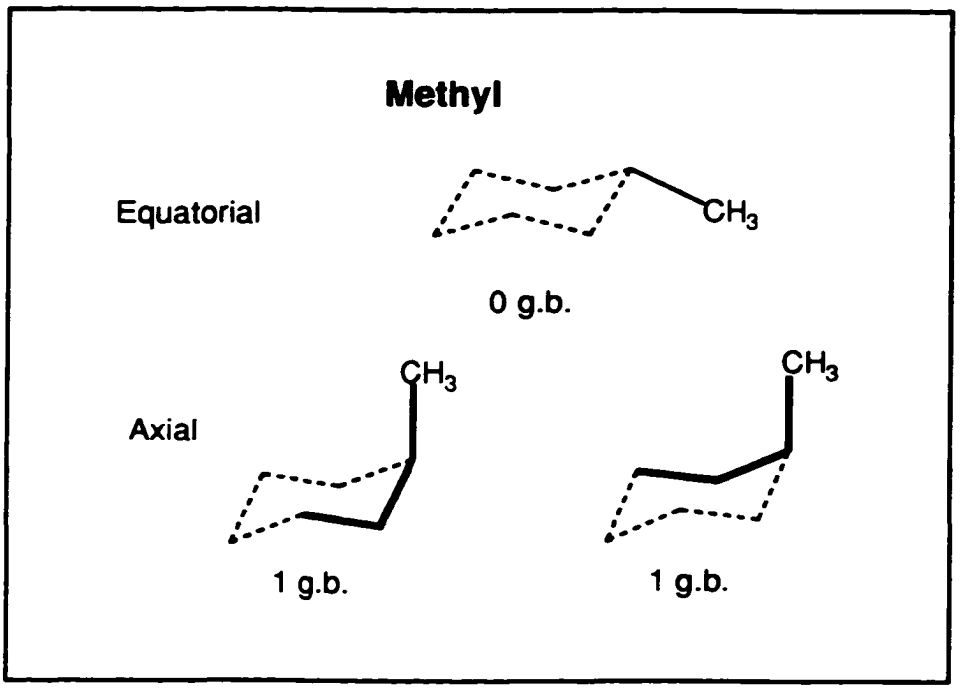

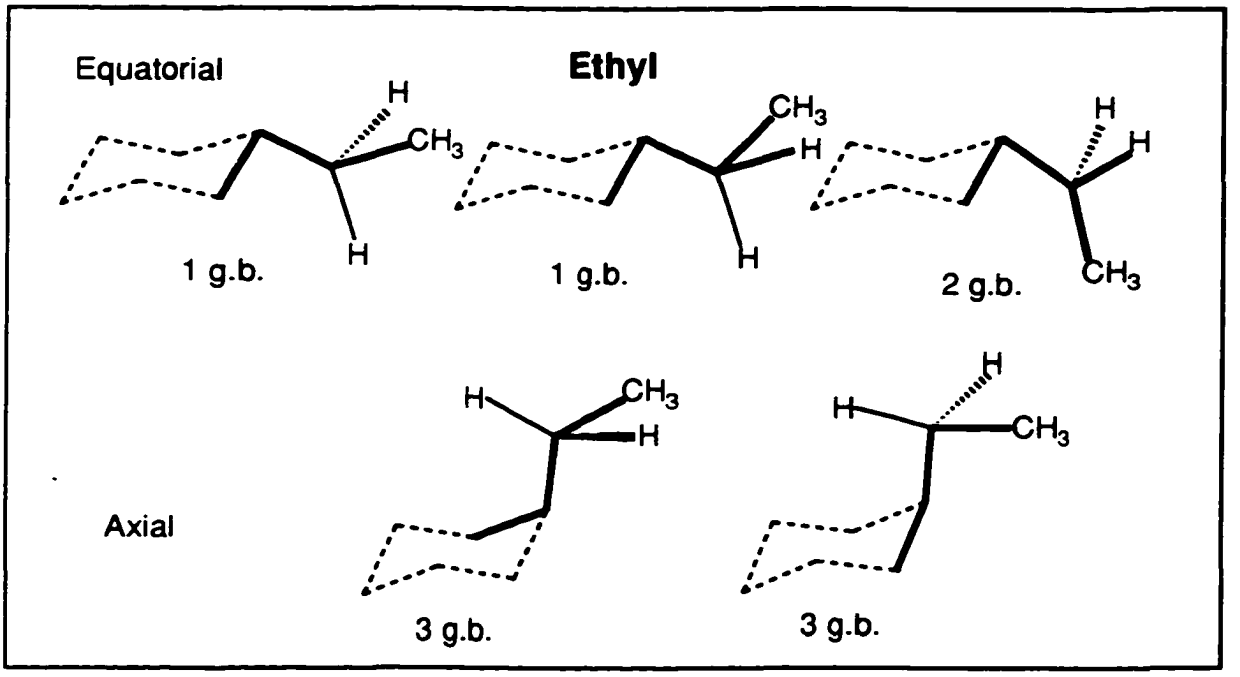

Figure 4.8. Possible axial and equatorial conformations of methyl and ethyl substituted cyclohexane. Gauche-butane interactions are shown in bold.

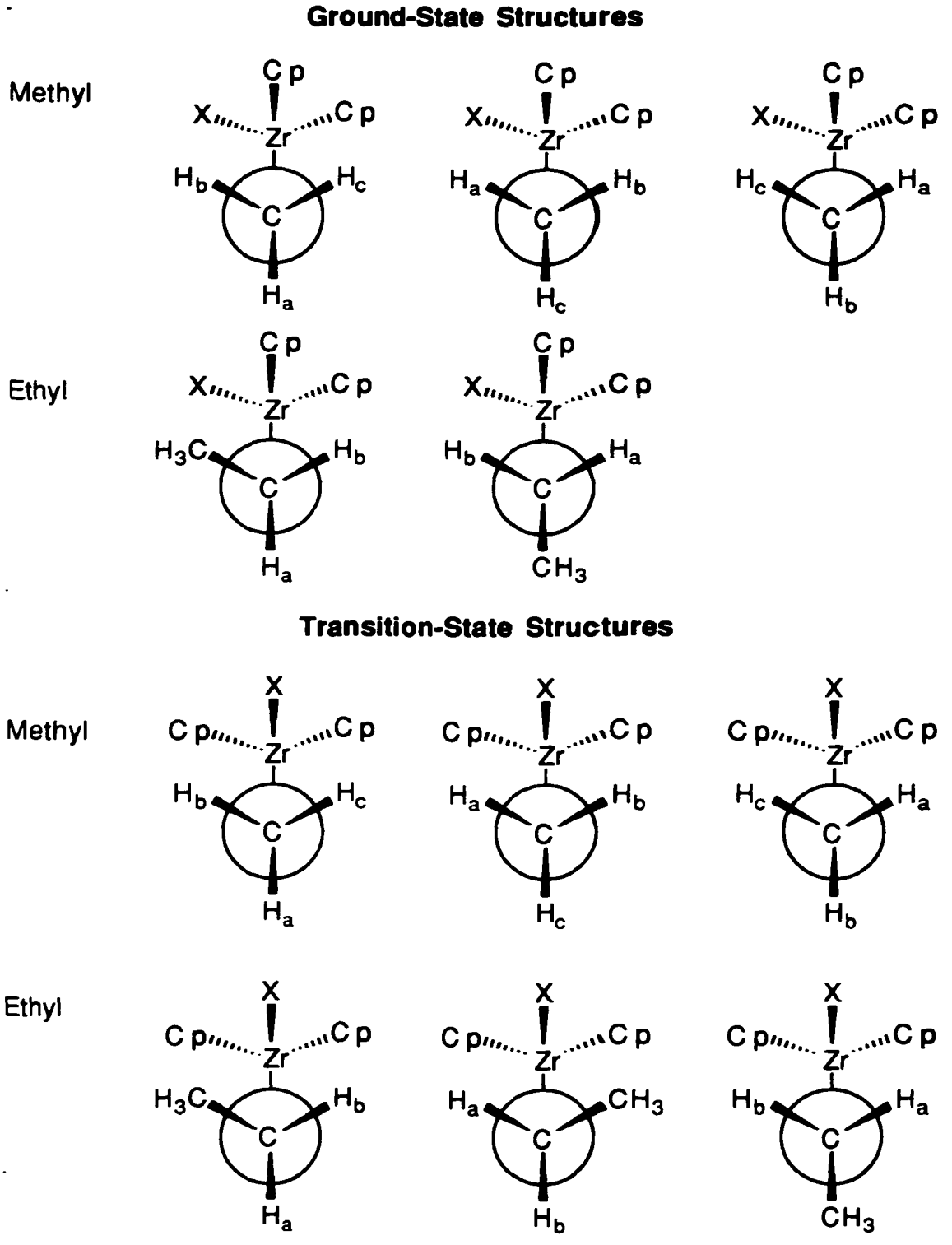

Figure 4.9. Possible ground-state and transition-state structures for $Cp_2Zr(Cl)(SR)$, R= Methyl, Ethyl.

The *ab initio* calculations which were carried out on the $Cp_2Zr(SR)(Cl)$ series using Gaussian methods help distinguish between the arguments presented above concerning the importance of the enthalpic and entropic contributions to the rotational barriers. The calculations showed an opposing trend of $\Delta H^{\ddagger}$ and $\Delta S^{\ddagger}$ for the methyl, ethyl and *iso*-propyl derivatives (Figure 4.7). The trend in $\Delta H^{\ddagger}$ is methyl > ethyl >*iso*-propyl , but the trend in $-\Delta S^{\ddagger}$ is methyl < ethyl < *iso*-propyl. From the magnitude of the enthalpic and entropic terms it is clearly seen that enthalpy is the dominant contributor to the rotational barrier about the M-S bond (Table 4.4). $\Delta H^{\ddagger}$ and $\Delta S^{\ddagger}$ both decrease from the *iso*-propyl to the *tert*-butyl derivative. This is reflected by a dramatic decrease in the rotational barrier. The M-S bond is much weaker for the *tert*-butyl derivative as well as fewer energetically accessible conformations. Metric parameters were calculated for ground-state and transition-state structures for the $Cp_2Zr(SR)(Cl)$ series (Table 4.5). Inspection of the data reveals that the origin of the dramatically lower enthalpic term originates from a difference in ground-state structure for the *tert*-butyl derivative. Figure 4.6 compares the trends of the ground-state and transition-state for the Zr-S bond lengths, Cl-Zr-S-C torsion angles and the Cp/Zr/Cp'-Cl/Zr/S dihedral angles. An irregular trend is observed for the *tert*-butyl derivative in the ground-state, but not in the transition-state (Figure 4.6). The steric repulsion between the bulky *tert*-butyl group and the Cp ligand is reflected in a longer Zr-S bond, and a much smaller Cl-Zr-S-C torsion angle and the Cp/Zr/Cp'-Cl/Zr/S dihedral angle. This results in a weaker Zr-S bond and a lower rotational barrier about the Zr-S bond. The Cl-Zr-S-C torsion angles are close to zero in the transition-state for all derivatives. In this conformation, the Mdπ-Spπ bonding interaction is minimized. In the rotational transition-state a significant lengthening of the Zr-S and Zr-Cp bonds are seen for the methyl, ethyl and *iso*-propyl derivatives, but the Zr-S and Zr-Cp bonds are shorter for the *tert*-butyl derivative (Table 4.5). It can be concluded from the calculated metric data that the lower rotational barrier is a result of a difference in ground-state structures.

Preliminary studies were undertaken with the hafnium derivatives. However, the rotational barriers of $Cp_2Hf(Cl)(SR)$ for R=Me,Et, and Ph were not significantly different from the zirconium derivatives. It is not understood why the hafnium rotational barrier would not show a KEE as in the case of $[M(bipy)_2(1,1'\text{-biiq})]^{2+}$ (M=Ru, Os). It is possible that the ground-state structures are not the same. X-ray crystal studies of the hafnium compounds would be helpful in answering this question. However, the hafnium dithiolate complexes were not synthesized and recrystallized. There are not identical zirconocene and hafnocene thiolate complexes in the literature. However, it may be useful to compare zirconium and hafnium complexes of pentamethylcylclopentadiene for which X-ray crystal structures have been solved. 1998, Yam published the crystal structures of $(\eta^5\text{-}C_5Me_5)_2Hf(SR)_2$ (R=^{n}Bu, C_6H_5).[146] In comparing these structures to $(\eta^5\text{-}C_5Me_5)_2Zr(SR)_2$ (R=^{n}Bu, C_6H_5), it is found that the M-S bond distances are slightly shorter for the hafnium derivatives than the zirconium derivatives. The S-M-S bond angles and the S-M-S-R torsion angles are also slightly more acute for the hafnium derivatives than the zirconium derivatives. Selected metric data are shown in Table 4.6. The shorter M-S bond lengths resulted in higher rotational barriers for the $Cp_2Zr(SR)(Cl)$ series. An inverse KEE would have been observed by a lower rotational barrier. The stronger third-row metal-sulfur bond should result in a higher barrier to rotation about the metal-sulfur bond. The Mdπ-Spπ bonding interaction is maximized in the ground-state and minimized in the transition-state. The Mdπ-Spπ orbitals are not completely misdirected due to a compromise between steric and electronic interactions. The Mdπ-Spπ bonding interaction would be ideally maximized at a R-S-M-S torsion angle of 90°, however the R-S-M-S torsion angle is approximately 60° in the $Cp_2Zr(SR)(Cl)$ complexes (Table 4.5) and $Cp_2Zr(SR)_2$ complexes (Table 4.3) and 50° in the $Cp^*M(SR)_2$ complexes (Table 4.6). Steric repulsions between the R group and the Cp ligand are very important in determining the extent of misdirection of the Mdπ-Spπ orbitals. The difference in

ground-state structures between the zirconium and hafnium derivatives could have cancelled out the KEE resulting in similiar rotational barriers for the CpM(Cl)(SR) compounds.

Table 4.6. Comparison of Zirconocene and Hafnocene Dithiolate Compounds

Compound	M-S	S-M-S	S-M-S-R	Reference
$Cp_2^*Zr(S^nBu)_2$	2.4987(8)	96.14	48.98	147
$Cp_2^*Hf(S^nBu)_2$	2.4761(9)	95.90(6)	48.17	146
$Cp_2^*Zr(SC_6H_6)_2$	2.522(1)	100.88	49.39	148
$Cp_2^*Hf(SC_6H_6)_2$	2.502(1)	100.52(5)	48.79	146

$Cp^*=\eta^5\text{-}C_5Me_5$

4.7 Summary

A series of $Cp_2Zr(Cl)(SR)$ (R=Methyl, ethyl, *iso*-propyl, *tert*-butyl) have been synthesized. Rotational barriers ($\Delta G^{\ddagger}$) about the Zr-S bond have been measured by ^1H NMR. For R=methyl, ethyl, and *iso*-propyl, the barriers are proportional to the steric demand of the ligand and the bond strength of the metal-sulfur bond at 32, 33, and 35 kJ $mole^{-1}$ respectively. A much lower barrier of 26 kJ $mole^{-1}$ was measured for R= *tert*-butyl. X-ray crystal structures were solved for $CpZr(SR)_2$ (R=methyl, ethyl, *iso*-propyl, *tert*-butyl). Nothing unusual was observed in these structures that would explain the lower rotational barrier for the *tert*-butyl derivative. *Ab initio* calculations carried out on $Cp_2Zr(Cl)(SR)$ (R=Methyl, ethyl, *iso*-propyl, *tert*-butyl) suggested that enthalpy was the dominant contributor to magnitude of the rotational barrier. A significantly lower enthalpic term was calculated for the *tert*-butyl derivative. Metric

parameters for the ground-state and transition-state structures were computed. Differences in the ground-state structure for the *tert*-butyl derivative suggest that the origin of the lower $\Delta H^{\ddagger}$ is due to a weaker M-S bond in the ground-state structure.

CHAPTER 5

EXPERIMENTAL DETAILS

5.1. Synthesis of Arene-Metal $[(\eta^6\text{-}C_6H_6)(M)(N\text{-}N)(X)]^+$ and Metal Bipyridine $[M(bipy)_2(N\text{-}N)]^{2+}$ Complexes (M=Ru(II), Os(II); X=Cl,I)

5.1.1 Materials and Sample Preparation

Acetone-d_6 was dried with molecular sieves and distilled before use. $Ru(bipy)_2Cl_2$, $[(\eta^6\text{-}C_6H_6)Ru(Cl)_2]_2$,[65] $[(\eta^6\text{-}C_6H_6)Ru(I)_2]_2$,[65] $[(\eta^6\text{-}C_6H_6)Os(Cl)_2]_2$,[93] $(\eta^6\text{-}C_6H_6)Os(NCCH_3)(Cl)_2$,[66] 1,1'-biphenyl-2,2'-diamine (dabp)[86] and 1,1'-biiq[59] were synthesized using literature methods. (S)-1,1'-binaphthyl-2,2'-diamine (dabn) was used as received from Aldrich. ^1H NMR spectra were recorded on a Varian XL-500 using residual acetone-d_5 (2.04 ppm) or methylene chloride-d (5.28 ppm) as an internal standard. The NMR samples were prepared in tubes that had been glass-blown onto Schlenk adapters. The solutions were freeze-pump thawed and the tubes were flame-sealed under vacuum. Combustion analyses were carried out by Midwest Microlab.

5.1.2. N-N = 2,2'diamino-biphenyl (dabp)

Synthesis of $[Ru(bipy)_2(dabp)](PF_6)_2$

$Ru(bipy)_2Cl_2$ (250 mg, 0.52 mmole), 1ml H_2O and 6 ml 95% ethanol were put into a 100 mL Schlenk flask. The solution was degassed, left under vacuum and placed in a 80° C oil bath for 1 hour. After cooling to room temperature dabp (95 mg, 0.52 mole) was added to the solution. The flask was put under vacuum and placed into a 80° C oil bath for 15 hours. The ethanol was removed by vacuum transfer and NH_4PF_6 (500 mg) was added to precipitate a bright red product. Crystals were obtained by vapor

diffusion of acetone and ether at room temperature. ^{1}H NMR: (methylene chloride-d_2, 500 MHz, 20°C): δ 8.46 (d, 2H, J = 8 Hz), 8.32 (d, 2H, J = 8 Hz), 8.29 (d, 2H, J = 5 Hz), 8.15 (t, 2H, J = 8 Hz), 7.87 (t, 2H, J = 8 Hz), 7.63 (d, 2H, J = 6 Hz), 7.55 (t, 2H, J = 8 Hz), 7.34 (m, 4H), 7.20 (t, 2H, J = 7 Hz), 6.97 (m, 4H), 5.90 (d, 2H, J = 8 Hz), 4.50 (br s, 4H).

Synthesis of $[(\eta^6\text{-}C_6H_6)Ru(dabp)(Cl)]PF_6$

$[(\eta^6\text{-}C_6H_6)Ru(Cl)_2]_2$ (144 mg, 0.29 mmol) and dabp (150 mg, 0.82 mmol) were dissolved in MeOH (20 mL). The resulting solution was freeze-pumped-thawed, left under vacuum, and the flask was placed in a 70 °C oil bath for 30 min. After cooling the solution to room temperature, excess NH_4PF_6 (500 mg) was added to precipitate the product. The resulting orange crystals were filtered, washed with MeOH, and dried under vacuum (213 mg, 0.39 mmol, 68 %). ^{1}H NMR: (acetone-d_6, 500 MHz, 20°C): δ 8.25 (br s, 1H, H_a), 7.84 (d, 1H, J = 8 Hz, H_3), 7.52 (t, 1H, J = 8 Hz, H_4), 7.47 (br s, 1H, H_c), 7.43 (br s, 1H, H_d), 7.38 (t, 1H, J = 8 Hz, H_5), 7.27 (m, 3H, $H_{4',5',6'}$), 7.10 (d, 1H, J = 8 $H_{6'}$), 7.02 (d, 1H, J = 8 Hz, $H_{3'}$), 5.92 (s, 6H, C_6H_6), 4.17 (br s, 1H, H_b); (acetone-d_6, 500 MHz, -88°C): δ 8.74 (d, 1H, J = 11 Hz, H_a), 7.95 (d, 1H, J = 11 Hz, H_d), 7.87 (d, 1H, J = 8 Hz, H_3), 7.76 (d, 1H, J = 11 Hz, H_c), 7.50 (t, 1H, J = 8 Hz, H_4), 7.37 (t, 1H, J = 8 Hz, H_5), 7.29 (t, 1H, J = 8 Hz, $H_{4'}$), 7.24 (m, 2H, $H_{5',6'}$), 7.04 (d, 1H, J = 8 Hz, $H_{6'}$), 6.94 (d, 1H, J = 8 Hz, $H_{3'}$), 5.91 (s, 6H, C_6H_6), 4.60 (d, 1H, J = 11 Hz, H_b). Anal. Calcd for $C_{19}H_{22}ClF_6N_2OPRu$ (**M=Ru**)·MeOH): C, 39.61; H, 3.85. Found: C, 38.68; H, 3.90. HRMS (FAB) *m/e* Calcd for M^+ ($C_{18}H_{18}IN_2Ru$): 399.0195. Found: 399.0215±0.013. The stoichiometry of methanol in the crystalline product was confirmed by ^{1}H NMR in CD_2Cl_2 and X-ray diffraction.

Synthesis of $[(\eta^6\text{-}C_6H_6)Os(dabp)(Cl)]PF_6$

$(\eta^6\text{-}C_6H_6)Os(NCCH_3)(Cl)_2$ (75 mg, 0.19 mmol) and dabp (56 mg, 0.30 mmol) were dissolved in MeOH (20 mL). The resulting solution was freeze-pumped-thawed, left under vacuum, and the flask was placed in a 70 °C oil bath for 20 h. After cooling the solution to room temperature, excess NH_4PF_6 (500 mg) was added, the volatiles were removed with a rotary evaporator, and the residue was dissolved in CH_2Cl_2. The resulting solution was filtered and the volatiles were removed under vacuum to afford (**M=Os**) as an brown solid (75 mg, 0.12 mmol, 60 %). ^{1}H NMR: (acetone-d_6, 500 MHz, 20°C): δ 8.72 (br s, 1H, H_a), 7.92 (br s, 1H, H_c), 7.77 (d, 1H, J = 8 Hz, H_3), 7.76 (br s, 1H, H_d), 7.52 (t, 1H, J = 8 Hz, H_4), 7.36 (m, 3H, $H_{4',5',5}$), 7.30 (d, 1H, J = 8, H_6), 7.20 (d, 1H, J = 8 Hz, $H_{6'}$), 7.15 (d, 1H, J = 8 Hz, $H_{3'}$), 6.21 (s, 1H, C_6H_6), 5.69 (br s, 1H, H_b); (acetone-d_6, 500 MHz, -90°C): δ 9.23 (br s, 1H, H_a), 8.32 (br s, 1H, H_d), 8.17 (br s, 1H, H_c), 7.78 (d, 1H, J = 8 Hz, H_3), 7.49 (t, 1H, J = 7 Hz, H_4), 7.33 (m, 3H, $H_{4',5',5}$), 7.26 (d, 1H, J = 7 Hz, H_6), 7.12 (d, 1H, J = 7 Hz, $H_{6'}$), 7.05 (d, 1H, J = 7 Hz, $H_{3'}$), 6.17 (s, 1H, C_6H_6), 6.15 (br s, 1H, H_b). The sample that was submitted for combustion analysis was recrystallized from acetone/ether. The stoichiometry of acetone in the crystalline product was confirmed by ^{1}H NMR in CD_2Cl_2. Anal. Calcd for $C_{21}H_{24}ClF_6N_2OPOs$ ((**M=Os**)•acetone): C, 36.58; H, 3.51. Found: C, 37.30; H, 3.51.

5.1.3 N-N = (S)-1,1'-binaphthyl-2,2'-diamine (dabn)

Synthesis of $[(\eta^6\text{-}C_6H_6)Ru(dabn)(Cl)]PF_6$

$[(\eta^6\text{-}C_6H_6)Ru(dabn)(Cl)]PF_6$was synthesized using a procedure analogous to the one that was used to synthesize $[(\eta^6\text{-}C_6H_6)Ru(dabp)(Cl)]PF_6$. (121 mg, 0.19 mmol, 65 %). ^{1}H NMR: (acetone-d_6, 500 MHz, 20°C): δ 8.44 (d, 1H, J = 9), 8.25 (q, 2H, J = 8), 8.10 (d, 1H, J = 8), 7.94 (m, 2H), 7.62 (d, 1H, J = 10 Hz), 7.54 (t, 1H, J = 8

Hz), 7.47 (m, 2H), 7.35 (m, 2H), 7.24 (t, 1H, J = 8 Hz), 6.98 (d, 1H, J = 8 Hz), 6.90 (d, 1H, J = 8), 5.96 (s, 6H), 4.37 (d, 1H, J = 10 Hz). Anal. Calcd for $C_{18}H_{18}ClF_6N_2PRu$: C, 48.49; H, 3.45. Found: C, 47.66; H, 3.50.

5.1.4 N-N = 1,1'-biisoquinoline (1,1'-biiq)

Synthesis of (η^6-benzene)(1,1'-biiq)(chloro)ruthenium(II) hexafluorophosphate

$[(\eta^6\text{-}C_6H_6)Ru(Cl)_2]_2$ (100 mg, 0.16 mmol) and 1,1'-biiq (150 mg, 0.59 mmol) were dissolved in MeOH (20 mL). The resulting solution was freeze-pumped-thawed, left under vacuum, and the flask was placed in a 70 °C oil bath for 30 min. After cooling the solution to room temperature, excess NH_4PF_6 (500 mg) was added to precipitate the product. The resulting yellow crystals were filtered, washed with MeOH, and dried under vacuum (215 mg, 87%). ^1H NMR: (acetone-d_6, 500 MHz, 20° C): δ 9.67 (d, $H_{3'}$, J = 6 Hz), 9.58 (d, H_3, J = 6 Hz), 8.39 (d, $H_{5'}$, J = 9 Hz), 8.38 (d, $H_{4'}$, J = 6 Hz), 8.34 (d, H_4, J = 6 Hz), 8.31 (d, H_5, J = 9 Hz), 7.13 (d, $H_{8'}$, J = 9 Hz), 8.08 (dd, $H_{6'}$, J = 8,9 Hz), 8.00 (dd, H_6, J = 8,9 Hz), 7.92 (d, H_8, J = 9 Hz), 7.82 (dd, $H_{7'}$, J = 8,9 Hz), 7.70 (dd, H_7, J = 8,9 Hz), 6.36(s, 6H, arene). HRMS (FAB) *m/e* Calcd for M^+ ($C_{24}H_{18}ClN_2Ru$): 471.0202. Found: 471.0176±0.026 (5 ppm error). Anal. Calcd for $C_{24}H_{18}ClF_6N_2PRu$: C, 46.80; H, 2.95. Found: C, 46.74; H, 3.11.

Synthesis of (η^6-benzene)(1,1'-biiq)(chloro)osmium(II) hexafluorophosphate

$(\eta^6\text{-}C_6H_6)Os(acetonitrile)Cl_2$ (75 mg, 0.19 mmole) and 1,1'-biiq (78 mg, 0.30 mmole) were mixed in degassed methanol (20mL). The reaction was freeze-pump-thawed, left under vacuum and put into a 70 °C oil bath for 20 hours. Excess NH_4PF_6 (500mg) was added to precipitate the product. The product was filtered, washed with ether and dried

under vacuum (81 mg, 60%).^{1}H NMR: (acetone-d_6, 500 MHz, 20° C): δ 9.64 (d, $H_{3'}$, J = 6 Hz), 9.62 (d, H_3, J = 6 Hz), 8.41 (d, $H_{5'}$, J = 9 Hz), 8.35 (d, H_5, J = 9 Hz), 8.34 (d, H_3, J = 6 Hz), 8.33 (d, $H_{3'}$, J = 6 Hz), 8.23 (d, $H_{8'}$, J = 9 Hz), 8.09 (dd, $H_{6'}$, J = 8,9 Hz), 8.08 (d, H_8, J = 9 Hz), 8.01 (dd, H_6, J = 8,9 Hz), 7.85 (dd, $H_{7'}$, J = 8,9 Hz), 7.77 (dd, H_7, J = 8,9 Hz), 6.50 (s, 6H, arene). HRMS (FAB) *m/e* Calcd for M^+ ($C_{24}H_{18}ClN_2Os$): 561.0773. Found: 561.0752±0.021 (5 ppm error). Anal. Calcd for $C_{24}H_{18}ClF_6N_2POs$: C, 40.89; H, 2.58. Found: C, 40.35; H, 2.61.

Synthesis of (η^6-benzene)(1,1'-biiq)(iodo)ruthenium(II) hexafluorophosphate

$[(\eta^6\text{-}C_6H_6)RuI_2]_2$ (82 mg, 0.10 mmole) and 1,1'-biiq (25 mg, 0.10 mmole) were dissolved in MeOH (20 mL). The resulting solution was freeze pump-thawed, left under vacuum and put into a 70 °C oil bath for 1 hour. After cooling to room temperature, excess NH_4PF_6(500 mg) was added to precipitate the product. The resulting red product was filtered and dried under vacuum (27 mg, 84%). ^{1}H NMR: (acetone-d_6, 500 MHz, 20° C): δ 9.58 (d, $H_{3'}$, J = 6 Hz), 9.55 (d, H_3, J = 6 Hz), 8.39 (d, $H_{5'}$, J = 9 Hz), 8.34 (d, $H_{4'}$, J = 6 Hz), 8.30 (d, H_5, J = 9 Hz), 8.28 (d, H_4, J = 6 Hz), 8.13 (d, $H_{8'}$, J = 9 Hz), 8.06 (dd, $H_{6'}$, J = 8,9 Hz), 8.00 (dd, H_6, J = 8,9 Hz), 7.95 (d, H_8, J = 9 Hz), 7.82 (dd, $H_{7'}$, J = 8,9 Hz), 7.71 (dd, H_7, J = 8,9 Hz), 6.43 (s, 6H, arene). HRMS (FAB) *m/e* Calcd for M^+ ($C_{24}H_{18}IN_2Ru$): 562.9558. Found: 562.9562±0.004 (1 ppm error).

Synthesis of $[(\eta^6\text{-}C_6H_6)OsI_2]_2$

The following procedure is essentially the same as that previously used to synthesize $[(\eta^6\text{-}C_6H_6)RuI_2]_2$. $[(\eta^6\text{-}C_6H_6)OsCl_2]_2$ (93 mg, 0.14 mmole) was dissolved in 95% EtOH by stirring for 2 hours. Excess NaI (500 mg) was added and the resulting

solution was stirred overnight. The brown precipitate was filtered washed with water and dried under vacuum (77mg). The product was used without further purification .

Synthesis of (η^6-benzene)(1,1'-biiq)(iodo)osmium(II)hexafluorophosphate

$[(\eta^6\text{-}C_6H_6)OsI_2]_2$ (77 mg, 0.07 mmole) and 1,1'-biiq (35 mg, 0.14 mmole) were dissolved in acetonitrile (20 mL). The resulting solution was freeze-pump thawed, left under vacuum, and put into a 70 °C oil bath for 19 hours. After cooling to room temperature, excess NH_4PF_6 (500 mg) was added, and the solvent removed under vacuum. The residue was dissolved in CH_2Cl_2 and filtered to remove a white impurity. The CH_2Cl_2 was removed on a roatry evaporator and the red product dried under vacuum. Yield: (66 mg, 56%). ^{1}H NMR: (acetone-d_6, 500 MHz, 20° C): δ 9.57 (d, $H_{3'}$, J = 6 Hz), 9.54 (d, H_3, J = 6 Hz), 8.38 (d, $H_{5'}$, J = 9 Hz), 8.32 (d, H_5, J = 9 Hz), 8.25 (d, 2H, $H_{4,4'}$, J = 6 Hz), 8.21 (d, $H_{8'}$, J = 9 Hz), 8.07 (d, H_8, J = 9 Hz), 8.03 (dd, $H_{6'}$, J = 8,9 Hz), 7.98 (dd, H_6, J = 8,9 Hz), 7.83 (dd, $H_{7'}$, J = 8,9 Hz), 7.75 (dd, H_7, J = 8,9 Hz), 6.55 (s, 6H, arene). HRMS (FAB) *m/e* Calcd for M^+ ($C_{24}H_{18}IN_2Os$): 653.0130. Found: 653.0101±0.029 (4 ppm error).

5.2 X-Ray Crystallography Studies of Arene-Metal $[(\eta^6\text{-}C_6H_6)(M)(N\text{-}N)(X)]^+$ and Metal Bipyridine $[M(bipy)_2(N\text{-}N)]^{2+}$ Complexes (M=Ru(II), Os(II); X=Cl)

Using Mo K_α radiation (0.71073 Å), θ/2θ data sets were collected at –85 °C with a Siemens P4 four-circle diffractometer. Three check reflections were collected after every 97 scans. Only random variation in the intensities of the check reflections was observed. The data were corrected for Lorentz and polarization effects and semi-empirical absorption corrections were applied. [149] SHELXTL was used for structure

solution and refinement.[150] The structures were solved by the heavy atom method and were refined by full matrix least-squares on F^2 using all of the reflections.

5.2.1. N-N = 2,2'diamino-biphenyl (dabp)

X-Ray crystal structure of $[Ru(bipy)_2(dabp)](PF_6)_2$

Thin plates of X-ray quality crystals were obtained by vapor diffusion of ether into a saturated acetone solution at room temperature. Crystallographic solution and refinement procedures are summarized in Table 5.1. The aromatic hydrogen atoms were refined with idealized parameters. Because of the plate-like nature of the crystal, diffraction data were generally weak, which necessitated slow scan speeds that ultimately resulted in somewhat higher random errors in the data. The systematic absences and intensity statistics suggested the non-centric space group Cc, and initially the structure was solved and refined in that space group. However, the refinement was unstable, the thermal parameters of several atoms became non-positive definite during the final refinement cycles, and the final metric data were chemically unreasonable. The structure was then solved and refined in the centric space group C2/c and converged properly. In the final cycles, all the non-hydrogen atoms were refined with anisotropic displacement parameters and the hydrogens were included with idealized parameters. The cation exhibits crystallographically-imposed two-fold symmetry and as a consequence each asymmetry unit contains half of the cation and one PF_6^- anion, and the Ru atom resides on a special position along the two-fold axis. The atomic coordinates are listed in Table 5.2. The anisotropic dispacement parameters are in Table 5.3. The hydrogen coordinates are in Table 5.4.

Table 5.1. Crystal data for Compound $[Ru(bipy)_2(dabp)](PF_6)_2$

formula	$C_{32}H_{28}F_{12}N_6P_2Ru$
fw	887.61
space group	C2/c
cryst syst	monoclinic
a, Å	19.530(3)
b, Å	9.289(2)
c, Å	19.636(3)
V, Å^3	3399.1(9)
T, K	188(2)
Z	4
D_{calc}, g·mL^{-1}	1.735
μ, mm^{-1}	0.657
cryst size, mm^3	0.22 x 0.12 x 0.04
Ind. reflections	3036
Θ Range (deg)	2.17-25.0
Final R indices	
[I>2σ(I)]	R1 = 0.0595
	wR2 = 0.1042
R indices [all data	
used in refinement]	R1 = 0.1124
	wR2 = 0.1235
GOF	1.053

Table 5.2. Atomic Coordinates and Equivalent Isotropic Displacement Parameters for $[Ru(bipy)_2(dabp)]^{2+}$. U(eq) is Defined as 1/3 of the Trace of the Orthogonalized U_{ij} Tensor

atom	x	y	z	U_{eq}
Ru(1)	0.0	0.8700(1)	0.2500(3)	0.0020(1)
N(1)	0.0370(3)	1.0170(5)	0.1913(2)	0.0022(1)
N(2)	-0.0873(2)	0.8867(6)	0.1590(2)	0.0023(1)
N(3)	0.0452(2)	0.7056(5)	0.1990(3)	0.0024(1)
C(1)	0.1019(3)	1.0816(7)	0.2117(3)	0.0029(2)
C(2)	0.1238(3)	1.1758(7)	0.1689(3)	0.0034(2)
C(3)	0.0787(3)	1.2056(8)	0.1016(4)	0.0040(2)
C(4)	0.0134(3)	1.1405(8)	0.0801(3)	0.0036(2)
C(5)	-0.0074(3)	1.0469(6)	0.1251(3)	0.0024(1)
C(6)	-0.0778(3)	0.9760(7)	0.1075(3)	0.0025(2)
C(7)	-0.1322(3)	0.9990(7)	0.00442(3)	0.0033(2)
C(8)	-0.1986(3)	0.9335(7)	0.0337(3)	0.0034(2)
C(9)	-0.2077(3)	0.8445(7)	0.0864(3)	0.0032(2)
C(10)	-0.1520(3)	0.8223(7)	0.1468(3)	0.0031(2)
C(11)	-0.0379(3)	0.5910(7)	0.0940(3)	0.0033(2)
C(12)	-0.0895(3)	0.4868(7)	0.0640(3)	0.0031(2)
C(13)	-0.1067(3)	0.3851(8)	0.1068(3)	0.0037(2)
C(14)	-0.0708(3)	0.3818(8)	0.1797(3)	0.0034(2)
C(15)	-0.191(3)	0.4855(6)	0.2103(3)	0.0025(1)
C(16)	-0.0039(3)	0.5917(6)	0.1674(3)	0.0024(2)
P(1)	0.2004(1)	1.2542(2)	0.6285(1)	0.0032(1)
F(1)	0.1684(2)	1.4112(5)	0.6302(2)	0.0057(1)
F(2)	0.2292(2)	1.0947(4)	0.6262(2)	0.0054(1)
F(3)	0.1947(2)	1.2260(5)	0.7074(2)	0.0054(1)
F(4)	0.2040(2)	1.2796(5)	0.5497(2)	0.0048(1)
F(5)	0.1185(2)	1.1958(5)	0.5958(2)	0.0046(1)
F(6)	0.2798(2)	1.3125(5)	0.6608(2)	0.0049(1)

Table 5.3. Anisotropic Displacement Parameters for $[Ru(bipy)_2(dabp)]^{2+}$. The Anisotropic Displacement Factor Exponent Takes the Form: $-2\pi^2 [h^2 a^2 U11 + ... + 2 h k a b U12]$

atom	U11	U22	U33	U23	U13	U12
Ru(1)	0.0023(1)	0.0019(1)	0.0018(1)	0.0	0.0004(1)	0.0
N(1)	0.0027(3)	0.0020(3)	0.0018(2)	0.0003(2)	0.0006(2)	-0.0002(2)
N(2)	0.0020(2)	0.0023(3)	0.0023(2)	-0.0005(2)	0.0004(2)	0.0001(2)
N(3)	0.0023(3)	0.0024(3)	0.0025(3)	0.0001(2)	0.0007(2)	-0.0005(2)
C(1)	0.0031(3)	0.0031(4)	0.023(3)	-0.0001(3)	0.0006(3)	-0.0002(3)
C(2)	0.0037(4)	0.0030(4)	0.0037(4)	-0.0004(3)	0.0015(3)	-0.0009(3)
C(3)	0.0041(4)	0.0044(4)	0.0037(4)	0.0007(3)	0.0016(3)	-0.0010(4)
C(4)	0.0042(4)	0.0031(4)	0.0031(3)	0.0012(3)	0.0008(3)	0.0004(4)
C(5)	0.0029(3)	0.0024(4)	0.0024(3)	-0.0001(3)	0.0014(3)	0.0003(3)
C(6)	0.0031(3)	0.0022(3)	0.0021(3)	-0.0004(3)	0.0005(3)	0.0006(3)
C(7)	0.0038(4)	0.0031(4)	0.0027(3)	0.0005(3)	0.0005(3)	0.0003(3)
C(8)	0.0028(3)	0.0037(4)	0.0030(4)	-0.0003(3)	-0.0002(3)	0.0004(3)
C(9)	0.0029(3)	0.0036(4)	0.0029(3)	-0.0007(3)	0.0003(3)	-0.0003(3)
C(10)	0.0024(3)	0.0032(4)	0.0035(4)	0.0002(3)	0.0008(3)	-0.0003(3)
C(11)	0.0037(4)	0.0033(4)	0.0029(3)	0.0008(3)	0.0010(3)	0.0001(3)
C(12)	0.0034(4)	0.0034(4)	0.0024(3)	-0.0009(3)	0.0007(3)	-0.0002(3)
C(13)	0.0040(4)	0.0035(4)	0.0036(4)	-0.0006(4)	0.0010(3)	-0.0017(4)
C(14)	0.0041(4)	0.0026(4)	0.0039(4)	-0.0004(3)	0.0020(3)	-0.0008(4)
C(15)	0.0030(3)	0.0020(3)	0.0029(3)	0.0002(3)	0.0014(3)	0.0003(3)
C(16)	0.0019(3)	0.0024(4)	0.0032(3)	-0.0005(3)	0.0010(3)	-0.0002(3)
P(1)	0.0025(1)	0.0043(1)	0.0027(1)	-0.0004(1)	0.0007(1)	-0.0001(1)
F(1)	0.0057(3)	0.0048(3)	0.0065(3)	-0.0010(2)	0.0016(2)	0.0009(2)
F(2)	0.0052(2)	0.0044(3)	0.0068(3)	-0.0001(2)	0.0023(2)	0.0006(2)
F(3)	0.0042(2)	0.0090(4)	0.0031(2)	0.0001(2)	0.0013(2)	0.000(2)
F(4)	0.0046(2)	0.0068(3)	0.0031(2)	-0.0001(2)	0.0013(2)	-0.0008(2)
F(5)	0.0030(2)	0.0068(3)	0.0041(2)	-0.0019(2)	0.0014(2)	-0.0011(2)
F(6)	0.0028(2)	0.0071(3)	0.0045(2)	-0.0020(2)	0.0006(2)	-0.0016(2)

Table 5.4. Hydrogen Coordinates and Equivalent Isotropic Displacement Parameters for $[Ru(bipy)_2(dabp)]^{2+}$. U(eq) is Defined as 1/3 of the Trace of the Orthogonalized U_{ij} Tensor

atom	x	y	z	U_{eq}
H(3A)	0.0610(2)	0.7477(5)	0.1641(3)	0.029
H(3B)	0.0844(2)	0.6664(5)	0.2323(3)	0.029
H(1A)	0.1337(3)	1.0608(7)	0.2577(3)	0.034
H(2A)	0.1697(3)	1.2201(7)	0.1854(3)	0.041
H(3C)	0.0929(3)	1.2703(8)	0.0710(4)	0.048
H(4A)	-0.0182(3)	1.1594(8)	0.0337(3)	0.043
H(7A)	-0.1240(3)	1.0591(7)	0.0083(3)	0.040
H(8A)	-0.2368(3)	0.9498(7)	-0.0088(3)	0.041
H(9A)	-0.2526(3)	0.7988(7)	0.0808(3)	0.039
H(10A)	-0.1590(3)	0.7585(7)	0.1820(3)	0.037
H(11A)	-0.0259(3)	0.6615(7)	0.0645(3)	0.040
H(12A)	-0.1128(3)	0.4863(7)	0.0141(3)	0.037
H(13A)	-0.1432(3)	0.3165(8)	0.0867(3)	0.045
H(14A)	-0.0816(3)	0.3087(8)	0.2087(3)	0.040

X-Ray crystal structure of $[(\eta^6\text{-}C_6H_6)Ru(dabp)(Cl)](PF_6)$

Diffraction quality crystals were grown from the reaction mixture. The asymmetric unit contains one $[(\eta^6\text{-}C_6H_6)Ru(dabp)Cl]^+$ cation, one PF_6^- anion, and a methanol solvent molecule. One of the fluorine atoms (F_3) of the PF_6^- anion and the oxygen atom of the methanol solvent molecule may exhibit weak H-bond contact with one of the nitrogen atoms (N) of the cation. Crystallographic solution and refinement procedures are summarized in Table 5.5. Atomic coordinates are listed in Table 5.6. Anisotropic displacement parameters are in Table 5.7. Hydrogen coordinates are listed in Table 5.8.

Table 5.5. Crystal Data for Compound $[(\eta^6\text{-}C_6H_6)Ru(dabp)(Cl)]^+$

formula	$C_{19}H_{22}ClF_6N_2OPRu$
fw	575.88
space group	$P2_12_12_1$
cryst syst	orthorhombic
a, Å	9.9001(13)
b, Å	11.099(2)
c, Å	19.462(2)
V, Å^3	2138.6(5)
T, K	188(2)
Z	4
D_{calc}, g·mL^{-1}	1.79
μ, mm^{-1}	1.00
cryst size, mm^3	0.18 x 0.26 x 0.26
Ind. reflections	2327
Θ Range (deg)	2.09-25.01
Final R indices	
[I>2σ(I)]	R1 = 0.0457
	wR2 = 0.1156
R indices [all data	
used in refinement]	R1 = 0.0508
	wR2 = 0.1291
GOF	1.139

Table 5.6. Atomic Coordinates and Equivalent Isotropic Displacement Parameters for $[(\eta^6\text{-}C_6H_6)Ru(dabp)(Cl)]^+$ U(eq) is Defined as 1/3 of the Trace of the Orthogonalized U_{ij} Tensor

atom	x	y	z	U_{eq}
Ru	0.84708(6)	0.78334(5)	0.38427(3)	0.0195(2)
Cl	1.0495(2)	0.8290(2)	0.44826(9)	0.0262(4)
N	0.7407(7)	0.8882(6)	0.4614(3)	0.021(3)
N'	0.8817(7)	0.9573(6)	0.3363(3)	0.023(4)
C1	0.6594(9)	1.0739(7)	0.4061(4)	0.025(2)
C2	0.6333(7)	0.9619(7)	0.4342(4)	0.023(2)
C3	0.5003(8)	0.9164(8)	0.4347(4)	0.028(2)
C4	0.3965(9)	0.9842(9)	0.4074(5)	0.034(2)
C5	0.4229(8)	1.0984(8)	0.3787(5)	0.034(2)
C6	0.5528(8)	1.1414(8)	0.3803(5)	0.032(2)
C1'	0.8004(9)	1.1242(7)	0.4073(4)	0.026(2)
C2'	0.9058(8)	1.0660(7)	0.3750(4)	0.023(2)
C3'	1.0375(8)	1.1140(7)	0.3777(4)	0.028(2)
C4'	1.0603(9)	1.2190(9)	0.4116(5)	0.036(2)
C5'	0.9572(9)	1.2788(8)	0.4443(4)	0.033(2)
C6'	0.824(1)	1.2326(8)	0.4416(4)	0.032(2)
C1''	0.822(1)	0.7091(8)	0.2824(4)	0.037(2)
C2''	0.6933(9)	0.714(1)	0.3136(5)	0.037(2)
C3''	0.6769(9)	0.6609(8)	0.3793(5)	0.037(2)
C4''	0.786(1)	0.5988(8)	0.4107(5)	0.036(2)
C5''	0.909(1)	0.5967(7)	0.3790(5)	0.036(2)
C6''	0.9313(9)	0.6482(8)	0.3148(5)	0.033(2)
P	0.6653(3)	1.0019(2)	0.1496(2)	0.0364(6)
F1	0.552(1)	1.031(1)	0.2027(5)	0.104(4)
F2	0.781(1)	0.977(1)	0.0938(5)	0.107(4)
F3	0.778(1)	1.029(3)	0.2037(6)	0.126(5)
F4	0.555(1)	0.9736(9)	0.0949(6)	0.114(4)
F5	0.6687(8)	0.8658(6)	0.1728(4)	0.076(2)
F6	0.6602(9)	1.1393(6)	0.1251(4)	0.073(2)
C1S	1.241(1)	0.855(2)	0.2389(5)	0.063(4)
O1S	1.147(1)	0.871(1)	0.2887(5)	0.085(3)

Table 5.7. Anisotropic Displacement Parameters for $[(\eta^6\text{-}C_6H_6)Ru(dabp)(Cl)]^+$ The Anisotropic Displacement Factor Exponent Takes the Form: $-2\pi^2 [h^2 a^2 U11 + ... + 2 h k a b U12]$

atom	U11	U22	U33	U23	U13	U12
Ru	0.0170(3)	0.0230(3)	0.0184(3)	-0.0001(2)	-0.0002(3)	-0.0008(3)
Cl	0.0202(8)	0.0323(9)	0.0262(9)	0.0028(8)	-0.0053(8)	-0.0003(8)
N	0.017(3)	0.032(3)	0.014(3)	0.001(3)	0.002(2)	0.001(3)
N'	0.020(3)	0.027(3)	0.024(3)	0.001(3)	0.000(3)	-0.001(3)
C1	0.022(4)	0.029(4)	0.023(3)	-0.002(3)	0.000(4)	0.008(4)
C2	0.009(4)	0.039(4)	0.021(3)	0.003(3)	0.002(3)	0.003(3)
C3	0.017(4)	0.041(5)	0.027(4)	0.006(4)	0.003(3)	-0.006(4)
C4	0.010(3)	0.052(5)	0.039(5)	0.009(4)	-0.001(4)	-0.002(4)
C5	0.016(4)	0.044(5)	0.041(5)	0.010(5)	-0.010(4)	0.004(4)
C6	0.019(4)	0.040(4)	0.036(4)	0.004(4)	0.007(4)	-0.003(4)
C1'	0.024(4)	0.026(4)	0.028(4)	0.009(3)	-0.003(3)	0.002(3)
C2'	0.025(4)	0.023(3)	0.022(4)	0.007(3)	-0.001(3)	0.004(3)
C3'	0.023(4)	0.030(4)	0.030(4)	0.005(4)	0.007(4)	-0.002(4)
C4'	0.031(4)	0.040(5)	0.037(4)	0.003(4)	-0.005(4)	-0.007(5)
C5'	0.032(4)	0.029(4)	0.038(4)	0.007(4)	-0.003(4)	-0.013(4)
C6'	0.035(5)	0.026(4)	0.034(4)	-0.001(4)	0.003(4)	-0.006(4)
C1''	0.050(6)	0.035(4)	0.025(4)	-0.017(4)	-0.004(4)	-0.002(5)
C2''	0.022(4)	0.050(5)	0.039(4)	-0.011(5)	-0.011(4)	-0.004(5)
C3''	0.038(5)	0.039(4)	0.033(4)	-0.018(4)	0.002(4)	-0.015(4)
C4''	0.053(6)	0.027(4)	0.029(4)	-0.003(4)	-0.001(4)	-0.004(4)
C5''	0.055(6)	0.020(3)	0.035(5)	-0.003(4)	-0.012(5)	0.002(4)
C6''	0.021(4)	0.035(4)	0.043(5)	-0.015(4)	0.000(4)	0.005(4)
P	0.030(1)	0.044(1)	0.034(1)	0.001(1)	-0.003(1)	0.003(1)
F1	0.088(6)	0.108(7)	0.117(8)	0.031(6)	0.062(6)	0.030(6)
F2	0.129(9)	0.109(7)	0.083(6)	0.035(6)	0.063(6)	0.061(7)
F3	0.096(7)	0.184(12)	0.099(7)	0.066(8)	-0.069(6)	-0.068(8)
F4	0.122(9)	0.084(6)	0.135(9)	-0.007(6)	-0.084(8)	0.000(6)
F5	0.065(5)	0.062(4)	0.100(6)	0.032(4)	0.017(5)	0.019(4)
F6	0.090(5)	0.045(3)	0.086(5)	0.006(4)	-0.004(6)	0.000(4)
C1S	0.09(1)	0.065(7)	0.032(5)	-0.003(5)	0.027(6)	0.014(8)
O1S	0.061(6)	0.096(7)	0.097(7)	0.004(6)	0.040(6)	0.007(7)

Table 5.8. Hydrogen Coordinates and Equivalent Isotropic Displacement Parameters for $[(\eta^6\text{-}C_6H_6)Ru(dabp)(Cl)]^+$. U(eq) is Defined as 1/3 of the Trace of the Orthogonalized U_{ij} Tensor

atom	x	y	z	U_{eq}
HA	0.7051(7)	0.8365(6)	0.4936(3)	0.026
HB	0.8018(7)	0.9372(6)	0.4835(3)	0.026
HD	0.9544(7)	0.9479(6)	0.3074(3)	0.028
HC	0.8080(7)	0.9722(6)	0.3088(3)	0.028
H3	0.4823(8)	0.8393(8)	0.4538(4)	0.034
H4	0.3069(9)	0.9538(9)	0.4080(5)	0.041
H5	0.3524(8)	1.1446(8)	0.3587(5)	0.040
H6	0.5704(8)	1.2200(8)	0.3631(5)	0.038
H3'	1.1100(8)	1.0731(7)	0.3558(4)	0.033
H4'	1.1490(9)	1.2515(9)	0.4128(5)	0.043
H5'	0.9752(9)	1.3512(8)	0.4687(4)	0.040
H6'	0.752(1)	1.2748(8)	0.4630(4)	0.038
H1''	0.836(1)	0.7466(8)	0.2392(4)	0.044
H2''	0.6198(9)	0.75321)	0.2913(5)	0.044
H3''	0.5925(9)	0.6665(8)	0.4023(5)	0.044
H4''	0.773(1)	0.5591(8)	0.4535(5)	0.043
H5''	0.983(1)	0.5586(7)	0.4016(5)	0.044
H6''	1.0171(9)	0.6428(8)	0.2931(5)	0.040
H1SA	1.2047(3)	0.881(8)	0.1945(9)	0.095
H1SB	1.266(7)	0.770(1)	0.236(3)	0.095
H1SC	1.322(4)	0.903(6)	0.249(2)	0.095
H1	1.073(4)	0.89(1)	0.2706(8)	0.102

5.2.2 N-N = 1,1'-biisoquinoline (1,1'-biiq)

X-Ray crystal structures of $[(\eta^6\text{-}C_6H_6)M(1,1'\text{-biiq})(Cl)](PF_6)$ (M=Ru(II),Os(II))

A Siemens P4 four-circle diffractometer was used to collect a $\theta/2\theta$ data set at 188 K (M=Ru) and 173 K (M=Os) using Mo K_α radiation (0.71073 Å).[150] The data were corrected for Lorentz and polarization effects and an empirical absorption correction based on psi-scans was applied.[149] The structure was solved by the heavy atom method using the Siemens SHELXTL system, and refined by full-matrix least squares of F^2 using all of the reflections.[150] All of the non-hydrogen atoms were refined anisotropically and all of the hydrogen atoms were included in the refinement at geometrically idealized positions with fixed temperature factors. Disorder of the arene ligand (M=Ru) was adequately treated with a two-site model with equal occupancy. Crystallographic solution and refinement procedures are summarized in Table 5.9 (M=Ru,Os). Atomic coordinates, anisotropic displacement parameters, and hydrogen coordinates are listed in Tables 5.10 - 5.12 (M=Ru) and Tables 5.13 - 5.15 (M=Os).

Table 5.9. Crystal Data for Compounds $[(\eta^6\text{-}C_6H_6)M(1,1'\text{-biiq})(Cl)](PF_6)$

	M=Ru	M=Os
formula	$C_{24}H_{18}ClF_6N_2PRu$	$C_{24}H_{18}ClF_6N_2POs$
fw	615.89	705.02
space group	P_1	P_1
cryst syst	Triclinic	Triclinic
a, Å	9.9564(7)	9.9798(1)
b, Å	10.9510(7)	10.9302(9)
c, Å	11.2730(11)	11.264(2)
α, deg	102.009(7)	101.98(1)
β, deg	93.963(7)	94.186(9)
γ, deg	110.276(6)	110.157(7)
V, Å^3	1114.3(2)	1114.2(2)
T, K	188(2)	173(2)
Z	2	2
D_{calc}, mg·cm^{-3}	1.836	2.101
μ, mm^{-1}	1.963	5.981
cryst size, mm^3	0.32 x 0.64 x 0.32	0.12 x 0.34 x 0.32
Ind. reflections	4795	4301
θ Range (°)	1.87-26.99	1.87-26.00
Final R indices		
[I>2σ(I)]	R1 = 0.0281	R1 = 0.0256
	wR2 = 0.0758	wR2 = 0.0636
R indices [all data used in	R1 = 0.0294	R1 = 0.0286
refinement]	wR2 = 0.0787	wR2 = 0.0659
GOF	1.109	1.056

Table 5.10. Atomic Coordinates and Equivalent Isotropic Displacement Parameters for $[(\eta^6\text{-}C_6H_6)Ru(1,1'\text{-biiq})(Cl)](PF_6)$. U(eq) is Defined as 1/3 of the Trace of the Orthogonalized U_{ij} Tensor

atom	x	y	z	U_{eq}
Ru	-0.0995(1)	-0.3334(1)	-0.2008(1)	0.021(1)
Cl	-0.0936(1)	-0.2845(1)	-0.3976(1)	0.026(1)
N	-0.2704(2)	-0.5069(2)	-0.2993(2)	0.022(1)
N'	0.0017(2)	-0.4673(2)	-0.2628(2)	0.022(1)
C1''	-0.0644(5)	-0.3232(4)	-0.0079(3)	0.053(1)
C2''	0.0592(4)	-0.2259(4)	-0.0334(4)	0.055(1)
C3''	0.0436(4)	-0.1324(4)	-0.0942(4)	0.050(1)
C4''	-0.0957(5)	-0.1317(3)	-0.1214(3)	0.042(1)
C5''	-0.2145(4)	-0.2230(3)	-0.0910(3)	0.036(1)
C6''	-0.1976(5)	-0.3200(4)	-0.0359(3)	0.046(1)
C1'''	-0.100(1)	-0.3430(8)	-0.0028(7)	0.054(3)
C2'''	0.033(1)	-0.2713(7)	-0.0215(6)	0.040(2)
C3'''	0.0683(8)	-0.1606(8)	-0.0700(7)	0.039(2)
C4'''	-0.044(1)	-0.1233(8)	-0.1129(8)	0.056(3)
C5'''	-0.188(1)	-0.1930(9)	-0.1028(7)	0.048(2)
C6'''	-0.2169(8)	-0.309(1)	-0.0499(8)	0.052(2)
C3	-0.4073(2)	-0.5085(2)	-0.3232(2)	0.026(1)
C4	-0.5078(2)	-0.6037(2)	-0.4152(2)	0.027(1)
C4a	-0.4677(2)	-0.6973(2)	-0.4959(2)	0.025(1)
C5	-0.5625(2)	-0.7863(2)	-0.6026(2)	0.032(1)
C6	-0.5168(2)	-0.8683(2)	-0.6839(2)	0.038(1)
C7	-0.3730(2)	-0.8623(2)	-0.6645(2)	0.034(1)
C8	-0.2787(2)	-0.7782(2)	-0.5620(2)	0.027(1)
C8a	-0.3245(2)	-0.6961(2)	-0.4721(2)	0.022(1)
C1	-0.2336(2)	-0.6039(2)	-0.3642(2)	0.021(1)
C1'	-0.0857(2)	-0.5932(2)	-0.3189(2)	0.020(1)
C8a'	-0.0380(2)	-0.7025(2)	-0.3250(2)	0.022(1)
C8'	-0.1329(2)	-0.8394(2)	-0.3550(2)	0.029(1)
C7'	-0.0771(2)	-0.9383(2)	-0.3603(2)	0.036(1)
C6'	0.0736(2)	-0.9067(2)	-0.3339(2)	0.034(1)
C5'	0.1663(2)	-0.7762(2)	-0.2970(2)	0.029(1)
4a'	0.1129(2)	-0.6712(2)	-0.2910(2)	0.023(1)
C4'	0.2043(2)	-0.5349(2)	-0.2473(2)	0.026(1)
C3'	0.1464(2)	-0.4378(2)	-0.2301(2)	0.024(1)
P	0.4539(1)	0.7581(1)	0.0867(1)	0.030(1)
F1	0.6163(2)	0.8634(2)	0.1046(2)	0.043(1)
F2	0.5134(2)	0.6431(2)	0.1020(2)	0.049(1)
F3	0.4533(2)	0.7178(2)	-0.0585(2)	0.055(1)
F4	0.4544(2)	0.7966(2)	0.2309(2)	0.050(1)
F5	0.3936(2)	0.8716(2)	0.0710(2)	0.059(1)
F6	0.2910(2)	0.6506(2)	0.0676(2)	0.051(1)

Table 5.11. Anisotropic Displacement Parameters for $[(\eta^6\text{-}C_6H_6)Ru(1,1'\text{-biiq})(Cl)](PF_6)$. The Anisotropic Displacement Factor Exponent Takes the Form: $-2\pi^2[h^2a^2U11 + ... + 2hkabU12]$

atom	U11	U22	U33	U23	U13	U12
Ru	0.021(1)	0.019(1)	0.022(1)	0.001(1)	0.000(1)	0.009(1)
Cl	0.025(1)	0.026(1)	0.029(1)	0.009(1)	0.003(1)	0.011(1)
N	0.019(1)	0.020(1)	0.026(1)	0.006(1)	0.002(1)	0.007(1)
N'	0.019(1)	0.020(1)	0.024(1)	0.003(1)	-0.001(1)	0.007(1)
C1''	0.098(3)	0.058(3)	0.023(2)	0.012(1)	0.007(2)	0.051(2)
C2''	0.046(2)	0.070(2)	0.041(2)	-0.027(2)	-0.022(2)	0.040(2)
C3''	0.035(2)	0.035(2)	0.052(2)	-0.022(2)	0.006(2)	-0.002(2)
C4''	0.072(2)	0.022(2)	0.033(2)	-0.001(1)	0.014(2)	0.023(2)
C5''	0.036(2)	0.041(2)	0.029(2)	-0.007(1)	0.004(1)	0.020(2)
C6''	0.070(2)	0.037(2)	0.030(2)	0.004(1)	0.021(2)	0.017(2)
C1'''	0.095(7)	0.029(4)	0.029(4)	0.000(3)	0.024(4)	0.011(4)
C2'''	0.067(5)	0.032(3)	0.023(3)	-0.008(3)	-0.004(3)	0.032(3)
C3'''	0.033(3)	0.041(4)	0.032(4)	-0.012(3)	-0.007(3)	0.014(3)
C4'''	0.107(8)	0.016(3)	0.034(4)	-0.001(3)	0.022(4)	0.012(4)
C5'''	0.080(5)	0.057(4)	0.030(4)	0.002(3)	-0.002(4)	0.060(4)
C6'''	0.022(3)	0.072(6)	0.036(4)	-0.018(4)	0.005(3)	0.005(4)
C3	0.022(1)	0.026(1)	0.035(1)	0.008(1)	0.005(1)	0.012(1)
C4	0.017(1)	0.028(1)	0.038(1)	0.010(1)	0.004(1)	0.011(1)
C4a	0.017(1)	0.023(1)	0.033(1)	0.007(1)	0.000(1)	0.005(1)
C5	0.020(1)	0.028(1)	0.042(1)	0.003(1)	-0.007(1)	0.007(1)
C6	0.028(1)	0.032(1)	0.042(1)	-0.004(1)	-0.012(1)	0.006(1)
C7	0.032(1)	0.031(1)	0.036(1)	-0.003(1)	-0.002(1)	0.013(1)
C8	0.023(1)	0.025(1)	0.031(1)	0.003(1)	-0.001(1)	0.008(1)
C8a	0.018(1)	0.018(1)	0.028(1)	0.006(1)	-0.001(1)	0.004(1)
C1	0.018(1)	0.018(1)	0.026(1)	0.007(1)	0.002(1)	0.006(1)
C1'	0.018(1)	0.021(1)	0.020(1)	0.004(1)	0.000(1)	0.007(1)
C8a'	0.021(1)	0.020(1)	0.024(1)	0.006(1)	0.001(1)	0.008(1)
C8'	0.024(1)	0.023(1)	0.037(1)	0.008(1)	-0.001(1)	0.007(1)
C7'	0.033(1)	0.020(1)	0.052(2)	0.010(1)	0.001(1)	0.009(1)
C6'	0.037(1)	0.028(1)	0.045(1)	0.011(1)	0.003(1)	0.020(1)
C5'	0.027(1)	0.033(1)	0.033(1)	0.009(1)	0.001(1)	0.018(1)
C4a'	0.021(1)	0.024(1)	0.022(1)	0.005(1)	-0.001(1)	0.010(1)
C4'	0.018(1)	0.028(1)	0.028(1)	0.002(1)	-0.002(1)	0.009(1)
C3'	0.019(1)	0.022(1)	0.027(1)	0.002(1)	-0.003(1)	0.005(1)
P	0.024(1)	0.029(1)	0.034(1)	0.005(1)	-0.002(1)	0.008(1)
F1	0.027(1)	0.041(1)	0.045(1)	-0.001(1)	0.000(1)	0.001(1)
F2	0.048(1)	0.040(1)	0.060(1)	0.005(1)	-0.004(1)	0.025(1)
F3	0.047(1)	0.063(1)	0.032(1)	0.004(1)	-0.007(1)	0.001(1)
F4	0.055(1)	0.050(1)	0.040(1)	0.005(1)	0.012(1)	0.016(1)
F5	0.049(1)	0.047(1)	0.092(1)	0.029(1)	0.004(1)	0.026(1)
F6	0.028(1)	0.046(1)	0.068(1)	0.018(1)	-0.001(1)	0.001(1)

Table 5.12. Hydrogen Coordinates and Equivalent Isotropic Displacement Parameters for $[(\eta^6\text{-}C_6H_6)Ru(1,1'\text{-biiq})(Cl)](PF_6)$. U(eq) is Defined as 1/3 of the Trace of the Orthogonalized U_{ij} Tensor

atom	x	y	z	U_{eq}
H1''	-0.0552(5)	-0.4015(4)	0.01963)	0.064
H2''	0.1538(4)	-0.2387(4)	-0.0266(4)	0.066
H3''	0.1266(4)	-0.0768(4)	-0.1288(4)	0.060
H4''	-0.1113(5)	-0.0766(3)	-0.776(3)	0.050
H5''	-0.3139(4)	-0.2325(3)	-0.1255(3)	0.043
H6''	-0.2854(5)	-0.3970(4)	-0.0299(3)	0.056
H1'''	-0.120(1)	-0.4303(8)	0.0203(7)	0.065
H2'''	0.109(1)	-0.3103(7)	-0.0125(6)	0.048
H3'''	0.1673(8)	-0.1211(8)	-0.0915(7)	0.047
H4'''	-0.023(1)	-0.0567(7)	-0.1644(8)	0.068
H5'''	-0.269(1)	-0.1753(9)	-0.1443(7)	0.058
H6'''	-0.3191(9)	-0.372(1)	-0.0566(8)	0.062
H3	-0.4332(2)	-0.4410(2)	-0.2740(2)	0.032
H4	-0.6046(2)	-0.6070(2)	-0.4250(2)	0.032
H5	-0.6586(2)	-0.7888(2)	-0.6175(2)	0.039
H6	-0.5819(2)	-0.9298(2)	-0.7539(2)	0.046
H7	-0.3411(2)	-0.9174(2)	-0.7235(2)	0.041
H8	-0.1819(2)	-0.7747(2)	-0.5510(2)	0.032
H8'	-0.2347(2)	-0.8623(2)	-0.3714(2)	0.034
H7'	-0.1410(2)	-1.0297(2)	-0.3821(2)	0.043
H6'	0.1103(2)	-0.9768(2)	-0.3412(2)	0.041
H5'	0.2672(2)	-0.7555(2)	-0.2775(2)	0.035
H4'	0.3061(2)	-0.5108(2)	-0.2298(2)	0.031
H3'	0.2082(2)	-0.3471(2)	-0.1944(2)	0.029

Table 5.13. Atomic Coordinates and Equivalent Isotropic Displacement Parameters for $[(\eta^6\text{-}C_6H_6)Os(1,1'\text{-biiq})(Cl)](PF_6)$. U(eq) is Defined as 1/3 of the Trace of the Orthogonalized U_{ij} Tensor

atom	x	y	z	U_{eq}
Os	0.4006(1)	0.1673(1)	0.3006(1)	0.017(1)
Cl	0.4071(1)	0.2137(1)	0.1023(1)	0.022(1)
N	0.2311(4)	-0.0063(3)	0.2008(3)	0.018(1)
N'	0.5008(4)	0.0325(3)	0.2385(3)	0.018(1)
C1''	0.5483(7)	0.2562(8)	0.4718(6)	0.064(2)
C2''	0.5522(7)	0.3603(7)	0.4147(6)	0.065(2)
C3''	0.4197(9)	0.3734(5)	0.3819(5)	0.052(2)
C4''	0.2923(6)	0.2877(5)	0.4070(4)	0.038(1)
C5''	0.2933(7)	0.1822(6)	0.4608(4)	0.046(1)
C6''	0.4221(8)	0.1698(7)	0.4956(4)	0.052(2)
C3	0.0938(4)	-0.0077(4)	0.1768(4)	0.022(1)
C4	-0.0068(5)	-0.1033(5)	0.0850(4)	0.026(1)
C4a	0.0314(4)	-0.1987(4)	0.0043(4)	0.022(1)
C5	-0.0639(5)	-0.2875(5)	-0.1028(4)	0.029(1)
C6	-0.0184(5)	-0.3693(5)	-0.1835(5)	0.035(1)
C7	0.1250(5)	-0.3641(5)	-0.1646(4)	0.031(1)
C8	0.2194(5)	-0.2800(4)	-0.0631(4)	0.023(1)
C8a	0.1745(4)	-0.1975(4)	0.0275(4)	0.020(1)
C1	0.2670(4)	-0.1051(4)	0.1353(4)	0.018(1)
C1'	0.4140(4)	-0.0943(4)	0.1802(3)	0.016(1)
C8a'	0.4628(4)	-0.2031(4)	0.1742(3)	0.018(1)
C8'	0.3693(5)	-0.3394(4)	0.1447(4)	0.025(1)
C7'	0.4242(5)	-0.4384(5)	0.1397(4)	0.032(1)
C6'	0.5749(5)	-0.4061(5)	0.1663(4)	0.032(1)
C5'	0.6670(5)	-0.2759(5)	0.2015(4)	0.026(1)
C4a'	0.6131(4)	-0.1708(4)	0.2079(3)	0.020(1)
C4'	0.7030(4)	-0.0349(4)	0.2525(4)	0.023(1)
C3'	0.64659(4)	0.0620(4)	0.2701(4)	0.021(1)
P	-0.0459(1)	0.2564(1)	-0.4133(1)	0.027(1)
F1	0.1154(3)	0.3626(3)	-0.3945(3)	0.038(1)
F2	-0.2084(3)	0.1488(3)	-0.4326(3)	0.048(1)
F3	-0.0466(4)	0.2962(3)	-0.2689(3)	0.046(1)
F4	-0.0457(3)	0.2149(3)	-0.5583(3)	0.048(1)
F5	0.0150(3)	0.1429(3)	-0.3958(3)	0.043(1)
F6	-0.1070(4)	0.3690(4)	-0.4310(4)	0.054(1)

Table 5.14. Anisotropic Displacement Parameters for [(η^6-C_6H_6)Os(1,1'-biiq)(Cl)](PF_6). The Anisotropic Displacement Factor Exponent Takes the Form: $-2\pi^2$ [$h^2 a^2$ U11 + ... + 2 h k a b U12]

atom	U11	U22	U33	U23	U13	U12
Os	0.020(1)	0.018(1)	0.014(1)	0.001(1)	0.002(1)	0.009(1)
Cl	0.025(1)	0.025(1)	0.020(1)	0.010(1)	0.004(1)	0.011(1)
N	0.018(2)	0.017(2)	0.021(2)	0.007(1)	0.005(1)	0.006(1)
N'	0.019(2)	0.021(2)	0.016(2)	0.004(1)	0.002(1)	0.009(1)
C1''	0.048(4)	0.096(6)	0.040(3)	-0.031(4)	-0.015(3)	0.049(4)
C2''	0.047(4)	0.049(4)	0.057(4)	-0.032(3)	0.028(3)	-0.013(3)
C3''	0.110(6)	0.023(3)	0.025(3)	-0.003(2)	0.018(3)	0.031(3)
C4''	0.050(3)	0.043(3)	0.026(2)	-0.007(2)	0.001(2)	0.033(3)
C5''	0.063(4)	0.044(3)	0.025(2)	-0.002(2)	0.025(2)	0.016(3)
C6''	0.102(5)	0.058(4)	0.012(2)	0.005(2)	0.003(3)	0.054(4)
C3	0.020(2)	0.023(2)	0.026(2)	0.006(2)	0.007(2)	0.012(2)
C4	0.019(2)	0.029(2)	0.034(2)	0.014(2)	0.009(2)	0.009(2)
C4a	0.015(2)	0.020(2)	0.028(2)	0.009(2)	0.000(2)	0.004(2)
C5	0.018(2)	0.027(2)	0.037(2)	0.004(2)	-0.005(2)	0.008(2)
C6	0.027(2)	0.031(3)	0.034(2)	-0.006(2)	-0.011(2)	0.006(2)
C7	0.030(2)	0.030(2)	0.028(2)	-0.001(2)	0.000(2)	0.012(2)
C8	0.020(2)	0.025(2)	0.025(2)	0.006(2)	0.002(2)	0.010(2)
C8a	0.019(2)	0.020(2)	0.021(2)	0.007(2)	0.002(2)	0.005(2)
C1	0.017(2)	0.020(2)	0.018(2)	0.006(2)	0.002(2)	0.007(2)
C1'	0.017(2)	0.019(2)	0.013(2)	0.007(1)	0.003(1)	0.007(2)
C8a'	0.023(2)	0.018(2)	0.017(2)	0.007(2)	0.004(2)	0.010(2)
C8'	0.025(2)	0.023(2)	0.028(2)	0.012(2)	0.001(2)	0.007(2)
C7'	0.035(2)	0.018(2)	0.040(3)	0.009(2)	-0.002(2)	0.008(2)
C6'	0.039(3)	0.028(2)	0.035(2)	0.011(2)	0.003(2)	0.022(2)
C5'	0.023(2)	0.031(2)	0.029(2)	0.009(2)	0.003(2)	0.015(2)
C4a	0.023(2)	0.027(2)	0.013(2)	0.004(2)	0.001(2)	0.012(2)
C4'	0.017(2)	0.027(2)	0.021(2)	0.003(2)	0.000(2)	0.007(2)
C3'	0.017(2)	0.020(2)	0.019(2)	0.000(2)	-0.004(2)	0.004(2)
P	0.022(1)	0.030(1)	0.028(1)	0.007(1)	0.000(1)	0.009(1)
F1	0.026(1)	0.038(2)	0.036(2)	-0.001(1)	0.000(1)	0.003(1)
F2	0.027(2)	0.046(2)	0.061(2)	0.020(2)	-0.001(1)	0.000(1)
F3	0.054(2)	0.049(2)	0.032(2)	0.007(1)	0.014(1)	0.017(2)
F4	0.044(2)	0.057(2)	0.026(2)	0.005(1)	0.005(1)	0.002(2)
F5	0.046(2)	0.038(2)	0.048(2)	0.007(1)	0.001(1)	0.024(1)
F6	0.045(2)	0.049(2)	0.083(3)	0.032(2)	0.009(2)	0.024(2)

Table 5.15 Hydrogen Coordinates and Equivalent Isotropic Displacement Parameters for $[(\eta^6\text{-}C_6H_6)Os(1,1'\text{-biiq})(Cl)](PF_6)$. U(eq) is Defined as 1/3 of the Trace of the Orthogonalized U_{ij} Tensor

atom	x	y	z	U_{eq}
H1''	0.6368(7)	0.2335(8)	0.4803(6)	0.077
H2''	0.6420(7)	0.4119(7)	0.3856(6)	0.078
H3''	0.4153(9)	0.4333(5)	0.3269(5)	0.063
H4''	0.1980(6)	0.2864(5)	0.3687(4)	0.046
H5''	0.2000(7)	0.1091(6)	0.4621(4)	0.055
H6''	0.4214(8)	0.0872(7)	0.5211(4)	0.062
H3	0.0682(4)	0.0603(4)	0.2259(4)	0.026
H4a	-0.1032(5)	-0.1060(5)	0.0751(4)	0.031
H5	-0.1596(5)	-0.2896(5)	-0.1179(4)	0.034
H6	-0.0837(5)	-0.4309(5)	-0.2535(5)	0.042
H7	0.1561(5)	-0.4200(5)	-0.2237(4)	0.037
H8	0.3161(5)	-0.2765(4)	-0.0527(4)	0.028
H8'	0.2677(5)	-0.3623(4)	0.1283(4)	0.030
H7'	0.3605(5)	-0.5300(5)	0.1181(4)	0.038
H6'	0.6119(5)	-0.4761(5)	0.1595(4)	0.038
H5'	0.7677(5)	-0.2551(5)	0.2219(4)	0.031
H4'	0.8046(4)	-0.0107(4)	0.2703(4)	0.027
H3'	0.7078(4)	0.1528(4)	0.3054(4)	0.025

5.3 Synthesis of Zirconocene Thiolate Complexes

5.3.1 Materials

The thiols used in this study (Aldrich) were purified by drying over $MgSO_4$ followed by vacuum transfer to Schlenk flasks. The thiols were stored under an argon atmosphere. $[(\eta^5\text{-}C_5H_5)_2Zr(Cl)(H)]_n$[151] and $CDCl_2F$,[152] were prepared by literature methods. $(\eta^5\text{-}C_5H_5)_2Zr(Cl)_2$was used as received from the Boulder Scientific Company. THF was dried over sodium benzophenone ketal and distilled under nitrogen. The ^1H NMR data for $(\eta^5\text{-}C_5H_5)_2Zr(Cl)(SR)$ were reference by $CHCl_2F$ (7.47 ppm, d, $J_{H\text{-}F}$ = 50 Hz) and the ^1H NMR data for $(\eta^5\text{-}C_5H_5)_2Zr(SR)_2$ were referenced by $CHDCl_2$ (5.28 ppm).

5.3.2 Bis(η^5-cyclopentadienyl)(chloro)(thiolato)zirconium(II), $(\eta^5\text{-}C_5H_5)_2Zr(Cl)(SR)$

Synthesis of $(\eta^5\text{-}C_5H_5)_2Zr(Cl)(SCH_3)$

Equal molar quantities of the sodium thiolate, synthesized from the corresponding thiol and NaH, and $(\eta^5\text{-}C_5H_5)_2Zr(Cl)_2$ were reacted in THF at room temperature. The resulting slurry was filtered to remove the NaCl, and the colorless (if relatively free of dithiolate) or pale yellow solution (if significant amounts of the dithiolate were present) was evaporated by vacuum transfer, to give an oil that was used in the NMR experiments without further purification. NEt_3 could be substituted for NaH in the *in situ* synthesis of the thiolate. ^1H NMR ($CDCl_2F$, -150 °C, 500 MHz): δ 6.39, 6.38 ($\eta^5\text{-}C_5H_5$); 2.71 (s, CH_3).

Synthesis of $(\eta^5\text{-}C_5H_5)_2Zr(Cl)(SCH_2CH_3)$

$(\eta^5\text{-}C_5H_5)_2Zr(Cl)(SCH_2CH_3)$ was synthesized using a procedure analogous to the one that was used to synthesize $(\eta^5\text{-}C_5H_5)_2Zr(Cl)(SCH_3)$. ^1H NMR ($CDCl_2F$, -150 °C, 500 MHz): δ unresolved (s, C_5H_5); 3.35,3.13 (br, CH_2); 1.3 (br, CH_3).

Synthesis of $(\eta^5\text{-}C_5H_5)_2Zr(Cl)(SCH(CH_3)_2)$

$(\eta^5\text{-}C_5H_5)_2Zr(Cl)(SCH(CH_3)_2)$ was synthesized using a procedure analogous to the one that was used to synthesize $(\eta^5\text{-}C_5H_5)_2Zr(Cl)(SCH_3)$. ^1H NMR ($CDCl_2F$, -125 °C, 500 MHz): δ 6.37, 6.35 (s, C_5H_5) ; 3.77 (m, CH); 1.40 (d, CH_3, J = 6 Hz); 1.25 (d, CH_3, J = 7 Hz).

Synthesis of $(\eta^5\text{-}C_5H_5)_2Zr(Cl)(SC(CH_3)_3)$

Equal molar quantities of the thiol and $[(\eta^5\text{-}C_5H_5)_2Zr(Cl)(H)]_n$ were reacted in THF at room temperature. When effervescence ceased, the reaction mixture was filtered to remove unreacted $[(\eta^5\text{-}C_5H_5)_2Zr(Cl)(H)]_n$, and the resulting solution (which was usually colorless) was evaporated by vacuum transfer. The products, which were characterized by ^1H NMR, were used for the NMR studies without further purification. ^1H NMR ($CDCl_2F$, -150 °C, 500 MHz): δ 6.48, 6.38 (s, C_5H_5); 1.51 (s, CH_3).

5.3.3 Bis(η^5-cyclopentadienyl)di(thiolato)zirconium(II), $(\eta^5\text{-}C_5H_5)_2Zr(SR)_2$

Synthesis of $(\eta^5\text{-}C_5H_5)_2Zr(SCH_3)_2$

Two molar equivalents of the sodium thiolate, synthesized from the corresponding thiol and NaH, and $(\eta^5\text{-}C_5H_5)_2Zr(Cl)_2$ were reacted in THF at room temperature, the resulting slurry was filtered to remove the NaCl, and the resulting pale yellow solution was evaporated by vacuum transfer. NEt_3 could be substituted for NaH. X-ray quality crystals were grown by vapor diffusion of pentane into THF solutions of $(\eta^5\text{-}C_5H_5)_2Zr(SR)_2$ in a glove box under a nitrogen atmosphere. ^1H NMR

(CD_2Cl_2, 20 °C, 300 MHz): δ 6.16 (s, C_5H_5); 2.42 (s, CH_3). Anal. Calcd for $C_{12}H_{16}S_2Zr$:C, 45.66; H, 5.12. Found: C, 45.64; H, 5.18.

Synthesis of $(\eta^5\text{-}C_5H_5)_2Zr(SCH_2CH_3)_2$

$(\eta^5\text{-}C_5H_5)_2Zr(SCH_2CH_3)_2$ was synthesized using a procedure analogous to the one that was used to synthesize $(\eta^5\text{-}C_5H_5)_2Zr(SCH_3)_2$. ^1H NMR (CD_2Cl_2, 20 °C, 300 MHz): δ 6.14 (s, C_5H_5); 2.88 (q, CH_2, J = 7.4 Hz); 1.15 (t, CH_3). Anal. Calcd for $C_{14}H_{20}S_2Zr$:C, 48.93; H, 5.88. Found: C,48.68; H, 5.66.

Synthesis of $(\eta^5\text{-}C_5H_5)_2Zr(SCH(CH_3)_2)_2$

$(\eta^5\text{-}C_5H_5)_2Zr(SCH(CH_3)_2)_2$ was synthesized using a procedure analogous to the one that was used to synthesize $(\eta^5\text{-}C_5H_5)_2Zr(SCH_3)_2$. ^1H NMR (CD_2Cl_2, 20 °C, 300 MHz): δ 6.13 (s, C_5H_5) ; 3.37 (sept, CH, J = 6.6 Hz); 1.23 (d, CH_3, J = 6.6 Hz). Anal. Calcd for $C_{16}H_{24}S_2Zr$: C, 51.69; H, 6.52. Found: C, 51.69; H, 6.49.

Synthesis of $(\eta^5\text{-}C_5H_5)_2Zr(SC(CH_3)_3)_2$

$(\eta^5\text{-}C_5H_5)_2Zr(SC(CH_3)_3)_2$ was synthesized using a procedure analogous to the one that was used to synthesize $(\eta^5\text{-}C_5H_5)_2Zr(SCH_3)_2$ with the exception that NEt_3 could not be substituted for NaH. ^1H NMR (CD_2Cl_2, 20 °C, 300 MHz): δ 6.19 (s, C_5H_5); 1.42 (s, CH_3). Anal. Calcd for $C_{18}H_{28}S_2Zr$: C, 54.21; H, 6.84. Found: C, 54.12; H, 6.91.

5.4 X-Ray Crystallography Studies of Bis(η^5-cyclopentadienyl)di-(thiolato)zirconium(II), $(\eta^5\text{-}C_5H_5)_2Zr(SR)_2$

A Siemens P4 four-circle diffractometer was used for R=Me,*i*-Pr,*t*-Bu and an Enraf Nonius CAD-4 diffractometer was used for R=Et. Using Mo K_α radiation (0.71073 Å), θ/2θ data sets were collected at the temperatures indicated. An attempt to collect data on an epoxy-coated crystal of R=*t*-Bu at room temperature yielded poor data

due to sample decomposition. Thereafter, all of the data sets (including a recollection of the data for R=*t*-Bu) were collected at low temperature. In each case, three check reflections were collected after every 97 scans. Only random variation in the intensities of the check reflections was observed when the data were collected at low temperature. The data were corrected for Lorentz and polarization effects and semi-empirical absorption corrections were applied.[149] SHELXTL was used for structure solution and refinement.[150] The structures were refined by full matrix least-squares on F^2 using all of the reflections. All of the hydrogen atoms were located in difference maps and they were refined isotropically in every case. The crystal data are summarized in Table 5.16 Atomic coordinates, anisotropic parameters and hydrogen coordinates are tabulated for each derivative in Tables 5.17-5.28.

Table 5.16. Crystal data for Compounds $Cp_2Zr(SR)_2$

	$(\eta^5C_5H_5)_2Zr(SCH_3)_2$	$(\eta^5C_5H_5)_2Zr(SCH_2CH_3)_2$	$(\eta^5C_5H_5)_2Zr(SCH(CH_3)_2)_2$	$(\eta^5C_5H_5)_2Zr(SC(CH_3)_3)_2$
formula	$C_{12}H_{16}S_2Zr$	$C_{14}H_{20}S_2Zr$	$C_{16}H_{24}S_2Zr$	$C_{18}H_{28}S_2Zr$
fw	315.62	343.64	371.69	399.74
space group	P2(1)2(1)2(1)	P1	Pbcn	P4(3)2(1)2
cryst syst	orthorhombic	triclinic	orthorhombic	tetragonal
a, Å	9.299(2)	8.322(2)	11.855(2)	9.9700(14)
b, Å	9.464(2)	9.551(2)	9.227(2)	9.9700(14)
c, Å	14.648(3)	10.844(2)	15.679(3)	19.238(4)
α, deg	90	71.08(3)	90	90
β, deg	90	77.90(3)	90	90
γ, deg	90	65.94(3)	90	90
V, Å^3	1289.1(4)	741.5(3)	1715.1(6)	1912.3(5)
T, K	198(2)	183(2)	188(2)	188(2)
Z	4	2	4	4
D_{calc}, g·cm^{-3}	1.626	1.539	1.440	1.388
μ, mm^{-1}	1.142	1.000	0.871	0.786
cryst size, mm^3	0.72 x 0.44 x 0.42	0.66 x 0.48 x 0.42	0.38 x 0.42 x 0.48	0.54 x 0.42 x 0.38
Final R indices[a]	R1 = 0.0212	R1 = 0.0201	R1 = 0.0270	R1 = 0.0224
[I>2σ(I)]	wR2 = 0.0562	wR2 = 0.0544	wR2 = 0.0655	wR2 = 0.0423
R indices [all data	R1 = 0.0219	R1 = 0.0222	R1 = 0.0347	R1 = 0.0288
used in refinement]	wR2 = 0.0585	wR2 = 0.0584	wR2 = 0.0711	wR2 = 0.0440
GOF	1.096	1.044	1.048	1.084

Table 5.17. Atomic Fractional Coordinates and Equivalent Isotropic Displacement Parameters for Compound $Cp_2Zr(SCH_3)_2$. The Equivalent Isotropic Factor, U_{eq}, is Defined as One-Third of the Trace of the Orthogonalized U_{ij} Tensor

atom	x	y	z	U_{eq}
Zr(1)	0.2212(1)	0.0376(1)	0.8732(1)	0.018(1)
S(1)	0.4279(1)	-0.228(1)	0.9756(1)	0.029(1)
S(2)	0.2419(1)	-0.1721(1)	0.7695(1)	0.028(1)
C(1)	0.1111(4)	0.0602(3)	1.0289(2)	0.032(1)
C(2)	0.0947(4)	-0.0829(3)	1.0045(2)	0.030(1)
C(3)	0.0006(3)	-0.0883(4)	0.9300(2)	0.036(1)
C(4)	-0.0395(3)	0.0491(5)	0.9074(2)	0.040(1)
C(5)	0.0269(4)	0.1417(4)	0.9695(2)	0.039(1)
C(6)	0.2150(3)	0.1501(3)	0.7178(2)	0.031(1)
C(7)	0.3625(3)	0.1383(3)	0.7409(2)	0.029(1)
C(8)	0.3877(4)	0.2282(3)	0.8158(2)	0.034(1)
C(9)	0.2590(4)	0.2924(3)	0.8398(2)	0.038(1)
C(10)	0.1509(4)	0.2465(3)	0.7783(2)	0.036(1)
C(11)	0.5908(4)	-0.0274(5)	0.9082(3)	0.044(1)
C(12)	0.2334(5)	-0.3302(3)	0.8396(3)	0.045(1)

Table 5.18. Anisotropic Displacement Parameters for $Cp_2Zr(SCH_3)_2$. The Anisotropic Displacement Factor Exponent Takes the Form: $-2\pi^2 [h^2 a^2 U11 + ... + 2 h k a b U12]$

atom	U11	U22	U33	U23	U13	U12
Zr(1)	0.021(1)	0.018(1)	0.015(1)	0.00(1)	0.00(1)	0.00(1)
S(1)	0.026(1)	0.032(1)	0.027(1)	0.007(1)	-0.005(1)	0.00(1)
S(2)	0.037(1)	0.023(1)	0.026(1)	-0.005(1)	0.006(1)	-0.003(1)
C(1)	0.042(2)	0.037(2)	0.018(1)	-0.007(1)	0.007(1)	0.00(1)
C(2)	0.035(1)	0.032(1)	0.023(1)	0.003(1)	0.009(1)	-0.003(1)
C(3)	0.027(1)	0.051(2)	0.029(1)	-0.005(1)	0.007(1)	-0.016(1)
C(4)	0.023(1)	0.068(2)	0.029(1)	0.007(2)	0.002(1)	0.007(2)
C(5)	0.043(2)	0.038(2)	0.036(1)	-0.002(1)	0.016(1)	0.016(2)
C(6)	0.039(1)	0.035(1)	0.019(1)	0.008(1)	-0.006(1)	-0.003(1)
C(7)	0.033(1)	0.035(1)	0.020(1)	0.008(1)	0.002(1)	-0.007(1)
C(8)	0.043(2)	0.033(2)	0.026(1)	0.009(1)	-0.009(1)	-0.018(1)
C(9)	0.063(2)	0.021(1)	0.030(1)	0.004(1)	0.000(2)	-0.002(1)
C(10)	0.043(2)	0.031(1)	0.032(1)	0.011(1)	-0.003(1)	0.010(1)
C(11)	0.031(1)	0.047(2)	0.055(2)	0.004(2)	0.002(2)	0.004(2)
C(12)	0.060(2)	0.026(1)	0.048(2)	0.002(1)	0.007(2)	0.002(2)

Table 5.19. Hydrogen Coordinates and Equivalent Isotropic Displacement Parameters for $Cp_2Zr(SCH_3)_2$. The Equivalent Isotropic Factor, U_{eq}, is Defined as One-Third of the Trace of the Orthogonalized U_{ij} Tensor

atom	x	y	z	U_{eq}
H(1)	0.175(4)	0.102(4)	1.073(2)	0.04(1)
H(2)	0.153(4)	-0.159(4)	1.027(2)	0.03(1)
H(3)	-0.033(4)	-0.165(4)	0.903(2)	0.04(1)
H(4)	-0.095(4)	0.081(4)	0.857(2)	0.04(1)
H(5)	0.009(4)	0.240(4)	0.973(2)	0.03(1)
H(6)	0.160(3)	0.098(3)	0.677(1)	0.027(8)
H(7)	0.432(3)	0.073(4)	0.714(2)	0.035(9)
H(8)	0.473(4)	0.239(4)	0.840(2)	0.03(1)
H(9)	0.248(4)	0.357(4)	0.892(2)	0.05(1)
H(10)	0.050(4)	0.272(3)	0.780(2)	0.032(9)
H(11)	0.656(4)	-0.076(4)	0.941(2)	0.05(1)
H(12)	0.578(5)	-0.060(5)	0.847(3)	0.06(1)
H(13)	0.623(4)	0.067(4)	0.897(2)	0.04(1)
H(14)	0.263(6)	-0.387(7)	0.804(3)	0.12(2)
H(15)	0.300(5)	-0.314(4)	0.888(2)	0.05(1)
H(16)	0.128(5)	-0.357(5)	0.854(2)	0.06(1)

Table 5.20. Atomic Fractional Coordinates and Equivalent Isotropic Displacement Parameters for Compound $Cp_2Zr(SCH_2CH_3)_2$. The Equivalent Isotropic factor, U_{eq}, is Defined as One-Third of the Trace of the Orthogonalized U_{ij} Tensor

atom	x	y	z	U_{eq}
Zr(1)	0.2883(1)	0.2519(1)	0.7713(1)	0.015(1)
S(1)	0.3478(1)	0.3664(1)	0.9274(1)	0.023(1)
S(2)	0.1844(1)	0.4987(1)	0.5911(1)	0.023(1)
C(1)	0.6210(2)	0.1237(2)	0.7459(2)	0.025(1)
C(2)	0.5735(2)	0.2319(2)	0.6242(2)	0.026(1)
C(3)	0.4756(3)	0.1790(2)	0.5697(2)	0.028(1)
C(4)	0.4632(3)	0.0388(2)	0.6577(2)	0.027(1)
C(5)	0.5508(2)	0.0048(2)	0.7682(2)	0.025(1)
C(6)	0.1065(3)	0.1781(2)	0.9823(2)	0.028(1)
C(7)	-0.0115(2)	0.3110(2)	0.9000(2)	0.028(1)
C(8)	-0.0241(3)	0.2652(3)	0.7926(2)	0.030(1)
C(9)	0.0871(3)	0.1050(2)	0.8076(2)	0.030(1)
C(10)	0.1677(3)	0.0506(2)	0.9256(2)	0.029(1)
C(11)	0.4992(3)	0.4692(2)	0.8426(2)	0.029(1)
C(12)	0.4033(4)	0.6460(3)	0.7962(2)	0.043(1)
C(13)	-0.0143(3)	0.6420(2)	0.6516(2)	0.035(1)
C(14)	-0.0422(4)	0.8079(3)	0.5666(3)	0.047(1)

Table 5.21. Anisotropic Displacement Parameters for $Cp_2Zr(SCH_2CH_3)_2$. The Anisotropic Displacement Factor Exponent Takes the Form: $-2\pi^2 [h^2 a^2 U11 + ... + 2 h k a b U12]$

atom	U11	U22	U33	U23	U13	U12
Zr(1)	0.017(1)	0.016(1)	0.013(1)	-0.003(1)	0.000(1)	-0.008(1)
S(1)	0.29(1)	0.025(1)	0.019(1)	-0.009(1)	0.001(1)	-0.015(1)
S(2)	0.023(1)	0.019(1)	0.020(1)	-0.001(1)	-0.003(1)	-0.005(1)
C(1)	0.018(1)	0.027(1)	0.029(1)	-0.011(1)	0.001(1)	-0.006(1)
C(2)	0.024(1)	0.022(1)	0.027(1)	-0.007(1)	0.010(1)	-0.008(1)
C(3)	0.031(1)	0.028(1)	0.017(1)	-0.009(1)	0.004(1)	-0.005(1)
C(4)	0.030(1)	0.023(1)	0.031(1)	-0.014(1)	0.003(1)	-0.008(1)
C(5)	0.025(1)	0.017(1)	0.026(1)	-0.003(1)	0.001(1)	-0.004(1)
C(6)	0.031(1)	0.037(1)	0.020(1)	-0.006(1)	0.007(1)	-0.022(1)
C(7)	0.020(1)	0.034(1)	0.032(1)	-0.012(1)	0.009(1)	-0.013(1)
C(8)	0.022(1)	0.043(1)	0.029(1)	-0.005(1)	0.000(1)	-0.020(1)
C(9)	0.033(1)	0.038(1)	0.031(1)	-0.012(1)	0.006(1)	-0.026(1)
C(10)	0.034(1)	0.028(1)	0.026(1)	-0.001(1)	0.004(1)	-0.020(1)
C(11)	0.034(1)	0.035(1)	0.031(1)	-0.014(1)	0.004(1)	-0.023(1)
C(12)	0.067(1)	0.035(1)	0.036(1)	0.000(1)	-0.010(1)	-0.032(1)
C(13)	0.028(1)	0.028(1)	0.040(1)	-0.009(1)	0.003(1)	-0.003(1)
C(14)	0.045(1)	0.026(1)	0.046(2)	-0.005(1)	0.005(1)	0.003(1)

Table 5.22. Hydrogen Coordinates and Equivalent Isotropic Displacement Parameters for $Cp_2Zr(SCH_2CH_3)_2$. U_{eq}, is Defined as One-Third of the Trace of the Orthogonalized U_{ij} Tensor

atom	x	y	z	U_{eq}
H(1)	0.678(3)	0.137(3)	0.799(2)	0.033(6)
H(2)	0.597(3)	0.324(3)	0.588(2)	0.031(6)
H(3)	0.427(3)	0.230(3)	0.488(2)	0.040(7)
H(4)	0.405(3)	-0.024(3)	0.649(2)	0.044(7)
H(5)	0.563(3)	-0.080(3)	0.845(2)	0.030(6)
H(6)	0.135(3)	0.176(3)	1.064(2)	0.037(6)
H(7)	-0.064(2)	0.406(3)	0.913(2)	0.025(5)
H(8)	-0.088(3)	0.328(3)	0.728(2)	0.044(7)
H(9)	0.101(3)	0.051(3)	0.746(2)	0.033(6)
H(10)	0.246(3)	-0.051(3)	0.959(2)	0.032(6)
H(11)	0.578(3)	0.448(3)	0.904(2)	0.029(6)
H(12)	0.566(3)	0.429(3)	0.769(2)	0.033(6)
H(13)	0.482(4)	0.701(3)	0.760(3)	0.057(8)
H(14)	0.336(4)	0.681(3)	0.869(3)	0.052(8)
H(15)	0.318(4)	0.676(3)	0.732(3)	0.057(8)
H(16)	-0.097(4)	0.618(3)	0.656(3)	0.055(9)
H(17)	0.002(3)	0.633(3)	0.743(3)	0.048(8)
H(18)	-0.130(4)	0.876(3)	0.602(3)	0.056(8)
H(19)	-0.056(4)	0.815(4)	0.481(4)	0.07(1)
H(20)	0.060(4)	0.832(3)	0.573(3)	0.064(9)

Table 5.23. Atomic Fractional Coordinates and Equivalent Isotropic Displacement Parameters for Compounds $Cp_2Zr(SCH(CH_3)_2)_2$. The Equivalent Isotropic Factor, U_{eq}, is Defined as One-Third of the Trace of the Orthogonalized U_{ij} Tensor

atom	x	y	z	U_{eq}
Zr(1)	0.5000(1)	0.1606(1)	0.2500(1)	0.023(1)
S(1)	0.6459(1)	0.3345(1)	0.1970(1)	0.032(1)
C(1)	0.5121(3)	-0.0212(3)	0.3669(2)	0.043(1)
C(2)	0.5221(2)	0.1132(3)	0.4072(2)	0.041(1)
C(3)	0.6228(2)	0.1766(3)	0.3810(2)	0.040(1)
C(4)	0.6769(2)	0.0797(3)	0.3251(2)	0.041(1)
C(5)	0.6087(3)	-0.0428(3)	0.3170(2)	0.042(1)
C(6)	0.5986(2)	0.4423(3)	0.1048(2)	0.035(1)
C(7)	0.6926(5)	0.4545(9)	0.0422(4)	0.122(3)
C(8)	0.5566(5)	0.5883(4)	0.1320(3)	0.079(1)

Table 5.24. Anisotropic Displacement Parameters for $Cp_2Zr(SCH(CH_3)_2)_2$. The Anisotropic Displacement Factor Exponent Takes the Form: $-2\pi^2 [h^2 a^2 U11 + ... + 2 h k a b U12]$

atom	U11	U22	U33	U23	U13	U12
Zr(1)	0.029(1)	0.022(1)	0.019(1)	0	0.001(1)	0
S(1)	0.030(1)	0.034(1)	0.032(1)	0.005(1)	-0.004(1)	-0.006(1)
C(1)	0.060(2)	0.035(2)	0.035(1)	0.014(1)	0.007(1)	0.009(1)
C(2)	0.062(2)	0.039(2)	0.021(1)	0.007(1)	0.004(1)	0.018(1)
C(3)	0.051(2)	0.039(2)	0.028(1)	0.002(1)	-0.015(1)	0.007(1)
C(4)	0.041(1)	0.049(2)	0.033(1)	0.008(1)	-0.004(1)	0.016(1)
C(5)	0.062(2)	0.033(2)	0.033(1)	0.004(1)	0.002(1)	0.018(1)
C(6)	0.038(1)	0.035(1)	0.032(1)	0.005(1)	0.00(1)	-0.004(1)
C(7)	0.078(3)	0.200(7)	0.088(3)	0.096(4)	0.045(3)	0.059(4)
C(8)	0.133(4)	0.044(2)	0.059(2)	0.001(1)	-0.031(3)	0.027(2)

Table 5.25. Hydrogen Coordinates and Equivalent Isotropic Displacement Parameters for $Cp_2Zr(SCH(CH_3)_2)_2$. The Equivalent Isotropic Factor, U_{eq}, is Defined as One-Third of the Trace of the Orthogonalized U_{ij} Tensor

atom	x	y	z	U_{eq}
H(1)	0.450(2)	-0.079(3)	0.369(2)	0.038(8)
H(2)	0.464(2)	0.147(3)	0.444(2)	0.047(8)
H(3)	0.649(2)	0.263(3)	0.397(2)	0.041(7)
H(4)	0.7435(2)	0.089(3)	0.297(2)	0.047(8)
H(5)	0.6252(2)	-0.127(3)	0.284(2)	0.052(8)
H(6)	0.5389(2)	0.391(3)	0.078(2)	0.050(8)
H(7)	0.7231(5)	0.343(6)	0.028(3)	0.18(3)
H(8)	0.7511(3)	0.473(4)	0.059(2)	0.08(1)
H(9)	0.6659(3)	0.504(4)	-0.005(2)	0.08(1)
H(10)	0.6162(4)	0.632(5)	0.162(3)	0.11(1)
H(11)	0.4963(4)	0.573(7)	0.170(4)	0.17(3)
H(12)	0.5280(3)	0.648(4)	0.080(3)	0.10(1)

Table 5.26. Atomic Fractional Coordinates and Equivalent Isotropic Displacement Parameters for Compounds $Cp_2Zr(SC(CH_3)_3)_2$. The Equivalent Isotropic Factor, U_{eq}, is Defined as One-Third of the Trace of the Orthogonalized U_{ij} Tensor

atom	x	y	z	U_{eq}
Zr(1)	0.7485(1)	0.7485(1)	0	0.017(1)
S(1)	0.8016(1)	0.9110(1)	0.0971(1)	0.025(1)
C(1)	0.8710(3)	0.5279(2)	0.0081(1)	0.027(1)
C(2)	0.9089(3)	0.6007(3)	0.0674(1)	0.027(1)
C(3)	0.7952(3)	0.6144(3)	0.1096(1)	0.029(1)
C(4)	0.6864(3)	0.5531(3)	0.0762(1)	0.030(1)
C(5)	0.7336(3)	0.4997(2)	0.0127(1)	0.030(1)
C(6)	0.7913(3)	1.0968(2)	0.0878(1)	0.027(1)
C(7)	0.6526(4)	1.1466(3)	0.0688(2)	0.043(1)
C(8)	0.8954(4)	1.1425(3)	0.0358(2)	0.048(1)
C(9)	0.8263(4)	1.1496(3)	0.1603(2)	0.043(1)

Table 5.27. Anisotropic Displacement Parameters for $Cp_2Zr(SC(CH_3)_3)_2$. The Anisotropic Displacement Factor Exponent Takes the Form: -2 p2 [h2 a2 U11 + ... + 2 h k a b U12]

atom	U11	U22	U33	U23	U13	U12
Zr(1)	0.017(1)	0.017(1)	0.017(1)	0.001(1)	-0.001(1)	-0.002(1)
S(1)	0.034(1)	0.019(1)	0.021(1)	-0.001(1)	-0.006(1)	0.001(1)
C(1)	0.035(2)	0.018(1)	0.029(1)	0.004(1)	0.002(1)	0.008(1)
C(2)	0.026(1)	0.024(1)	0.030(1)	0.008(1)	-0.007(1)	0.001(1)
C(3)	0.040(2)	0.024(1)	0.022(1)	0.005(1)	0.000(1)	0.004(1)
C(4)	0.031(2)	0.025(1)	0.034(1)	0.011(1)	0.004(1)	-0.006(1)
C(5)	0.037(2)	0.017(1)	0.036(1)	0.003(1)	-0.007(1)	-0.004(1)
C(6)	0.038(1)	0.016(1)	0.027(1)	-0.002(1)	-0.002(1)	0.002(1)
C(7)	0.050(2)	0.022(2)	0.055(2)	-0.001(2)	-0.012(2)	0.008(1)
C(8)	0.063(2)	0.028(2)	0.052(2)	0.005(2)	0.020(2)	-0.002(2)
C(9)	0.055(2)	0.032(2)	0.041(2)	-0.013(1)	-0.007(2)	-0.001(2)

Table 5.28. Hydrogen Coordinates and Equivalent Isotropic Displacement Parameters for $Cp_2Zr(SC(CH_3)_3)_2$. The Equivalent Isotropic Factor, U_{eq}, is Defined as One-Third of the Trace of the Orthogonalized U_{ij} Tensor

atom	x	y	z	U_{eq}
H(1)	0.924(2)	0.503(3)	-0.025(1)	0.020(7)
H(2)	0.991(3)	0.627(3)	0.077(1)	0.034(8)
H(3)	0.791(3)	0.653(3)	0.151(1)	0.033(7)
H(4)	0.597(3)	0.550(2)	0.092(1)	0.026(7)
H(5)	0.682(3)	0.452(3)	-0.018(1)	0.045(9)
H(6)	0.648(3)	1.242(3)	0.070(1)	0.040(8)
H(7)	0.633(3)	1.128(3)	0.019(1)	0.043(9)
H(8)	0.584(3)	1.117(3)	0.102(1)	0.06(1)
H(9)	0.893(3)	1.239(3)	0.033(1)	0.048(9)
H(10)	0.983(3)	1.112(3)	0.048(1)	0.05(1)
H(11)	0.873(3)	1.109(3)	-0.009(1)	0.043(9)
H(12)	0.826(3)	1.247(3)	0.158(1)	0.035(7)
H(13)	0.762(3)	1.126(3)	0.192(1)	0.05(1)
H(14)	0.906(4)	1.121(4)	0.175(1)	0.08(1)

5.5. Computational Studies of Bis(η^5-cyclopentadienyl)(chloro)-(thiolato)zirconium(II) complexes, (η^5-$C_5H_5)_2$Zr(Cl)(SR)

The *ab initio* electronic structure computations were performed primarily using density functional theory (DFT) as implemented in GAUSSIAN 94 AND 98. [138,139] For R= Me, Et, *i*-Pr, *t*-Bu, the B3LYP method[140] (method **A** of Table 5.29) based on Becke's 3-parameter hybrid exchange functionals[141] and Lee-Yang-Parr correlation functionals[142,143] was used. Energetics, geometries, and analytical second derivatives were calculated at the B3LYP level with the following basis sets:[153-158] LANL2DZ-ECP for Zr, Cl, and S; 3-21G for C and H atoms of the Cp ligands; LANL2DZ for the remaining atoms. Optimized ground-state and transition-state geometries were obtained using non-redundant internal coordinates and starting Hessians calculated at the restricted Hartree-Fock (RHF) level. Analytical second derivatives were calculated to verify stationary points on the potential energy surface using the criteria of zero and one imaginary frequency for ground-states and transition-states, respectively. The analytical second derivatives were also used to calculate the real frequencies that were subsequently used in the harmonic approximation of various thermodynamic properties: free energies ($\Delta G^{\ddagger}$), free enthalpies ($\Delta H^{\ddagger}$), entropies ($\Delta S^{\ddagger}$), and zero-point energies.

The role of the basis sets was tested for R=Me and *t*-Bu by repeating the calculations with a 6-31G basis set in place of the 3-21G basis set (method **B** of Table 5.29). The effect of DFT functional was investigated by replacing the B3LYP method with the BLYP functional (i.e., Becke 88 exchange[159] and Lee-Yang-Parr correlation)[142,143] with the same basis sets at method **A** (method **C** of Table 5.29). In both methods **B** and **C**, the geometries were fully optimized. In order to check the sensitivty of the computed energies with respect to correlation methodology, single-point calculations using second-order Moller-Plesset perturbation theory[160-164]

(MP2) were performed on **R**=Me and *t*-Bu using the optimized geometries that were obtained from method **A** (method **D** in Table 5.29).

Table 5.29. Details of Computation Methods

Method	Geometry	Exchange and Correlation Functionals	Basis Set Cp Ligand C and H atoms	Basis Set Zr, Cl, S	Basis Set Thiolate Ligand C and H atoms
A, DFT	Optimized at the present level	B3LYP	3-21G	LANL2DZ/ECP	LANL2DZ
B, DFT	Optimized at the present level	B3LYP	6-31G	LANL2DZ/ECP	LANL2DZ
C, DFT	Optimized at the present level	BLYP	3-21G	LANL2DZ/ECP	LANL2DZ
D, MP2	Optimized from method A	-	3-21G	LANL2DZ/ECP	LANL2DZ

5.6. NMR Experiments – Assignment of Resonances

5.6.1. Variable Temperature

Chemical shifts of peaks can shift as a function of temperature. This shifting can be unrelated to the line-broadening effects and coalescence caused by chemical exchange which will be discussed in the following sections. It becomes important when making the absolute assignment of resonances of a compound to investigate the chemical shifts as a function of temperature. This behavior seems to be especially important for amine protons. All of the compounds with hydrogens attached to the amine nitrogens showed movement of these chemical shifts with temperature. For this reason most assignments in this project were made at a lower temperature limit past which no further movement was seen. This differentiated the static assignment from the dynamic exchange seen at higher temperatures. The 500 MHz spectrometer was temperature calibrated with methanol or ethylene glycol standard samples as outlined in the manufacturer's manual to insure proper temperatures were recorded for all kinetic experiments.

5.6.2. Two Dimensional Experiments: COSY and NOESY

Proton assignments of synthesized compounds were made by using the two-dimensional NMR experiments: COSY and NOESY. As explained in the previous section, care was taken as to what temperature these experiments were performed at as to not confuse the static assignment with assignment of the peaks when undergoing chemical exchange.

Scalar coupling relationships between the protons were obtained using ^{1}H-^{1}H double-quantum-filtered homonuclear correlation spectroscopy (dqf-COSY).[165] This shows which protons are bound to the same atoms. Scalar couplings cannot be seen past one or two bonds.

The phase-sensitive nuclear Overhouser spectroscopy (NOESY) can help establish stereochemistry in a molecule which cannot be seen by other methods. Applying a strong radiofrequency pulse on a resonance can destroy or invert that signal. The effect is also seen in resonances which have a dipolar interaction with the inverted signal. This phenomenon is the nuclear overhouser effect.[166] By applying this concept to two-dimensional pulse sequences the 2D-NOESY reveals cross peaks between protons which have dipolar or through space interaction with each other. NOE's can also give information concerning dynamic exchange. This will be explained in section 5.7.4. 2D-NOESY experiments were carried out in order to establish absolute stereochemistry when necessary.

5.7. NMR Experiments – Kinetics of Exchange

Nuclear Magnetic Resonance can be used to study the dynamic behavior of molecules in solution. The simplest case that can be considered is the conversion between two conformations of equal energy and equal population. This would result in equal forward and reverse rate constants ($k_a = k_b$).

$$A \underset{k_b}{\overset{k_a}{\rightleftharpoons}} B$$

If the frequency of proton A is ν_A and the frequency of proton B is ν_B, then the average time (τ) that it takes proton A to exchange with proton B by moving from ν_A to ν_B is related to the equation:

$$\tau = 1/k$$

where k is the rate of the exchange. A very slow exchange results in the observation of two separate and distinct peaks at ν_A and ν_B. As the rate increases the difference between ν_A and ν_B moves toward zero until they are only one peak.[167] There are

three time regimes to be considered in the dynamics of exchange: slow exchange, intermediate exchange and fast exchange.[168]

Slow exchange is observed by the presence of a static spectrum. There are two distinct peaks at ν_A and ν_B. As the exchange becomes faster the spectrum lines are broadened. This broadening can be related to the rate of exchange.

$$\Delta\nu = k/\pi = 1/\pi\tau$$

$\Delta\nu$ is defined as the linewidth at half height of the peak.

Fast exchange is observed by a single broadening peak which becomes narrower as the rate increases. In this case the rate is related to the equation:

$$\Delta\nu = \pi(\nu_A - \nu_B)^2/2k = (1/2)(\nu_A - \nu_B)^2\tau$$

Measuring the rate in the fast exchange regime requires assuming that the frequency of the broadening peak is the average of the frequency of proton A and proton B because is is impossible to accurately measure ν_A and ν_B.

Intermediate exchange is the regime in between fast and slow. This regime offers the most opportunity for measuring the kinetics of exchange. The separate peaks can actually coalesce into a single resonance at some temperature if the exchange process is intermediate on the NMR time-scale. The rate of exchange at the coalescence temperature can be calculated from the equation below:

$$k = \pi(\nu_A - \nu_B)/\sqrt{2}$$

Techniques to measure the kinetics of exchange can be utilitzed withing these time regimes. Three such techniques have been utilized: coalescence temperature, line-shape analysis and spin-inversion transfer. 2D-Exchange is another technique that was used to identify the exchange but not to quantify the rate constants.[169] The best possible case is a system in which it is possible to measure the rate constant at several temperatures employing more than one technique. These methods will be explained in more detail in the following sections.

5.7.1. Coalescence Temperature

In the slow-exchange regime of the NMR spectra the separate exchanging resonances coalesce into a single peak. The temperature at which this happens is defined as the coalescence temperature (T_c).[170]

To use the coalescence temperature to calculate the rate of this exchange at this temperature, it is necessary to see two distict resonances at some lower temperature. Ideally this is above the lower temperature limit of the solvent and the peaks do not move further apart as the exchange is effectively so slow it is not happening. The rate and energy of rotation can calculated by measuring the coalescence temperature and the difference in herz of the decoalesced peaks at the lower temperature limit. The rate constants are determined using the standard equation:

$$k = \pi(\Delta\delta)/\sqrt{2}$$

where $\Delta\delta$ is the difference in frequency in Hz of the resonances of the stereotopic hydrogens in the static spectrum.[167] The corresponding energy barriers can be estimated at the coalescence temperature:

$$\Delta G^{\ddagger} = -RT_c[\ln(k/T_c)+\ln(h/K)]$$

where $R = 8.314\ J{\cdot}mol^{-1}{\cdot}K^{-1}$ is the gas constant, T_c is the coalescence temperature, $h = 6.626\times10^{-34}\ J{\cdot}s$ is Planck's constant, and $K = 1.381\times10^{-23}\ J{\cdot}K^{-1}$ is Boltzmann's constant. This method was successfully utilitzed in the $Cp_2Zr(SR)(Cl)$ (Chapter Two) series of compounds. Coalescence was seen in each case. However the T_c was so low it was not possible to utilitze any other technique for this system.

5.7.2. Line-Shape Analysis (LSA)

Line-shape analysis (LSA) uses the fact that the exchange dynamics cause the peaks to broaden, coalesce and then sharpen.[171] Theoretically, LSA can be used in all three time regimes. Practically, the experiment is performed by measuring the spectrum at several different temperatures. It is important that the NMR is carefully

shimmed as so that poor shims do not interfere with the line-widths. Each spectrum is digitized, the portion of interest cut out and analyzed by the program DNMR5.[172] DNMR5 simulates the spectrum and gives the rate constant as a part of the program output. LSA was utilized for $[(Ar)M(1,1'\text{-biiq})(I)]^+$, M=Ru, Os. For this system, it was the broadening of the peaks that was fitted by the DNMR5 program. Coalescence was seen for these compounds at relatively high temperatures, 79°C and 93°C for osmium and ruthenium respectively. Rates were not measured above these temperatures.

5.7.3. Spin-Inversion Transfer (SIT)

Spin-inversion transfer is a magnetization transfer experiment in which one of the exchanging resonances is excited by a selective radio frequency pulse which causes the resonance to be inverted. The recovery is observed in the resonance which is in chemical exchange with the excited resonance. This experiment is slow on the NMR time-scale as a static spectrum is collected with two distinct resonances for the exchanging protons. However, it is fast on the spin-relaxation time-scale. This means that the exchange takes place before the spin has completely relaxed from the selective radio frequency pulse. SIT rate data are obtained using the pulse sequence: d_1, $\pi/2$, d_2, $\pi/2$, τ_m, $\pi/2$, aq.[173-176] The transmitter offset frequency was set equal to υ_A, the frequency of the nucleus to be inverted. The relaxation delay d_1 was set equal to five times the longest T_1 to allow complete longitudinal relaxation between pulses. The second delay was set equal to $1/(2|\upsilon_A-\upsilon_B|)$, where $|\upsilon_A-\upsilon_B|$ is the frequency difference between the nucleus to be inverted and the exchanging nucleus. The mixing time τ_m was typically varied from 0.001 s to about 5 x T_1. The 90° pulse width ($\pi/2$) was determined experimentally prior to each kinetics run. The intensity of peaks at any time can be represented by modified Bloch equations:[173]

$$M_z^A(t) = c_1 \exp(\lambda_1 t) + c_2 \exp(\lambda_2 t) + M_\infty^A \quad (1)$$

$$M_z^B(t) = (c_1/k_b)(\lambda_1 + k_a^{eff}) \exp(\lambda_1 t) + (c_2/k_b)(\lambda_2 + k_a^{eff}) \exp(\lambda_2 t) + M_\infty^B \quad (2)$$

The constants c_1, c_2, λ_1, and λ_2 are defined by:

$$\lambda_1 = (1/2)\{-(k_a^{eff} + k_b^{eff}) + \sqrt{((k_a^{eff} + k_b^{eff})^2 - 4((k_a^{eff} k_b^{eff}) - (k_a k_b))}\} \quad (3)$$

$$\lambda_2 = (1/2)\{-(k_a^{eff} + k_b^{eff}) - \sqrt{((k_a^{eff} + k_b^{eff})^2 - 4((k_a^{eff} k_b^{eff}) - (k_a k_b))}\} \quad (4)$$

$$c_1 = (M_0^A - M_\infty^A) - c_2 \quad (5)$$

$$c_2 = (k_b/\lambda_1 - \lambda_2))(\lambda_1 + k_a^{eff})(M_\infty^A - M_0^A)/k_b + M_0^B - M_\infty^B \quad (6)$$

The effective first-order rate constants are represented as the sum of the two first-order rate constants for the pathways that lead to a loss of magnetization, chemical exchange and spin-lattice relaxation:

$$k_a^{eff} = k_a + 1/T_{1a} \quad (7)$$

$$k_b^{eff} = k_b + 1/T_{1b} \quad (8)$$

The problem becomes simpler when the equilibrium constant is 1 and T_{1a} equal to T_{1b}. This was the case for the arene metal systems with C_1 symmetry in which the chemical exchange was between enantiomers of equal populations. $[M(bipy)_2(1,1'\text{-biiq})]^{3+}$ has C_2 symmetry and the exchange was between two diastereomers of different populations. The equilibrium constant was not equal to one. It becomes important to be careful about which rate constant is being measured. Considering again the reaction in which A is exchanging with B and the forward rate constant is k_a and the reverse rate constant is k_b. k_b is related to k_a by the relationship:

$$Keq = k_a/k_b$$

The equilibrium constant is also related to the concentrations of the species in solution:

$$Keq=[B]/[A]$$

If A is the major diastereomer, then the equilibrium constants is defined by:

$$Keq=[minor]/[major] = k_{(maj \leftarrow min)}/k_{(min \leftarrow maj)}$$

Therefore, inverting A which is the major diastereomer results in the measurement of $k_{(maj \leftarrow min)}$. The data consisting of peak amplitude versus delay time τ_m were analyzed by

fitting Equations 1 and 2 to the experimental data. The numerical analysis was performed on a Silicon Graphics IRIS Indigo XS24 running the non-linear least-squares regression program SPIRAL.[177] Using the known values of M_{∞}^{A} and M_{∞}^{B}, the non-linear regression yielded values and estimated errors for k_{obs}, M_0^A, M_0^B, and T_1. The data with the fits from the program were simulated by a in house MATLAB program and included in each chapter as figures.

5.7.4. 2D-Exchange Spectroscopy

Two dimensional exchange spectroscopy (2D-EXSY) pulse sequence is essentially the same as that used for phase-sensitive nuclear Overhauser effect spectroscopy (NOESY): d_1, $\pi/2$, d_2, $\pi/2$, τ_m, $\pi/2$, aq.[169] However, the 2D-EXSY is collected at temperatures at which chemical exchange is slow on the NMR time scale, but fast on the spin-relaxation time scale. This allows a static spectrum to be collected, but cross peaks are observed which relate to chemical exchange of proton resonances. The relaxation delay d_1 was set equal to five times the longest T_1 to allow complete longitudinal relaxation between pulses. Because of the long d_1 delay time, a homospoil-$\pi/2$-homospoil presequence was unnecessary. In all cases a mixing time of $\tau_m = 0.5$ s was used to obtain the spectra. Varying τ_m had little effect on the position of the cross peaks, but shorter mixing times resulted in spectra which were of lesser quality.[178] At temperatures in which chemical exchange is observed in the 2D-EXSY, the spectrum is dominated by the positive exchange peaks. Weaker negative cross peaks that correspond to NOE coupling can be seen, but are of a much less intensity. Quantitative rate information can be obtained from 2D-EXSY spectroscopy.[179-185] One disadvantage to this method is that the cross peak and diagonal peak intensities need to measurable. Errors in these measurements are propagated into the rate calculations.[186] Another disadvantage is that several mixing times must be used leading to the need for large amounts of instrument time.[185] The

advantage to this method is in calculating rate constants in multi-site systems. For a two-site system, there is no advantage in using 2D-EXSY to determine rate constants. For such systems, LSA and magnetization-transfer experiments are preferable.[187] Only two-site systems were observed in this study. For these reasons the 2D-EXSY experiment was used to identify the chemical exchange taking place,[188] but not to measure the rate constant associated with this exchange.

CHAPTER 6
CONCLUSION

6.1 Dynamic Effects of Misdirected Metal-ligand Bonds

Bent metal-ligand bonds can result in misdirection of the metal-ligand orbitals. Three types of misdirection are illustrated in Figure 1.1. The static properties of misdirected orbitals have been investigated by Gerloch, which is explained in detail in Section 1.2. The purpose of this research was to investigate the dynamic properties of misdirected metal-ligand orbitals by NMR methods. It had previously been shown that $[M(bipy)_2(1,1'\text{-biiq})]^{2+}$ exhibited faster kinetic rates for osmium than ruthenium for atropisomerization of the 1,1'-biiq ligand.[60] The twisting of the 1,1'-biiq ligand resulted in metal-biiq bonds which are bent in the ground-state structure. It was observed that ruthenium exhibited faster kinetic rates than osmium for isomerization of $M(bipy)_2$(tetrahydrothiophenene)] which proceeds by a mechanism of inversion at the sulfur atom.[61] The metal-thioether bond is not bent in the ground-state structure (Figure 1.4). Third-row transition metals have stronger metal-ligand bonds than second-row transition metals[20] and thereby it would be expected that second-row transition metal complexes would exhibit faster kinetic rates of reactions than their third-row congeners (Table 1.3). This was explained in detail in Section 1.3 and Section 1.4. The anomalous behavior of $[Ru(bipy)_2(1,1'\text{-biiq})]^{2+}$ and $[Os(bipy)_2(1,1'\text{-biiq})]^{2+}$ led to the experiments of this dissertation.

6.2 Summary of Experimental Work

Metal complexes of the ligand dabp were studied in order to answer the question as to whether the inverse relationship between thermodynamic stability and kinetic lability observed for $[M(bipy)_2(1,1'\text{-biiq})]^{2+}$ (M=Ru, Os) was a special case of

the 1,1'-biiq ligand or whether this inverse relationship is a general trend for metal complexes containing ligands with misdirected metal-ligand bonds. As it was not possible to measure the rates of isomerization for $[Ru(bipy)_2(dabp)]^{2+}$, $[(\eta^6\text{-}C_6H_6)M(Cl)(dabp)]^+$ for M = Ru and Os were synthesized. Spin-labeling NMR methods were carried out which measured the rate of isomerization in solution. It was only possible to compare the rates at one temperature due to the decomposition of the osmium derivative at higher temperatures. A mechanistic study was carried out which demonstrated that $[(\eta^6\text{-}C_6H_6)M(Cl)(dabp)]^+$ isomerized by a mechanism of atropisomerization of the dabp ligand.

$[(\eta^6\text{-}C_6H_6)M(1,1'\text{-biiq})(X)]^+$ (M=Ru, Os; X=Cl, I) complexes were synthesized and studied in order to investigate the role that ancillary ligands play in the inverse relationship between thermodynamic stability and kinetic lability of the metal-biiq bond. Spin-labeling NMR experiments were carried out which measured the rate of isomerization in solution. It was found that the osmium complexes exhibited faster kinetic rates than the ruthenium derivatives for both X=Cl and X=I. X-ray crystal structures were solved for M=Ru, Os; X=Cl, showing the structures to have comparable metric parameters.

Group 4 thiolate compounds were synthesized in order to compare the energy of rotation about the M-S bond. The Mdπ-Spπ bond is misdirected in the transition-state for electron deficient early transition metal compounds (Figure 2.1). $(\eta^5\text{-}C_5H_5)_2Zr(Cl)(SR)$ and $(\eta^5\text{-}C_5H_5)_2Zr(SR)_2$ were synthesized for R=methyl, ethyl, *iso*-propyl and *tert*-butyl. Metal-Sulfur rotational barriers were measured for the monothiolate zirconium compounds. X-ray crystal structures were solved for the dithiolate compounds. DFT calculations were carried out for the monothiolate zirconium series in order to separate the enthalpic and entropic contriubtions to the energy of rotation and to calculate the metric parameters of the ground-state and transition-state structures. Preliminary comparisions of the zirconium and hafnium

derivatives showed no difference in the rotational barriers. An unusual trend was observed for the rotational barriers of $(\eta^5\text{-}C_5H_5)_2Zr(Cl)(SR)$ (R=methyl, ethyl, *iso*-propyl and *tert*-butyl). For R=methyl, ethyl, and *iso*-propyl the barriers are proportional to the steric demand of the ligand and the bond strength of the metal-sulfur bond at 32, 33, and 35 kJ mole^{-1} respectively. A much lower barrier of 26 kJ mole^{-1} was measured for R= *tert*-butyl. DFT calculations suggested that enthalpy was the dominant contributor to magnitude of the rotational barrier.

6.3 Results

6.3.1 Kinetic Element Effect (KEE)

Comparison of the rates of isomerization of the ruthenium and osmium derivatives of $[M(bipy)_2(1,1'\text{-biiq})]^{2+}$ has led to the introduction of the term Kinetic Element Effect (KEE). The KEE is the ratio of the rates of isomerization reactions of second-row and third-row metal-ligand complexes ($KEE=k_{2nd}/k_{3rd}$). Section 1.5 defined this concept by comparing it to the kinetic isotope effect. The ratio of the rates of reactions of secondary kinetic isotope effects can give information concerning the transition-state of the reaction (Figure 1.5). The KEE is related to the kinetic isotope effect because of the lanthanide contraction. Similar to hydrogen and deuterium, second-row and third-row transition metals are the same size with different masses.[20] The different bond dissociation energies of the second-row and third-row transition metals give rise to an opportunity to explore bond strength without changing the steric effects in a system. Therefore, comparison of rates of second-row and third-row transition metal isomerization reactions that do not involve the breaking of bonds can give information concerning the transition-states of these reactions. In the context of misdirected ligands, rates of isomerization reactions in which the ligand atropisomerizes can be used to compare bond strength of second-row and third-row transition metal complexes. A KEE of greater than one is indicative of a weakening of the bonds in the

transition-state, while a KEE of less than one demonstrates a strengthening of bonds in the transition-state. The KEE gives information on how a misdirected metal-ligand bond effects the dynamic properties of a metal complex.

An inverse KEE is observed for the 1,1'-biiq ligand complexes $[M(bipy)_2(1,1'\text{-biiq})]^{2+}$, $[(\eta^6\text{-}C_6H_6)M(1,1'\text{-biiq})(Cl)]^+$, $[(\eta^6\text{-}C_6H_6)M(1,1'\text{-biiq})(I)]^+$ and the dabp ligand complex $[(\eta^6\text{-}C_6H_6)M(dabp)(Cl)]^+$ (M=Ru,Os). These values are shown in Table 6.1. The magnitude of the KEE varies among the 1,1'-biiq compounds. It is interesting that KEE is similiar in magnitude for the arene-metal-halide complexes, but very different for the bisbipyridine complex. Changing the ancillary ligands does not change the effect of the metal-biiq misdirection. However, the ancillary ligands may determine the magnitude of the KEE. Observing faster kinetic rates for the osmium derivative of the dabp complex suggests that the inverse relationship between thermodynamic stability and kinetic lability is not a special property of 1,1'-biiq but could be a general trend for complexes with misdirected metal-ligand bonds.

Table 6.1. Comparison of Thermodyamic Data for Atropisomerization Reactions of Ruthenium and Osmium.

Compound	$\Delta H^{\ddagger}$ kJ/mole	$\Delta S^{\ddagger}$ J/K mole	$\Delta G^{\ddagger}$ kJ/mole	KEE	KHE
[a][$Ru(bipy)_2(1,1'\text{-biiq})]^{2+}$	70(2)	-17(5)	76(2)		
[a][$Os(bipy)_2(1,1'\text{-biiq})]^{2+}$	63(2)	-23(6)	68(2)		
[b][$M(bipy)_2(1,1'\text{-biiq})]^{2+}$				0.12	0.93
[(η^6-C_6H_6)Ru(1,1'-biiq)(Cl)]$^+$	77.3(2)	4.8(7)	75.8		
[(η^6-C_6H_6)Os(1,1'-biiq)(Cl)]$^+$	71.2(2)	-11.6(7)	75.0		
[(η^6-C_6H_6)M(1,1'-biiq)(Cl)]$^+$				0.66	0.93
[(η^6-C_6H_6)Ru(1,1'-biiq)(I)]$^+$	76.5(3)	-5(1)	78.4		
[(η^6-C_6H_6)Os(1,1'-biiq)(I)]$^+$	70.2(5)	-21(1)	77.1		
[(η^6-C_6H_6)M(1,1'-biiq)(I)]$^+$				0.57	0.92
[(η^6-C_6H_6)Ru(dabp)(Cl)]$^+$	-	-	66.8		
[(η^6-C_6H_6)Os(dabp)(Cl)]$^+$	-	-	65.3		
[(η^6-C_6H_6)M(dabp)(Cl)]$^+$				0.50	-

[a]The values shown correspond to the interconversion of the minor→major diastereomerization.[60]

[b]KEE and KHE are an average of minor→major and major→minor diastereomerization reactions.

6.3.2 Kinetic Ethalpy Effect (KHE)

It is also useful to compare the enthalpy of activation ($\Delta H^{\ddagger}$) for these reactions. $\Delta H^{\ddagger}$ is directly related to bond strength. This is explained in detail in Section 1.3. The ratio of enthalpy of activation between the second-row and third-row transition metal complexes is defined as the Kinetic Enthalpy Effect ($KHE=\Delta H^{\ddagger}_{3rd}/\Delta H^{\ddagger}_{2nd}$). As third-

row bonds are presumably stronger than second-row bonds (Section 1.3) a regular KHE would be seen when KHE>1, while an inverse effect is observed when KHE<1. An inverse KHE is observed for each of the 1,1'-biiq ligand systems. It was not possible to calculate KHE for $[(\eta^6\text{-}C_6H_6)M(dabp)(Cl)]^+$ because enthalpic and entropic contributions could not be separated for the osmium dabp compound. These values are shown in Table 6.1. It is interesting to note that while the KEE varies among the 1,1'-biiq compounds, the KHE is nearly the same for each system. KHE may be a better indicator of the misdirected metal-ligand bond. In each case the entropy is more negative for the osmium compound than the ruthenium compound. While it is understandable that the activativation enthalpy would be less for osmium than for ruthenium due to a strengthening of the metal-ligand bonds in the transition state, it is unclear why more negative entropy term for the osmium derivatives. It can be seen from these results that changing the ancillary ligands does not effect the magnitude of the KHE.

Recently, Jordan has published a study concerning the substitution labilities of mononuclear iron, ruthenium, and osmium carbonyls.[189,190] Kinetic studies of substitution reactions of group 8 carbonyls with phosphines have determined that dissociation of CO is the rate determining step. The reaction is shown below:

$$M(CO)_5 + PPH_3 \rightarrow M(CO)_4(PPH_3) + CO$$

The rate is independent of phosphine concentration in all cases, which would be indicative of a dissociative mechanism. The rate of ligand substitution is much greater for the ruthenium derivative than the osmium derivative. Replacing one CO ligand with an η^2-alkyne ligand dramatically changed the magnitudes of the rate constants (Table 1.4). Enhancement of the rate of CO dissociation is 10^5 times greater for the osmium derivative than the ruthenium derivative. It is interesting to note that the enthalpy of activation, $\Delta H^{\ddagger}$, is less for the osmium derivative than the ruthenium derivative for $M(CO)_4(\eta^2\text{-}C_2(CF_3)_2)$. First bond dissociation energies for the loss of CO were

calculated by nonlocal density functional theory to be 175.3 and 60.7 kJ mol^{-1} for ruthenium and osmium, respectively.[191] The authors explain the rate enhancement effect by suggesting that the alkyne ligand becomes a four electron donor in the transition state as compared to a two electron donor in the ground state. This would effectively stabilize the $M(CO)_3L$ intermediate. This stabilization would be more pronounced for the osmium derivative which has presumably stronger bonds than the ruthenium derivative. This idea was tested by comparing the kinetics of different alkyne ligands. C_2H_2 was compared with $C_2(CF_3)_2$ on the basis that C_2H_2 would be a better electron donor than $C_2(CF_3)_2$. $Os(CO)_4(\eta^2\text{-}C_2H_2)$ was found to be about 10 times more reactive than $Os(CO)_4(\eta^2\text{-}C_2(CF_3)_2)$. $\Delta H^{\ddagger}$ was more favorable for $Os(CO)_4(\eta^2\text{-}C_2H_2)$ by 7 kJ/mole, suggesting stronger bonds for the intermediate. X-ray crystal structure studies were carried out for both the Ru and Os derivatives of $M(CO)_4(\eta^2\text{-}C_2(CF_3)_2)$. These compounds have nearly identical geometric parameters.[192] This is an example of how strengthening the bonds in the transtition state of a reaction has a greater influence on the kinetics of the third row complex compared to the second row complex.

Table 6.2. Comparison of Reactivity of Group 8 Metal Carbonyl Compounds with PPh_3 at 25°C.

Compound	Rate s^{-1}	$\Delta H^{\ddagger}$ kJ $mole^{-1}$	$\Delta S^{\ddagger}$ J $mole^{-1}$ K^{-1}	Reference
$Fe(CO)_5$	3×10^{-13}	167	75	192
$Ru(CO)_5$	7×10^{-5}	114(4)	60(12)	193
$Os(CO)_5$	3.3×10^{-10}	133(3)	21(7)	189
$Fe(CO)_4(\eta^2\text{-}C_2(CF_3)_2)$	9.5	88(2)	70(10)	189
$Ru(CO)_4(\eta^2\text{-}C_2(CF_3)_2)$	1.25×10^{-2}	104(2)	66(9)	189
$Os(CO)_4(\eta^2\text{-}C_2(CF_3)_2)$	3.5×10^{-3}	99.0(8)	42(3)	189
$Os(CO)_4(\eta^2\text{-}C_2H_2)$	3.2×10^{-2}	92(2)	36(8)	190

A KHE can be calculated for $M(CO)_4(\eta^2\text{-}C_2(CF_3)_2)$ from the data listed in Table 6.2 to be 0.95. The entropy term is less for the osmium derivative with its presumably stronger transition-state bonds than the ruthenium derivative. It is interesting the KHE is nearly the same for every example described at 0.92-0.95. The KHE and trend in entropy is consistent with the results from our study of misdirected ligands. The entropy term is even less for $Os(CO)_4(\eta^2\text{-}C_2H_2)$ than $Os(CO)_4(\eta^2\text{-}C_2(CF_3)_2)$. The transition-state bonds for $Os(CO)_4(\eta^2\text{-}C_2H_2)$ should be stronger than $Os(CO)_4(\eta^2\text{-}C_2(CF_3)_2)$. Entropy can be described as freedom of motion. The more restricted the molecule, the more negative the entropy. Stronger transition-state bonds result in a more negative $\Delta S^{\ddagger}$ in every example described. Stronger bonds are generally shorter bonds. It is possible that in the transition-state structures the metal-ligand bonds are shorter for the osmium compounds. This would result in a more compact structure for which it would be reasonable to observe a more negative entropy of activation. These results from the experimental studies and from the literature suggest that comparison of enthalpic and entropic terms is more useful than rate comparisons in observing the effect of misdirected metal-ligand bonds.

6.3.3 Ground-State Effect

A KEE was not observed for the zirconium and hafnium thiolate compounds. Preliminary studies were undertaken with the hafnium derivatives which showed that the rotational barriers of $Cp_2Hf(Cl)(SR)$ for R=Me,Et, and Ph were not significantly different from the zirconium derivatives. It is not understood why the hafnium rotational barrier would not show a KEE as in the case of $[M(bipy)_2(1,1'\text{-biiq})]^{2+}$ (M=Ru, Os). It is possible that in this type of complex the magnitude of the KEE is extremely small. It has been shown that the magnitude of the KEE changes as a function of the types of ancillary ligands coordinated to the metal center (vide supra).

In order to rule out the existance of a dynamic effect resulting from the misdirection of the metal-sulfur orbitals, the enthalpic and entropic contributions of the rotational barriers must be separated and compared for the zirconium and hafnium compounds. The *ab initio* calculations which were carried out on $Cp_2Zr(Cl)(SR)$ for R=Me,Et,*i*-Pr, *t*-Bu, demonstrated that enthalpy is the dominant contributor to the magnitude of the rotational barrier. A significantly lower enthalpic term for the *tert*-butyl derivative resulted in a dramatic decrease in the rotational barrier compared to the methyl, ethyl, and *iso*-propyl derivatives. It is also possible that the ground-state structures are not the same. The metric parameters for the ground-state and transition-state structures for $Cp_2Zr(Cl)(SR)$ (R=Me,Et, *i*-Pr, *t*-Bu) were calculated by DFT methods (Table 4.5). It was clear from comparing the ground-state and transition-state structures that the lower rotational barrier for the *tert*-butyl derivative is a result of a difference in the ground-state structure (Figure 4.6). The degree of misdirection of the Mdπ-Spπ orbitals is sensitive to the Cl-M-S-R torsion angle. Maximum bonding interaction occurs when the torsion angle is 90° and minimum bonding interaction occurs when the torsion angle is 0°. Small differences in the ground-state structures of the hafnium derivatives could result in a different amount of misdirection of the Mdπ-Spπ orbitals as compared to the zirconium derivatives which would make a KEE comparison invalid.

A study of 1,1'-biiq derivatives reveals a similiar ground-state which results in an inverse relationship between steric size and kinetic rates. A series of 8,8'-dialkyl-1,1'-biiq complexes have been synthesized.[194-196] The atropisomeric 1,1'-biiq derivatives were separated into both enantiomers. The racemization was measured for each dialkyl derivative. It was determined that the rate of racemization is inversely proportional to the steric size of the alkyl groups. The rate constants and activation parameters are shown in Table 6.3. The inverse relationship between the rate constant and the steric size of the 8 and 8' substituent was suggested to be caused by

destabilization of the ground state. This argument is based on X-ray crystallography and PM3 calculated ground-state and transition-state energies.[196]

Table 6.3. Racemization-Rate Constants at 30°C and Activation Parameters for Racemization in 1,1'-Biiq Derivatives.

8,8'-dialkyl - 1,1'-biiq	k s^{-1}	E_a kJ mol^{-1}	$\Delta H^{\ddagger}$ kJ mol^{-1}	$\Delta S^{\ddagger}$ J K^{-1} mol^{-1}	$\Delta G^{\ddagger}_{298}$ kJ mol^{-1}
methyl	5.8×10^{-6}	113(2)	110(2)	19(7)	105
ethyl	2.2×10^{-5}	103(1)	100(1)	-3(3)	101
iso-propyl	5.3×10^{-5}	95(1)	92(1)	-22(4)	99

6.4 Future Work

There remains questions to be answered concerning the KEE and KHE. It still remains unclear if the observed inverse KEE and KHE is a special case of ruthenium and osmium. Preliminary studies undertaken with Rh(III) and Ir(III) have determined that it is possible to synthesize and measure the rates of interconversion of diastereomers of $[Rh(bipy)_2(1,1'\text{-biiq})]^{3+}$ and $[Ir(bipy)_2(1,1'\text{-biiq})]^{3+}$ at several temperatures, which would allow for the separation and comparison of the entropy and enthalpy of this isomerization reaction. $[Rh(bipy)_2(1,1'\text{-biiq})]^{3+}$ and $[Ir(bipy)_2(1,1'\text{-biiq})]^{3+}$ represent a potentially excellent system in which to determine if another transition metal group can exhibit an inverse KEE and KHE. Pd(II) and Pt(II) would also be a good system in which to measure the rates of isomerization of 1,1'-biiq complexes. A tremendous amount of kinetic data is available for Pd(II) and Pt(II) complexes in which Pd derivatives exhibit faster rates of isomerization than Pt derivatives (Table 1.3 and Table 1.4). The existance of an inverse KEE and KHE for compounds such as $[M(1,1'\text{-biiq})(R)(X)]^{+}$ (M=Pd(II), Pt(II)) would be very indicative of the dynamic effects caused by a misdirected metal-ligand bond.

It is also dersirable to answer the question as to why $Cp_2M(SR)(Cl)$ compounds have similiar rotational barriers for zirconium and hafnium compounds. It is necessary to compare the enthalpic and entropic contributions to the rotational barrier. This can be done by *ab initio* calculations. However, it is necessary to determine the X-ray crystal structures of either $Cp_2Hf(SR)(Cl)$ or $Cp_2Hf(SR)_2$ for R=Me, Et, *i*-Pr, and *t*-Bu. The enthalpy and entropy of activation for $Cp_2Zr(SR)(Cl)$ were calculated by using the metric parameters for the dithiolate complexes since the monothiolate X-ray crystal structures were not available (Section 4.5). It is also necessary to compare the ground-state structures for the zirconium and hafnium compounds. Collection of the X-ray crystal structures of $Cp_2Hf(SR)_2$ for R=Me, Et, *i*-Pr, and *t*-Bu would allow the ground-state structures of the dithiolate compounds to be compared. Using the metric parameters of the hafnium dithiolate compounds would allow the determination of the ground-state and transition-state structures by computational methods. A comparison of the ground-state structure, transition-state structure and the entropic and enthalpic contributions to the rotational barrier should reveal the reason for the similiar rotational barriers of the zirconium and hafnium compounds.

6.5 Conclusion

$[M(bipy)_2(1,1'\text{-biiq})]^{2+}$, $[(\eta^6\text{-}C_6H_6)M(1,1'\text{-biiq})(Cl)]^+$, $[(\eta^6\text{-}C_6H_6)M(1,1'\text{-biiq})(I)]^+$ and $[(\eta^6\text{-}C_6H_6)M(dabp)(Cl)]^+$ (M=Ru, Os) are the only examples in the literature of third-row transition metal complexes having faster rates of atropisomerization than their second-row congeners. The misdirected ligand 1,1'-biiq has bent metal-ligand bonds in the ground-states of these complexes and directed metal-ligand bonds in the transition-states of these isomerization reactions. The KEE is the ratio of the rates of isomerization reactions of second-row and third-row metal-ligand complexes ($KEE=k_{2nd}/k_{3rd}$). An inverse KEE is observed for $[M(bipy)_2(1,1'\text{-biiq})]^{2+}$, $[(\eta^6\text{-}C_6H_6)M(1,1'\text{-biiq})(X)]^+$, and $[(\eta^6\text{-}C_6H_6)M(dabp)(Cl)]^+$ (M=Ru,Os; X=Cl,I). The

magnitude of the KEE varies among the biiq compounds. The KEE is similiar in magnitude for the arene-metal-halide complexes, but very different as compared to the metal-bipyridine complex. Changing the ancillary ligands does not influence the effect of the metal-biiq misdirection; however, the ancillary ligands may determine the magnitude of the KEE. Observing faster kinetic rates for the osmium derivative of the dabp complex suggests that the inverse relationship between thermodynamic stability and kinetic lability is not a special property of 1,1'-biiq but could be a general trend for complexes with misdirected metal-ligand bonds. A Kinetic Enthalpy Effect (KHE) can be defined as the ratio of enthalpy of activation for the third row and second-row atropisomerization reactions (KHE= $\Delta H^{\ddagger}_{3rd}/\Delta H^{\ddagger}_{2nd}$). An inverse KHE is also observed for each of the ruthenium and osmium systems. While the KEE varies among the biiq compounds, the KHE is nearly the same for each system. It can be seen from these results that changing the ancillary ligands does not effect the magnitude of the KHE. KHE may be a better indicator of the misdirected metal-ligand bond.

References

1) Zeise, W. C. "Besondero Platinverbindung" *Ann. Phys.* **1827**, *9*, 632.

2) Hein, F. "Chromo-Organic Compounds" *Ber.* **1919**, *52*, 195.

3) Werner, A. "Beitrag zur Konstitution Anorganischer Verbindungen" *Z.Anorg Chem.* **1893**, *3*, 267.

4) Pauling, L. *The Nature of the Chemical Bond, 3rd ed.*; Cornell University: Ithaca, NY, 1960.

5) Ballhausen, C. J. "Quantum-Mechanics and Chemical Bonding in Inorganic Complexes.2. Valency and Inorganic Metal-Complexes" *J. Chem. Educ.* **1979**, *56*, 294.

6) Hehre, W. J. "Ab-Initio Molecular-Orbital Theory" *Acc. Chem. Res.* **1976**, *9*, 399.

7) Duer, M. J.; Fenton, N. D.; Gerloch, M. "Bent bonds Probed by Ligand-Field Analysis" *Int. Rev. Phys. Chem.* **1990**, *9*, 227.

8) Liehr, A. D. "Interaction of Electromagnetic Radiation with Matter. I. Theory of Optical Rotatory Power: Topic A. Trigonal Dihedral Compounds." *J. Phys. Chem.* **1964**, *68*, 665.

9) Deeth, R. J.; Duer, M. J.; Gerloch, M. "Ligand Fields from Misdirected Valency. 1. Lone-Pair Contributions in Planar Cobalt(II) Schiff-Base Complexes" *Inorg. Chem.* **1987**, *26*, 2573.

10) Deeth, R. J.; Duer, M. J.; Gerloch, M. "Ligand Fields from Misdirected Valency. 2. Bent Bonding in Copper(II) Acetylacetonates" *Inorg. Chem.* **1987**, *26*, 2578.

11) Deeth, R. J.; Gerloch, M. "Ligand Fields from Misdirected Valency. 3. Ligands Hybridization in Tetragonal-Octahedral Nickel(II) Thiocyanates" *Inorg. Chem.* **1987**, *26*, 2582.

12) Fenton, N. D.; Gerloch, M. "Ligand Fields from Misdirected Valency. 4. Magnetic Susceptibilities and Electron Spin Resonance and Optical Spectra of

Tetrakis(diphenylmethylarsine oxide)(nitrato)cobalt(II) and -nickel(II) Nitrates" *Inorg. Chem.* **1987**, *26*, 3273.

13) Duer, M. J.; Gerloch, M. "Ligand Fields from Misdirected Valency. 5. Consequences for Spectral Intensity Distributions" *Inorg. Chem.* **1989**, *28*, 4260.

14) Fenton, N. D.; Gerloch, M. "Energies, Intensities, and Circular Dichroism of d-d Transitions in Trigonal-Bipyramidal Cobalt(II) and Nickel(II) Chromophores" *Inorg. Chem.* **1990**, *29*, 3726.

15) Fenton, N. D.; Gerloch, M. "Chirality and Bonding in the First Coordination Shells of Three CoN_2Cl_2 Chromophores: Quantitative Reproduction of Rotatory Strengths" *Inorg. Chem.* **1990**, *29*, 3718.

16) Fenton, N. D.; Gerloch, M. "A Ligand-Field Probe of Transition-Metal-Oxygen Ligations" *Inorg. Chem.* **1989**, *28*, 2767.

17) Bridgeman, D. J.; Jupp, K. M.; Gerloch, M. "Correlation of Vibrational and Electronic Spectra. Static and Vibronic Contributions ot the Polarized Spectrum of Trisethylendiaminenickel(II) Dinitrate" *Inorg. Chem.* **1994**, *33*, 5424.

18) Simões, J. A. M.; Beauchamp, J. L. "Transition Metal-Hydrogen and Metal-Carbon Bond Strengths: The Keys to Catalysis" *Chem. Rev.* **1990**, *90*, 629.

19) Martinho Simões, J. A.; Beauchamp, J. L. "Transition Metal-Hydrogen and Metal-Carbon Bond Strengths: The Keys to Catalysis" *Chem. Rev.* **1990**, *90*, 629.

20) Ohanessian, G.; Goddard, W. A., III "Valence-Bond Concepts in Transition Metals: Metal Hydride Diatomic Cations" *Acc. Chem. Res.* **1990**, *23*, 386.

21) Lewis, K. E.; Golden, D. M.; Smith, G. P. "Organometallic Bond-Dissociation Energies : Laser Pyrolysis of $Fe(CO)_5$, $Cr(CO)_6$, $Mo(CO)_6$, and $W(CO)_6$" *J. Am. Chem. Soc.* **1984**, *106*, 3905.

22) Ziegler, T.; Tschinke, V.; Ursenbach, C. "Thermal-Stability and Kinetic Lability of the Metal-Carbonyl Bond : A Theoretical-Study on $M(CO)_6$ (M = Cr, Mo, W), $M(CO)_5$ (M = Fe, Ru, Os), and $M(CO)_4$ (M = Ni, Pd Pt)" *J. Am. Chem. Soc.* **1987**, *109*, 4825.

23) Li, J.; Schreckenbach, G.; Ziegler, T. " A Reassessment of the First Metal-Carbonyl Dissociation-Energy in $M(CO)_4$ (M=Ni, Pd, Pt), $M(CO)_5$ (M=Fe, Ru, Os), and $M(CO)_6$ (M=Cr, Mo, W) by a Quasi-Relativistic Density-Functional Method" *J. Am. Chem. Soc.* **1995**, *117*, 486.

24) Ziegler, T.; Tschinkey, V.; Fan, L. Y.; Becke, A. D. "Theoretical-Study on the Electronic and Molecular-Structures of $(C_5H_5)M(L)$ (M = Rh, Ir, L = CO, PH_3) And $M(CO)_4$ (M = Ru, Os) and their Ability to Activate the C-H Bond in Methane" *J. Am. Chem. Soc.* **1989**, *111*, 9177.

25) Schock, L. E.; Marks, T. J. "Organometallic Thermochemistry: Metal Hydrocarbyl, Hydride, Halide, Carbonyl, Amide, and Alkoxide Bond Enthalpy Relationships and their Implications in Pentamethylcyclo-pentadienyl and Cyclopentadienyl Complexes of Zirconium and Hafnium" *J. Am. Chem. Soc.* **1988**, *110*, 7701.

26) King, W. A.; DiBella, S.; Gulino, A.; Lanza, G.; Fragala, I. L. "Absolute Metal-Ligand Sigma Bond Enthalpies in Group 4 Metallocenes. A Thermochemical, Structural, Photoelectron Spectroscopic, and Ab Initio Quantum Chemical Investigation" *J. Am. Chem. Soc.* **1999**, *121*, 355.

27) Calhorda, M. J.; Dias, A. R.; Minas da Piedade, M. E.; Saleman, M. S.; Martinho Simoes, J. A. "Studies on the Transferability of Transition-Metal Carbon and Transition-Metal Hydrogen-Bond Enthalpies in Bis(Cyclopentadienyl) Complexes" *Organometallics* **1987**, *6*, 734.

28) Tilset, M.; Parker, V. D. "Solution Homolytic Bond-Dissociation Energies of Organotransition-Metal Hydrides" *J. Am. Chem. Soc.* **1989**, *111*, 6711.

29) Ziegler, T.; Cheng, W.; Baerends, E.; Ravenek, W. "Theoretical-Study on the Difference in the Relative Strengths of Metal Hydrogen and Metal Methyl Bonds in Complexes of Early Transition-Metals and Complexes of Middle to Late Transition-Metals" *Inorg. Chem.* **1988**, *27*, 3458.

30) Ziegler, T.; Tschinke, V.; Becke, A. "A Theoretical-Study on the Relative Strengths of the Metal Hydrogen and Metal Methyl Bonds in Complexes of Middle to Late Transition-Metals" *J. Am. Chem. Soc.* **1987**, *109*, 1351.

31) Ziegler, T.; Tschinke, V.; Versluis, L.; Baerends, E. J. "A Theoretical-Study of Metal-Ligand Bond Strengths (M-OH, M-OCH_3, M-SH, M-NH_2, M-Ph_2, M-CH_3, M-SiH_3, M-CN, M-H) in the Early Transition-Metal Systems Cl_3TiL, Cl_3ZrL, Cl_3HfL and Late Transition-Metal Systems $LCo(CO)_4$" *Polyhedron* **1988**, *7*, 1625.

32) Dias, A. R.; Martinho Simoes, J. A. "Thermochemistry of Ti(η-5-$C_5H_5)_2N$, Mo(H-5-$C_5H_5)_2N$, W(H-5-$C_5H_5)_2N$ Complexes" *Polyhedron* **1988**, *7*, 1531.

33) House, D. A. "Anionopentaaminecobalt(III) Complexes with Polyamine Ligands.17. Mercury(II)-Assisted Aquation Rates of Chloropentaamine-Cobalt(III) Complexes: Effect of High Ionic-Strength" *Inorg. Chim. Acta* **1981**, *51*, 273.

34) Taube, H. "Rates and Mechanisms of Substitution in Inorganic Complexes in Solution" *Chem. Rev.* **1952**, *50*, 69.

35) Lawrance, G. A. "Solvolysis Kinetics of Pentaammine(trifluoromethanesulfonato-O) Complexes of Cobalt(III), Rhodium(III), and Iridium(III)" *Inorg. Chem.* **1985**, *24*, 323.

36) Poulopoulou, V. G.; Li, Z. W.; Taube, H. "Comparison of the Rates of Substitution in $[Ru(NH_3)H_2O]^{3+}$ and $[Os(NH_3)H_2O]^{3+}$ by Hexacyano

Complexes: Substitution Coupled to Electron Transfer" *Inorg. Chim. Acta.* **1994**, *225*, 173.

37) Dadci, L.; Elias, H.; Frey, U.; Hornig, A.; Koelle, U.; Merbach, A. E.; Paulus, H.; Schneider, J. S. "π-Arene Aqua Complexes of Cobalt, Rhodium, Iridium, and Ruthenium: Preparation, Structure, and Kinetics of Water Exchange and Water Substitution" *Inorg. Chem.* **1995**, *34*, 306.

38) Cusanelli, A.; Frey, U.; Richens, D. T.; Merbach, A. E. "The Slowest Water Exchange at a Homoleptic Mononuclear Metal Center: Variable-Temperature and Variable-Pressure ^{17}O NMR Study on $[Ir(H_2O)_6]^{3+}$" *J. Am. Chem. Soc.* **1996**, *118*, 5265.

39) Brindley, P. B.; Scotton, M. J. "Free Radical Substitution Reactions on Zirconium and Hafnium Organometallics" *J. Organomet. Chem.* **1981**, *222*, 89.

40) Tong, S. B.; Swanddle, T. W. "Exchange Of Oxygen-18 Between Aquopentaammineiridium(III) Ion and Solvent Water: Pressure Effect and Mechanism" *Inorg. Chem.* **1974**, *13*, 1538.

41) Laurenczy, G.; Rapaport, L.; Zbinden, D.; Merbach, A. E. "Variable-Pressure Oxygen-17-NMR Study Of Water Exchange On Hexaaquarhodium(III)" *Magn. Reson. Chem.* **1991**, *29*, 845.

42) Hynes, M. J.; Brannick, P. F. "Rates and Mechanisms of Substitution Reactions of Square-Planar Dithiocarbamate and Dithiophosphate Complexes of the Nickel Triad in Methanol" *J. Chem. Soc., Dalton Trans.* **1977**, 2281.

43) Helm, L.; Elding, L. I.; Merbach, A. E. "High-Pressure NMR Kinetics.23. Water-Exchange Mechanism of Tetraaquapalladium(II): A Variable-Pressure and Variable-Temperature O-17 NMR-Study" *Helv. Chim. Acta* **1984**, *67*, 1453.

44) Helm, L.; Elding, L. I.; Merbach, A. E. "High-Pressure NMR Kinetics.21. Activation Parameters and Mechanism for Water Exchange of

Tetraaquaplatinum(II) Studied by High-Pressure O-17 NMR-Spectroscopy" *Inorg. Chem.* **1985**, *24*, 1719.

45) Pesek, J. J.; Mason, W. R. "Cyanide Exchange Kinetics for Planar Tetracyanometalate Complexes by C-13 NMR" *Inorg. Chem.* **1983**, *22*, 2958.

46) Hallinan, N.; Besancon, V.; Forster, M.; Elbaze, G.; Ducommun, Y.; Merbach, A. E. "High-Pressure NMR Kinetics.47. Solvent-Exchange Mechanisms of Nonaqueous Square-Planar Tetrasolvates: A High-Pressure H-1-NMR Investigation" *Inorg. Chem.* **1991**, *30*, 1112.

47) Frey, U.; Elmroth, S.; Moullet, B.; Elding, L. I.; Merbach, A. E. "^{1}H NMR Kinetic Study of Ligand Exchange on Bis(1,4-dithiane)platinum(II), Bis(1,4-dithiane)palladium(II), and Tetrakis(dimethyl sulfide)Platinum(II)" *Inorg. Chem.* **1991**, *30*, 5033.

48) Abel, E. W.; Bhargava, S. K.; Orrell, K. G. "The Stereodynamics of Metal Complexes of Sulfur-, Selenium-, and Tellurium-Containing Ligands" *Prog. Inorg. Chem.* **1984**, *32*, 1.

49) Kutzelnigg, W. "Chemical Bonding in Higher Main Group Elements" *Angew. Chem. Int. Ed. Engl.* **1984**, *23*, 272.

50) Ashby, M. T. "Concerning the Spatial Nature of Metal-Thiolate π-bond" *Comments Inorg. Chem.* **1990**, *10*, 297.

51) Ashby, M. T.; Sheshtawy, N. A. "Barriers to Rotation about the B-X Bonds of Coordinatively Unsaturated Borates and Thioborates R_2BSR' (X = O,S) are not Measures of the Relative Strengths of Their B=O and B=S π Bonds" *Organometallics* **1994**, *3*, 236.

52) Abel, E. W.; Bhargava, S. K.; Kite, K.; Orrell, K. G.; Sik, V.; Williams, B. L. "Structural Dependencies of Pyramidal Inversion at Sulfur and Selenium in Thio-Ether and Seleno-Ether Complexes of Palladium(II) And Platinum(II): A Nuclear Magnetic-Resonance Study" *Polyhedron* **1982**, *1*, 289.

53) Cross, R. J.; Hunter, G.; Massey, R. C. "Dynamic Nuclear Magnetic-Resonance Studies of Complexes of1 ,2-Bis(Benzylthio)Ethane with Chromium, Molybdenum, and Tungsten Carbonyl-Complexes" *J. Chem. Soc., Dalton, Trans.* **1976**, 2015.

54) Abel, E. W.; Orrell, K. G.; Qureshi, K. B.; Sik, V. "An NMR-Study of the Fluxionality of Group-VI Metal Pentacarbonyl Complexes of 1,3-Dithiolanes" *Polyhedron* **1990**, *9*, 703.

55) Abel, E. W.; Farrow, G. W.; Orrell, K. G.; Sik, V. "Nuclear Magnetic-Resonance Study of Inversion at Sulfur and Selenium Atoms in Complexes of Palladium(II) And Platinum(II) .1. Complexes of Bis(Trimethylsiylmethyl) Sulfide and Selenide" *J. Chem. Soc., Dalton Trans.* **1977**, 42.

56) Abel, E. W.; Ahmed, A. K. S.; Farrow, G. W.; Orrell, K. G.; Sik, V. "Nuclear Magnetic-Resonance Study of Inversion at Sulfur and Selenium Atoms in Complexes of Palladium(II) And Platinum(II).2. Complexes of Methyl and Phenyl Trimethylsilylmethyl Sulfide and Selenide" *J. Chem. Soc., Dalton Trans.* **1977**, 47.

57) Abel, E. W.; Booth, M.; Orrell, K. G. "Effect of Variation in Ligand Ring Size upon the Inversion Barrier at Sulfur in Complexes of Palladium(II) and Platinum(II) : Dynamic H-1 Nuclear Magnetic-Resonance Study" *J. Chem. Soc., Dalton Trans.* **1979**, 1994.

58) Abel, E. W.; Orrell, K. G.; Qureshi, K. B.; Sik, V. "Nuclear Magnetic-Resonance Investigations of the Fluxionality of Trans-Palladium(II) and Trans-Platinum(II) Dichloride Complexes of 1,3-Dithiolanes.1. 1,3-Dithiolane and 2,2-Dimethyl-1,3-Dithiolane Complexes" *Polyhedron* **1988**, *7*, 1321.

59) Ashby, M. T.; Govindan, G. N.; Grafton, A. K. "Metal-Assisted Racemization of the Atropisomers of a 1,1'-Binaphthyl Skeleton via a *Syn* Transition State" *J. Am. Chem. Soc.* **1994**, *116*, 4801.

60) Ashby, M. T. "Inverse Relationship between the Kinetic and Thermodynamic Stabilities of the Misdirected Ligand Complexes Δ/Λ-(δ/λ-1,1'-Biisoquinoline)-bis(2,2'-bipyridine)metal(II) (metal = Ruthenium, Osmium)" *J. Am. Chem. Soc.* **1995**, *117*, 2000.

61) Ashby, M. T.; Schwane, J. D.; Daniel, T. A., *Inorg. Chem.*, submitted.

62) Hascall, T.; Rabinovich, D.; Murphy, V. J.; Beachy, M. D.; Friesner, R. A. "Mechanistic and Theoretical Analysis of the Oxidative Addition of H_2 to Six-Coordinate Molybdenum and Tungsten Complexes $M(PMe_3)_4X_2$ (M = Mo, W; X = F, Cl, Br, I): An Inverse Equilibrium Isotope Effect and an Unprecedented Halide Dependence" *J. Am. Chem. Soc.* **1999**, *121*, 11402.

63) Consigli, G.; Morandini, F. "Half-sandwich Chiral Ruthenium Complexes" *Chem. Rev.* **1987**,*87*.

64) Winkhaus, G.; Singer, H. "Ruthen(II)-Komplexe mit Zweizahnigem Cycloheptatrien und Benzol" *J. Organomet. Chem.* **1967**,*7*, 487.

65) Zelonka, R. A.; Baird, M. C. "Benzene Complexes of Ruthenium (II)" *Can. J. Chem.* **1972**, *50*, 3063.

66) Freedman, D. A.; Magneson, D. J.; Mann, K. R. "Synthesis, Characterization, and Photochemistry of Bis(arene) and Acetonitrile Complexes of Osmium(II)" *Inorg. Chem.* **1995**, *34*, 2617.

67) LeBozec, H.; Touchard, D.; Dixneuf, P. H. "Organometallic Chemistry of Arene Ruthenium and Osmium Complexes" *Adv. Organomet. Chem.* **1989**, *29*, 163.

68) Crabtree, R. H.; Pearman, A. J. "Arene-Ruthenium Complexes Containing Nitrogen Donor Ligands" *J. Organomet. Chem.* **1977**, *141*, 325.

69) Robertson, D. R.; Stephenson, T. A. "Some η^5-Cyclohexadienyl Complexes of Ruthenium" *J. Organomet. Chem.* **1977**, *142*, C31.

70) Faraone, F.; Loprete, G. A.; Tresoldi, G. "Neutral Binuclear and Cationic Mononuclear η^6-benzeneruthenium(II) Complexes Containig Neutral Bidentate Ligands" *Inorg. Chim. Acta.* **1979**, *34*, L251.

71) Brunner, H.; Oeschey, R.; Nuber, B. "Optically Active Transition Metal Complexes. 109. Novel (η^6-benzene)ruthenium Complexes with a Chiral Pyrrolecarbaldiminato Chelate Ligand: Synthesis, Crystal Structures, Properties, and Stereochemistry at the Ruthenium Atom" *Organometallics* **1996**, *15*, 3616.

72) Brunner, H.; Oeschey, R.; Nuber, B. "Synthesis, Properties, Stereochemistry and Crystal Structures of Diastereometric Benzene-Ruthenium(II) Complexes with a Chiral Salicylideneaminato Ligand" *J. Chem. Soc., Dalton Trans.* **1996**, 1499.

73) Brunner, H.; Oeschey, R.; Nuber, B. "Optically Active Transition Metal Complexes. Part 108. Synthesis, Crystal Structure and Properties of a Novel "quasi-meso" Dinuclear η^6-benzene-ruthenium (II) Complex with Chiral Salicylaldiminato Ligands" *J. Organomet. Chem.* **1996**, *518*, 47.

74) Brunner, H.; Oeschey, R. "Stereochemistry at the Chiral Ruthenium Atom in Half-sandwich Compounds of the Type [η^6-Ar)Ru(LL*)L']X and [η^6-Ar)Ru(LL*)Hal]. X-ray Structure Analysis of [η^6-cymene)Ru(LL*)$_4$-Mepy]PF_6 and Appeal for the Proper use of Stereochemical Terminology" *Inorg. Chem.* **1995**, *34*, 3349.

75) Brunner, H.; Oeschey, R.; Nuber, B. "Propeller Isomerism of the Triphenylphosphane Ligand in Half-sandwich Ru(III) Complexes" *Angew. Chem., Int. Ed. Engl.* **1994**, *33*, 866.

76) Brunner, H.; Gastinger, R. G. "Synthesis of Optically Active η^6-Benzene-Ruthenium Complexes" *J. Chem. Soc., Chem. Commun.* **1977**, 488.

77) Sargeson, A. M. "Conformations of Coordinated Chelates" *Transition Metal Chem.* **1967**, *3*, 303.

78) Tanimura, T.; Ito, H.; Fujita, J.; Saito, K.; Hirai, S.; Yamasaki, K. "Optical isomers of 2,2'-Diaminobiphyenylbis(ethylenediamine) Cobalt(III) chloride and its related complexes" *J. Coord. Chem.* **1973**, *3*, 161.

79) Boucher, H.; Bosnich, B. "Conformational Dissymmetry. Circular Dichroism and Stereospecificty Induced by Skew Six-Membered Chelate Rings" *Inorg. Chem.* **1976**, *15*, 1471.

80) Hawkins, C. J.; Palmer, J. A. "Conformational Analysis of Chelate Ring Systems by NMR" *Coord. Chem. Rev.* **1982**, *44*, 1.

81) Kuroda, Y.; Tanaka, N.; Goto, M.; Sakai, T. "Conformational Interconversion Rates of 1,2-Diamine Chelates: Determination by Paramagnetic NMR Spectra of Low-spin Iron(III) Complexes" *Inorg. Chem.* **1989**, *28*, 997.

82) Su, C. C.; Lin, Y.-L.; Liu, S.-J.; Change, T.-H.; Wang, S.-L.; Liao, F.-L. "Bonding Properties of Copper(II)-N Chromophores: Molecular and Electronic Structures of Copper(II) Complexes Containing Ethylenediamine and Heterocyclic Diimine Ligands" *Polyhedron* **1993**, *12*, 2687.

83) Radlowski, C.; Liu, C. F.; Kim, C. H.; Choi, S. R.; Jun, M. J. "Diamine Platinum(II) Complexes of 2,2'-Diaminobiphenyl" *Polyhedron* **1985**, *4*, 769.

84) Radlowski, C. A.; Liu, C. F.; Jun, M. J. "Crystal and Molecular-Structure of the (2 ;2'-Diaminobiphenyl)-(R ;R-Trans-1 ;2-Diaminocyclohexane)Platinum(II) Complex" *Inorg. Chim. Acta* **1984**, *86*, 101.

85) Jordan, W. T.; Lin, C. Y.; Douglas, B. E. "Circular Dichroism of Some Cobalt(III) Complexes with 2,2'-Diaminobiphenyl and R-6,6'-Dimethyl-2,2'-Diaminobiphenyl" *J. Coord. Chem.* **1973**, *3*, 1.

86) Smith, W. B. "Observations on the Reduction of Aryl Nitro Groups with Palladium-Sodium Borohydride" *J. Heterocycl. Chem.* **1987**, *24*, 745.

87) Ottersen, T. "The Crystal and Molecular Structure of 2,2'-Diaminodiphenyl at -165" *Acta Chem. Scand.* **1977**, *A31*, 480.

88) Pignolet, L. H.; Taylor, R. P.; Horrocks, W. D. J. "The Absolute Configuration of a Dissymmetric Pseudotetrahedral Coordination Compound Containing a Restricted Biphenyl. Molecular Structure of D-2,2'-Bis(salicylidenaminato)- $(+)_D$ - (R)- 6,6'-Dimethylbiphenylcobalt(II)." *J. Am. Chem. Soc.* **1969**, *91*, 5457.

89) Frydendahl, H.; Toftlund, H.; Becher, J.; Dutton, J. C.; Murray, K. S.; Taylor, L. F.; Anderson, O. P.; Tiekink, E. R. T. "Changes in Geometries and Spin States of Thiolato-Schiff Base NiN_2S_2 Complexes Containing N,N' Biphenyl Backbones" *Inorg. Chem.* **1995**, *34*, 4467.

90) Ligtenbarg, A. G. J.; Van den Beuken, E. K.; Meetsma, A.; Veldman, N.; Smeets, W. J. J.; Spek, A. L.; Feringa, B. L. "New Mono- and di-Nuclear Complexes of Pd(II), Pt(II) and Ni(II) of PNNP Ligands with a 2,2'-Biaryl Bridging Unit" *J. Chem. Soc., Dalton Trans.* **1998**, 263.

91) Maslak, P.; Chopra, A.; Moylan, C. R.; Wortmann, R.; Lebus, S.; Rheingold, A. L.; Yap, G. P. A. " Optical Properties of Spiroconjugated Charge-Transfer Dyes" *J. Am. Chem. Soc.* **1996**, *118*, 1471.

92) Griffith, W. P.; Reddy, B.; Shoair, A. G. F.; Suriaatmaja, M.; White, A. J. P.; Williams, D. J. "Ruthenate(VI)-Catalysed Dehydrogenation of Primary Amines to Nitriles, and Crystal Structures of Cis-$[Ru(Bipy)_2(NH_2CH_2Ph)_2][PF_6]_2$ ·0.5MeOH and Cis-$[Ru(Bipy)_2(NCPh)_2][PF_6]_2$ ·CH_2Cl_2" *J. Chem. Soc., Dalton Trans.* **1998**, *17*, 2819.

93) Arthur, T.; Stephenson, T. A. "Synthesis of Triple Halide-Bridged Arene Complexes of Ruthenium(II) and Osmium(II)" *J. Organomet. Chem.* **1981**, *208*, 369.

94) Alguindigue, S. S.; Khan, M. A.; Ashby, M. T. "Kinetics and Mechanism of the Stereochemical Isomerization of an Arene-Ruthenium Complex of the Atropisomeric Ligand 1,1'-Biphenyl-2,2'-Diamine" *Organometallics* **1999**, *18*, 5112.

95) Mandal, S. K.; Chakravarty, A. R. "Arene Ruthenium Complexes of N,N'-Donor and N,O-Donor Schiff-Base Ligands : An X-Ray Structure of [(H-6-Para-Cymene)RuCl(C_5H_4N-2-CH=NC_6H_4-Para-Me)]Cl-Bullet-C_6H_6• H_2O" *Polyhedron* **1992**, *11*, 823.

96) McCormick, F. B.; Cox, D. D.; Gleason, W. B. "Synthesis, Structure, and Disproportionation of Labile (η-6-C_6H_6)Ru($CH_3CN)_2Cl^+$ Salts" *Organometallics* **1993**, *12*, 610.

97) Gould, R. O.; Jones, C. L.; Robertson, D. R.; Stephenson, T. A. "Diammine(η^6-benzene)chlororuthenium(II)hexafluorophosphate (3/1) ammonium hexafluorophosphate [C_6H_6RuCl($NH_3)_2]_3$" *Cryst. Struct. Commun.* **1978**, *7*, 27.

98) Davies, D. L.; Fawcett, J.; Garvatt, S. A.; Russell, D. R. "Chiral Arene Ruthenium Complexes as Asymmetric Diels-Alder Catalysts" *J. Chem. Soc., Chem. Commun.* **1997**, 1351.

99) Elsegood, M. R. J.; Tocher, D. A. "The Synthesis of New Paracyclophane Complexes of Ruthenium(II) : Crystal-Structure of [Ru(η-6-C_6H_{16})Cl-($C_5H_5N)_2$][PF_6]" *J. Organomet. Chem.* **1988**, *356*, C29.

100) Mosny, K. K.; de Gala, S. R.; Crabtree, R. H. "Arene Ruthenium Complexes of the Thermally Resistant Ligand tri-2-pyridylamine" *Trans. Met. Chem.* **1995**, *20*, 595.

101) Ashby, M. T.; Manke, I. A.; Khan, M. A. **Unpublished crystal structure of Ir(bipy)$_2$(biiq)$^{3+}$.**

102) Cheng, L.-K.; Yeung, K.-S.; Che, C.-M.; Chang, M.-C.; Wang, Y. "X-Ray Structure and Spectroscopic Properties of Platinum(II) Complexes of 1,1'-Biisoquinoline" *Polyhedron* **1993**, *12*, 1201.

103) Kopt, H.; Schmidt, M. "Uber Einige π-Komplexstabilisierte Titan-schwefel-heterocyclen" *J. Organomet. Chem.* **1967**, *4*, 426.

104) Green, M. L. H.; Lindsell, W. E. "Some Bis-π-Cyclopentadienyl-Molybdenum and -Tungsten Complexes with Sulphur or Oxygen Ligands" *J. Chem. Soc. A.* **1967**, 1455.

105) Muller, E. G.; Watkins, S. F.; Dahl, L. F. "Preparation of $V(\eta^5\text{-}C_5H_5)_2(SC_6H_5)_2$ and Stereochemical Characterization of $M(\eta^5\text{-}C_5H_5)_2(SC_6H_5)_2$ (M=Ti,V): The Geometrical Effect of an Unpaired Electron on a $M(\eta^5\text{-}C_5H_5)_2L_2$ Complex" *J. Organomet. Chem.* **1976**, *111*, 73.

106) Darensbourg, M. Y.; Silva, R.; Reibenspies, J.; Prout, C. K. "Structural Studies of $(\eta^5\text{-}C_5H_5)_2Nb(SC_6H_4)_2$, $[(\eta^5\text{-}C_5H_5)_2Nb(SC_6H_4)_2^+]$ and $(\eta^5\text{-}C_5H_5)_2Nb(\mu\text{-}SC_6H_5)_2Mo(CO)_4^+]$" *Organometallics* **1989**, *8*, 1315.

107) Peterson, J. L.; Dahl, L. F. "Nonparameterized Molecular Orbital Calculations and Photoelectron Spectroscopy of Open- and Closed-Shell M(IV) $M(\eta^5\text{-}C_5H_5)_2L_2$ complexes" *J. Am. Chem. Soc.* **1975**, *97*, 6433.

108) Calhorda, M. J.; Carrondo, M. A. A. F. d. C. T.; Dias, A. R.; Frazão, C. F.; Hursthouse, M. B.; Martinho Simões, J. A.; Teixeira, C. "Energetics of Metal-Sulfur Bonds in the Complexes $M(\eta^5\text{-}C_5H_5)_2(SC_2H_5)_2$ (M=Ti,W) and $W(\eta^5\text{-}C_5H_5)_2(SC_6H_5)_2$. Molecular Structure of $Ti(\eta^5\text{-}C_5H_5)_2(SC_2H_5)_2$." *Inorg. Chem.* **1988**, *27*, 2513.

109) Simpson, C. Q.; Hall, M. B. "Ab Initio Calculations on the Structure and Conformation of Group V Bent Metallocenethiolates" *New J. Chem.* **1991**, *15*, 763.

110) Lauher, J. W.; Hoffmann, R. "Structure and Chemistry of Bis(Cyclopentadienyl)-MLn Complexes" *J. Am. Chem. Soc.* **1976**, *98*, 1729.

111) Peterson, J. L.; Dahl, L. F. "Single-Crystal Electron Paramagnetic Resonance and Nonparameterized Fenske-Hall Molecular Orbital Calculations Substantiating the Demise of the Balhausen-Dahl Bonding Model for d^1 and d^2 M(IV) $M(\eta^5\text{-}C_5H_5)_2L_2$ complexes" *J. Am. Chem. Soc.* **1974**, *96*, 2248.

112) Peterson, J. L.; Dahl, L. F. "Dilute Single-Crystal Electron Paramagnetic Resonance Study of Bis(cyclopentadienyl)vanadium Pentasulfide, $V(\eta^5\text{-}C_5H_5)_2S_5$. The Coupe de Grace to the Ballhausen-Dahl Bonding Model Applied to $M(\eta^5\text{-}C_5H_5)_2L_2$ -Type complexes" *J. Am. Chem. Soc.* **1975**,*97*, 6416.

113) Peterson, J. L.; Dahl, L. F. "Synthesis and Structural Characterization by X-Ray Diffraction and Electron Paramagnetic Resonance Single-Crystal Techniques of $V(\eta^5\text{-}C_5H_4CH_3)_2Cl_2$ and $Ti(\eta^5\text{-}C_5H_4CH_3)_2Cl_2$. A Study of the Spatial Distribution of the Unpaired Electron in a $V(\eta^5\text{-}C_5H_5)_2L_2$ -Type Complex" *J. Am. Chem. Soc.* **1975**, *97*, 6422.

114) Darensbourg, M. Y.; Bischoff, C. J.; Houliston, S. A.; Pala, M.; Reibenspies, J. "Conformation of $(\eta^5\text{-}C_5H_5)_2Nb(S\text{-}p\text{-}C_6H_4X)_{2n}$ (n=0,1): Responsiveness to Para Substituents of Aryl Groups and to d-Electron Count" *J. Am. Chem. Soc.* **1990**, *112*, 6905.

115) Ashby, M. T.; Alguindigue, S. S.; Khan, M. A. "Misdirected π-Donor Ligands: $(\eta^6\text{-}C_5H_5)Zr(Cl)(SR)$ with Sterically More Demanding R Groups have Lower Rotational Barriers" *Inorg. Chim. Acta* **1998**, *270*, 227.

116) Calhorda, M. J.; Carrondo, M. A. A. F. d. C. T.; Garcia, M. H. "The X-ray Crystal Structure of di-η^5-cyclopentadienylthiphenolatoamminemolybdenum(IV) hexafluorophosphate solvate, $[Mo(\eta^5\text{-}C_5H_5)_2(NH_3)(SC_6H_5)][PF_6]$ $(CH_3)_2CO$" *J. Organomet. Chem.* **1988**, *342*, 209.

117) Carrondo, M. A. A. F. d. C. T.; Jeffrey, G. A. "Bis(η^5-cyclopentadienyl)bis(methanethiolato) titanium(IV), $(\eta^5\text{-}C_5H_5)_2Ti(SCH_3)_2$" *Acta Crystallogr.* **1983**, *C39*, 42.

118) White, G. S.; Stephan, D. W. "Synthesis and Structural Studies of Ti-Rh Heteobimetallic Complexes. Characterization and Electrochemistry of the Redox Partners $[Ti(Cp)_2(SCH_2CH_2CH_2PPh_2)_2Rh]BF_4$ and $[Ti(Cp)_2(SCH_2CH_2CH_2PPh_2)_2Rh]^0$" *Organometallics* **1987**, *6*, 2169.

119) Wark, T. A.; Stephan, D. W. "Early Metal Thiolato Species as Metalloligands in the Formation of Early/Late Heterobimetallic Complexes: Synthesis and Molecular Structures of $Cp_2Ti(SMe)_2$, $Cp_2V(SMe)_2$, $(Cp_2Ti(\mu\text{-}SMe)_2)_2Ni$ and $(Ni(\mu\text{-}SMe)_2)_6$." *Organometallics* **1989**, *8*, 2836.

120) Hunter, J. A.; Lindsell, W. E.; McCullough, K. J.; Parr, R. A.; Scholes, M. L. "Bis(η-5-Cyclopentadienyl) Complexes Of Niobium(IV) And Tantalum(IV) : Electron-Spin-Resonance and Electrochemical Studies and the Molecular-Structure of$[Ta(SCOPh)_2(H\text{-}5\text{-}C_5H_5)_2]$" *J. Chem. Soc., Dalton Trans.* **1990**, *7*, 2145.

121) Carrondo, M. A. A. F. d. C. T.; Matias, P. M.; Jeffrey, G. A. "Bis(*tert*-butylthio)bis(η^5-cyclopentadienyl)molybdenum(IV), $[Mo(C_5H_5)_2(C_4H_9S)_2]$" *Acta Crystallogr.* **1984**, *C40*, 932.

122) Dias, A. R.; Simoes, J. A. M.; Teixeira, C. "Enthalpies of Formation of $[Mo(\eta\text{-}C_5H_5)_2(SR)_2]$ Complexes : R=n-C_3H_7, i-C_3H_7, n-C_4H_9, or t-C_4H_9" *J. Chem. Soc., Dalton Trans.* **1980**, 1178.

123) Calhorda, M. J.; Dias, A. R.; Simoes, J. A. M.; Teixeira, C. "Enthalpies of Formation of Complexes $[M(\eta\text{-}C_5H_5)_2(SR)_2]$ (M=Mo, W, Or Ti R=C_3H_7, C_4H_9, Or C_6H_5) : Metal-Sulfur Bond Enthalpies" *J. Chem. Soc., Dalton Trans.* **1984**, 2659.

124) Stephan, D. W. "Early Late Heterobimetallics" *Coord. Chem. Rev.* **1989**, *95*, 41.

125) White, G. S.; Stephan, D. W. "Synthesis, Electrochemistry, Reactivity, and Structural Studies of the Early Late-Transition-Metal Heterobimetallic Complex $[Cp_2Ti(SCH_2CH_2CH_2PPh_2)_2Ni]$" *Organometallics* **1988**, *7*, 903.

126) White, G. S.; Stephan, D. W. "Synthesis, Electrochemistry, and Crystal and Molecular-Structure of $[(C_5H_5)_2Ti(SCH_2CH_2P(C_6H_5)_2)_2Cu]BF_4$: A Heterobimetallic Species With a Copper To Titanium Dative Bond" *Inorg. Chem.* **1985**, *24*, 1499.

127) Wark, T. A.; Stephan, D. W. "Synthesis, Characterization, and Structural Studies of Thiolato-Bridged Titanium(IV)-Copper(I) Species : Heterobimetallic Complexes Containing D10-D0 Dative Bonds" *Inorg. Chem.* **1987**, *26*, 363.

128) Darensbourg, M. Y.; Pala, M.; Houliston, S. A.; Kidwell, K. P.; Spencer, D.; Chojnacki, S. S.; Reibenspies, J. H. "Stereochemical Nonrigidity in Heterobimetallic Complexes Containing the Bent Metallocene Thiolate Fragment" *Inorg. Chem.* **1992**, *31*, 1487.

129) Wark, T. A.; Stephan, D. W. "Early Late Heterobimetallic Complexes : Syntheses and Spectral and Structural Studies of Thiolato-Bridged Ti/Cu and V/Cu Complexes" *Inorg. Chem.* **1990**, *29*, 1731.

130) Senocq, F.; Viguier, N.; Gleizes, A. "Bis(η^5-Cyclopentadienyl)Bis(Thiolato)Titanium(IV) And Zirconium(IV): Synthesis And Crystal Structure Of $Cp_2M(StBu)_2$(M=Ti,Zr). Use Of $Cp_2Ti(StBu)_2$ and $Cp_2Ti(SEt)_2$ As Single-Source Precursors for the Chemical Vapour Deposition of Titanium Sulfides" *Eur. J. Solid State Inorg. Chem.* **1996**, *33*, 1185.

131) Shaver, A.; McCall, J. M.; Bird, P. H.; Ansari, N. "Preparation and Structure of $(\eta^5\text{-}C_5H_5)_2Ti(SC_6H_6)(SSSC_6H_5)$: The Product of a Sulfur Catenation Reaction" *Organometallics* **1983**, *2*, 1894.

132) Yam, V. W. W.; Qi, G. Z.; Cheung, K. K. "Synthesis of Luminescent Zirconium Thiolate Complexes. Crystal Structures of $(\eta^5\text{-}C_5H_5)_2Zr(SC_6H_4Cl\text{-}p)_2$ and $[(\eta^5\text{-}C_5H_5)_2Zr(SC_6H_4OMe\text{-}p)]_2O$" *J. Organomet. Chem.* **1997**, *548*, 289.

133) Petersen, J. L. "Preparation and Structural Characterization of $[(\eta^5\text{-}C_5H_5)_2Zr(SC_6H_5)]_2O$. A Qualitative Description of the Bonding in Oxo-Bridged Dicyclopentadienyl-Transition Metal Dimers" *J. Organomet. Chem.* **1979**, *166*, 179.

134) Piers, W. E.; Koch, L.; Ridge, D. S.; MacGillivray, L. R.; Zaworotko, M. "C-S Bond cleavage at an Electrophilic Zirconium Center: Synthesis, Structure, and

Thermal Decomposition of [$Cp_2Zr(S\text{-}t\text{-}C_4H_9)(THF)[BPh_4]$]" *Organometallics* **1992**, *11*, 3148.

135) Kubick, M. M.; Kergoat, R.; Gomes De Lima, L. C.; Cariou, M.; Scordia, H.; Guerchais, J. E.; L'Haridon, P. "Transition Metal-Cyanocarbon Chemistry. Part V*. Crystal and Molecular Structures of biscyclopentadienyl Complexes Containng a σ-Cyanoalkyl and a σ-Cyanoalkenyl Ligand: (η^5-$C_5H_5)_2Mo[S(C_6H_5)](\sigma$–$CH(CN)$-$CH_3)$ and (η^5-$C_5H_5)_2Mo[S_2CN(C_2H_5)_2)$-($\sigma$–$C(CN)=CH_2)$" *Inorg. Chim. Acta* **1985**, *104*, 191.

136) Carrondo, M. A. A. F. d. C. T.; Dias, A. R.; Garcia, M. H.; Matias, P. M.; Robalo, M. P.; Green, M. L. H.; Higgings, J.; Yang, Y. Y. "Syntheses and Reactivity of *p*-Substituted Benzonitrile Complexes Derived from Dicyclopentadienyl-Molybdenum and -Tungsten. Oxidative Electrochemistry. The Crystal Structure of [$Mo(\eta^5\text{-}C_5H_5)_2(SC_6H_5)(p\text{-}(CH_3)_2NC_6H_4CN)][PF_6]$" *J. Organomet. Chem.* **1990**, *395*, 279.

137) Sandstrom, J. *Dynamic NMR Spectroscopy*; Academic Press: New York, 1982.

138) Frisch, M. J.; Trucks, G. W.; Schlegel, H. B.; Gill, P. M. W.; Johnson, B. G.; Robb, M. A.; Cheeseman, J. R.; Keith, T.; Petersson, G. A.; Montgomery, J. A.; Raghavachari, K.; Al-Laham, M. A.; Zakrzewski, V. G.; Ortiz, J. V.; Foresman, J. B.; Cioslowski, J.; Stefanov, B. B.; Nanayakkara, A.; Challacombe, M.; Peng, C. Y.; Ayala, P. Y.; Chen, W.; Wong, M. W.; Andres, J. L.; Replogle, E. S.; Gomperts, R.; Martin, R. L.; Fox, D. J.; Binkley, J. S.; Defrees, D. J.; Baker, J.; Stewart, J. P.; Head-Gordon, M.; Gonzalez, C.; Pople, J. A. *Gaussian 94*; Revision C.3 ed.; Gaussian, Inc.: Pittsburgh, PA, 1995.

139) Frisch, M. J.; Trucks, G. W.; Schlegel, H. B.; Scuseria, G. E.; Robb, M. A.; Cheeseman, J. R.; Zakrzewski, V. G.; Montgonery, J. A.; Stratmann, R. E.; Burant, J. C.; Dapprich, S.; Milliam, J. M.; Daniels, A. D.; Kudin, K. J.; Strain, M. C.; Farkas, O.; Tomasi, J.; Varone, V.; Cossi, M.; Cammi, R.; Mennucci, B.;

Pomelli, C.; Adamo, C.; Clifforn, S.; Ochterski, J.; Petersson, G. A.; Ayala, P. Y.; Cui, Q.; Morokuma, K.; Malick, D. K.; Rabuck, A. D.; Raghavachari, K.; Foresman, J. B.; Cioslowski, J.; Ortiz, J. V.; Stefanov, B. B.; Liu, G.; Liashenko, A.; Piskorz, P.; Komaromi, I.; Gomperts, R.; Martin, R. L.; Fox, D. J.; Keith, T.; Al-Laham, M. A.; Peng, C. Y.; Nanayakkara, A.; Gonzalez, C.; Challacombe, M.; Gill, P. M. W.; Johnson, B.; Chen, W.; Wong, M. W.; Andres, J. L.; Gonzalez, C.; Head-Gordon, M. R.; Pople, J. A. *Gaussian 98*; R ed.; Gaussian, Inc.: Pittsburgh, PA., 1998.

140) Stephens, P. J.; Devlin, F. J.; Chabalowski, C. F.; Frisch, M. J. "Ab-Initio Calculation of Vibrational Absorption and Circular-Dichroism Spectra using Density-Functional Force-Fields" *J. Phys. Chem.* **1994**, *98*, 11623.

141) Becke, A. D. "A New Mixing of Hartree-Fock and Local Density-Functional Theories" *J. Chem. Phys.* **1993**, *98*, 1372.

142) Lee, C.; Yang, W.; Parr, R. G. "Development of the Colle-Salvetti Correlation-Energy Formula into a Functional of the Electron Density" *Phys. Rev. B* **1988**, *37*, 785.

143) Miehlich, B.; Savin, A.; Stoll, H.; Preuss, H. "Results Obtained with the Correlation-Energy Density Functionals of Becke and Lee, Yang and Parr" *Chem. Phys. Lett.* **1989**, *157*, 200.

144) Booth, H.; Everett, J. R. "The Experimental Determination of the Conformational Free Energy, Enthalpy, and Entropy Differences for Alkyl Groups in Alkylcyclohexanes by Low Temperature Carbon-13 Magnetic Resonance Spectroscopy" *J. Chem. Soc., Perkin Trans. 2* **1980**, 255.

145) Abel, E. W.; Budgen, D. E.; Moss, I.; G., O. K.; Sik, V. "A Multinuclear (^{1}H, ^{13}C and ^{95}Mo) NMR Investigation of Sulphur Inversion in Molybdenum Tetracarbonyl Complexes of Chelating Dithioethers" *J. Organomet. Chem.* **1989**, *362*, 105.

146) Yam, V. W. W.; Qi, G. Z.; Cheung, K. K. "Synthesis, Emission, and Molecular Orbital Studies of Luminescent Hafnium Thiolate Complexes. Crystal Structures of $(\eta 5\text{-}C_5Me_5)_2Hf(SR)_2$ (R = Bu-N, C_6H_5, C_6H_4OMe-p)" *Organometallics* **1998**, *17*, 5448.

147) Yam, V. W. W.; Ai, G. A.; Cheung, K. K. "Synthesis, Emission and Molecular Orbital Studies of Luminescent Zirconium Thiolate Complexes. Crystal Structure of $[Zr(\eta^5\text{-}C_5Me_5)_2(S^nBu)_2]$" *J. Chem. Soc., Dalton Trans.* **1998**, *11*, 1819.

148) Howard, W. A.; Trnka, T. M.; Parkin, G. "Syntheses of the Phenylchalcogenolate Complexes $(\eta^5\text{-}C_5Me_5)_2Zr(EPh)_2$ (E= O,S,Se,Te) and $(\eta^5\text{-}C_5H_5)_2Zr(OPh)_2$: Structural Comparisons within a Series of Complexes Containing Zirconium-Chalcogen Single Bonds" *Inorg. Chem.* **1995**, *34*, 5900.

149) North, A. C. T.; Phillips, D. C.; Mathews, F. S. "A Semi-Empirical Method of Absorption Correction" *Acta Crystallogr.* **1968**, *A24*, 351.

150) SHELXTL Software Package for the Determination of Crystal Structures, R., Siemens Analytical X-Ray Instruments, Inc., Madison, WI, 1995. .

151) Cardin, D. J.; Lappert, M. F.; Raston, C. L. *Chemistry of Organo-Zirconium and Hafnium Compounds*; Wiley: New York, 1986.

152) Siegel, J. S.; Anet, F. A. L. "Dichlorofluoromethane-d: A Versatile Solvent for VT-NMR Experiments" *J. Org. Chem.* **1988**, *53*, 2629.

153) Binkely, J. S.; Pople, J. A.; Hehre, W. J. "Self-Consistent Molecular-Orbital Methods .21. Small Split-Valence Basis-Sets for 1st-Row Elements" *J. Am. Chem. Soc.* **1980**, *102*, 939.

154) Gordon, M. S.; Binkley, J. S.; Pople, J. A.; Pietro, W. J.; Hehre, W. J. "Self-Consistent Molecular-Orbital Methods .22. Small Split-Valence Basis-Sets For 2nd-Row Elements" *J. Am. Chem. Soc.* **1982**, *104*, 2797.

155) Pietro, W. J.; Grancl, M. M.; Hehre, W. J.; Defree, D. J.; Pople, J. A.; Binkley, J. S. "Self-Consistent Molecular-Orbital Methods .24. Supplemented Small Split-Valence Basis-Sets For 2nd-Row Elements" *J. Am. Chem. Soc.* **1982**, *104*, 5039.

156) Hay, P. J.; Wadt, W. R. "Abinitio Effective Core Potentials For Molecular Calculations : Potentials for the Transition-MetalAtoms Sc to Hg" *J. Chem. Phys.* **1985**, *82*, 270.

157) Wadt, W. R.; Hay, P. J. "Abinitio Effective Core Potentials for Molecular Calculations : Potentials for Main Group Elements Na to Bi" *J. Chem. Phys.* **1985**, *82*, 284.

158) Hay, P. J.; Wadt, W. R. "Abinitio Effective Core Potentials for Molecular Calculations : Potentials for K to Au Including the Outermost Core Orbitals" *J. Chem. Phys.* **1985**, *82*, 299.

159) Becke, A. D. "Density-Functional Exchange-Energy Approximation with Correct Asymptotic Behavior" *Phys. Rev. A* **1988**, *38*, 3098.

160) Head-Gordon, M.; Pople, J. A.; Frisch, M. J. "MP2 Energy Evaluation By Direct Methods" *Chem. Phys. Let.* **1988**, *153*, 503.

161) Frisch, M. J.; Head-Gordon, M.; Pople, J. A. "A Direct MP2 Gradient-Method" *Chem. Phys. Let.* **1990**, *166*, 275.

162) Frisch, M. J.; Head-Gordon, M.; Pople, J. A. "Semidirect Algorithms for the MP2 Energy and Gradient" *Chem. Phys. Let.* **1990**, *166*, 281.

163) Head-Gordon, M.; Head-Gordon, T. "Analytic MP2 Frequencies Without 5th-Order Storage : Theory and Application to Bifurcated Hydrogen-Bonds in the Water Hexamer" *Chem. Phys. Let.* **1994**, *220*, 122.

164) Saebo, S.; Almlof, J. "Avoiding the Integral Storage Bottleneck in LCAO Calculations of Electron Correlation" *Chem. Phys. Let.* **1989**, *154*, 83.

165) Rance, M.; Sorensen, O. W.; Bodenhausen, G.; Wagner, G.; Ernst, R. R.; Wüthrich, K. "Improved Spectral Resolution In COSY H-1-NMR Spectra of Proteins Via Double Quantum Filtering" *Biochem. Biophys. Res. Commun.* **1983**, *117*, 479.

166) Kumar, A.; Wagner, G.; Ernst, R.; Wuthrich, K. "Buildup Rates of the Nuclear Overhauser Effect Measured by Two-Dimensional Proton Magnetic Resonance Spectroscopy: Implications for Studies of Protein Conformation" *J. Am. Chem. Soc.* **1981**, *103*, 3654.

167) Green, M. L. H.; Wong, L.-L.; Sella, A. "Relationship Between Intramolecular Chemical-Exchange And NMR-Observed Rate Constants" *Organometallics* **1992**, *11*, 2660.

168) Hore, P. J. *Nuclear Magnetic Resonance*; Oxford University Press: Oxford, 1995.

169) Meier, B. H.; Ernst, R. R. "Elucidation of Chemical Exchange Networks by Two-Dimensional NMR Spectroscipy The Heptamethylbenzenonium Ion" *J. Am. Chem. Soc.* **1979**, *101*, 6441.

170) Shanan-Atidi, H.; Bar-Eli, K. H. "A Convenient Method for Obtaining Free Energies of Activation by the Coalescence Temperature of an Unequal Doublet" *J. Phys. Chem.* **1970**, *74*, 961.

171) Perrin, C. L.; Johnston, E. R.; Lollo, C. P.; Kobrin, P. A. "NMR Studies of Base-Catalyzed Proton Exchange in Amides" *J. Am. Chem. Soc.* **1981**, *103*, 4691.

172) QCPE 364. DNMR5: Iterative Nuclear Magnetic Resonance Program for Unsaturated Exchange-Broadened Bandshapes by David S. Stephenson and Gerhard Binsch, I. o. O. C., University of Munich, Munich, FRG. .

173) Alger, J. R.; Prestegard, J. H. "Investigation of Peptide-Bond Isomerization by Magnetization Transfer NMR" *J. Mag. Res.* **1977**, *27*, 137.

174) Kuchel, R. W.; Chapman, B. E. "NMR Spin Exchange Kinetics at Equilibrium in Membrane-Transport and Enzyme-Systems" *J. Theor. Biol.* **1983**, *105*, 569.

175) Robinson, G.; Kuchel, P. W.; Chapman, B. E. "A Simple Procedure for Selective Inversion of NMR Resonances for Spin Transfer Enzyme Kinetic Measurements" *J. Mag. Res.* **1985**, *63*, 314.

176) Bellon, S. F.; Chen, D.; Johnston, E. R. "Quantitative 1D Exchange Spectroscopy" *J. Mag. Res.* **1987**, *73*, 168.

177) Jones, A. "Spiral-A New Algorithm for Non-linear Parameter Estimation Using Least Squares" *Comput. J.* **1970**, *13*, 301.

178) Wang, D.; Shen, H.; Richmond, M. G.; Schwartz, M. "Carbonyl Fluxionality In the Nido Cluster $Ru_3(Co)_9(\mu_3\text{-}CO)(\mu_3\text{-}NPh)$: NMR Evidence and Mechanism for the Exchange of the Triply-Bridging CO With the Terminal CO Groups" *Organometallics* **1995**, *14*, 3636.

179) Perrin, C. L.; Gipe, R. K. "Multisite Kinetics by Quantitative Two-Dimensional NMR" *J. Am. Chem. Soc.* **1984**, *106*, 4036.

180) Willem, R.; Biesemans, M.; Hallengas, K.; Leppens, G.; Malaisse-Lagae, F.; Malaisse, W. J. "Dual Anomeric Specificity and Dual Anomerase Activity of Phosphoglucoisomerase Quantified By 2-Dimensional Phase-Sensitive C-13 EXSY NMR" *J. Biol. Chem.* **1992**, *267*, 210.

181) Ni, J.; Kubiak, C. P. "Dynamic Exchange Between the Covalent and Dative Metal-Metal Bonded Isomers of the Heterodinuclear Complex $[NiPd(CNMe)_3(Dppm)_2][PF_6]_2$ By $^{31}P(1H)$ NOESY" *Inorg. Chem.* **1990**, *29*, 4345.

182) Ramachandran, R.; Knight, C. T. G.; Kirkpatrick, R. J.; Oldfield, E. "A Two-Dimensional NMR Approach to the Study of Intermolecular Scrambling Reactions" *J. Magn. Reson.* **1985**, *65*, 136.

183) Bodenhausen, G.; Ernst, R. R. "Direct Determination of Rate Constants of Slow Dynamic Processes by Two-Dimensional "Accordion" Spectroscopy in Nuclear Magnetic Resonance" *J. Am. Chem. Soc.* **1982**, *104*, 1304.

184) Abel, E. W.; Coston, T. P. J.; Orrell, K. G.; Sik, V.; Stephenson, D. "Two-dimensional NMR Exchange Spectroscopy. Quantitative treatment of multisite exchanging systems" *J. Mag. Res.* **1986**, *70*, 34.

185) Heise, J. D.; Raftery, D.; Breedlove, B. K.; Washington, J.; Kubiak, C. P. "Variable-Temperature Kinetic Analysis of a Three-Site Terminal Ligand Exchange In Nickel A-Frames By Quantitative P-31{H-1} EXSY NMR" *Organometallics* **1998**, *17*, 4461.

186) Macura, S.; Farmer, B. T. I.; Brown, L. R. "An Improved Method for the Determination of Cross-Relaxation Rates from NOE Data" *J. Magn. Res.* **1986**, *70*, 493.

187) Perrin, C. L.; Dwyer, T. J. "Application of 2-Dimensional NMR To Kinetics of Chemical-Exchange" *Chem. Rev.* **1990**, *90*, 935.

188) Wyants, C.; VanBinst, G.; Mugge, C.; Jurkschat, K.; Tzschach, A.; Pepermans, H.; Gielen, M.; Willem, R. "Two-Dimensional ^{119}Sn NMR Exchange Spectroscopy as a Tool for the Elucidation of the Dynamic Stereochemistry of Tin Compounds" *Organometallics* **1985**, *4*, 1906.

189) Pearson, J.; Cooke, J.; Takats, J.; Jordan, R. B. "Alkyne Ligand Enhancement of the Substitution Lability of Mononuclear Osmium, Ruthenium, and Iron Carbonyls" *J. Am. Chem. Soc.* **1998**, *120*, 1434.

190) Mao, T.; Zhang, Z.; Washington, J.; Takats, J.; Jordan, R. B. "Reactions of $Os(CO)_4(\eta^2\text{-}C_2H_2)$ with Phosphines: Substitution and Facile CO Insertion into Osmium-Alkyne Bonds. Combined Synthetic and Kinetic Studies." *Organometallics* **1999**, *18*, 2331.

191) Decker, S. A.; Klobukowski, M. "The First Carbonyl Bond Dissociation Energies of $M(CO)_5$ and $M(CO)_4(C_2H_2)$ (M=Fe, Ru, and Os): The Role of the Acetylene Ligand from a Density Functional Perspective" *J. Am. Chem. Soc.* **1998**, *120*, 9342.

192) Marinelli, G.; Streib, W. E.; Huffman, J. C.; Caulton, K. G.; Gagne, M. R.; Takats, J.; Dartiguenave, M.; Chardon, C.; Jackson, S. A.; Eisenstein, O. "The Origin of Structural Variety of Alkyne Complexes of D8 Metals : An Example of Structural Isomerism" *Polyhedron* **1990**, *9*, 1867.

193) Huq, R.; Poe, A. J.; Chawla, S. "Kinetics of Substitution and Oxidative Elimination Reactions of Pentacarbonylruthenium(O)" *Inorg. Chim. Acta* **1980**, *38*, 121.

194) Tsue, H.; Fujinami, H.; Itakura, T.; Tsuchiya, R.; Kobayashi, K.; Takahashi, H.; Hirao, K. "Absolute Configuration of 8,8'-Dialkyl-1,1'-Biisoquinoline" *Chem. Lett.* **1999**, *1*, 17.

195) Tsue, H.; Fujinami, H.; Itakura, T.; Hirao, K. "Unexpected Racemization Behavior of 8,8'-Dialkyl-1,1-Biisoquinoline" *Tetrahedron: Asymmetry* **1999**, *10*, 2975.

196) Tsue, H.; Fujinami, H.; Itakura, T.; Tsuchiya, R.; Kobayashi, K.; Takahashi, H.; Hirao, K. "8,8'-Dialkyl-1,1'-Biisoquinolines: Preparation, Absolute Configuration and Unexpected Racemization Behavior" *J. Chem. Soc., Perkin Trans. 1* **1999**, *24*, 3677.